



HPC-EUROPA3 THIRD RESEARCH PROJECTS DIRECTORY

April 2020 - June 2021

HPC-Europa3 aims to maintain a persistent and high-quality service offering Transnational Access to the most advanced HPC infrastructures in Europe which are currently available to the scientific research community. This third HPC-Europa programme builds on the success of previous Transnational Access programmes, which operated in Europe for almost two decades.

As would be expected from a Transnational Access programme, HPC-Europa3 offers collaborative visits to research groups in a different country from the one in which the participant currently works. Researchers collaborate with a scientific host in their own area of research, while also receiving mentoring from one of the partner HPC centres, to help them make the best use of the HPC facilities for their research.

HPC-Europa3 therefore represents a powerful mechanism to support researchers to become proficient in the use of HPC and numerical simulation.

HPC-Europa3 is a truly multi-disciplinary programme attracting applications from all computational disciplines. From its beginning in 2017, almost 800 transnational visits were approved by the programme.

The present Third Research Projects Directory presents the results of 90 projects that have been completed between April 2020 and June 2021 in wide range of scientific disciplines.

Reading the contributions presented in this report, the importance of the scientific results can be seen. This is also evidenced by the number of publications produced, confirming the significant contribution of the HPC-Europa programme to support European researchers in computational science.

Summary

Chemistry		
Cabriolu R.	TA_RETIS (Translocation of Antibiotics with Replica Exchange Transition Interface Sampling)	1
Castro Latorre P.	Ceria-supported transition metal particles: adsorption properties and charge transfer	2
Comas Vilà G.	Can donor-acceptor bonds stabilize E_4^{+2} (E=B-TL) aromatic rings?	3
Danielis N.	AgPd, AuPd and AuPt nanoalloys with Ag- or Au-rich compositions: modeling the interplay between chemical ordering and optical properties	4
Figueiredo N.	New set-up polarizable force field for [Emim][FeCl ₄]	5
George J.	Accurate phonons with machine-learned interatomic potentials	6
Gouveia J.D.	MXenes as promising catalysts for water dissociation	7
Hanselman S.	Hydrogen binding and transport on graphene-covered Pt(111) surfaces	8
Hariharaputran S.	Computational modelling of optical properties of biomarkers in membranes environments	9
Heilemann Myhre R.	Biorthogonal orbital optimization in perfect paired coupled cluster	10
Heshmat M.	Free energy landscape of hydrogenation of carbonyl compounds by Frustrated Lewis Pairs	11
Janoš P.	Mechanism of Cu(i) translocation via CTR1 transporter	12
Lengvinaitė D.	NMR spectra of water-ionic liquid mixtures: large-scale quantum mechanics/molecular mechanics modelling	13
Laranjeira J.	Exploring Buckminsterfullerene Polymerization	14
Michalchuk A.A.I.	An ab initio approach to predicting energetic material impact sensitivity	15
Mulks F.F.	Sesquicarbene complexes: allylic carbon-bridged bimetallic complexes, dicarbene complexes with one carbon p-orbital?	16
Paragi G.	Cooperativity and solvation	17
Pareras G.	Successive Diels-Alder cycloadditions of cyclopentadiene over [10]CPP \rightarrow C60	18
Pérez De Alba Ortíz A.	The dark-state recovery mechanism of blue light-using flavin proteins	19
Pruszkowska K.	Steric and polarity effects in acacen Ni(ii) complexes with enamino-ketone ligands and their reaction products with heterocyclic amines	20
Pujal L.	Oxidation states in periodic systems from quantum mechanics	21
Rashidian A.	Molecular modelling to select specific LXR α -agonists able to induce lipotoxicity in HCC cancer models	22
Roet S.	Using decision trees to understand deprotonation in formic acid	23
Salom Català A.	Ab initio molecular dynamic simulations on the interaction of phosphines with Rh nanoparticles	24
Sargeant E.	Calculations for investigating gas hydrates of CO ₂ in aqueous brines at the electrochemical interface	25
Sieffert N.	Halide complexation to uranyl in liquid ammonia: a DFT molecular dynamics study	26
Škulj S.	Reaction of reactive aldehyde HNE with amino acid cysteine from UCP2 protein	27
Stoycheva J.	Chemical functionalization and topology: a new strategy for high-performance organic photovoltaic materials	28
Tuppurainen V.	Solvent screening for extraction of furfural by using quantum mechanics-based COSMO-CAMPD framework	29
Tychengulova A.	Electronic structure and properties of synthetic complexes mimicking the S2 state of oxygen-evolving complex	30

Zborowski K.	Aromaticity of pyrrole and pyridine in the water environment	31
Earth sciences & environment		
Fuckar N.	Climate modelling and attribution of summer 2018 heatwaves and droughts in Northern Europe	32
Li Y.	Comparison between METIS, SCOTCH, ParMETIS and PT-SCOTCH for 3D frequency-domain wave modelling using MUMPS	33
Mendes De Moura Y.	Unveiling forest degradation in the tropics: new approaches using 3D terrestrial LiDAR	34
van Dongen E.	Improved Elmer/ice calving model: integrated 3D remeshing	35
Energy		
Äkäslompolo S.	Serpent neutronics model of Wendelstein 7-X	36
Kontula J.	Modelling of TJ-II plasmas with Monte Carlo orbit-following code ASCOT	37
Engineering and technology		
Bal B.	Molecular dynamics simulations on hydrogen embrittlement	38
Mirkov N.	Performance analysis of parallel simulation code for cardiovascular hemodynamic flows	39
Fernandes C.	Three-dimensional direct numerical simulations of a shear-thinning viscoelastic flow past a stationary sphere	40
Przytarski P.J.	Data-driven analysis of high-fidelity multi-stage compressor simulation data	41
Vencels J.	Numerical model development for convective cooling of electrical devices	42
Information and Communication Technologies		
Colonnelli I.	Practical parallelization of MPI applications	43
Górski Ł.	Native communication support for the PCJ library	44
Lorenzon A.	Enhancing resource management through prediction-based policies	45
Maroñas M.	Efficiently exploiting distributed large many-core systems	46
Nuriyev E.	Model-based selection of optimal MPI broadcast algorithms for multi-core clusters	47
Redondo A.	Adversarial risk analysis for obfuscation attacks (extension)	48
Life Sciences and Biotechnology		
Jalalypour F.	Perturbation response scanning and clustering, methods for investigating dynamics of proteins	49
Katsila T.	Delineating the role of adaptive immunity in coeliac disease comorbidities, the role of MALT1	50
Lolicato F.	The NA, K-ATPASE acts upstream of phosphoinositide PI(4,5)P2 facilitating unconventional secretion of fibroblast growth factor 2	51
Marinazzo D.	Dynamic causal model of auditory steady state responses	52
Montagna M.	Modelling Src conformational transitions by means of classical molecular dynamics and essential dynamic sampling	53
Negrello M.	Dynamical clustering of the inferior olive	54
Skorniakov V.	BCPNN for text prediction	55
Tiemann J.K.S.	Investigating the dynamical steps of arrestin-GPCR pre-complex formation & sharing and analysing MDs of GPCRs at GPCRmd	56
Material sciences		
Diez Cabanes V.	Understanding the structural and electronic properties of photoactive tungsten oxide (WO ₃) nanoparticles from DFT and GW approaches	57
Jovanović D.	DFT study of a relaxed amino acid, glutamine, on TiO ₂ surfaces	58

Ricci E.	Multiscale modelling of gas separation with poly(2,6-dimethyl-1,4-phenylene oxide) (PPO)	59
Segalina A.	Structure and energetics of dye-sensitized NiO interfaces in water from ab-initio MD and GW calculations	60
Tanis I.	Molecular dynamics simulations of graphene oxide-based nanocomposites targeted for the removal of water pollutants	61
Mathematics		
Acebron J.	An efficient parallel code for solving fractional partial differential equations in complex geometries	62
Chiocchetti S.	A parallel semi-implicit solver for viscous two-phase flows with surface tension	63
Gurova S.-M.	Predator-prey model with SEIR (Susceptible-Exposed-Infectious-Recovered) Epidemic disease	64
Raievska I.	Local nearrings	65
Raievska M,	Nearrings with identity	66
Physics		
Antosiewicz T.J.	Modifying ground state chemistry of molecules by ultra strong coupling to plasmonic resonances	67
Attems M.	Initial stage of the spinodal instability	68
Bowal K.	Fighting bacteria: a computational exploration of chemical and physical interactions between sphere-shaped and rod-shaped bacteria	69
Carenza L.N.	Defect rotation controls the dynamics of Saturn rings	70
Cikojevic V.	Dynamics of equilibration and collisions in ultradilute quantum droplets	71
Çokluk K.A.	Numerical simulation of binary neutron stars	72
Da Silva Estelina L.	Theoretical study of phase transitions in Sb ₂ Se ₃ under compression	73
Del Sordo F.	Global simulations of Tayler instability in stellar interiors: The stabilizing effect of gravity	74
Del Sordo F.	Global simulations of Tayler instability in stellar interiors: The stabilizing effect of rotatio	75
Del Sordo F.	Expectations for the confirmation of Proxima c from a long-term radial velocity follow-up	76
Del Sordo F.	Calculating the rotational period of Iota Horologii with a fractal approach	77
Evans M.L.	High-throughput materials discovery for sustainable battery materials	78
Ferrari P.	The geometry of palladium doped gold clusters	79
Gent F.	Modelling supernova-driven dynamo with cosmic rays	80
Girych M.	Role of complex glycans in epidermal growth factor receptor	81
Gonçalves J.N.	First-principles study of structure and magnetism in triazolium/guanidinium Cu hypophosphites and imidazolium Cu formate	82
Ibragimova R.	Distribution and composition of functional groups on 2D MXene surfaces	83
Lo Piccolo G.M.	First principles simulations of pure and germanium-doped amorphous silica	84
Masys Š.	Magnetic properties of nanodiamonds: theoretical investigation	85
Musari A.A.	First-principles investigation of structural, electronic and magnetic properties of two-dimensional CrGeTe ₃ magnet	86
Negro G.	Topology and dynamics of confined three-dimensional active nematics	87
Peuron J.	Quark production and chemical thermalization at the initial stages in ultra-relativistic heavy-ion collisions	88
Talarico N.W.	Double quantum dots thermocouple	89

TA_RETIS (Translocation of Antibiotics with Replica Exchange Transition Interface Sampling)

R. Cabriolu

Laboratory of Molecular Simulation (LSMO), Institute des sciences et ingénierie chimiques (ISIC), École polytechnique fédérale de Lausanne (EPFL) Valais, Switzerland.

Introduction

The translocation of antibiotics across the outer membrane (OM) of pathogenic bacteria, constitute an exceptionally important topic because of the broad implications in human health. The last data from the World Health Organization are showing an increase in the levels of bacteria resistance to antibiotics. The Outer Membrane Protein OmpF from "Escherichia coli" is considered to be the main channel pathway through which small molecules, including antibiotics, can cross the OM and reach the core of the cell. It was shown by single-molecule single-channel electrophysiology that ampicillin, diffuses through the OM, with typical time from hundreds of microseconds to millisecond [1].

Because of this time scale, the problem of translocation of antibiotic by simulations without approximated models, cannot be addressed using standard Molecular Dynamics (MD) simulation. Different accelerated powerful MD algorithms have been applied to different biological systems [16]. Nonetheless, the physical-chemical rates for penetration through these transmembrane channels have not been faithfully predicted. This work aims to apply an unbiased rare event technique, "RETIS", to study the translocation of the antibiotic meropenem through the bacterial porin OmpF, from the outer membrane of Escherichia coli bacteria.

Methods

The aim of the Replica Exchange Method (RETIS) [2] is to generate an ensemble of dynamical "trajectories" that reproduce the transition or the rare event, taking the system from the initial state A to the initial state B.

In our case, for example, being the rare event the translocation of the protein, state A and B are represented by the antibiotic outside the bacteria and inside the bacteria respectively. In practice, the algorithm uses a series of different methods or "moves" to generate paths, among them the "shooting move" is the most central, as for many other path sampling techniques. Among many exclusive features of RETIS, the "swapping-move" is surely improving the computational efficiency. Besides the fundamental moves, many other details make the exact method "RETIS" the most efficient among previous path sampling techniques, without adding any conceptual assumption nor bias to the process. RETIS provides accurate information on the reaction mechanism, rate constants and reaction barriers of the rare event under examination.

Results

The system under analysis is composed of 102122 atoms for a total of 18685 molecules. Three identical OmpF porin channels represent the Escherichia Coli outer membrane. Furthermore, 34757 atoms represent the lipids, and 17372 water molecules make the surrounding membrane environment. In addition, 33 potassium ions are added to

balance the negative charge of the OmpF and finally, we have used 33 atoms to representing the antibiotic Meropenem. The calculations were implemented in the PYRETIS software that uses the Gromacs engine as MD simulation code.

Simulations are still ongoing, we have been able to develop a suitable order parameter, and, at the moment, we are collecting the necessary statistic to build the rate of the process. Furthermore, soon we would also recover other kinetic properties, and, especially, fundamental transport properties that can be directly compared with experimental results.

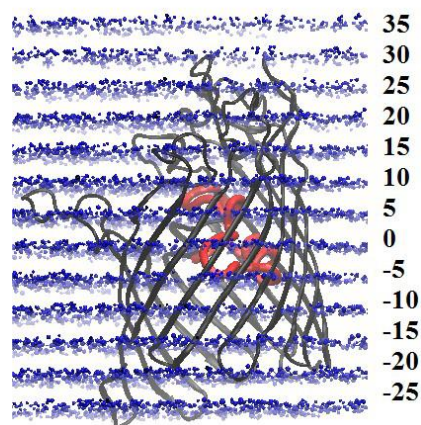


Figure 1 – Representation of the porin channel in grey and of the antibiotics, in red, inside the outer membrane. On the right side, the distance of the porin centre from the porin channel boundaries are shown.

Conclusions

The project allowed to develop simulation settings to obtain rate and to gain insight on the mechanism of translocation of Meropenem antibiotic without imposing any bias on the system. The simulation setup could easily be applied to any translocation process, not only in the biophysical system and it allows to obtain information that can be readily compared with other simulations predictions and experimental. We are aiming to apply the same setup to other biophysical systems.

References

- [1] Nestorovich et al., Proc. Natl. Acad. Sci. USA. 99:9789-9794 (2002).
- [2] Cabriolu R., Kjelbred Refnes K. M., Bolhuis P. G., van Erp T.S., The Journal of Physical Chemistry 147 (15), 1527722 (2017).

Acknowledgements

The work has been performed under the Project HPC-EUROPA3 (INFRAIA-2016-1-730897), with the support of the EC Research Innovation Action under the H2020 Programme; in particular, the author gratefully acknowledges the support of Prof. Ceccarelli and Dr. Bodrenko from the Physics department at Cagliari University, Italy, Prof. Van Erp from the Department of Chemistry in NTNU, Norway, and the computer resources and technical support provided by HPC Cineca consortium.

Ceria-supported transition metal particles: adsorption properties and charge transfer

P. Castro-Latorre¹, K.M. Neyman^{2,3}

¹Faculty of Science, University of Chile; ²Departament de Ciència de Materials i Química Física, Universitat de Barcelona, Spain ³Institució Catalana de Recerca i Estudis Avançats, Spain

Introduction

The chemical properties of metal particles supported on metal oxides such as CeO₂ are affected by metal-support interactions [1], which can lead to the stabilization of certain particle structures and oxidation states [2-3]. In this work we explore the electronic structure of clusters of different metals (Pd, Pt and Rh) on CeO₂(111), evaluating stability of different cluster geometries, their adsorption energies and charge transfer profile.

Methods

Density Functional Theory calculations are performed using GGA PW91 exchange-correlation functional and the Projector Augmented Wave (PAW) method, with a cut-off energy of 400 eV and slab size of 3x3x1 and 3 trilayers if CeO₂(111) using Quantum Espresso software. To describe the localization of f-electrons on Ce atoms, we used Hubbard's +U correction with a value of 4 eV. For assessing the charge transfer in these systems, bader charges are calculated using the most stable electronic state obtained.

Results

The adsorption energies of M₈ (Pd, Pt, Rh) clusters on CeO₂ (111) are calculated following equation (1)

$$|E_{ads} = E(M_8 / CeO_2) - E(M_8) - E(CeO_2) \quad (1)$$

The adsorption energies are calculated in reference to the respective 3D geometric configuration of the M₈ cluster, which was found to be more stable than the 2D one. These energies are shown if Figure 1.

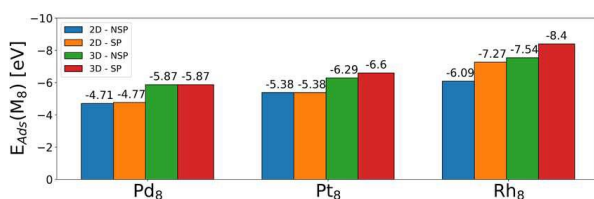


Figure 1 – Adsorption energies of M₈/CeO₂.

For the three metals considered in this study, the 3D geometric configuration is more stable in the range of 0.9 –

1.3 eV. For Pd cluster, there are no differences due to the stability of its d¹⁰ electronic configuration. For Pt and Rh, in their 3D configuration there are up to two electrons transferred which are located in f orbitals of Ce atoms, as can be seen in Figure 2.

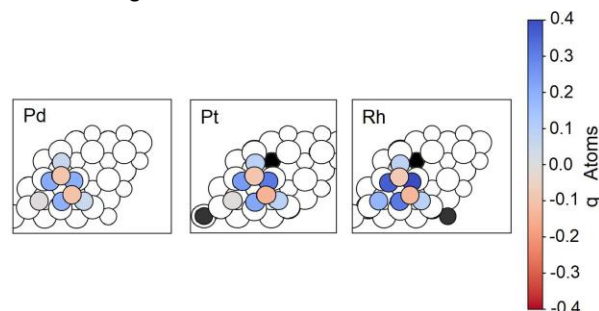


Figure 2 – Bader charges for M₈/CeO₂ systems.

Metal atoms are coloured according to their Bader charge, large and small white circles correspond to O and Ce⁺⁴, respectively, while black circles correspond to Ce⁺³ species (with localized f electron).

Conclusions

The 3D geometric configuration is the most stable for each M₈ cluster. Also, charge transfer stabilizes the interaction between the M₈ cluster and the CeO₂ support. Controlling the electronic state of supported cluster allows to evaluate the interplay between charge transfer and adsorption properties.

References

- [1] Suchorski, Y.; Kozlov, S.; et al. Nature Mater., 17: 519, 2011.
- [2] Lykhach, Y.; Kozlov, S.; et al. Nature Mater. 15: 284, 2016.
- [3] Bruix, A. et al., Phys. Chem. Chem. Phys. 13:11384, 2011.

Acknowledgements

The work has been performed under the Project HPC-EUROPA3 (INFRAIA-2016-1-730897), with the support of the EC Research Innovation Action under the H2020 Programme; in particular, the author gratefully acknowledges the support of Prof. Dr. Konstantin Neyman, Department de Ciència de Materials i Química Física and the computer resources and technical support provided by BSC.

Can donor-acceptor bonds stabilize E_4^{+2} (E=B-Tl) aromatic rings?

G. Comas I Vilà¹, D.M. Andrada²

¹Universitat de Girona, Spain; ²Saarland University, Germany

Introduction

Molecules containing boron-boron multiple bond are of considerable current interest due to the electron deficiency of the boron element.

The chemistry of low-coordinate main-group compounds of Group 13 elements has been intensive investigated and molecules containing boron-boron multiple bonds have been recently isolated. These new compounds can have applications in areas such as catalysis and energy storage activating small molecules such as H_2 and CO_2 .

Braunschweig et al. synthesized the first boron-boron triple bond complex stabilized by these two carbenes: $C\{N(2,6-iPr_2C_6H_3)CH\}_2$ and N-heterocyclic carbene (NHC) [1]. The related NHC complexes $B_n(NHC)_n$ and B_nCO_n have subject of previous theoretical studies showing the aromaticity of these systems [2]. Frenking and Holzmann pointed out that the donor strength of the NHC is much stronger than that of CO. For this reason, the stability of diborane compounds containing NHC groups is better than those containing CO [3].

This project will employ the concept of stabilization by donor-acceptor bonding using carbenes and aromaticity in order to access highly reactive group 13 species.

Methods

In this work we examine the features of structure, chemical bonding and stability of the E_4^{+2} and $E_4(NHC)_4^{+2}$ where E is (B, Al, Ga, In and Tl) and NHC is a N-heterocyclic carbene.

For this purpose, we optimize the different complexes in the singlet and triplet state at BP86-D3(BJ)/def2-SVP level of theory using Gaussian16. For the naked rings we consider different isomers such as planar and tetrahedral. For the carbene rings we use different point groups (C₂, C_{2v}, D₄, D₂, D_{2d}, D_{2h} and D_{4h}). The shape of the different molecular orbitals is important and also we use the Natural Bond orbitals and EOS (Effective Oxidation State) analysis to observe the occupations of each orbital.

Finally, the interatomic interactions are investigated by an Energy Decomposition Analysis in combination with the Natural Orbitals for Chemical Valence at BP86-GD3(BJ)/TZ2P//BP86-GD3(BJ)/def2-SVP level of theory.

Results

For the E_4^{+2} rings the most stable isomer for the boron is D_{4h} in the singlet state and for all the other elements are the D_{3h} in the triplet state. The bond lengths in all these isomers are in the range of the simple single bond and all the Wiberg Bond Orders show the non-aromaticity of these compounds. For the $E_4(NHC)_4^{+2}$ rings we systematically explore different isomers for the singlet and triplet state. We analysed the nature of the donor-acceptor bonds with the energy decomposition analysis with natural orbitals of chemical valence (EDA-NOCV) for the most stable geometry in the singlet state. The strongest attraction between the ligand and the remaining fragment $NHC E_4(NHC)_3^{+2}$ comes from the

orbital interactions in the boron ring and electrostatic interaction for the other elements. The largest contribution to the ΔE_{orb} arises from the donation of the lone pair orbitals of the NHC to the LUMO of $E_4(NHC)_3^{+2}$ (Figure 1a). There is also a π backdonation from the HOMO of $E_4(NHC)_3^{+2}$ to the LUMO of NHC. (Figure 1b). There is a shortening of the E-E bond length and increase of the Wiberg Bond Order when the Lewis base (NHC) is bonded to the E_4 ring.

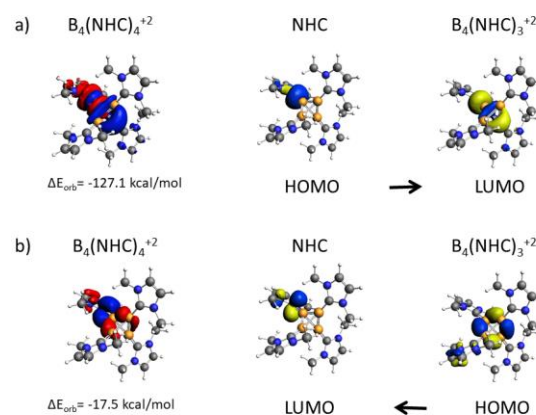


Figure 1 – Plot of the deformation densities $\Delta\rho$ of the pairwise orbital interactions between $[E_4(NHC)_3]^{+2}$ and NHC in $[E_4(NHC)_4]^{+2}$ and associated stabilization energies in kcal/mol. The colour code of the charge flow is red to blue. Shape of the most important interacting orbitals of $[E_4(NHC)_3]^{+2}$ and NHC.

Conclusions

Finally, to sum up we are going to remark the more important aspects about this work. The calculations show that the carbene ligand NHC is a strong donor that can stabilize the different rings. The structural features of the different complexes can be explained in terms of donor-acceptor interactions between the donors NHC and the acceptor E_4 which have been analysed quantitatively with the EDA method. The results may be considered as exploration of a new field of ligand-stabilized complexes E_4L_4 .

References

- [1] H. Braunschweig, R. D. Dewhurst, K. Hammond, J. Mies, K.Radacki, A. Vargas, Science, 2012, 336, 1420-1422.
- [2] T. B. Tai, M. T. Nguyen, Angew. Chem. Int. 2013, 52, 4554-4557.
- [3] G. Frenking, N. Holzmann, Science. 2012, 336, 1394-1395.

Acknowledgements

The work has been performed under the Project HPC-EUROPA3 (INFRAIA-2016-1-730897), with the support of the EC Research Innovation Action under the H2020 Programme; in particular, the author gratefully acknowledges the support of Diego Andrada from the Saarland University and the computer resources and technical support provided by HRLS.

AgPd, AuPd and AuPt nanoalloys with Ag- or Au-rich compositions: modeling the interplay between chemical ordering and optical properties

N. Danielis¹, L. Vega², G. Fronzoni¹, M. Stener¹, A. Bruix², K.M. Neyman^{2,3}

¹Dipartimento di Scienze Chimiche e Farmaceutiche, Università di Trieste, Italy; ²Departament de Ciència del Materials i Química Física & Institut de Química Teòrica i Computacional, Universitat de Barcelona, Spain; ³ICREA (Institució Catalana de Recerca i Estudis Avançats), Barcelona, Spain

Introduction

The chemical ordering and optical properties of AgPd, AuPd, AuPt nanoparticles (NPs) have been studied computationally. One of the main aims was to clarify whether layered ordered phases similar to the (L11) observed in the core of AgPt NPs [1] are also stabilized in other nanoalloys of coinage metals with platinum-group metals or the remarkable ordering is a peculiarity only of AgPt NPs. Furthermore, the effects of different chemical orderings and compositions of the nanoalloys on their optical properties have been explored. Particles with a truncated octahedral geometry containing 201 and 405 atoms have been modelled. For each NP, the studied stoichiometries of the Ag- or Au-rich compositions, ca. 4:1 for 201-atomic particles and ca. 3:1 for 405-atomic particles, corresponded to the layered structures (L1₁) and (L1₀) inside the monatomic coinage-metal skins (Figure 1).

Methods

The chemical ordering has been investigated using the topological energy method (TOP) [2], which defines the energy of each homotop of a chosen AxPx NP (with a fixed shape and stoichiometry) as follows:

$$E_{TOP} = E_0 + \epsilon_{BOND}^{Ax-Px} N_{BOND}^{Ax-Px} + \epsilon_{CORNER}^{Ax} N_{CORNER}^{Ax} + \epsilon_{EDGE}^{Ax} N_{EDGE}^{Ax} + \epsilon_{TERRACE}^{Ax} N_{TERRACE}^{Ax}$$

Where E_0 is a constant offset between the TOP and DFT energy scales, N_{BOND}^{Ax-Px} is the number of heterometallic bonds in the homotop under scrutiny, and N_{CORNER}^{Ax} , N_{EDGE}^{Ax} , $N_{TERRACE}^{Ax}$ are the numbers of Ax atoms in the corner, edge and terrace positions, respectively. The terms ϵ represent the energy contributions to the total energy of the homotop E_{TOP} of either one Ax-Px bond or one Ax atom located in the corresponding surface position of the NP. The optimization of ϵ terms allows finding the lowest energy homotops (LEHs) for a NP with a defined shape and composition.

The optical properties have been investigated for 201-atomic NPs at the TDDFT level. To solve the TDDFT equations the complex polarizability method [3] has been employed. This tool allows calculating the photoabsorption spectrum $\sigma(\omega)$ from the imaginary part of the dynamical polarizability $\alpha(\omega)$, where ω is the complex frequency:

$$\sigma(\omega) = \frac{4\pi\omega}{c} \text{Im}[\alpha(\omega)]$$

Results

In AgPd 201-atomic NPs both the ordered (L1₀) and (L1₁) layered structures show lower total energies than the (LEH) structures (-0.41 eV and -0.33 eV, respectively). However, in AgPd 405-atomic NPs the energy difference becomes positive for (L1₀) and smaller for (L1₁) orderings (+1.68 eV and -0.20 eV, respectively).

In AuPt and AuPd NPs the (L1₀) and (L1₁) orderings show in both cases significant higher total energies (even several eV) than the corresponding (LEH) structures.

The comparison of optical spectra shows similar features in the photoabsorption for the four AxPx bimetallic nanoalloys. While (Px-Ax) electronic transitions are dominant at low excitation energies, the (Ax-Ax) ones show a major contribution at high excitation energies. The comparison of the absorption spectra of NPs with different chemical orderings in their cores does not show relevant differences.

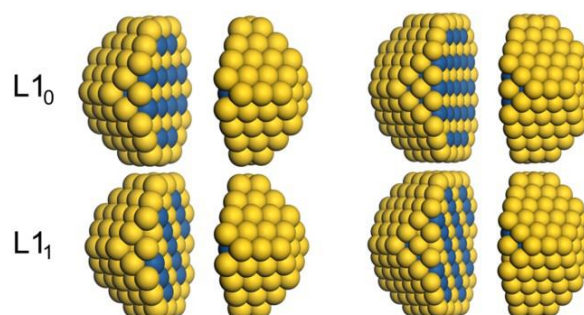


Figure 1 – (L1₀) and (L1₁) orderings in the cores of truncated octahedral NPs with 201 atoms (left) and 405 atoms (right)

Conclusions

The results obtained for chemical orderings in the various combinations of coinage metals with Pt and Pd species suggest that the appearance of peculiar ordered core structures is not a general behaviour, but it is quite specific for Ag nanoalloys.

The subsequent analysis on the optical properties showed that both the electronic structure and the excitation spectra of bimetallic NPs display a weak dependence on the chemical ordering of their cores, but a strong dependence on the chemical composition. However, similar features in the evolution of the photoabsorption spectra were found in terms of fragments involved in the electronic transitions.

References

- [1] Pirart J. et al., Nature Communications, volume 10 (1982), 2019.
- [2] Kozlov S. et al., Chem. Sci., volume 6: 3868-3880, 2015.
- [3] Baseggio O. et al., J. Chem. Phys., volume 143 (024106), 2015.

Acknowledgements

The work has been performed under the Project HPC-EUROPA3 (INFRAIA-2016-1-730897), with the support of the EC Research Innovation Action under the H2020 Programme; in particular, the author gratefully acknowledges the support of Prof. Konstantin Neyman from the University of Barcelona and the computer resources and technical support provided by Barcelona Supercomputing Center (BSC).

New set-up polarizable force field for [Emim][FeCl₄]

N. Figueiredo¹, S. Tovey², C. Holm²

¹LABQV@REQUIMTE, Faculty of Sciences of University of Porto, Portugal; ²Institute for Computational Physics, University of Stuttgart, Germany

Introduction

Magnetic ionic liquids (MILs) are a new generation of ionic liquids that contain a transition metal or lanthanides in their cation or anion structure. In addition they have same attractive characteristics as ionic liquids, such as low flammability, and vapor pressure, and high thermal stability, with the advantage of responding to an external magnetic field.¹ This magnetic behaviour allows it to be attractive for a wide range of applications as diverse as solvent-based extractions, gas absorption, biomedical imaging, and sensing.² Through molecular dynamics simulations, it is possible to study magnetic ionic liquids and understand the relationship between the atomic level and the thermodynamic and transport properties. However, additive force fields (FFs) lead a slow dynamics, and, consequently, transport properties, such as self-diffusion coefficients, are not very accurate. This project aims to develop a new polarizable FF for MILs based on the anion [FeCl₄] to improve the transport properties obtained from MD simulations.

Methods

A new polarizable model was tested in this work for 1-ethyl-3-methylimidazolium tetrachloroferrate [Emim][FeCl₄], based on the strategy implemented by Pádua and coworkers.³ [Emim] cation parameters were simulated using CL&P FF⁴, and [FeCl₄] parameters were previously calculated by us. The scheme described by Goloviznina et al. was applied to set-up polarizable FF.³ MD simulations were performed with the LAMMPS package with the USER-DRUDE package active. A cubic box containing 300 ion pairs was generated, using `fftool` and `packmol`. Ewald method was applied, and a cutoff of 10 Å was considered for non-bonded interactions. The system was equilibrated for 3 ns in the *NVT* ensemble. Then, a production run of 10 ns in the *NpT* ensemble to obtain the density of the system and, finally, a long run in *NVT* ensemble of 20 ns for self-diffusion coefficients. All runs were performed at 300 K, and 1 bar. The Nosé-Hoover thermostat and barostat were used. The Langevin thermostat was maintained constant Drude particles at a temperature of 1 K.

Results

The density value obtained for [Emim][FeCl₄] at 300 K from MD simulations was 1.445 g cm⁻³. This value shows good agreement with the reference data in the literature for experimental density (1.420 g cm⁻³).⁵ Figure 1 shows the analysis of the radial distribution function for the system under study. The FeCl₄ anion has a stronger interaction with the N atom of the cation imidazolium ring (FE...N interaction) than the carbon atom (FE...C1 interaction) of the alkyl chain the cation. The interaction of the iron atom (FE) has a strong interaction with the ring hydrogen atom (FE...HCR) than the H

from the alkyl chain (FE...HC interaction). Thus, the anion's interaction with the H of the imidazolium ring is more probable than with the alkyl chain's H atoms. The self-diffusion values were evaluated from mean-square displacement using Einstein relation. For [Emim][FeCl₄], the values obtained for the self-diffusion coefficient (*D*) were 5.403 × 10⁻¹² m² s⁻¹ for [Emim]⁺ and 3.856 × 10⁻¹² m² s⁻¹ for the anion [FeCl₄].

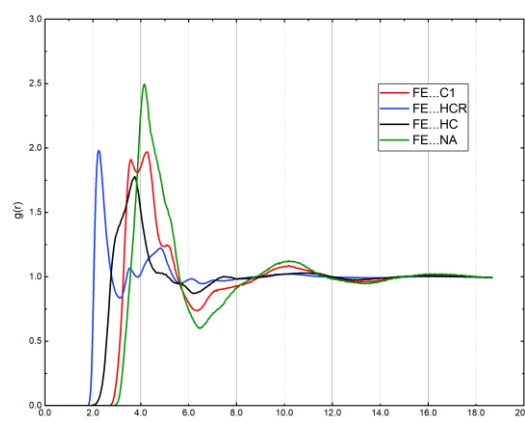


Figure 1 – Radial distribution functions, $g(r)$, between atomic sites of [Emim][FeCl₄] at 300 K.

Conclusions

The main contribution of this project was applied for the first time a polarizable FF for [Emim][FeCl₄]. Density, radial distribution functions, and self-diffusion coefficients were performed. This work offers new opportunities to study metal-containing ionic liquids using a yet more reliable computational approach, paving the way to an efficient rational design of MILs forward, improving their applicability.

References

- [1] Joseph A et al., *J. Mol. Liq.*, 218: 319-331, 2016.
- [2] Sajid M, *Trends Anal. Chem.*, 113: 210- 223, 2019.
- [3] Goloviznina K et al., *J. Chem. Theory Comput.*, 15: 5858-5871, 2019.
- [4] Canongia Lopes JN et al., *Theor. Chem. Acc.*, 131: 1129, 2012.
- [5] Yoshida Y et al., *J. Mater. Chem.*, 16: 1254-1262, 2006.

Acknowledgements

The work has been performed under the Project HPC-EUROPA3 (INFRAIA-2016-1-730897), with the support of the EC Research Innovation Action under the H2020 Programme; in particular, the author gratefully acknowledges the support of Prof. Christian Holm from Institute for Computational Physics and the computer resources and technical support provided by HLRS.

Accurate phonons with machine-learned interatomic potentials

J. George¹, V.L. Deringer²

¹Université catholique de Louvain, Belgium, ²University of Oxford, United Kingdom

Introduction

Vibrational and thermal properties of materials are of high importance for practical applications. Materials with good thermoelectric properties should have very low thermal conductivity. Standard quantum-mechanical approaches via density functional theory to calculate the thermal conductivity and other properties are typically very slow and can, therefore, not be performed on a large scale. During this HPC-Europa3 project, we explored how machine-learned interatomic potentials can be used to calculate phonons and thermal conductivities and thereby aim at an accelerated calculation of these properties.

Methods

We are using Gaussian Approximation Potentials (GAPs), [1] which belong to the class of machine-learned interatomic potentials, to compute phonon properties for a range of silicon allotropes. [2] These potentials are typically fitted to data points from density functional theory. To improve the accuracy of the phonon properties, we follow two strategies: 1) We test how one can build reference databases that allow to calculate very accurate phonon properties. 2) We improve the fitting procedure of the GAPs by using an adaptive regularisation of the regression task. To compute the phonon properties, we combine the Python packages quippy, phonopy, phono3py, pymatgen and ASE within a unified workflow. Details may be found in an original paper resulting from this visit [2], which we briefly summarise here.

Results

The general-purpose potential GAP-18 [3] was first tested for the phonon band structures of 13 dynamically stable silicon allotropes from the materials project database (see Figure 1b). The results for diamond (mp-149) were in very good agreement with the reference calculation from DFT. We calculated a very low RMS that compares the phonon band structures from the potential to the DFT reference values (0.15 THz). This is, however, markedly different for clathrate-I. Here, some of the frequencies deviate by over 10% (see red circle at Gamma). This is more than twice as large as the mean relative error (-3.6%) that comes from the DFT approximation in comparison to experimental frequencies which was evaluated in a recent high-throughput study on phonon computations. [4] Most of the dynamically stable compounds are predicted to be dynamically stable with this potential, but one shows erroneous imaginary modes.

We then explored in detail how we can build new reference databases for phonon properties. We started from the silicon allotropes in the Materials Project database. We created additional reference data with the help of random cells and cells where only one atom is displaced and added this to the initial reference database of GAP-18. Additionally, we included an adaptive regression procedure in the fitting of the potentials. This allowed us to calculate phonon band structures for all 13 relevant dynamically stable phases from the materials project database with a very high accuracy (rms up to 0.3 THz, see Fig. 1b) and arrive at a new general-purpose potential with high phonon accuracy for a range of silicon allotropes, GAP-18+SCs.

Furthermore, we tested the newly developed potential GAP-18+SCs ($f=0.01$) in the initial design space of GAP-18, for example, for disordered phases. It arrives at very similar energies and forces during a melt-quench simulation as GAP-18.

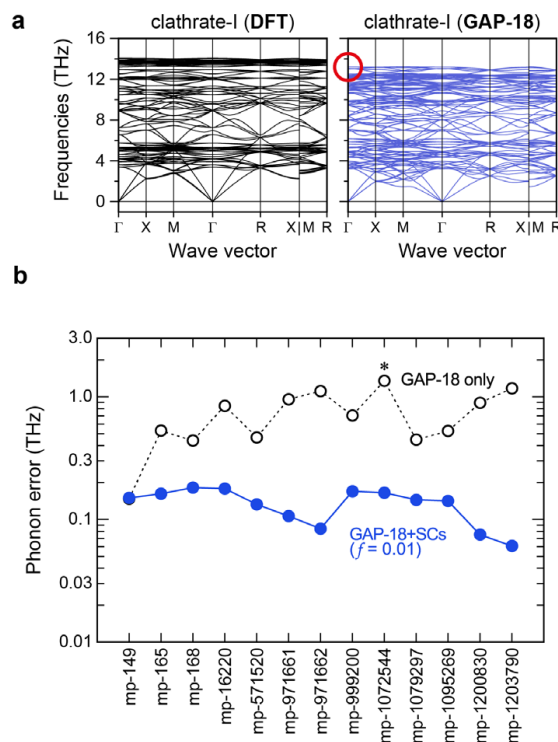


Figure 1 – a) Phonon band structure for clathrate-I as calculated by DFT and GAP-18. GAP-18 underestimates the frequencies. b) Comparison of an RMS value that compares the phonon band structure from DFT to the one from the GAP potential for a variety of dynamically stable structures. The new potential GAP-18+SCs shows significantly better agreement with the phonons from DFT than GAP-18. The figures are adapted from George, et al., J. Chem. Phys. 153, 044104: 2020. with the permission of AIP Publishing.

Conclusions

We have explored how very accurate phonons with Gaussian Approximation Potentials can be calculated. We have fitted a potential that can compute accurate phonons but also retain transferability across structural space, including highly disordered liquid and amorphous phases.

References

[1] Bartók, et al., Phys. Rev. Lett. 104: 136403, 2010. [2] George, et al., J. Chem. Phys. 153, 044104: 2020. [3] Bartók, et al. Phys. Rev. X. 8: 041048, 2018. [4] Petretto, et al. Comput. Mater. Sci. 144: 331-337, 2018.

Acknowledgements

The work has been performed under the Project HPC-EUROPA3 (INFRAIA-2016-1-730897), with the support of the EC Research Innovation Action under the H2020 Programme; in particular, the author gratefully acknowledges the support of the Inorganic Chemistry Laboratory of the University of Oxford and the computer resources and technical support provided by the ARCHER staff.

MXenes as promising catalysts for water dissociation

J.D. Gouveia, Á. Morales-García, F. Viñes, F. Illas, J.R.B. Gomes

CICECO – Aveiro Institute of Materials, Department of Chemistry, University of Aveiro, Portugal; Departament de Ciència de Materials i Química Física & Institut de Química Teòrica i Computacional (IQTCUB), Universitat de Barcelona, Barcelona, Spain

Introduction

Two-dimensional few-layered transition-metal nitrides and carbides, called MXenes, have attracted a great interest given their large surface areas and their unique physicochemical properties. Motivated by the known reactivity of surfaces of bulk transition metal carbides on the mechanism behind the water-gas shift (WGS) reaction, density functional theory (DFT) calculations were employed to investigate the bonding of water and its dissociation on a set of eighteen M₂X MXene (M = Ti, Zr, Hf, V, Nb, Ta, Cr, Mo, and W, while X = C or N) surfaces.

Methods

The overall study relies on first-principles calculations carried out in the framework of density functional theory (DFT) using the Vienna Ab initio Simulation Package (VASP). The calculations were carried out within the generalized gradient approximation (GGA) to the many-body exchange-correlation potential, namely using the functional introduced by Perdew, Burke, and Ernzerhof (PBE), with the contribution of dispersion terms approximated through the D3 method as proposed by Grimme. The valence electron density was expanded in a plane wave basis set with an energy cutoff of 415 eV. The effect of the atomic inner cores on the valence electron density was considered by means of the projector augmented wave (PAW) method. The convergence criterion for the self-consistent field energies was set to 10⁻⁶ eV and structures were considered relaxed when the forces acting on all atoms were lower than 0.01 eV/Å. To carry out the necessary numerical integrations in the reciprocal space, the Brillouin zone was sampled using a Monkhorst-Pack 5x5x1 grid of special k-points. The saddle point configuration for the minimum-energy pathway for H₂O dissociation on each MXene was located by using the dimer method.

Results

Depending on the MXene surface, the adsorption of the H₂O molecule takes place on either bridge (B) or top (T) sites (Fig. 1). On B (T) sites, the distance between the O atom and the surface plane is around 1.8 Å (2.2 Å), with small (between 0.2 and 0.4 eV) energy differences between the two most stable configurations. Our results indicate that *d*³ and *d*⁴ MXenes adsorb water preferably on the T configuration, whereas *d*² MXenes can adsorb on either T or B. The adsorption energies range from -0.8 to -1.1 eV, being slightly stronger on MXenes that prefer the B configuration. On B sites, all dissociation

energy barriers are lower than 0.1 eV, while on the T site they can go up to 0.44 eV, which is considerably low compared to today's industrial standards.

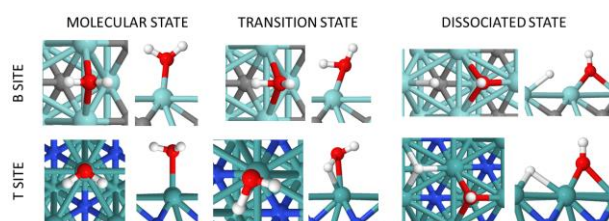


Figure 1 – Top and side views of the molecular, transition and dissociated states for the water dissociation reaction on bridge sites (first row panels) and on top sites (second row panels).

Conclusions

Water molecular adsorption is an exothermic process on all the analysed MXenes. Depending on the considered surface, the water molecule adsorbs either on a bridge or a top position. Ti₂N and Zr₂C emerge as the most reactive substrates of all nitrides or carbides, respectively. No trend was observed between H₂O adsorption energies along periods or groups, or with the distance between the adsorbed molecule and the surface. In all cases, H₂O dissociation on MXenes is exothermic with absolute reaction energies higher than 1 eV on most MXenes, up to 3.35 eV for Hf₂N. Different transition state configurations were found depending on the preferential bridge or top H₂O adsorption site. In all MXenes, the reaction activation energy barriers were found to be relatively small, i.e., below 0.44 eV. Barriers tend to be slightly larger for nitride MXenes than for the corresponding carbide counterparts, and to increase along the periodic table periods.

References

- [1] Gouveia, J.D. et al., App. Cat. B: Env., 260:118191, 2020.
- [2] Henkelman G. et al., J. Chem. Phys., 111:7010, 1999.
- [3] Fajin J. L. C. et al, J. Phys. Chem. A, 118: 5832-5840, 2014.

Acknowledgements

The work has been performed under the Project HPC-EUROPA3 (INFRAIA-2016-1-730897), with the support of the EC Research Innovation Action under the H2020 Programme; in particular, the author gratefully acknowledges the support of Dr Francesc Illas of the Department of Materials Science & Physical Chemistry and the computer resources and technical support provided by BSC – Barcelona Supercomputing Center.

Hydrogen binding and transport on graphene-covered Pt(111) surfaces

S. Hanselman

Leiden Institute of Chemistry, Leiden University, Leiden, The Netherlands

Introduction

Graphene-covered Pt(111) is a promising hydrogen evolution reaction (HER) catalyst. Its graphene overlayer blocks undesired species from the active Pt(111) surface, increasing its reliability.[1] Moreover, Pt(111) overbinds hydrogen atoms by ~ 0.09 eV relative to the HER rate optimum on Pt;[2] graphene may weaken Pt-H bonds and improve HER rates. However, how graphene affects *H binding is unknown, as is the nature of H atom transport across and underneath the overlayer. Hence, I computed H atom binding energies and *H surface diffusion barriers on Pt(111) with and without graphene overlayer, and studied H transport through graphene and its vacancies, using density functional theory (DFT).

Methods

All calculations were performed using VASP 5.4.4,[3] using the PBE exchange-correlation functional,[4] with DFT-D3 van der Waals corrections.[5] All calculations used a plane-wave cutoff of 450 eV; a $4 \times 4 \times 1$ Γ -centred Monkhorst-Pack k -point grid was used for slabs.[6]

Firstly, the lattice constant of a $3 \times 3 \times 3$ supercell of bulk fcc Pt was optimised using a $4 \times 4 \times 4$ Γ -centred Monkhorst-Pack k -point grid. The resulting interatomic distances were used to model one pristine 4-layer 3×3 Pt(111) slab, and three 4-layer 3×3 Pt(111) slabs covered by one layer of $\sqrt{3} \times \sqrt{3}R30^\circ$ graphene. Up to 9 H atoms (1 ML) were distributed on top of pristine Pt(111) in all possible configurations; similarly, 1, 2, 7, 8 or 9 H atoms were distributed between graphene and Pt(111). For all systems described above, the two topmost Pt layers, H atoms and graphene were relaxed up to 0.02 eV/Å, yielding their internal energies. Finally, for each total *H coverage, its lowest energy *H configurations were used to calculate free energies with vibrational corrections and configurational entropies, from which binding energies were calculated with respect to the equivalent 0 ML *H slab and $H_2(g)$ under standard conditions.

Barriers for *H transport on Pt(111) with and without a graphene overlayer were calculated using nudged elastic band (NEB) calculations between *H adsorption sites. Similarly, H transport through the full graphene overlayer was simulated using NEB, in which H was moved from 1.5 Å above to 1.5 Å below the overlayer. Graphene monovacancies were created by removing one C atom from graphene-covered Pt(111); close and far divacancies were created by removing two C atoms, either adjacent or on opposite sides of a graphene ring, respectively. Terminal carbon atoms were passivated using H atoms; *H adsorption energies underneath the most stable passivated vacancies were calculated.

Results

The graphene overlayer weakens binding energies for *H on Pt(111) by 0.06 ± 0.02 eV; this weakening occurs both at low (near-0 ML) and at high (near-1 ML) *H coverages, as shown in Figure 1.

The barrier for *H surface diffusion on pristine Pt(111) is 0.06 eV, and 0.10 eV under a graphene overlayer. However, an H atom crossing the overlayer experiences a 2.0 eV barrier, suggesting vacancies are necessary for H transport onto Pt(111). Passivated monovacancies contain two C-H bonds which block the surface for H transport. Under a passivated far divacancy, strong C-Pt interactions cause *H to bind 0.23 eV more weakly than under a full graphene overlayer, which is thermodynamically unfavourable near 1 ML coverage. Conversely, under a fully passivated close divacancy, *H binds 0.08 eV more weakly versus the full overlayer which is close to calculated surface diffusion barriers.

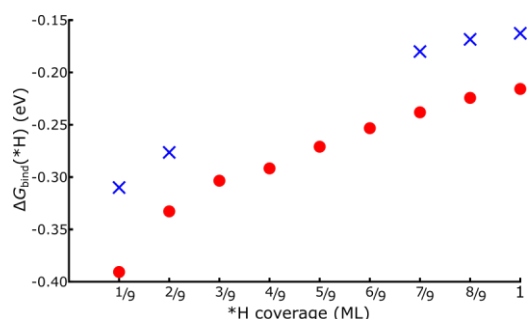


Figure 1 – *H binding energies as a function of *H coverage on pristine Pt(111) (circles) and Pt(111) covered by $\sqrt{3} \times \sqrt{3}R30^\circ$ graphene (crosses).

Conclusions

The graphene overlayer does not significantly impede *H surface diffusion required for HER on Pt(111), and may improve the overall HER rate by shifting the binding energy towards its optimum. Moreover, a two-atom vacancy is sufficient for H transport if it does not interact with Pt(111) too strongly, implying other sufficiently passivated defects allow for H transport as well. These findings provide theoretical support for the hypothetical advantages of using graphene-covered Pt(111) for HER.

References

- [1] Fu Y et al., *Angew. Chem. Int. Ed. Engl.*, 56(42):12883-12887, 2017. [2] Pohl M D et al., *ACS Omega*, 2(11):8141-8147, 2017.
- [3] Kresse G et al., *Phys. Rev. B*, 54(16):11169-11186, 1996.
- [4] Perdew J P et al., *Phys. Rev. Lett.*, 77(18):3865-3868, 1997.
- [5] Grimme S et al., *J. Chem. Phys.*, 132(issue):154104, 2010.
- [6] Monkhorst H et al., *Phys. Rev. B*, 13:5188-5192, 1976.

Acknowledgements

The work has been performed under the Project HPC-EUROPA3 (INFRAIA-2016-1-730897), with the support of the EC Research Innovation Action under the H2020 Programme; in particular, the author gratefully acknowledges the support of dr. Federico Calle-Vallejo (IQTC, University of Barcelona) and the computer resources and technical support provided by BSC.

Computational modelling of optical properties of biomarkers in membranes environments

S. Hariharaputran, Z. Rinkevicius, P. Norman

Kaunas University of Technology, Kaunas, Lithuania; KTH Royal Institute of Technology, Stockholm, Sweden

Introduction

Biomarkers are simply certain biomolecules that are aberrantly expressed during the disease condition. So, by monitoring the population of these marker molecules one can monitor the status of disease and its progress.

Methods

We build membrane models to analyse small organic molecules interaction with Gram-negative bacteria. The basic membrane complex models are built using CHARMM-GUI web-based platforms. Based on the previous research works on Gram-negative bacteria we developed membrane systems using heterogeneous lipid combinations consisting of POPE and POPG i.e. phosphatidylethanolamine and phosphatidylglycerol lipids following the steps in the platform. Further molecular dynamics simulations were performed on them in this order: (a) minimization (b) constant volume simulation (c) Constant volume constant pressure ensemble simulation. The simulations were carried out at room temperature and 1 atm pressure. The time scale for the integration of Newton's equation of motion was 2 fs. A short time scale equilibration run was carried out first. A long-time scale simulation for a time scale of 20-40ns was carried out and the trajectories from the production run were used for further analysis. Structural properties of the systems such as area per lipid, volume, density, electron density and other properties were analysed.

Next our aim is to study the structure of vancomycin and fluorescein tagged vancomycin within membrane and to study the photophysics of vancomycin and fluorescein tagged vancomycin when they are bound to membrane. To carry out the MD simulations for these molecules, we need the optimized geometry and charges in aqueous environment. To achieve this, we have built the molecular structures and then to geometry optimization using density functional theory. The molecular structures for fluorescein and vancomycin have been built using Molden software. We also built the structure for fluorescein tagged vancomycin. All three molecules were subjected to QM calculations for geometry optimization. To reduce geometry optimization time, we used a lower level of theory for the optimization first. In particular, we used the PM7 semi-empirical level of theory. Followed by this the geometries were optimized using B3LYP/6-31g* level of theory in water solvent which is described using a polarizable continuum model. The two of the molecule geometries were optimized (fluorescein and vancomycin). The fluorescein tagged vancomycin geometry was optimized but still not satisfactory and time taken to optimize the structure is more than anticipated. We used Gaussian, GROMACS, Amber, Veloxchem (1) packages for our analysis.

Results

To confirm that the optimized structures correspond to minimum energy structures, we did frequency calculations. For the two cases, all the frequencies found to be positive confirming that in fact the optimized structures correspond to minimum energy structures. This was also carried out for fluorescein tagged vancomycin resulting in similar non-negative frequencies. Followed by this the simulations will be set up for all three molecules in the membrane.

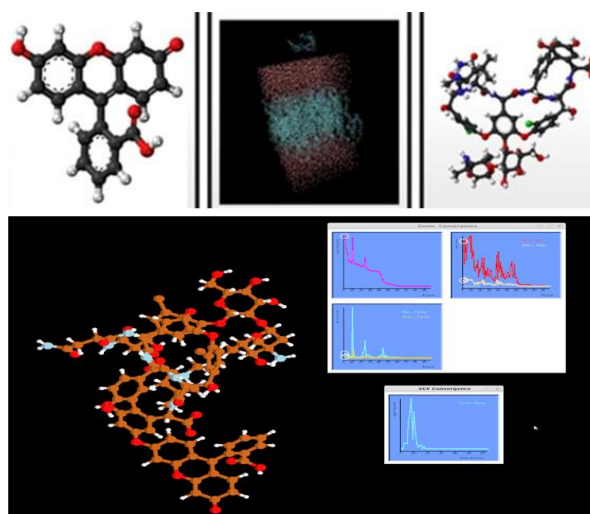


Figure 1 – Top: (a) Fluorescein, (b) Heterogeneous Lipid Membrane, (c) Vancomycin. Bottom: Fluorescein tagged vancomycin

Conclusions

Understanding the photophysical (absorption, fluorescence) properties of these optical probes in a membrane-like environment, we can optimize them in a way they can be used to probe membrane structure.

References

- [1] Rinkevicius Z et al., WIREs Computational Molecular Science, 10:e:1457, 2020.
- [2] Hariharaputran S et al., In: Medical Physics in the Baltic States / [ed] Adliene, D, KTU Press, 2019, p. 102-104.

Acknowledgements

The work has been performed under the Project HPC-EUROPA3 (INFRAIA-2016-1-730897), with the support of the EC Research Innovation Action under the H2020 Programme; in particular, the author gratefully acknowledges the support of KTH Royal Institute of Technology, Department of Theoretical Chemistry and Biology S-106 91 Stockholm, Sweden and the computer resources and technical support provided by PDCC -KTH, Sweden, Dr. Lilit Axner at the PDC Center for High Performance Computing, Stockholm, Sweden. Kaunas University of Technology, Research Council of Lithuania (LMT).

Biorthogonal orbital optimization in perfect paired coupled cluster

R. Heilemann Myhre

Department of Chemistry, Norway

Introduction

The goal of quantum chemistry is to predict and explain physical and chemical properties of molecules by describing their electronic structure. This usually requires solving the Schrödinger equation for the electrons. With infinite computational resources, one could solve the equation to any accuracy. In practice, however, it is only possible to find the exact solution for the very smallest molecules and a compromise between accuracy and computational cost must be made for larger systems. Usually, the form of the searched for solution is approximated by discarding parameters that are thought to be the least important. The coupled cluster (CC) family of models is especially powerful for this purpose. These models are based on an exponential parametrization that is much more compact than the equivalent linear parametrization used in the configuration interaction (CI) approach [1]. This means that much fewer CC parameters (commonly known as amplitudes) suffice to yield the same accuracy as an equivalent CI wave function.

Discussion

The CC amplitudes correspond to excitations from a reference configuration. This reference should be a reasonable approximation to the exact wave function if accurate results are to be obtained from a truncated CC model, that is, one where only a subset of the amplitudes have been included. Most applications of coupled cluster theory employ a Hartree-Fock reference, as it is usually qualitatively correct for molecules around their minimum energy geometry. However, Hartree-Fock does not yield reliable electronic structures for molecules at stretched geometries and radicals, and truncated CC may yield inaccurate or even unphysical results in such cases.

Although the accuracy of CC can be improved by including higher order excitations, this results in a much steeper computational scaling in the conventional approach where all individual amplitudes up to a specific excitation level are included. In the perfect pairing hierarchy, only a small subset of higher excitation amplitudes that are deemed the most important are included. However, this approach breaks the usual invariances of the CC wave function, making it important to optimize the reference configuration. This is typically done by minimizing the energy through orthogonal transformations of the orbitals [2].

Unfortunately, orthogonally optimized calculations do not converge to the correct limit [3,4]. An alternative approach is to use a biorthogonal optimization [5]. Unlike the orthogonal approach, the biorthogonal approach will converge to the correct limit if all amplitudes are included [6]. In the truncated case, ground state energies obtained using orthogonal and biorthogonal optimization tend to be similar in the limited

studies conducted so far, but the biorthogonal case exhibits faster convergence in the orbital optimization.

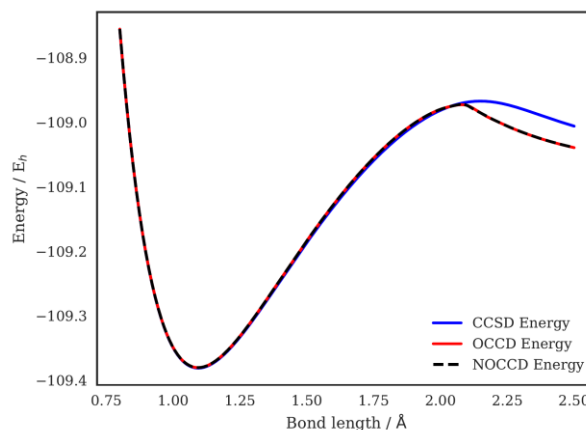


Figure 1 – Ground state energy of N₂ calculated with CCSD, OCCD and NOCCD at various bond lengths.

Conclusions

Biorthogonal orbital optimization has been used in the simplest perfect pairing model, with promising results [7]. In this HPC action, we investigated the use of biorthogonal orbital optimization for higher models in the perfect pairing hierarchy. Unfortunately, extending the existing code for orthogonal orbital optimization to biorthogonal orbital optimization turned out to be much more complicated and time consuming than expected, and we have not been able to produce any computational results yet. However, combining biorthogonal orbital optimization with perfect pairing is still an interesting project and we hope to solve the remaining problems as soon as possible.

References

- [1] Lehtola, S. et al. *J. Chem. Phys.* 147(15):1540105, 2017.
- [2] Sherrill, C. D. et al. *J. Chem. Phys.* 109(11):4171, 1998.
- [3] Köhn, A. et al. *J. Chem. Phys.* 122(8):084116, 2005.
- [4] Lehtola, S. et al. *Mol. Phys.* 116(5-6):547, 2018.
- [5] Pedersen, T. B. et al. *J. Chem. Phys.* 114(16):6983, 2001.
- [6] Myhre, R. H. *J. Chem. Phys.* 148(9):094110, 2018.
- [7] Voorhis T. V. et al. *J. Chem. Phys.* 112(13):5633, 2000.

Acknowledgements

The work has been performed under the Project HPC-EUROPA3 (INFRAIA-2016-1-730897), with the support of the EC Research Innovation Action under the H2020 Programme; in particular, the author gratefully acknowledges the support of Susi Lehtola at the Department of Chemistry at the University of Helsinki and the computer resources and technical support provided by CSC.

Free energy landscape of hydrogenation of carbonyl compounds by Frustrated Lewis Pairs

M. Heshmat, B. Ensing

Stockholm University Sweden; University of Amsterdam, The Netherlands

Introduction

The H₂ molecule is an essential component in various chemical processes. It has a promising role as a clean energy source and supplies hydrogen atoms in hydrogenation reactions, hence, the activation of the hydrogen molecule is always a subject of important studies in catalysis. Since the H₂ molecule has a strong covalent bond and very low polarizability, activation of the hydrogen molecule remains a hard task. The catalytic H₂ activation process hinges on the use of transition metals taking advantage of the catalytic properties of these d-block elements. While transition metal catalysis remains indisputably important in many fields of chemistry, the advent of the metal-free Frustrated Lewis Pair (FLP) concept for activation of small molecules, such as H₂, and FLP-catalyzed hydrogenations has attracted increasing interest ever since Stephan et al. reported their pioneering metal-free reversible H₂ activation in 2006 [1]. The goal of current project is quantitative understanding of the entropic stabilization and calculation of Gibbs free energy of a realistic flexible system, including FLP catalysis for hydrogenation of C=O compounds [2], using metadynamics technique. By computing the free energy landscape, we can obtain the reaction rates and interpret the experimental observations connected to FLP hydrogenation of the carbonyl compounds.

Methods

We have used CP2K program to perform ab initio molecular dynamics (AIMD) simulations with DFT in combination with Gaussian and plane-wave (GPW) method. PBE exchange correlation functional plus D3BJ dispersion correction and DZVP-MOLOPT in combination with GTH and GPW basis sets have been used. Density Functional Theory is the most widely used approach in the field of condensed matter electronic structure calculations, which provides predictions of specific properties of bulk materials and surfaces. Plumed plug-in program was used to analyse features of the dynamics on-the-fly and to calculate free energy surface. Using PLUMED plug-in, the metadynamics and path-metadynamics and steered molecular dynamics simulations may be carried out in combination with CP2K.

Results

For FLP-catalyzed hydrogenation of the C=O bond, according to experiment, a typically used LA is BCF or its derivatives with various electron withdrawing groups and 1,4-dioxane, THF or diethylether donorsolvents with suitably Lewis basic character due to O atom donor. According to basic principles, one might think that a low-barrier transformation in the hydride transfer step of the FLP hydrogenation mechanism, scheme 1, with the reported $\Delta E^\ddagger \approx 1.5$ kcal/mol should correspond to consistently short reactive trajectories.³

However, this might not be the case for an intermediate with a large configurational space generating entropic stabilization. Figure 1 indicates that the period of time from the start of a simulation until hydride transfer can vary in 10 ps to 100 ps range and thus the geometry of the oxocarbenium/borohydride ion pair does not appear to be localized to a specific minimum. Therefore, we expect that this behaviour can extend well above 100 ps range, but statistically meaningful exploration of such long-time interval is beyond the unbiased molecular dynamics computational capabilities at present. But one may conclude that regions of configuration space sampled by the dynamics at T = 325 can be far apart.

Given these results, a conclusion that a single optimized structure does really represent the configurational space of this cation/anion system is to some extent doubtful. This is in accord with the notion of weak cation/anion pairing for related species compose of oxonium cation and a borat as anion.

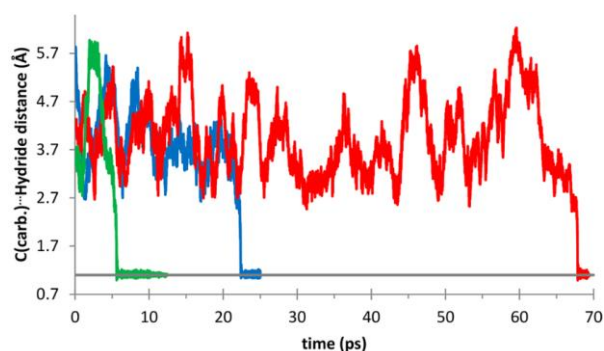


Figure 1 – Time evolution of C(carb)...hydride distances in [dioxane-H⁽⁺⁾-acetone][[(C₆F₅)₃B-H⁽⁻⁾] at T = 325 K. Three representative BOMD-trajectories with different configurations are compared. The period of time from the start of a simulation until hydride transfer is in 10 to 100 ps range.

References

- [1] Stephan D. W. et al., Science, 314(5802): 1124-1126, 2006.
- [2] Heshmat M., Privalov, T., J. Phys. Chem. A, 122 (23): 5098-5106, 2018.
- [3] Das, S.; Pati, S. K., Chem. Eur. J., 23: 1078-1085, 2017.

Acknowledgements

The work has been performed under the Project HPC-EUROPA3 (INFRAIA-2016-1-730897), with the support of the EC Research Innovation Action under the H2020 Programme; in particular, the author gratefully acknowledges the support of Prof. Bernd Ensing and computational chemistry department of University of Amsterdam and the computer resources and technical support provided by SURFSARA.

Mechanism of Cu(I) translocation via CTR1 transporter

P. Janoš, A. Magistrato

CNR-IOM c/o International School for Advanced studies (SISSA/ISAS), Trieste, Italy

Introduction

Transmembrane Copper Transporter 1 (CTR1) is a key part of Copper (Cu) metabolism and a critical gateway for in-cell Cu entrance. The in-cell Cu metabolism must be meticulously regulated to ensure appropriate in-cell Cu levels and the tight balance between its two oxidation states: Cu(II) and Cu(I). While Cu(II) is responsible for the toxic effects, Cu(I) is essential for Cu-metalloproteins functions. The process of Cu transport as mediated by CTR1 can be divided into 3 steps: 1) Capture and reduction of Cu(II) into Cu(I); 2) Binding and translocation of Cu(I) through the selectivity filter; 3) Delivery of Cu(I) to the Cu-metallochaperone ATOX1. The selectivity filter at the extracellular side of CTR1 is composed of two aligned methionine triads (Met-triads) with each CTR1 subunit providing one methionine (Met). In this study we apply quantum-classical (QM/MM) MD simulations to unprecedentedly unravel the atomic details of the Cu(I) translocation from the upper Met-triad to the bottom Met-triad.

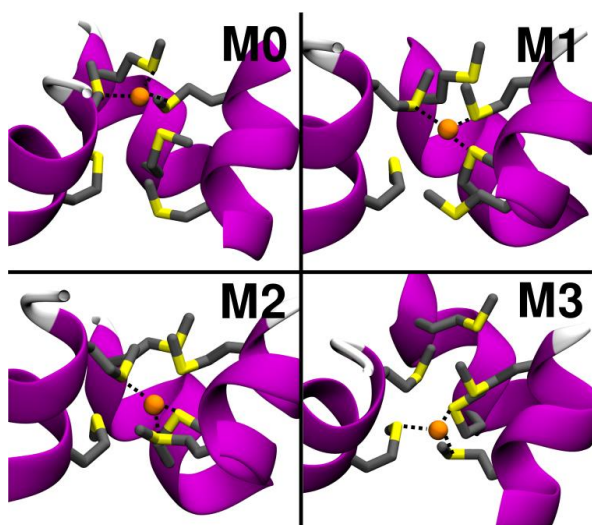


Figure 1 – Close-ups of the Cu(I) translocation from upper Met-triad to the bottom Met-triad.

Methods

The structure of CTR1 was taken from crystallographic structure (PDB ID: 6M98) [1] and placed into a membrane bilayer. The QM/MM MD simulations were performed using CP2K version 6.1 [2]. The QM zone contained all six methionine residues, the Cu(I) ions and nearby water molecules. The QM zone was described using BLYP functional. Metadynamics (MTD) enhanced sampling method was used

to study the Cu(I) translocation mechanism [3]. We employed two collective variables (CVs): CV1 – distance of the Cu(I) to the plane of the top Met-triad; CV2 - coordination number of the Cu(I) with respect to sulphur (S) atoms of the bottom Met-triad.

Results

The Cu(I) starts in Minimum 0 (M0), where it is fully coordinated by the upper Met-triad. It then moves to M1 by overcoming $\Delta G^\ddagger = 5.8 \pm 2.8$ kcal/mol and is coordinated by two Met from the upper Met-triad and one from bottom. Next, by overcoming a $\Delta G^\ddagger = 7.6 \pm 2.7$ kcal/mol, Cu(I) heads into M2, where it is coordinated by one Met from the upper Met-triad and two from the bottom. From here, the Cu(I) overcomes a $\Delta G^\ddagger = 4.3 \pm 4.0$ kcal/mol barrier to reach the final state M3, where it is fully coordinated by the methionines of the bottom Met-triad.

Conclusions

Our investigation of the Cu(I) translocation mechanism of CTR1 unprecedentedly reveals that during the translocation the Cu(I) visits two stable intermediate steps, one in which it is coordinated by two methionines from upper Met-triad and one from the bottom; and second in which it is coordinated by one methionine from the upper Met-triad and two from the bottom. It is, in fact, the movement between these two states that is associated with the highest free energy barrier in the translocation process. From the M3 minimum two scenarios are possible: the Cu(I) can either dissociate on its own or require the binding of a second Cu(I) to the upper Met-triad to co-adjuvate its dissociation.

References

- [1] Ren F, Logeman BL, Zhang X, Liu Y, Thiele DJ, Yuan P. X-ray structures of the high-affinity copper transporter Ctr1. *Nat Commun.* 2019 Dec;10(1):1386.
- [2] Hutter J, Iannuzzi M, Schiffmann F, VandeVondele J. CP2K: atomistic simulations of condensed matter systems. *Wiley Interdisciplinary Reviews: Computational Molecular Science.* 2014;4(1):15–25.
- [3] Laio A, Parrinello M. Escaping free-energy minima. *Proceedings of the National Academy of Sciences.* 2002 Oct 1;99(20):12562–6.

Acknowledgements

The work has been performed under the Project HPC-EUROPA3 (INFRAIA-2016-1-730897), with the support of the EC Research Innovation Action under the H2020 Programme; in particular, the author gratefully acknowledges the support of Alessandra Magistrato and the computer resources and technical support provided by CINECA.

NMR spectra of water-ionic liquid mixtures: large-scale quantum mechanics/molecular mechanics modelling

D. Lengvinaitė¹, A. Laaksonen²

¹Institute of Chemical Physics, Faculty of Physics, Vilnius University, Lithuania; ²Department of Materials and Environmental Chemistry, Stockholm University, Sweden

Introduction

Ionic liquids, ILs, are substances composed of solely organic cations and organic or inorganic anions that have a melting point below 100 °C. Many ILs remain liquid at or near room temperature and are called room-temperature ionic liquids (RTILs) [1]. The imidazolium based IL are in fact among the most widely studied RTIL. Recently, some interesting NMR measurements on mixtures of water and ILs based on 1-butyl-3-methyl-imidazolium, C₄Mim, and on different anions such as halides, Cl⁻/Br⁻/I⁻, tetrafluoroborate, BF₄⁻, and nitrate, NO₃⁻, were carried out by the NMR spectroscopy group of Vilnius University, Lithuania. Curiously, the ¹H NMR chemical shift of water was found to evolve non-monotonically with the changing concentration of the binary solution of IL and water. These experimental findings reflect the structural changes of the samples with changing molar fractions of IL and water. In this communication, we briefly discuss our NMR results for mixtures of [C₄Mim][Cl] and [C₄Mim][BF₄] ILs and water based on large-scale quantum mechanics/molecular mechanics calculations.

Methods

Classical molecular dynamics (MD) simulations were performed for mixtures of [C₄Mim][Cl] IL and water where the system was composed of 1000 ionic pairs and 3000 water molecules ($\chi_w=0.75$). An OPLS-AA [2,3] and TIP4Pew force fields were used for the IL and water molecules, respectively. MD simulations of neat water were conducted as well. All simulations were performed using AMBER program [4]. We have performed extensive equilibration of all molecular systems at the NPT ensemble by heating them gradually to 500 K and then cooling to the desired temperature of 298 K. The final equilibration at ambient conditions of around 16 ns was necessary to get the density converged. We finally switched to NVT ensemble in order to record 8 ns long trajectories. Based on previous and new molecular trajectories we have constructed several sets of molecular configurations to be used in the QM/MM calculations of NMR shielding constants. Each set contains 100 configurations. The QM/MM calculations of the ¹H NMR isotropic shielding constants have been carried out using the QMMM module of the Dalton 2016.1 program [5]. The shielding constants have been computed using the KT3 exchange–correlation functional along with the def2-TZVP basis set.

Results

Our previous MD simulations on IL/water mixtures where molar fraction of water does not exceed 50% showed that the expected so-called water-pockets do not form in these systems. Water molecules rather form hydrogen bonds with the anions and to some lesser degree with the imidazolium cations through the C-H bonds in their imidazolium rings. For the mixtures of water and [C₄Mim][BF₄], the QM/MM results for proton NMR signal of water show a marked up-field shift as compared to that in the neat water. These results

are in line with experimental findings which show that the proton chemical shift of water decreases with the rising concentration of IL in the binary mixture.

A rather different behaviour of ¹H NMR chemical shifts of water was observed in the [C₄Mim][Cl]/water mixtures. When the concentration of water is low, the chemical shift of water protons moves down-field with decreasing concentration of water. Our computational results suggest that this behaviour is explained by the formation of abundant aggregates of water molecules and chloride anions with strong intermolecular hydrogen bonds. These hydrogen bonds lead to the deshielding of the hydrogen atoms in water molecules as compared to those in pure water. However, we do not reproduce the initial decrease of the chemical shift of water protons at low [C₄Mim][Cl] IL concentration.

The structural analysis of the [C₄Mim][Cl]/water mixtures at molar fraction of water ($\chi_w=0.75$) showed formation of abundant aggregates of water molecules where hydrogen bonding between them is not mediated by the anions of the IL (see Figure 1).

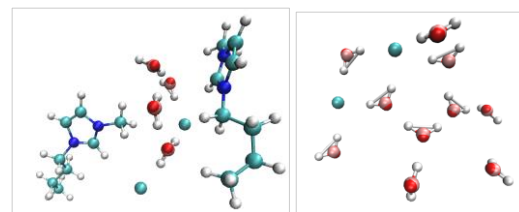


Figure 1 – the associates of water-chlorine anion and water-water in the ionic liquid: [C₄Mim][Cl].

Conclusions

The QM/MM results obtained thus far allowed for partial explanation of the behaviour of the NMR chemical shift of water with its changing concentration in the [C₄Mim][Cl] and [C₄Mim][BF₄] ionic liquids.

References

- [1] Welton T., Chem. Rev., 99(8):2071, 1999. [2] Lopes J. N.C. et al., J. Phys. Chem. B, 108(6):2038, 2004. [3] Andrade J. et al., J. Phys. Chem. B, 106(51):13344, 2002. [4] Case D. A. et al., Amber 2012, University of California, San Francisco, 2012. [5] Aidas K. et al., "The Dalton quantum chemistry program system", WIREs Comput. Mol. Sci., 2014.

Acknowledgements

The work has been performed under the Project HPC-EUROPA3 (INFRAIA-2016-1-730897), with the support of the EC Research Innovation Action under the H2020 Programme; in particular, the authors gratefully acknowledge the support of Prof. Aatto Laaksonen of the Department of Materials and Environmental Chemistry, Stockholm University, and the computer resources and technical support provided by PDC center for high performance computing at Royal Institute of Technology.

Exploring Buckminsterfullerene Polymerization

J. Laranjeira, Manuel Melle-Franco, Leonel Marques, Emilio Martínez Núñez

CICECO, Aveiro Institute of Materials, University of Aveiro, Portugal; Faculdade de Química Universidade de Santiago de Compostela, Spain

Introduction

C_{60} is an amazing allotrope of carbon which, when subjected to high pressures high temperatures (HPHT), forms extend polymerized networks with different dimensionalities [1,2]. A lot is unknown regarding the bonding schemes that C_{60} adopts in these crystalline networks. Furthermore, there is a correlation between the molecular centers of mass (CM) distance in the crystals and in dimers when the same bonding scheme is considered. We present an extensive search of C_{60} dimers. The stability of the new dimers was checked using DFTB+ with 3OB parameters and Gaussian09 at B3LYP 6-31G(d,p) theory level.

Methods

AutoMeKin (AMK) [3] is a quantum chemistry software designed to find reaction mechanisms. To perform this task AMK uses a molecular dynamics capable third-party software (mopac, qcore, etc), to perform thousands of simulations at high energy, while checking for structural transformations. If a structural transformation (for instance a bond is broken/formed) is found, AMK checks if it is a transition state via second derivatives calculation and then saves this transition state. Afterwards the minima are obtained from the transition states following the intrinsic reaction coordinate (IRC). Here we used AMK interfaced with Mopac to search for new C_{60} dimers, in a non-human guided way.

We also interfaced AMK with DFTB+ nevertheless our attempts of doing an AMK search of C_{60} dimers using DFTB+ were unfruitful because DFTB+ uses numerical derivatives instead of analytical ones, thus the calculation was too time demanding on such a system. Yet the interface may be used in small systems since DFTB+ gives a much better description of atomic interactions than Mopac at a fraction of the cost of Gaussian09 calculations.

Results

AMK interfaced with mopac yielded 10466 different minima but just ~60 were proper C_{60} dimers. The other minima had C_{60} with their cage broken or were repetitions. From this ~60 dimers we could only minimize with DFTB+ and afterwards in gaussian09 ~40 of them, all the others were unstable. Nevertheless, most of the found dimers were unexplored before and there are several new bonding schemes such as the ones presented in figure 1.

We also checked the distance between molecular centers of mass of all the dimers and got values from 8.07 Å to 9.15Å. Some of these bonding schemes have distances that may

explain experimental data, in particular distances between C_{60} molecules in 3D crystals.

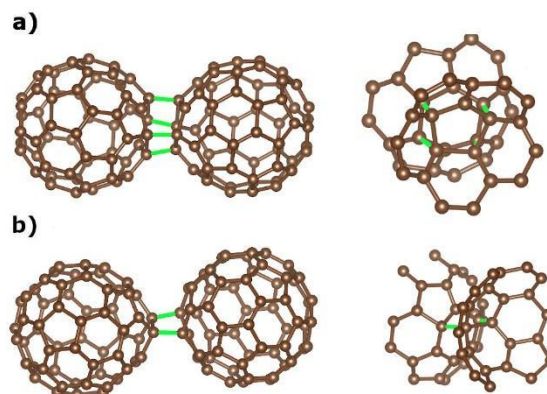


Figure 1 – New C_{60} dimers found with AMK and optimized with Gaussian09. a) 5/6 3+3 & 2+3 cycloaddition. b) 5/6 2+3 cycloaddition.

Conclusions

An extensive search of C_{60} dimers was done using AMK interfaced with Mopac. Several new C_{60} bonding schemes that may be present in polymeric phases were found and had their energetics studied.

The new dimers have bonding schemes that may justify experimental observation on HPHT C_{60} polymers.

AMK was interfaced with DFTB+ unfortunately it proved to be very time demanding for our task.

References

- [1] J. Laranjeira, L. Marques, M. Mezouar, M. Melle-Franco, K.Strutynski, Phys. Stat. Sol. - RRL 2017, 11, 1700343
- [2] J. Laranjeira and L. Marques, Mat.Is Today Comm. 2020, 23, 100906.
- [3] Martinez-Nunez, E. J. Comput. Chem. 2015, 36, 222–234.

Acknowledgements

The work has been performed under the Project HPC-EUROPA3 (INFRAIA-2016-1-730897), with the support of the EC Research Innovation Action under the H2020 Programme; in particular, the author gratefully acknowledges the support of Emilio Martínez Núñez, Faculdade de Química Universidade de Santiago de Compostela and the computer resources and technical support provided by BSC.

An *ab initio* approach to predicting energetic material impact sensitivity

A.A.L. Michalchuk¹ and C. A. Morrison²

¹Federal Institute for Materials Research and Testing, Berlin, Germany; ²EaStChem School of Chemistry, University of Edinburgh, United Kingdom

Introduction

The impact sensitivity (IS) of an energetic material (explosive, propellant, pyrotechnic; EM) is an internationally recognized material hazard classification. If an EM is highly sensitive (i.e. initiates on mild impacts), it is generally unfit for real-world applications. Significant efforts have attempted to characterize, rationalize, and design low sensitivity EMs (LSEMs). Experimental testing protocol such as the BAM Fall-Hammer require the preparation of bulk quantities of the EM, posing significant risk to health and safety especially if new EMs are being studied. The need for advanced theoretical approaches to predict the IS of EMs – thus allowing EM properties to be design *in silico* – are required [1]. A promising theoretical model is based on vibrational up-pumping. Following the seminal work of Dlott *et al* [2], we presented an *ab initio* phonon up-pumping approach for predicting EM IS [3]. This up-pumping model captures critical features of the impact event, including compression-induced excitation and vibrationally induced metallisation [4]. This early model was based on computationally expensive phonon dispersion curves (PDCs), posing a substantial barrier to implementing our model for larger-scale material screening. We herein develop this model towards the use of Brillouin zone centre spectra.

Methods

DFT calculations were done using CASTEP 19.11 [5]. Wavefunctions were expanded in plane waves to 1200 eV using norm-conserving pseudopotentials. The Brillouin zone was sampled on grid $< 0.05 \text{ \AA}^{-1}$. The exchange-correlation functional of Perdew-Burke-Ernzerhof (PBE) [6] was used with the Grimme D2 dispersion correction [7]. Zone centre phonons were calculated *via* linear response theory, and converted to two-phonon density of states, $\rho^{(2)}$ according to our two-step up-pumping model.³ This model first transfers excited phonon populations to intermediate frequency ‘doorway’ states, followed by subsequent up-pumping into higher-frequency ‘target’ states. The rate of vibrational up-pumping for each step (τ) was calculated according to,

$$\tau_1 = \rho^{(2)}(\omega = \omega_{T/2}) \times [n_{ph} - n_d] \quad \text{Equation 1}$$

$$\tau_2 = \rho^{(2)} \times [n_{ph} + n_d - n_T] \quad \text{Equation 2}$$

where n_i represents the Bose-Einstein populations for the phonon (ph), target (t) and doorway (d) states.

Results

The vibrational up-pumping model requires identifying an upper bound for the phonon region, Ω_{max} . The phonon region for a primitive cell containing Z molecules comprises $6Z$ external modes, and a system-dependent number of amalgamated internal modes. The composition of the phonon bath was hence identified by analysis of the zone centre eigenvector displacements. The selection of Ω_{max} allowed us to calculate the relative shock heating of the phonon bath using knowledge of the total vibrational heat capacity. This shocked population was up-pumped according to Equations 1 and 2, transferring the excess phonon populations into localised internal molecular vibrations.

Consistent with RRKM theory, we take the total up-pumped density within the region $2\Omega_{max}$ to $3\Omega_{max}$ as indication of the material’s intrinsic sensitivity. By performing these simulations across our test materials, excellent correlation against experimental sensitivity is obtained, Figure 1.

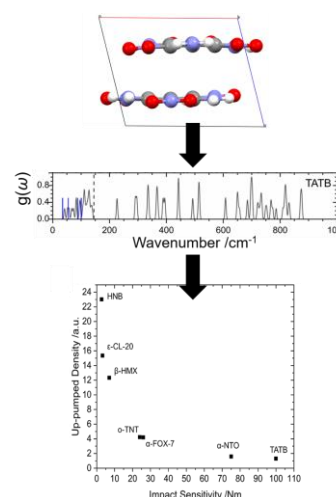


Figure 1 – The (top) crystal structure is used to simulate phonon spectra (middle), which is subsequently used for up-pumping simulations to predict (bottom) the relative sensitivity.

Conclusions

From knowledge of the crystal structure, the relative impact sensitivity of EMs can be successfully predicted. This requires calculation only of Brillouin zone centre vibrational spectra, and calculation of vibrational energy transfer from the phonon modes into higher frequency molecular modes. Our developments open the door to *in silico* design of LSEMs.

References

- [1] R. Tsyshkevsky, O. Sharia and M. Kukulja, *Molecules*, 2016, 21, 236.
- [2] D. D. Dlott and M. D. Fayer, *J Chem Phys*, 1990, 92, 3798–3812.
- [3] A. A. L. Michalchuk, M. Trestman, S. Rudić, P. Portius, P. T. Fincham, C. R. Pulham and C. A. Morrison, *J. Mater. Chem. A*, 2019, 7, 19539–19553.
- [4] A. A. L. Michalchuk, S. Rudić, C. R. Pulham and C. A. Morrison, *Phys. Chem. Chem. Phys.*, 2018, 20, 29061–29069.
- [5] S. J. Clark, M. D. Segall, C. J. Pickard, P. J. Hasnip, M. I. J. Probert, K. Refson and M. C. Payne, *Z Krist*, DOI:10.1524/zkri.220.5.567.65075.
- [6] J. P. Perdew, K. Burke and M. Ernzerhof, *Phys. Rev. Lett.*, 1996, 77, 3865–3868.
- [7] S. Grimme, *J. Comput. Chem.*, 2006, 27, 1787–1799.

Acknowledgements

The work has been performed under the Project HPC-EUROPA3 (INFRAIA-2016-1-730897), with the support of the EC Research Innovation Action under the H2020 Programme; in particular, the author gratefully acknowledges the support of the School of Chemistry, University of Edinburgh and the computer resources and technical support provided by the EPCC (Edinburgh).

Sesquicarbene complexes: allylic carbon-bridged bimetallic complexes, dicarbene complexes with one carbon p-orbital?[1]

F.F. Mulks^{1,2}, A.S. K. Hashmi², S. Faraji¹

¹Zernike Institute for Advanced Materials, Groningen, The Netherlands; ²Organisch-Chemisches Institut, Ruprecht-Karls Universität Heidelberg, Germany

Introduction

By reacting cyclopropen-1-ylgold(I) complexes with gold(I) cations, we recently discovered highly reactive 1,1-diaurated allylium cations [2, 3]. They contain a bridging carbon atom with a cationic charge which allows for π -backbonding. They showed absorption bands in the near IR spectrum, indicating lower energy excitations than in any gold carbene complex. We now report our computational investigation of the electronic structure of the experimentally investigated digold complexes and of dichromium complexes with stronger π -backdonation to gain an understanding of these complexes and of their potential applications (Figure 1).

Methods

Optimizations and single point calculations were performed with the Q-Chem 5.2 quantum chemistry package. Geometries were optimized at the PBEh-3c/def2-mSVP level of theory. Single point calculations at the ω B97M-V/def2-TZVP level of theory were then employed. The effective core potential (ECP) def2-ECP was employed for the computational treatment of metal complexes and the solvent influence of methylene chloride ($\epsilon = 8.51$) was modelled using the integral equation formalism polarizable continuum model (IEFPCM). The canonical orbitals generated this way were then used as input for the generation of IBOs (exponent 2). This study covers 30 allylium derivatives, comparing non-metalated and mono-metalated analogs to the sesquicarbene complexes. See ref. [3] for details and references therein.

Results

We found that both gold centers in the previously experimentally detected digold sesquicarbene complexes (Figure 2) have a double bond character comparable to gold carbene complexes, averaging to 7% (trans) and 8% (cis) for the two bonds versus 7% in the monogold complexes. The hypothetical dichromium sesquicarbene complexes have a reduced carbene character (trans: 12% and cis: 13%) compared to the monochromated complexes (28%); but exceeding gold by far in this respect. They participate in substantial π -backbonds for a significant carbene character at both centers.

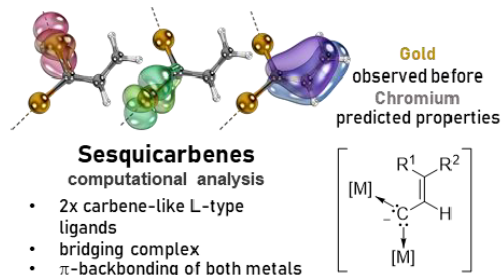


Figure 1 – Sesquicarbene complexes were investigated.

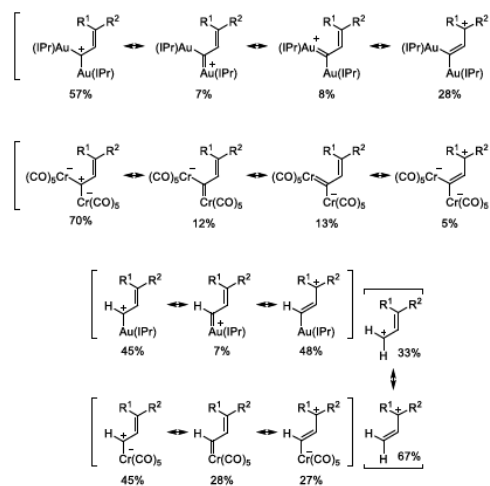


Figure 2 – Mesomeric structures by IBO analysis.

Conclusions

The electronic structures of the $[M_2C(vinyl)]^+$ ($M = Au(IPr), Cr(CO)_5^-$) complexes investigated in this work is on the interface between M–C single bonds and M=C double bonds. The coordinating carbon atom acts as a significantly stronger σ -donor than the IPr ligand towards both metal centers. The coordinating atom is an allylic carbon atom that donates σ -bonds to bridge two metal centers as a double L-type ligand. An empty π -orbital accepts π -backdonation from both metal centers and, in many cases, further resonance stabilization by the vinyl function. Incorporating two carbene-type dative bonds to both metal centers with only one carbon p-atom orbital accepting π -backbonds, these compounds can be described as sesquicarbene complexes.

References

- [1] Adapted in part with permission from F. F. Mulks, A. S. K. Hashmi, S. Faraji, *Organometallics*, DOI: 10.1021/acs.organomet.0c00102, 2020. Copyright 2020 American Chemical Society. References and further details can be found therein.
- [2] F. F. Mulks, P. W. Antoni, J. H. Gross, J. Graf, F. Rominger, A. S. K. Hashmi, *J. Am. Chem. Soc.*, 141 (11), 4687-4695, 2019.
- [3] F. F. Mulks, P. W. Antoni, F. Rominger, A. S. K. Hashmi, *Adv. Synth. Catal.*, 360 (9), 1810-1821, 2018.

Acknowledgements

The work has been performed under the Project HPC-EUROPA3 (INFRAIA-2016-1-730897), with the support of the EC Research Innovation Action under the H2020 Programme.

Cooperativity and solvation

G. Paragi

University of Szeged, Department of Medicinal Chemistry, Hungary

Introduction

Self-assembly have a key role in the formation of various molecular complexes, like self-assembling 1D or 2D structures on metal surfaces or larger biomolecular structures. Quadruplex structure (Gu4) is a well-known example of these systems, which based on the four-fold tetrameric arrangement of guanine (Gu) bases. An interesting character of this structure is that it contains an extra stabilization effect between adjacent Gu units in vacuum, which extra energy gain disappears in the presence of solvent [1]. In Density Functional Theory (DFT) calculations, the Ziegler-Rauk Energy Decomposition Analysis (EDA) [2] provides an excellent tool for the chemical interpretation of interaction energy between fragments, although in its original form the theory was only applicable to vacuum calculations. Therefore, in the frame of the present project, we tried to make a first step towards the extension of the EDA for solvated systems, where the solvation was taken into account in an implicit manner. Applying the new method for the Gu4 system, we compared the EDA terms provided by vacuum and by different implicit water calculations.

Methods

All DFT calculations were carried out by the ADF program package using BLYP-D/TZ2P level of theory without the application of frozen core or relativistic approximation. Normal level numerical integration was selected, and regarding the geometrical optimization the gradient as well as the total energy convergence criteria was set to 10^{-4} Hartree/Å and 10^{-5} Hartree, respectively.

Results

First, geometric optimizations were carried out in vacuum and implicit solvent. Then, the original and the modified EDA was performed in vacuum and in implicit solvent, respectively. Our adjustment utilized the special properties of the applied implicit solvent method (COSMO [3]). Briefly, in COSMO a solvent is substituted by a polarizable continuous medium and the ligand-target complex is placed into a cavity within the dielectric continuum. The shape of the cavity as well as the induced charges on the surface of the cavity is determined by the COSMO. For EDA in COSMO, it is an open question which cavity and induced surface charges should be applied when the molecular orbitals (MO) of the fragments are calculated. More precisely, we can have fragment calculations in its own cavity, or we can put the fragment into the cavity of the complex and calculate the MOs of the fragment in this extended environment. Obviously, we got different MOs in various environments, which provided different EDA values. In Table 1 the EDA terms are presented in vacuum and in different implicit solvent calculations for the Gu4 complex. We would like to note that preliminary calculations were carried out for simple complexes, like water dimer to check the consequences of different EDA calculations in COSMO. The EDA values in Table 1 were provided by the interaction of

the 4 fragments, where each fragment contained single Gu unit.

EDA terms*	Vacuum.	COSMO	
		fragment size cavity	complex size cavity
ΔE_{Pauli}	119.8	121.2	120.7
$\Delta E_{el.stat.}$	-106.8	-149.0	-89.2
$\Delta E_{orb.int.\sigma}$	-71.7	-57.7	-89.5
$\Delta E_{orb.int.\pi}$	-12.7	-1.0	-16.7
$\Delta E_{tot\ orb.int.}$	-84.4	-58.7	-106.2
ΔE_{disp}	-17.0	-17.4	-17.4
ΣE_{EDA}	-88.4	-104.0	-92.2
$E(solv. eff.)$		68.5	56.7
$E(tot.interact)$	-88.4	-35.5	-35.4

* For the definition of the EDA terms see ref. [4], while $E(solv. eff.)$ includes both solvation and cavitation energy changes.

Table 1 – EDA terms (in kcal/mol) of Gu4 complex in vacuum and in implicit solvent using fragment size or complex size cavity in the fragment calculations.

As we can see, the Pauli and the dispersion terms were almost the same not just in the two COSMO cases, but also in the vacuum calculation. Larger changes were found for the electrostatic and the orbital interaction terms, but we could not see strict tendencies comparing the vacuum and the COSMO calculations. The total interaction energies decreased significantly in the presence of the water, but we could not explain this change with the help of the new EDA terms. In the preliminary water dimer complexes similar statements could be done.

Conclusions

Here, we extended the original EDA protocol to implicit solvent calculations; but the calculated EDA terms could not help to select a unique EDA method in solvent at the present state.

References

- [1] Fonseca Guerra C et al., Chem. Eur. J., 17:12612, 2011.
- [2] Ziegler T et al., Inorg. Chem., 18:1558, 1979.
- [3] Klamt A et al., J. Chem. Soc., Perkin Trans., 2:799, 1993.
- [4] Bickelhaupt F M et al., Rev. Comp. Chem., 15:1, 2000.

Acknowledgements

The work has been performed under the Project HPC-EUROPA3 (INFRAIA-2016-1-730897), with the support of the EC Research Innovation Action under the H2020 Programme; in particular, the author gratefully acknowledges the support of Prof. Celia Fonseca Guerra in the Department of Theoretical Chemistry at the Free University of Amsterdam (VU) and the computer resources and technical support provided by the SARA center.

Successive Diels-Alder cycloadditions of cyclopentadiene over [10]CPP \supset C60

G. Pareras^{1,2}, D. Tiana¹, A. Poater², M. Solà²

¹School of Chemistry, University College Cork, Ireland; ²Institut de Química Computacional i Catàlisi, Departament de Química, Universitat de Girona, Spain

Introduction

Based on previous studies of Solà and co-workers with fullerenes,[1] the main objective here is to study the capacity of successive Diels-Alder cycloadditions of cyclopentadiene over Nano-Saturn complexes of fullerene. We aim to extend the knowledge of this kind of process from the kinetic and thermodynamic point of view by locating the TSs of the successive Diels-Alder cycloadditions of cyclopentadiene on the [10]CPP \supset C60 leading to the Th-symmetric hexakisadduct. It will be also studied the solvent effect and finally discussed the possibility of the existence of the heptakisadduct.

Methods

Calculations have carried out using the functional B3LYP [2] in conjunction with 6-31G* basis set [3] and empirical dispersion GD3BJ [4].

Results

It has been studied the possibility of multiple additions of cyclopentadiene over the Nano-Saturn complex [10]CPP \supset C60 reaching up to six possible additions (hexakisadduct). Same additions have been studied over the fullerene C60 in order to compare the role of the Saturn-ring [10]CPP. First addition does not show major differences between the two systems, however, is already perceived a small interaction between the Saturn-ring and the cyclopentadiene. Since it has been spotted such interaction, it has been considered two possible positions on the cyclopentadiene that could interact with the ring as well as, three possible approximations on the [10]CPP \supset C60 considering such possible interactions. It has been observed that the system is over stabilized when hydrogens on C2 carbons of the cyclopentadiene are the ones interacting with the ring. Subsequent additions have shown that are more favourable when happening on [10]CPP \supset C60. Enthalpic energies show that each addition is lower in energy than the previous one. However, when analysing each addition relative to the adduct or the product the trend is different. In the first case the energy for each barrier is higher after each addition, while in the second case additions 2, 4 and 6 are more favourable than 1, 3 and 6. Both relative energies are always lower in energy in [10]CPP \supset C60 system. Gibbs energies explain a different behaviour. First of all, adducts are no longer more stable than the reactant (previous product). Secondly additions from 1 to 4 are lower in energy respect to reactant 0 however, fifth and sixth additions are

not only higher in energy but also show an endothermic character. Relative to adduct and reactant energies for each step show, in the first case, that barrier energies for each step increases after each addition moreover, additions 2, 3 and 4 are lower in energy in C60. Relative-to-reactant energies show how additions 2, 4 and 6 are more favourable than 1, 3 and 5. In this last case all the additions are lower in energy in [10]CPP \supset C60. Even though it has been spotted differences in each step, the additions are energetically more favourable on [10]CPP \supset C60 and in C60, the possible interaction between the cyclopentadiene and the Saturn-ring not only stabilizes adducts and transition states but also slightly the products of each addition. Moreover, the fact that the energy of the system changes depending how the cyclopentadiene is interacting with ring shows how this system could be selective through different dienes.

Conclusions

It has been demonstrated that it is possible the formation of the hexakisadduct when working with [10]CPP \supset C60. Moreover, compared with the C60 system, Diels-Alder instructions are promoted when working with the [10]CPP \supset C60 as the adducts and transition states are stabilized due to non-bonding interactions with the [10]CPP ring.

References

- [1] Sola, M.; M. Duran.; Mestres, J. J. Am. Chem. Soc. 118, 8920-8924 (1996).
- [2] Stephens, P. J., Devlin, F. J., Chabalowski, C. F. & Frisch, M. J. J. Phys. Chem. 98, 11623-11627 (1994).
- [3] Kendall, R. A., Dunning, T. H. & Harrison, R. J. J. Chem. Phys. 96, 6796-6806 (1992).
- [4] Grimme, S., Antony, J., Ehrlich, S. & Krieg, H. J. Chem. Phys. 132, 154104 (2010).

Acknowledgements

The work has been performed under the Project HPC-EUROPA3 (INFRAIA-2016-1-730897), with the support of the EC Research Innovation Action under the H2020 Programme; in particular, the author gratefully acknowledges the support of Dr. Albert Poater and the computer resources and technical support provided by Barcelona Supercomputing Centre (BSC).

The dark-state recovery mechanism of blue light-using flavin proteins

A. Pérez de Alba Ortíz¹, C. Rovira^{2,3}, B. Ensing¹

¹Van 't Hoff Institute for Molecular Sciences, AI4Science Laboratory, and Amsterdam Center for Multiscale Modeling, University of Amsterdam, Amsterdam, The Netherlands; ²Departament de Química Inorgànica i Orgànica (Secció de Química Orgànica) & Institut de Química Teòrica i Computacional (IQTCUB), Universitat de Barcelona, Barcelona, Spain; ³Institució Catalana de Recerca i Estudis Avançats (ICREA), Barcelona, Spain.

Introduction

Blue light-using flavin (BLUF) proteins are light-sensors that regulate responsive movement, gene expression and enzyme activity in diverse organisms [1]. Their signalling times range from seconds to minutes, indicating a uniquely flexible dark-state recovery mechanism. Unlike other light-sensors, the flavin chromophore is non-covalently bonded to the protein. Hence, the switching occurs via a change in the protein-flavin hydrogen-bond network, involving conserved residues transferring protons, tautomerizing, rotating, and approaching or leaving the chromophore pocket; triggering secondary structure displacements. The specific deactivation steps and residue roles have remained controversial. The detailed process is difficult to probe experimentally, and although simulations can track it, the computational effort is daunting. We combine forefront techniques to simulate, for the first time, explicit dynamics of the deactivation. A hybrid quantum mechanics/molecular mechanics (QM/MM) scheme focuses the computational resolution in the flavin's vicinity, while our path-based methods sample the mechanism of dark-state recovery with high efficiency.

Methods

We present simulations at the QM/MM level for the hydrogen-bond rearrangement near the chromophore. Moreover, rather than obtaining potential-energy profiles along energy-minimized intermediate states, we perform QM/MM-based molecular dynamics (MD) to validate our mechanistic pathways and calculate free-energy profiles. This task, which is particularly expensive for QM/MM MD, becomes feasible thanks to our in-house developed path-based free-energy methods [2]. By sampling along an adaptive light-to-dark path in the space of key transition descriptors, i.e. collective variables (CVs), we efficiently calculate a free-energy profile. For our QM/MM simulations of the change in hydrogen-bonding within the active site, we use CVs inspired by the currently accepted mechanism [3,4], and we render free-energy profiles for the AppA and BlrB BLUF proteins, which we compare with previous work and experimental recovery rates [4,5].

Results

For the first time, dynamics and free-energy calculations were performed of the Gln tautomerization and rotation associated with the deactivation of BLUF photoreceptors. In a QM/MM MD setup, we corroborate the stability of the currently accepted light- and dark-state structures in two different BLUF proteins: BlrB and AppA. We confirm the BlrB dark-state recovery mechanism proposed by Khrenova and coworkers [4] via path-steered and -constrained MD;

obtaining a remarkable agreement for the energy of the rate-determining step. For the AppA protein, we also obtain a free-energy profile and a mechanism, which explain its 750-fold longer recovery rate with respect to BlrB.

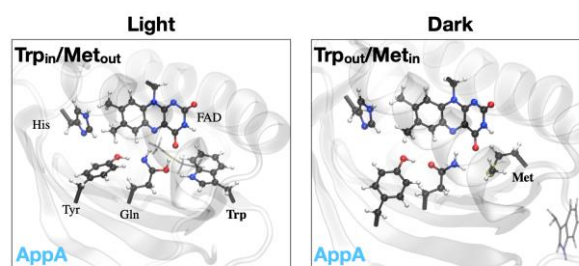


Figure 1 – Light- (Trp_{in}/Met_{out}) and dark-state (Trp_{out}/Met_{in}) structures of the AppA BLUF protein, based on the 1YRX and 2IYG PDB entries, respectively. In the BlrB protein, the Met is inside of the active site at both states [3].

Conclusions

Our protocol delivers free-energy profiles for the deactivation of two BLUF proteins, BlrB and AppA; corroborating a proposed mechanism based on the rotation and tautomerization of a conserved Gln. We find that the conformation of a Trp and a Met near the flavin is crucial to modulate the rate-determining barrier, which differs significantly between the BlrB and AppA proteins. Our work evidences how specific variations of the deactivation mechanism control vast differences in signaling times.

References

- [1] Fujisawa T et al., *Biophys. Rev.* 10:327, 2018.
- [2] Pérez de Alba Ortíz A et al., *J. Chem. Phys.*, 149: 072320, 2018.
- [3] Iwata T et al. *J. Am. Chem. Soc.*, 140:11982, 2017.
- [4] Khrenova MG et al. *Chem. Phys. Lett.* 676:25, 2017.
- [5] Gil AA et al., *J. Am. Chem. Soc.*, 139:14638, 2017.

Acknowledgements

The work has been performed under the Project HPC-EUROPA3 (INFRAIA-2016-1-730897), with the support of the EC Research Innovation Action under the H2020 Programme; in particular, the author gratefully acknowledges the support of Prof. Carme Rovira (Departament de Química Inorgànica i Orgànica & Institut de Química Teòrica i Computacional, Universitat de Barcelona) and the computer resources and technical support provided by BSC.

Steric and polarity effects in acacen Ni(II) complexes with enaminoketone ligands and their reaction products with heterocyclic amines

K. Pruszkowska¹, O.A. Stasyuk², M. Solà²

¹Faculty of Chemistry, University of Warsaw, Poland; ²Institute of Computational Chemistry and Catalysis, University of Girona, Spain

Introduction

Transition metal complexes containing tetradentate ONNO coordinating ligands (salens, salphens, acacen and acaphens) are currently an intensively studied group of materials due to the interest in their applicability as catalysts, building blocks in creating new functional materials or because of capability to coordination-induced spin-state switching (CISSS) [1-4]. Herein we present symmetrical acacen type square planar Ni(II) cores with different length of alkyl bridge – with two or three carbon atoms in the bridge (C2 and C3). This small modification causes different behaviour of Ni(II) cores in reaction with N-heterocyclic aromatic amines. In contrast to red C2 compound, green crystals of C3 core create orange octahedral complexes in reaction with pyridine.

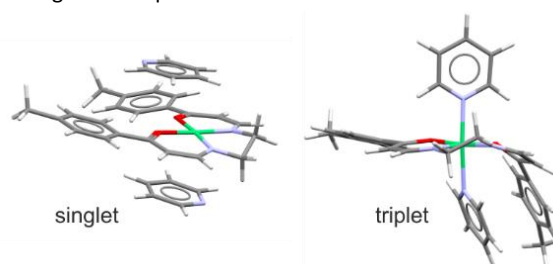
Methods

Computations of square planar acacen Ni(II) cores and octahedral Ni(II) complexes with heterocyclic amines in different spin states were carried out using the ADF package with DFT functionals: B3LYP, BP86, PBE0, including ZORA scalar relativistic correction, D3 dispersion correction by Grimme, and COSMO solvation model (pyridine). UV-Vis spectra for Ni(II) cores were simulated using SAOP and CAM-B3LYP functionals [5].

Results

On account of the fact that Ni(II) complexes may exist in two different spin states, the computations were performed for singlet and triplet states. The results confirm that singlet state is more favourable for investigated Ni(II) square planar cores ($\Delta E_{\text{triplet-singlet}} \sim 15 \text{ kcal/mol}$). However, their complexes with pyridine can have different geometry depending on the spin state. In singlet complexes with pyridine, ligands are not connected directly by nitrogen to nickel atom, but they are located in parallel to the Ni(II) core making π - π interactions between aromatic amine and enaminoketone part of core. The complexes in triplet state have octahedral geometries with direct interactions of pyridine ligands with Ni atom. Comparison of total energies has shown that for C2 Ni(II) system, creation of sandwich type complex with pyridine is more preferable than that of octahedral geometry, while for C3 Ni(II) core the energies of both complexes with pyridine are similar. Important to note that in crystals the only octahedral complexes of C3 Ni(II) core were observed. In addition, simulations of different mutual orientations of axial ligands in octahedral systems revealed that complexes with perpendicular orientation of axial ligands are more stable

than complexes where ligands are parallel to each other. Bent Ni(II) core in perpendicular complexes provides larger dispersion interactions between acacen Ni(II) core and N-heterocyclic ligands that are responsible for their greater stability. Different substituents in ligands also affect stability – for more polar substituents, stability of Ni(II) complexes increases. The results from simulations of UV-Vis spectra enabled a better understanding of the transitions in the investigated complexes.



Conclusions

Implementation of the project allowed us to understand why square planar acacen Ni(II) complexes with different length of alkyl bridge behaves differently in reactions with heterocyclic amines. Moreover, we answered how the orientation of N-heterocyclic ligands affects the geometry and stability of the Ni(II) octahedral complexes. Analysing the role of the substituent effect, we simulated complexes not yet synthesized and compared their stability. The simulated UV-Vis spectra helped us to assign transitions in the experimental spectra.

References

- [1] Whiteoak C.J. et al., Chem. Soc. Rev. 41:622 631, 2012.
- [2] Wenzelberg S.J. et al., Angew. Chem. Int. Ed. 47:2354 2364, 2008.
- [3] Weber B. et al., Angew. Chem. Int. Ed. 47:10098 10101, 2008.
- [4] Thies S, et al., Chem. Eur. J. 16:10074 10083, 2010.
- [5] te Velde G. et al., J. Comput. Chem. 22:931 967, 2001.

Acknowledgements

The work has been performed under the Project HPC-EUROPA3 (INFRAIA-2016-1-730897), with the support of the EC Research Innovation Action under the H2020 Programme; in particular, the author gratefully acknowledges the support of the Institute of Computational Chemistry and Catalysis, University of Girona and the computer resources and technical support provided by BSC.

Oxidation states in periodic systems from quantum mechanics

L. Pujal^{1,2}, D. Tiana¹ and P. Salvador²

¹School of Chemistry, University College Cork, Ireland; ²Institut de Química Computacional i Catàlisi i Departament de Química, Universitat de Girona, Spain

Introduction

Computer simulations, and in particular quantum chemical calculations, produce an immense amount of numbers that can hardly be comprehended by humans. It is of utmost relevance, from a practical but also conceptual point of view, to be able to extract some chemically meaningful quantities that may be put into direct correspondence with the respective classical chemical concepts. In this sense, the oxidation state (OS) is one of the most fundamental chemical concepts that is widely used for rationalization, categorization, and prediction of chemical reactivity. Specifically, focusing in extended systems, it is particularly interesting to know their oxidation state as some of its applications include, photovoltaics or photocatalysis, that rely on separation of photogenerated charges. Thus, the goal of this HPC Europa project was to extend to periodic systems the effective oxidation state method to obtain oxidation state from first principles, developed by Salvador et al. [1].

Methods

Let us consider a molecular system described with a single-determinant wavefunction build up a set of N molecular spinorbitals, $\{\varphi_i^\sigma(\mathbf{r})\}$. We identify the atom-in-the-molecule by introducing an atomic weight function $w_A(\mathbf{r})$ for every atom A , satisfying $\sum_A w_A(\mathbf{r}) = 1$. In the framework of the Quantum theory of Atoms in Molecule (QTAIM), $w_A(\mathbf{r}) = 1$ within the atomic basin of A and zero otherwise.

The intra-atomic part of each MO is defined as

$$\varphi_i^{A,\sigma}(\mathbf{r}) = \varphi_i^\sigma(\mathbf{r}) w_A(\mathbf{r}).$$

For each spin case, we can build the overlap matrix of the intra-atomic MOs, $Q^{A,\sigma}$ with elements:

$$Q_{ij}^{A,\sigma} = \int \varphi_i^{A,\sigma*}(\mathbf{r}) \varphi_j^{A,\sigma}(\mathbf{r}) d\mathbf{r}$$

The diagonalization of the Hermitian $Q^{A,\sigma}$ matrix by the unitary matrix $U^{A,\sigma}$ yields the so-called effective atomic orbitals (eff-AOs, eigenvectors) together with their occupation number (eigenvalues)

$$U^{A,\sigma\dagger} Q^{A,\sigma} U^{A,\sigma} = \text{diag} \{\lambda_i^{A,\sigma}\}$$

The oxidation state for each atom in the molecule is obtained using these occupation numbers. The strategy followed for each spin case is as follows: i) sort significantly populated eff-AOs for all defined centres from highest to lowest occupied, ii) assign integer alpha/beta electrons to eff-AOs of the centres with higher occupation number, until the number of electrons is reached. The difference in occupation number between the last occupied eff-AO and the first unoccupied eff-AO is used to quantify the reliability of the OS assignment. This strategy is known as effective oxidation states (EOS) analysis.

Results

First part of the project was to develop the computational protocol necessary to extend the EOS formalism to periodic systems. Three external software were employed namely, Quantum Espresso [2] for quantum mechanical calculations

of periodic systems, wannier90 [3] for generation of maximally localized Wannier functions (MLWFs) and critic2 [4] for real-space QTAIM analysis. As a result, the QTAIM atomic overlap matrices in terms of the MLWFs can be obtained. These data were used as input to our own developed code to calculate the effective oxidation state for each atom (attractor) in the unit cell of the corresponding quantum mechanical calculation. It is worth mentioning that the present approach is restricted to non-metallic extended systems, as MLWFs cannot be obtained in this case. The second part of the project was aimed at testing and benchmarking the computational protocol for a number of periodic systems. The first group tested were a series of binary oxides including FeO, NiO, CuO, CoO, MgO, MnO, Fe₂O₃ and TiO₂, for which the expected oxidation state, i.e. oxygen atom as an oxo (2-) group, was obtained in all cases. In addition, the code was applied to representative systems described in the IUPAC's report [5], namely CrO₃ and perovskites Cs₃AuO, Rb₂CuCl₄ and Rb₃AuO. In all cases the EOS agreed with those suggested in IUPAC's report. After the HPC stage finished we continued investigating more interesting/challenging systems with our code, such as a series of Xenon oxides under pressure proposed by Oganov et al. [6], in collaboration with dr. Otero de la Roza.



Conclusions

In conclusion, thanks to this HPC Europa project we were able to extend EOS formalism to extended systems. Moreover, we were able to test the computational protocol developed against several well-known systems and assessed the validity of the formalism. We are currently working in a manuscript describing the new methodology and applications.

References

- [1] Ramos-Cordoba, E. et al, J. Chem. Theory Comput 2 11, 1501–1508 (2015).
- [2] P. Giannozzi et al., J. Phys.:Condens. Matter 29 465901 (2017).
- [3] AA Mostofi, et.al, An updated version of wannier90: A tool for obtaining maximally-localised Wannier functions, Comput. Phys. Commun. 185, 2309 (2014).
- [4] A. Otero-de-la-Roza et al., Comput. Phys. Commun. 185 (2014) 1007–1018.
- [5] Karen, P.; McArdle, P.; Takats, J. Pure Appl. Chem. 2016, 88, 831–839.
- [6] Zhu, Q., et al. Stability of xenon oxides at high pressures. Nature Chem 5, 61–65 (2013).

Acknowledgements

The work has been performed under the Project HPC-EUROPA3 (INFRAIA-2016-1-730897), with the support of the EC Research Innovation Action under the H2020 Programme; in particular, the author gratefully acknowledges the support of Davide Tiana, School of Chemistry, UCC and the computer resources and technical support provided by ICHEC.

Molecular modelling to select specific LXR α -agonists able to induce lipotoxicity in HCC cancer models

A. Rashidian¹, T. Kronenberger¹, A. Poso²

¹Dept. Internal Medicine VIII, University Hospital of Tübingen, Germany; ²School of Pharmacy, University of Eastern Finland (UEF), Kuopio, Finland

Introduction

Hepatocellular carcinoma accounts for 85–90% of all cases of primary liver cancers [1]. Preliminary data from the group of Dr. Daniel Dauch (University Hospital of Tübingen, Department of Internal Medicine VIII) suggests that pharmacologically induced lipotoxicity by the activation of LXR α -signalling via small molecules can be a promising therapeutic strategy for the treatment of hepatocellular carcinoma (HCC). In this regard, we aimed to understand the structural features of the interaction between those small-molecules and LXR α by the means of long molecular dynamics (MD) simulations.

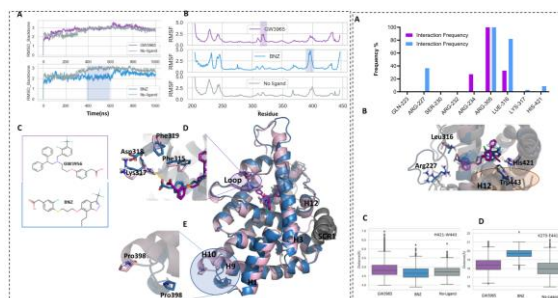
Methods

As part of our study, two structures of LXR α – PDB IDs: 3IPQ/GW3965 and 3IPS/Benzisoxazole urea (herein BNZ) were retrieved from the PDB server based on the chemical similarity of their co-crystallized ligands with small molecules (Resolution <2.26 Å). Structures were prepared according to previously published protocol (2). All crystal complexes together with the apostructure underwent molecular dynamic (MD) simulation according to previously published protocol (2) for 1000ns. The visualization of the protein ligand interaction and figure generation were carried out using PyMol (v2.3.2, Schrödinger, Inc., New York, USA). The data were generated using Maestro Simulation interaction and event analysis tool (Schrödinger, LLC, New York, NY).

Results

Global investigation of MD trajectories revealed that the protein folding remained unchanged after simulation compared to the initial structure. RMSD values variation along the simulation suggests that both ligand-bound and apostructure systems were stable during simulation (Figure 1A). However, a minor transition state in LXR α /BNZ during 400-600 ns, could indicate that this system undergoes conformational changes upon BNZ binding, although the nature of this change requires a more refined analytical approach, such as PCA. After 600 ns this system also remains stable until the end of the simulation. Globally, all simulations show similar flexibility pattern, however in detailed it was revealed that GW3965 can cause a higher fluctuation in Phe315-Tyr321 loop region, covering the binding pocket, when compared to the BNZ and apostructure simulations (Figure 1B, 1C and 1D). Due to the adopted conformation by Lys317, where its backbone nitrogen atom has a stable hydrogen-bond with the terminal acidic group of BNZ (Figure 1C and 1D). Lys317's vicinity then undergoes a conformational change that allows the salt bridge between its side-chain and Asp318 to happen stabilizing the region. In contrast, BNZ-binding leads to higher mobility in the L:H9-H10 (His396-Leu402, Figure 1E). This region is near the heterodimerization interface with RXR, which might will require further analysis with the full-complex. Comparative inspection of the network of hydrogen bonds reveals that BNZ has more interaction points than GW3965 (Figure 2A). Additionally, ligand-binding affects the conformation of His421 and Trp443, which by consequence affects the H12

conformation and the coactivator binding affinity (Figure 2B and 2C). Based on the stable hydrogen bond interaction with His421 and occupation of His421/Trp443 region it could be expected that BNZ would be a more potent agonist than GW3. However, the data obtained from binding and transactivation assays by Fradera, Xavier, et al. shows the two ligands have similar binding affinities [3]. In order to inspect the position of H12 relative to the ligand binding pocket (LBP), the distance between Lys273 (located on H3) and Asp441 (H12) was measured (Figure 2D). Since both residues interact with the coactivator protein, we hypothesised that the changes in this distance could be indicate whether H12's position would be close to the LBP (agonistic mode) or far from that (antagonist mode), in comparison to the apostructure. The smallest distance can be found in the apostructure (ranging from 17–18 Å), while the LXR α /BNZ has the largest distance (~20 Å). Meanwhile, the distances between H12 and H3 in LXR α /GW3 simulations lie somewhere between that of apo and LXR α /BNZ structures (~19 Å).



Conclusions

Our simulations provided insights into the interaction network of GW3965 and BNZ over the course of 1000 ns simulation time. The result of trajectory analysis is consistent with functional assay reported for those ligands [3], where both ligands have similar potency and efficacy. However, minor differences can be observed in their interaction pattern (His421-W443). It can be also concluded that the GW3965 and BNZ induce different dynamic behaviour on different region of protein compared to the apostructure. As a following step, these results will be used to develop novel lipotoxic small-molecules to treat therapy resistant HCC.

References

[1] Llovet JM et al., Hepatocellular carcinoma. *Nat Rev Dis Primers*, 2:16018, 2016. [2] Kronenberger T et al., *ChemMedChem*, 14(23):1995-2004, 2019. [3] Fradera, X et al., *Molecular Biology*, 399.1:120-132, 2010.

Acknowledgements

The work has been performed under the Project HPC-EUROPA3 (INFRAIA-2016-1-730897), with the support of the EC Research Innovation Action under the H2020 Programme; in particular, the author gratefully acknowledges the support of Prof. Dr. Antti Poso, School of Pharmacy, University of Eastern Finland (UEF) and the computer resources and technical support provided by CSC-IT centre, Finland.

Using decision trees to understand deprotonation in formic acid

*S. Roet*¹, *C.D. Daub*²

¹Department of Chemistry, Norwegian University of Science and Technology, Sweden; ²Department of Chemistry, University of Helsinki, Finland

Introduction

Formic acid (FA) contributes a large proportion of the acidity in acid rain, particularly in forested regions far from urban areas [1], has higher atmospheric concentrations than previously believed [2], and contributes to the formation of sulphuric acid in the atmosphere [3].

These reasons make the study of various proton exchange reactions involving FA a topic of current interest. In addition, its status as the simplest organic and carboxylic acid makes it an ideal model system for the study of these reactions.

Metadynamics simulations have recently been used to examine FA deprotonation in aqueous solution [1,4]. While these studies led to valuable new insights, they also showed some of the limitations of existing methods, and suggested that novel methodologies such as Replica Exchange Transition Interface Sampling (RETIS) [5] might be a viable way forward.

With RETIS, a new set of reactions is generated from a reactive path. The rules for a path in RETIS are simple, a simulation has to start in stable state A (our protonated state), need to cross an interface, and then end up either back at state A, an unreactive path, or in state B (the deprotonated state), a reactive path.

To predict if a point from before the reaction barrier is part of a reactive path or not is a classification problem, that you can train Machine Learning (ML) algorithms on. The prediction, on its own, is not very useful information to have, but if we use a understandable ML algorithm, we can gain insight into the reaction by looking at what differentiates reactive from unreactive paths in the trained ML algorithm.

To be able to achieve this insight we used decision tree (DT) classifiers with a maximum depth of 3 to predict whether conformations came from reactive or unreactive paths. [6] We then inspected the resulted DT to understand what differentiates reactive trajectories from unreactives ones and gained insight in the deprotonation of FA.

Methods

The test system for our study consists of FA solvated by 6 water molecules. As the initial state for the RETIS simulations we used configurations found to be local minima by geometry optimization calculations using DFT-BLYP and a DZVP basis set with dispersion corrections using NWChem. The collective variable, $s(r)$, is similar to the one used previously in a RETIS investigation of water autoionization [6], modified to deal with FA deprotonation. This scheme allows us to track the transport of the proton away from the FA molecule. Initial state A is defined as having $s(r) < 1.06 \text{ \AA}$, and the final state B is defined as $s(r) > 3.0 \text{ \AA}$. The trajectories were generated using CP2K.

For the DT, the trajectories were labelled as reactive if $s(r) > 2.9 \text{ \AA}$ at any point in the trajectory.

The coordinates that had $1.1 < s(r) < 1.25$ were used to train and test the decision tree. This leads to a training data set with 30101:2264 (unreactive:reactive) coordinates.

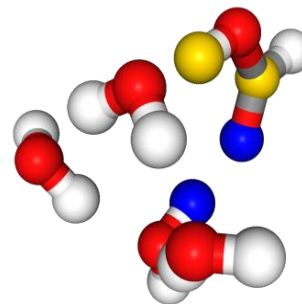


Figure 1 – A representative structure of formic acid in water, with the O5, H5 (in blue) and C0, H1 (in gold).

Results

The two question to recognize a reactive path are: Is the O0-H5 distance $\leq 1.29 \text{ \AA}$? If that is true, then: Is the C0-H1 distance $> 2.19 \text{ \AA}$? These are enough to go from the original 30101:2264 split to 165:1484. The atoms involved in the two questions are highlighted in figure 1.

Conclusions

From the DT and figure 1 we can conclude that for the FA deprotonation reaction, the other oxygen needs to have a hydrogen bond, while the hydrogen-oxygen bond of FA is elongated. This leads to a resonance structure. This is the first time, known to the authors, that such a data-driven approach is used to gain insight into a chemical reaction. The used method can be easily transferred to investigate other reactions as well.

References

- [1] Murdachaew G et al., Phys. Chem. Chem. Phys., 18:29756, 2016.
- [2] Millet DB et al., Atmos. Chem. Phys. 15:6283, 2015.
- [3] Daub CD et al., PeerJ Phys. Chem., 2:e7, 2020.
- [4] Daub CD and Halonen L, J. Phys. Chem. B, 123:6823, 2019.
- [5] van Erp, TS, Phys. Rev. Lett. 98(26):268301, 2007.
- [6] Moqadam M et al., Proc. Nat. Acad. Sci., 115:E4569, 2018.

Acknowledgements

The work has been performed under the Project HPC-EUROPA3 (INFRAIA-2016-1-730897), with the support of the EC Research Innovation Action under the H2020 Programme; in particular, the author gratefully acknowledges the support of the Department of Chemistry at the University of Helsinki and the computer resources and technical support provided by CSC.

Ab initio molecular dynamic simulations on the interaction of phosphines with Rh nanoparticles

A. Salom-Català¹, F. Baletto², J.J. Carbó¹, J.M. Ricart¹

¹Departament de Química Física I Inorgànica, Universitat Rovira I Virgili, Tarragona, Spain; ²Physics Department, King's College London, UK

Introduction

Metal Nanoparticles (MNP) have emerged as a very efficient tools in a very wide range of fields such as medicine, pigments or catalysis [1]. In the last, MNP have the trait to combine the advantages of homo- and heterogeneous catalysis, that is a very high selectivity as well as recyclability and robustness. Castellón et. al. at Universitat Rovira I Virgili synthesised small and well-defined Ru and Rh nanoparticles stabilised by N-Heterocyclic Carbenes (NHC) or Polyvinylpyrrolidone (PVP), and they observed a selective catalytic deuteration of different phosphine ligands [2]. We performed a systematic computational study on the adsorption of some phosphine ligands (PPh₃, P(o-tolyl)₃) on a Rh₅₅ icosahedral (ICO) nanoparticle since these two ligands shown a different pattern of selective H/D exchange. We observed a strong π interaction between the rings of the ligands and the NP surface. Here, we have performed Ab Initio Molecular Dynamics (AIMD) simulations to elucidate the effect of the solvent on the adsorption mode of the ligands, its eventual effect on the reactivity, and the influence of phosphine coverage on the interaction among the ligands and the nanoparticle.

Methods

All our calculations have been carried out within the Density Functional Theory (DFT) level of theory using the Quickstep method based on the mixed Gaussian and plane-wave approach (GPW) implemented in the CP2K software package. The rev-PBE exchange-correlation functional was used. The basis set for Rh atoms was DZVP-MOLOPT-SR-GTH and for the rest of the atoms (P, C, H, O) was DZVP-MOLOPT-GTH. All basis sets were associated with a GTH-PBE pseudopotential. The energy cut-off for the plane waves was set on 400 eV. Spin-polarized calculations were carried out in all cases. Self-consistent electronic minimization was converged to 0.001 meV between consecutive steps whereas the convergence criterion for geometry optimization was set at 0.003 eV. For all simulations, the temperature was set at 343 K and controlled with a Nosé thermostat with a timestep of 0.5 fs. Periodic Boundary Conditions were used in all cases.

We performed an AIMD Simulation on three different systems, where tetrahydrofuran (THF) was used as a solvent: 1) Rh₅₅-ICO + 1 PPh₃ + 55 THF (cubic box of 21 Å); 2) Rh₅₅-ICO + 1 P(o-tolyl)₃ + 63 THF (cubic box of 22 Å); 3) Rh₅₅-ICO + 7 PPh₃ + 112 THF (cubic box of 27 Å). The total simulation time in all cases was 5 ps.

Results

During the simulation time we did not observe changes on the adsorption mode of the different ligands, and there was not competition between the ligand and the solvent for the same adsorption site. However, the THF molecules were adsorbed on the nanoparticle through their O atom. The solvent structure was analysed by means of the radial distribution function (Figure 1). The solvent was structured around the nanoparticle forming a solvation shell with 22 THF molecules.

In average, five solvent molecules adsorb on the corner Rh atoms and one on the edges.

Furthermore, we observed a strong effect on the electronic structure of the NP as a consequence of the solvent adsorption and the increase of the ligand coverage. In system 1 the total magnetization drops from 33.3 at the initial point of the simulation (no solvent molecule adsorbed) to 19.1 after 3.2 ps (THF molecules adsorbed on the NP surface). In the case of system 3 the initial total magnetization was 5 whereas in the naked NP the magnetization was 47. Using the local Density Of States (DOS) analysis, we determined a stabilization of the Rh d orbitals along the simulation on system 1; and ongoing from naked to phosphine-functionalized nanoparticle.

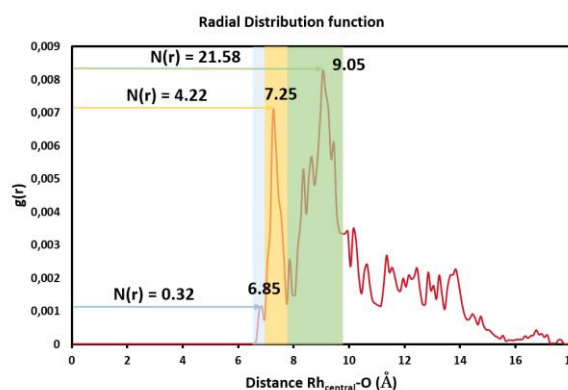


Figure 1 – Radial Distribution function analysis on system 1. Colorized zones represent the THF molecules situations respect the Rh central atom of the NP. Blue: adsorption on edge atoms; Yellow: adsorption on corner atoms; Green: first solvation shell.

Conclusions

We can summarize the results in three important points: 1) The adsorption mode of phosphines does not vary after introducing the explicit role of the solvent. 2) The THF solvent molecules can be adsorbed through their O atoms, preferably on the corner sites of MNP. 3) The adsorption of THF molecules has a high impact on the electronic structure of the nanoparticle, dropping the total magnetization of the system and stabilizing the Rh d orbitals of the NP.

References

- [1] Schmid, G. Nanoparticles: From Theory to Application, 2nd ed.; Wiley-VCH: Weinheim, 2010. [2] Castellón, S. et al., Chem. Commun., 51, 16342, 2015.; and unpublished results.

Acknowledgements

The work has been performed under the Project HPC-EUROPA3 (INFRAIA-2016-1-730897), with the support of the EC Research Innovation Action under the H2020 Programme; in particular, the author gratefully acknowledges the support of Dr. Francesca Baletto at Physics Department of King's College London and the computer resources and technical support provided by EPCC.

Calculations for investigating gas hydrates of CO₂ in aqueous brines at the electrochemical interface

E. Sargeant¹, F. Calle-Vallejo²

¹School of Chemistry, University of Birmingham, United Kingdom; ²Departament de Ciència de Materials i Química Física & Institut de Química Teòrica i Computacional (IQTCUB), Universitat de Barcelona, Spain

Introduction

Experimental studies have shown that at low temperature in concentrated electrolytes (brines) the hydrogen evolution reaction, which is the main competing reaction to the CO₂ reduction reaction, is hindered [1]. At low temperature or high pressure, in the presence of a gas molecule, water forms clathrate hydrate structures. If these water cages form under the conditions of these experimental studies, the level of solvation of CO₂ and its reaction intermediates will vary. This work aims to understand the effect of solvation on the reduction of CO₂ to CO on Pd, Au and Cu surfaces.

Methods

The DFT calculations were performed using the Vienna Ab initio Simulation Package (VASP) [2]. All atoms were relaxed using the conjugate gradient method until the maximum force on any atom was below 0.05 eV/Å, using the Perdew-Burke-Ernzerhof (PBE) exchange-correlation functional with the generalized-gradient approximation (GGA) [3], and a plane-wave cutoff of 450 eV. The effect of the core electrons on the valence electron density were described by Projector Augmented Wave (PAW) potentials [4], and the Methfessel-Paxton method was used to smear the Fermi level with an electronic temperature of 0.2 eV. The reaction free energies were obtained as $\Delta G_0 = \Delta E_{DFT} + \Delta ZPE - T\Delta S_0$ where the zero-point energies were calculated using the harmonic oscillator approximation. The standard total entropies (S₀) and the experimental standard free energies (ΔG_{0exp}) were obtained from available thermodynamic data [5] at T=298.15 K. Extended slabs of (111), (100) and (211) surfaces were used for each metal. Each slab was made up of 4 atomic layers where the lowest two were fixed in their optimised bulk positions and the upper two with the adsorbed molecule were allowed to fully relax. 3x3 cell sizes were used to calculate the adsorption energy of reaction intermediates. For implicit solvation, the VASPsol method was used [6]. For explicit solvation, the method described in reference [7] was used where water molecules were added sequentially to solvate the adsorbate and the energy of the system compared to the energy of water molecules solvating themselves.

Results

Figure 1 shows the results on the (111) surfaces but the trends are similar on (100) and (211) surfaces. The desorption of CO is thermodynamically favourable on Au but not Pd. This fits with experimental results where Au produces mainly CO(g) whereas Pd is poisoned by it. Fig. 1. shows that when solvation effects are applied, *CO and *COOH are both stabilised in energy. Explicit solvation accounts for the effects of H-bonding whereas the implicit solvation model only accounts for the dielectric screening effect. Only *COOH forms H-bonds with solvating water molecules so there is a difference in energy depending on the solvation method used.

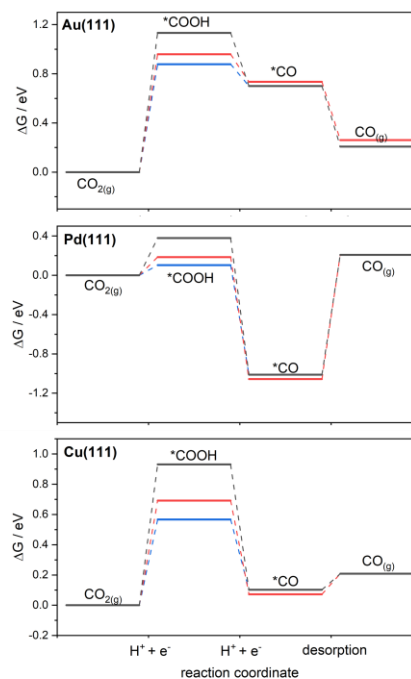


Figure 1 – Free energy diagram showing the energy of reaction intermediates in vacuum (black), implicitly solvated (red), explicitly solvated (blue).

Conclusions

Solvation effects can significantly alter the adsorption energy of reaction intermediates. Explicit solvation methods are preferable since they can account for H-bonding giving more accurate results.

References

- [1] E. Sargeant, A. Kolodziej, C.S. Le Duff, P. Rodriguez, ACS Catal. 10 (2020) 7464–7474.
- [2] G. Kresse, J. Furthmüller, Phys. Rev. B. 54 (1996) 11169–11186.
- [3] J.P. Perdew, K. Burke, M. Ernzerhof, Phys. Rev. Lett. 77 (1996) 3865–3868.
- [4] G. Kresse, D. Joubert, Phys. Rev. B. 59 (1999) 1758–1775.
- [5] D.R. Lide, CRC handbook of chemistry and physics, 85th ed., CRC press, 2004.
- [6] K. Mathew, R. Sundararaman, K. Letchworth-Weaver, T.A. Arias, R.G. Hennig, J. Chem. Phys. 140 (2014) 1–9.
- [7] A. Rendón-Calle, S. Builes, F. Calle-Vallejo, Appl. Catal. B Environ. 276 (2020) 119147.

Acknowledgements

The work has been performed under the Project HPC-EUROPA3 (INFRAIA-2016-1-730897), with the support of the EC Research Innovation Action under the H2020 Programme; in particular, the author gratefully acknowledges the support Federicó Calle-Vallejo and IQTCUB and the computer resources and technical support provided by BSC.

Halide complexation to uranyl in liquid ammonia: a DFT molecular dynamics study

N. Sieffert¹, M. Bühl²

¹Univ. Grenoble Alpes & CNR, Grenoble. France; ²University of St Andrews, School of Chemistry, St Andrews, United Kingdom

Introduction

Uranium (generally found as uranyl UO_2^{2+} cation) is of key importance in the framework of radioactive waste management. In order to efficiently recycle UO_2^{2+} , a detailed knowledge of its complexation properties is essential. The latter are significantly influenced by the nature of the solvent, so that the understanding of solvation effects is intimately linked to the study of complexation equilibria. Herein, we explored uranyl chemistry considering liquid ammonia as solvent. The latter is widely used in inorganic chemistry, however, it is still little employed as far as uranyl is concerned, so that structural, thermodynamic and kinetic information is scarce in the literature. Recently, uranyl halides have been characterised in liquid ammonia [1], however their stability constants as well as their structural properties in this solvent have not yet been reported. Herein, we undertook a computational study to tackle these important issues.

Methods

Born-Oppenheimer Molecular Dynamics simulations have been performed on systems typically composed of 1 UO_2^{2+} cation, n X^- counterions ($n = 0-2$, $\text{X} = \text{F}$ or Cl) and $(37-n)$ NH_3 molecules, in a periodic cubic box of cell-length 13.22 Å, corresponding to a liquid density of *ca.* 0.71, in conjunction with the BLYP-D3 functional. Trajectories have been computed over *ca.* 200 ps, in the NVT ensemble (at 300 K), using a timestep of 0.5 fs. All H have been replaced by D. Free energies surfaces have been computed using the Well-Tempered Metadynamics algorithm [2], using either one or two collective variables (referred to as CV1 and CV2). CV1 is the (C,N) coordination number and CV2 is the U-X interatomic distance. These simulations have been performed using the CP2K package, on Archer at EPCC.

Results

We first considered the $[\text{UO}_2(\text{NH}_3)_5]^{2+}$ complex, in explicit ammonia solution, and computed the free energy profile corresponding to the coordination/decoordination of a single NH_3 ligand from UO_2^{2+} . For that purpose, a series of metadynamics simulations have been performed, all using CV1 as collective variable, but with different density functionals and simulation parameters. We found that the penta- coordination is systematically preferred. The relative stability of the tetra- vs hexa-coordinated complexes is found to depend on the nature of the functional, in keeping with our previous “static” calculations [3].

Next, we considered mixed $[\text{UO}_2(\text{NH}_3)_{5-n}(\text{X})_n]^{2-n}$ complexes (with $n = 1$ or 2 , and $\text{X} = \text{F}$ or Cl) and we investigated the free energies surfaces underlying NH_3/X^- ligand exchanges in explicit ammonia solution (see Figure 1). Again, penta-coordination is found to be the most stable, and the relative

stability of $[\text{UO}_2(\text{NH}_3)_4(\text{X})]\cdot\text{NH}_3^-$ vs $[\text{UO}_2(\text{NH}_3)_5]\cdot\text{X}^-$ naturally depends on the nature of X^- , F⁻ being more strongly bonded to the metal than Cl⁻. Our metadynamics simulations show that the NH_3/X^- ligand exchanges follow an associative reaction mechanism: starting from $[\text{UO}_2(\text{NH}_3)_5]^{2+}$, the first step is coordination of the X^- ligand (to afford the hexacoordinated $[\text{UO}_2(\text{NH}_3)_5\text{X}]^+$ complex) followed by dissociation of NH_3 , to afford $[\text{UO}_2(\text{NH}_3)_4(\text{X})]^+$.

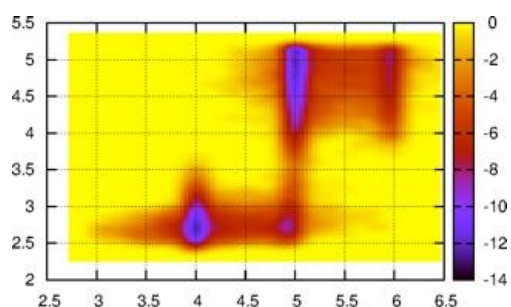


Figure 1: Typical free energy surface (kcal/mol), as obtained from a metadynamics simulation starting from $[\text{UO}_2(\text{NH}_3)_5\text{X}]^+$ in explicit ammonia

Conclusions

We performed a Density Functional Theory Molecular Dynamics study on the reactivity of uranyl in explicit ammonia solution, to investigate its affinity for halides and to characterise the underlying reaction mechanisms for NH_3/X^- ligand exchange processes. Using the metadynamics approach, we found that uranyl is found as $[\text{UO}_2(\text{NH}_3)_5]^{2+}$ in ammonia, and that it possesses a good binding affinity for F⁻ and Cl⁻. The resulting complexes also prefer pentacoordination of their equatorial ligands, and NH_3/X^- ligand exchanges generally follow an associative reaction mechanism.

References

- [1] S. S. Rudel, S. A. Baer, P. Woity, T. G. Müller, H.-L. Deubner, B. Scheibe and F. Kraus, *Z. Kristallogr. Cryst. Mater* 2018, 233, 817–844.
- [2] A. Barducci, G. Bussi and M. Parrinello, *Phys. Rev. Lett.* 2008, 100, 020603.
- [3] N. Sieffert, A. Thakkar and M. Bühl, *Chem. Commun.* 2018, 54, 10431-10434.

Acknowledgements

The work has been performed under the Project HPC-EUROPA3 (INFRAIA-2016-1-730897), with the support of the EC Research Innovation Action under the H2020 Programme; in particular, the author gratefully acknowledges the support of EASTCHEM and the computer resources and technical support provided by EPCC.

Reaction of reactive aldehyde HNE with amino acid cysteine from UCP2 protein

S. Škulj¹, F. Himo², Z. Brkljača¹, M. Vazdar¹

¹Ruđer Bošković Institute, Croatia; ²Stockholm University, Sweden

Introduction

Proton transport across mitochondrial cell membranes is one of the main metabolic processes in organism. In conditions of oxidative stress different reactive oxidative species (ROS) are constantly produced. They can react with biomolecules in cell membranes, in turn significantly increasing proton transport across phospholipid bilayers. The consequence of this increase is the disorder in cell metabolism which is still not completely understood. This can activate various deleterious processes in living organisms and in the end lead to different dangerous diseases such as diabetes type 2, cancer, Parkinson's disease, Alzheimer's disease, atherosclerosis, etc. The most prominent ROS formed in cellular membranes during oxidative stress is reactive aldehyde (RA) 4-hydroxy-2-nonenal (HNE), which readily reacts with surrounding membrane proteins and lipids. We have already proposed and published detailed model reaction mechanism of two products of the oxidative stress, HNE and 4-oxo-2-nonenal (ONE) with different polar amino acids [1,2]. Transmembrane uncoupling protein II (UCP2) serves as the regulator of oxidative stress and can be modified by RA. In this work we determined a position of HNE in the membrane (in the vicinity of the protein), thus discovering a possible arrangement of the reaction site for the most reactive amino acid cysteine. As an extension of the aforementioned model system, we develop new and more realistic all-atom QM system based on density functional theory (DFT). The prepared system can be used as a starting point in investigations of aforementioned chemical reactions in bilayers.

Methods

We performed 300 ns of molecular dynamics (MD) simulations of UCP2 homology modelled structure and 11 HNE molecules in a hybrid lipid bilayer, corresponding to inner mitochondrial membrane composition in physiological concentration of 0.1 M NaCl. This hybrid lipid bilayer consists of 230 lipid molecules. Composition of the cytoplasmic side of the leaflet is ~30 % DOPC, ~15 % DOPE and ~5 % CDL molecules, with the matrix side of the leaflet composed of ~10 % DOPC, ~20 % DOPE and ~20 % CDL. All QM calculations were performed using density functional theory (DFT), where we employed B3LYP functional.

Results

At the end of 300 ns classical MD simulation all HNE molecules entered the phospholipid bilayer (Figure 1a), where we found that carbonyl groups of all present HNE molecules are oriented toward bulk water surrounding the lipid bilayer. Since cysteine is the most reactive amino acid, we choose cysteine as a target amino acid for this modification. As it can be seen from Figure 1, cysteine at position 216 in UCP2 protein represents the most appropriate choice due to its favourable position, i.e. it is position-wise readily available to

react with reactive groups present in HNE molecules (double bond and carbonyl group). Results of the MD simulations enabled us to appropriately set up QM system consisting of all the necessary reactants and solvent molecules surrounding the reaction site, thus improving upon our already published model in which we treated present solvents (water and acetonitrile) implicitly. More precisely, both water and phospholipid environments are treated explicitly in the newly developed all-atom QM system. We performed preliminary calculations of optimization on this system.

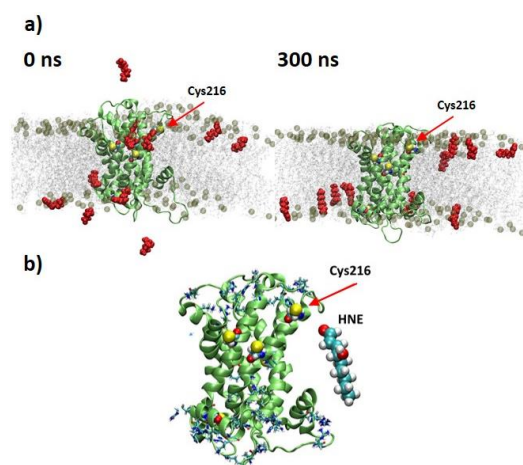


Figure 1 - a) Snapshots of MD simulations of UCP2 protein with 11 HNE molecules at the beginning (left panel) and after 300 ns (right panel) of simulation. b) UCP2 protein with HNE molecule.

Conclusions

In this work we performed an all-atom classical MD simulation of UCP2 protein with HNE molecules in hybrid lipid bilayer with the aim of finding most favourable arrangement of the reaction site. In this respect, we chose cysteine 216 for modification with HNE and successfully prepared an all-atom QM system where water and phospholipid environments are treated explicitly.

References

- [1] Škulj S et al., *J Org Chem.*, 84(2):526-535, 2019.
- [2] Škulj S, et al., *Croat Chem Acta.*, 92(2):229-239, 2019.

Acknowledgements

The work has been performed under the Project HPC-EUROPA3 (INFRAIA-2016-1-730897), with the support of the EC Research Innovation Action under the H2020 Programme; in particular, the author gratefully acknowledges the support of Professor Fahmi Himo, Stockholm University and the computer resources and technical support provided by KTH-PDC HPC centre.

Chemical functionalization and topology: a new strategy for high-performance organic photovoltaic materials

J. Stoycheva^{1,2}

¹Sofia University, Bulgaria; ²Università degli Studi di Bologna, Italy

Introduction

To date, organic photovoltaics are still with low efficiency, but they allow in principle the overcoming of the Shockley-Queisser limit^[1] by means of a phenomenon known as "singlet fission^[2] (SF)". In this process a high-energy singlet exciton is converted into two lower-energy triplet ones, thus obtaining from one photon two excitons. There are energetic requirements for the process to be favourable and our lab has shown that diboron-doped anthracenes and phenanthrenes are molecules meeting these requirements and having a future potential for SF materials.^[3] The only drawback of these unfunctionalized molecules is that they have low stability. This HPC project was focused on the study of the thus far unresearched functionalized (and more stable) diboron-doped anthracenes and phenanthrenes.

Methods

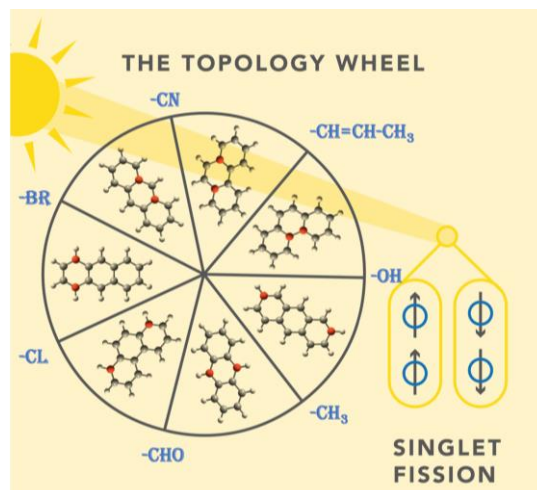
The potential application of the functionalized molecules as SF materials was evaluated with the high-level multiconfigurational methods SA-RASSCF/RASPT2, applied to MP2-optimized geometries.

The first stage of the investigation addressed the adequate choice of active space (AS) and number of electronic states to be used for the state averaging procedure. The benchmark test for the AS size and the number of states treated was done on one of the functional derivatives, for which empirical data are available.^[4] The second stage of the study included the calculation of the key excited states and their excitation energies $E(S_1)$, $E(T_1)$, $E(T_2)$ by means of single point SA-RASPT2/aug-cc-pVDZ calculations, as well as the subsequent evaluation of the energy differences ΔE_{ST} and ΔE_{TT} . The simulations were performed with the MOLCAS8 software package.

Results

The effect of the following substituents on the parent diboron-doped anthracenes and phenanthrenes was tested: $-\text{CH}_3$, $-\text{Cl}$, $-\text{Br}$, $-\text{CH}=\text{CH}-\text{CH}_3$, $-\text{CN}$, $-\text{CHO}$ and $-\text{OH}$. The functional groups were chosen in such a way that a wide range of electron donating/electron withdrawing properties is spanned. The latter were positioned symmetrically first at the two boron atoms and then at a pair of equivalent carbon atoms. Compared with the AS of the parent compounds, the AS for the functionalized derivatives was increased by additional $(\pi+n)$ electrons as follows: $2x(0\pi+0n)$ for

$-\text{CH}_3$; $2x(0\pi+2n)$ for $-\text{Cl}$, $-\text{Br}$ and $-\text{OH}$; $2x(2\pi+0n)$ for $-\text{CH}=\text{CH}-\text{CH}_3$; $2x(2\pi+0n)$ for $-\text{CN}$ and $-\text{CHO}$.



Conclusions

This project had both methodological and applied aspects – on the one hand, further assessing and fine-tuning the computational protocol for investigation of SF capacity, and on the other hand, discovery of efficient and stable organic photovoltaics. The realization of the project provided insight into the role of topology and type of substituents on the SF properties and can afford guidelines for the molecular design of novel SF materials.

References

- [1] Shockley W. et al., J. Appl. Phys., 32: 510-519, 1961.
- [2] Smith, M. B.; Michl, J., Chem. Rev., 110: 6891-6936, 2010.
- [3] Stoycheva J. et al., J. Phys. Chem. Lett., 11(4): 1390-1396, 2020.
- [4] Grothuss E. et al., Asian J. Org. Chem., 7: 37-53, 2018.

Acknowledgements

The work has been performed under the Project HPC-EUROPA3 (INFRAIA-2016-1-730897), with the support of the EC Research Innovation Action under the H2020 Programme; in particular, the author gratefully acknowledges the support of Dr. Artur Nenov from the Department of Industrial Chemistry "Toso Montanari", Università degli Studi di Bologna, and the computer resources and technical support provided by CINECA.

Solvent screening for extraction of furfural by using quantum mechanics-based COSMO-CAMPD framework

V. Tuppurainen¹, L. Fleitmann², J. Kangas¹, K. Leonhard²

¹Chemical Process Engineering research unit, University of Oulu, Finland; ²Institute of Technical Thermodynamics, RWTH Aachen University, Germany

Introduction

A novel conceptual chemical process is proposed to recover furfural, a promising hemicellulose derived platform chemical, from dilute aqueous solution using solvent extraction. Furfural is subsequently oxidized to C4 lactones and diacids, followed by their recovery from the solvent in an integrated manner. As the solvent is present throughout the process, its selection strongly determines the overall performance of the process, emphasizing the importance of computational tools to allow optimization in a process level (Figure 1).

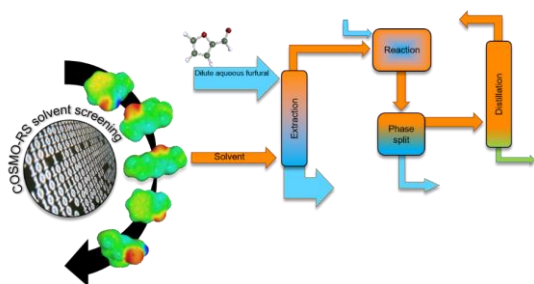


Figure 1 - Schematic of the process flowsheet investigated during solvent screening.

Methods

COSMO-RS based solvent screening framework^{1,2} was used in the work. A quantum mechanics based COSMO-RS property method³ provides a priori estimates of essential fluid phase properties. This thermodynamic equilibrium data allows the evaluation of the performance of chemical engineering unit operations. Extraction and distillation are modelled using advanced pinch-based models, where full non-ideal thermodynamics are used to provide accurate information on process-level performance indicators such as minimum solvent flow rate in extraction and minimum energy demand in distillation. The search was limited by several process-related constraints e.g. the necessity of having an immiscibility gap between the solvent and water and having a feasible topology of vapor-liquid equilibrium to allow final separation of products by distillation.

Results

Out of the initial set of nearly 12 000 molecular structures, around 2500 were identified as initially feasible solvents. Focusing on candidates containing only carbon, oxygen and hydrogen with saturated bonds and being quotable from laboratory chemical vendor, 427 components remained. Ranking of the solvent candidates was done based on the distillation column reboiler duty, the amount of products recovered and the amount of solvent lost (Figure 2).

Finally, the quantum mechanics based computational solvent screening was combined with engineering judgment on e.g. solvent reactivity, commercial availability and safety considerations.

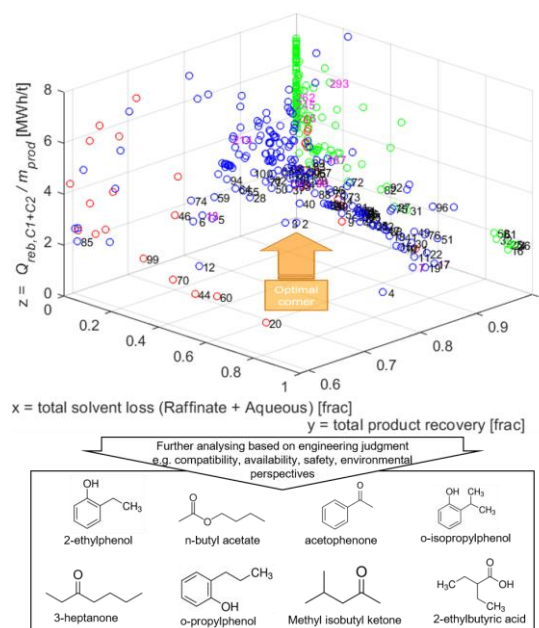


Figure 2 - Solvent screening based on energy consumption, recovery of products and solvent loss results from the framework. Further narrowing down to eight preliminary promising solvent candidates.

Conclusions

Using COSMO-RS solvent screening framework, some solvent candidates with initially better characteristics than any commercially or experimentally proposed were identified. As a result, the number of promising solvent candidates was further narrowed down to certain novel solvent candidates to be considered in further experimental studies of furfural valorization.

References

- [1] Scheffczyk J et al., Chem Eng Res Des, 115:433-442, 2016.
- [2] Scheffczyk J et al., Mol Syst Des Eng, 3(4):645-657, 2018.
- [3] Klamt A et al., Ann Rev Chem Biomol Eng, 1:101-122, 2010.

Acknowledgements

The work has been performed under the Project HPC-EUROPA3 (INFRAIA-2016-1-730897), with the support of the EC Research Innovation Action under the H2020 Programme; in particular, the author gratefully acknowledges the support of Lorenz Fleitmann and Kai Leonhard, Institute of Technical Thermodynamics, RWTH Aachen University and the computer resources and technical support provided by HLRS.

Electronic structure and properties of synthetic complexes mimicking the S2 state of oxygen-evolving complex

A. Tychenkulova¹, L. Guidoni²

¹Laboratory of Cryophysics and Cryotechnology al-Farabi Kazakh NaBonal University, Almaty, Kazakhstan; ²Department of Physical and Chemical Science, University of L'Aquila, Italy

Introduction

Current understanding of the S2 state structure is based on theoretical modeling studies [1, 2, 3] starting from the high-resolution X-ray structures of OEC in S1 state [4, 5] combined with the XAS and EPR spectroscopy available data. Nevertheless, structural and spectroscopic studies of model complexes in S2 state remain rare [6, 7]. In order to help to understand the discrepancies in the interpretation of EPR spectra of Natural and Synthetic complexes, Agapie and coworkers [8] proposed the systematic studies showing that electronic structure of tetranuclear Mn complexes is highly sensitive to small geometric changes and the nature of the bridging ligands. Present work is dedicated to the theoretical investigation of structural and electronic properties of 3-ox synthetic Mn4O4 model complex spectroscopically mimicking the S2 state of OEC.

Methods

The full structural model of 3-ox was used for geometric and electronic structure calculations.

Crystallographic coordinates of the Synthetic complex 3-ox were used as the starting geometry (Figure 1).

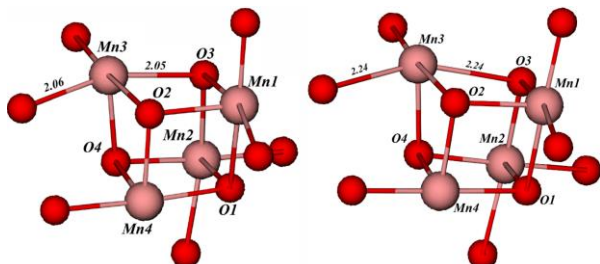


Figure 1 - Cluster structures of the truncated optimized model with TPSSh functional and $e=8.5$ (right) comparing to the experimental cluster model (len).

All structures have the same valence state distribution of the Mn ions (4434). Full optimisations were performed in total HS and selectively in some of the BS states with PBE+U, B3LYP, TPSSh, M06 functionals. The single-point energies of all BS states (including HS) were calculated. In the second step, using these energies and the calculated values of the spin square we obtain the coupling constants J following Heisenberg-Dirac (HDvV) model. For PBE functional we have used the D3 dispersion corrections and 10-5 SCF parameters together with the DZVP basis set and the Hubbard correction $U=1.16$ eV.

Results

The system has a strong propensity to put the unique Mn(III) oxidation state on Mn3 atom in the absence of any changes

in geometry. The position of the Mn(III) atom is defined by the Mulliken population analysis.

Furthermore it is observed the Mn3-O3 bond elongation by more than 0.1 Å together with the distance from Mn3 to the unique carboxylate ligand both in the calculation and experiment. This indicates that the orientation of the Jahn-Teller axis is along this elongation. The strong elongation of Mn3-O3 bond distance for about 0.15-0.2 Å comparing to the experimental value is observed in all the calculations using different functionals and basis sets.

In order to exclude the crystal packing effects on the key bond distances of the inorganic core, we have performed periodic DFT calculations with the PBE+U/ TZVP level of theory. The RMSD value for the system in the lowest energy BS state without H atoms is 0.174 Å while for the cluster is around 0.11 Å. The calculated J values by PBE+U/TZVP and B3LYP/TZVP reflect the differences reported in the geometries, being contradictory to most of the experimental values.

This leads to the conclusion that the difference in Mn3-O3 distance of about 0.2 Å is crucial in determining the electronic structure and magnetic properties of the Synthetic complex.

Conclusions

We discussed our preliminary results on the electronic and structural properties of the novel Mn4O4 synthetic compound mimicking the EPR spectroscopic nature of OEC in S2 state.

In summary the present work demonstrates how electronic structure calculations in combination with other computational methods are now mature to approach complex biological systems and they can be of valuable help in the rationalization and understanding of structure/function relationships in molecular Biophysics.

References

- [1] Pantazis, D.A. et al., *Angew Chemie Int Ed*, 51 (2012), 9935
- [2] Narzi, D. et al., *PNAS*, 111 (2014), 8723
- [3] Bovi, D. et al., *Angew Chemie Int Ed*, 52 (2013), 11744.
- [4] Suga, M., et al. *Nature*, 517 (2014), 99
- [5] Umena, Y. et al., *Nature*, 473 (2008), 55.
- [6] Mukhopadhyay, S. et al., *Chem Reviews*, 104 (2004), 3981.
- [7] Paul, S. et al., *Inorganic Chemistry*, 7 (2017), 3875.
- [8] Lee, H. B. et al., *JACS*, 140 (2018), 17175.

Acknowledgements

The work has been performed under the Project HPC-EUROPA3 (INFRAIA-2016-1-730897), with the support of the EC Research Innovation Action under the H2020 Programme; in particular, the author gratefully acknowledges the support of Professor Guidoni Leonardo and the computer resources and technical support provided by CINECA.

Aromaticity of pyrrole and pyridine in the water environment

K.K. Zborowski¹, J. Poater²

¹Faculty of Chemistry, Jagiellonian University in Krakow, Kraków, Poland; ²Departament de Química Inorgànica, Institut de Química Teòrica i Computacional (IQTCUB), Universitat de Barcelona, Barcelona, Spain; ³ICREA, Barcelona, Spain

Introduction

The cyclic electron delocalization, i.e. so called aromaticity, is a very important task in some parts of chemistry. It is present in many chemical species of key importance and often decides about their structures and reactivity [1]. As most of other properties, theoretical studies on aromaticity studies started with isolated molecules. If solvent effects were taken into account, they were modelled by so called continuum models of solvation, which does not need much more computer resources than for calculations of free molecules. However, today's supercomputers are capable of studying chemical species solvated by discrete water molecules. Such a study was done for benzene in a water environment. Aromatic properties of benzene in a cage constructed by fifty water molecules were studied. [2] In this work, the aromatic properties of pyrrole and pyridine in the water environment are investigated using the same model of solvation.

Methods

All structural quantum-chemistry calculations were executed using the 6-31G** basis and the B3LYP functional [3]. The structures of pyrrole and pyridine molecules in different environments were determined. We calculated isolated structures of studied molecules, and their structures in water cages with explicit solvation (each water cage surrounding studied molecules contains fifty water molecules, ten different geometries of clusters containing a ligand molecule and a cage of fifty water molecules were calculated for each studied compound). Aromaticity of pyrrole and pyridine in different environments were evaluated using several approaches, namely HOMA, NICS, PDI (pyridine only), FLU and MCI. All above mentioned aromaticity indices are described in this special issue of Chemical Review [4]. The Atoms in Molecules method [5] was used to calculate atomic charges and energies as well as study the strength of hydrogen bonds formed between studied molecules and water.

Results

Benzene is a hydrophobic compound, which does not interact strongly with water molecules. Thanks to that, benzene can easily maintain its high aromaticity in a water solution [2]. The situation in both, pyrrole and pyridine, is different. These compounds can effectively interact with water cage through NH (pyrrole) or N (pyridine) groups. Performed calculations give us an insight into details of both studied compounds interactions with water. Both molecules interact strongly with one water molecule, see Fig. 1. We determined geometrical and electronic parameters of formed ligand-water hydrogen

bond. It was shown that, pyridine form significantly stronger hydrogen bond than pyrrole. As a result, pyridine dissolves in water much better than pyrrole. The charge transfer between pyridine and water is also much higher for pyridine than for pyrrole. Both molecules are energetically destabilized in their water solutions. The most important parts of the study are aromatic properties of pyrrole and pyridine in water. Values of aromaticity indices for pyridine and pyrrole in water cages were obtained and compared with the same data for isolated molecules at the same level of theory. Such a comparison shown that aromaticity of investigated compounds in water solution is, in a similar way as for benzene, only slightly perturbed.

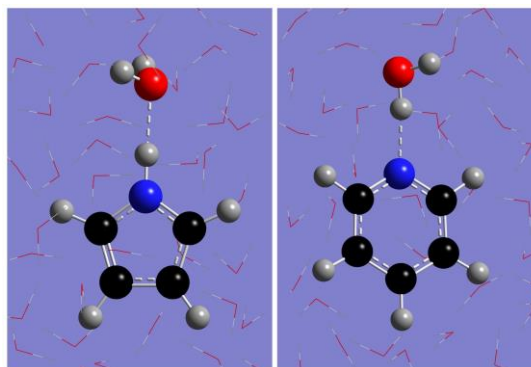


Figure 1 - Examples of pyrrole and pyridine structures in water.

Conclusions

There are important differences between pyrrole and pyridine. However, both these compounds are strongly aromatic. Thus, both studied systems prefer to retain their aromatic levels also in the water environment.

References

- [1] Krygowski TM et al., ChemTexts, 1(article 12):1-12, 2015.
- [2] Zborowski KK., Chem. Phys. Lett., 602:1-3, 2014.
- [3] Becke AD, J. Chem. Phys., 98:5648-5652, 1993.
- [4] Schleyer PvR (Ed.), Chem. Rev. 105:3433-3947,2005.
- [5] Bader RWF, Atoms in Molecules: A Quantum Theory, Oxford University Press, Oxford, 1990.

Acknowledgements

The work has been performed under the Project HPC-EUROPA3 (INFRAIA-2016-1-730897), with the support of the EC Research Innovation Action under the H2020 Programme; in particular, the author gratefully acknowledges the support of Departament de Química Teòrica i Computacional (IQTCUB) Universitat de Barcelona and the computer resources and technical support provided by Barcelona Supercomputing Center BSC-CNS.

Climate modelling and attribution of summer 2018 heatwaves and droughts in Northern Europe

N. Fučkar¹, T. König², and T. Kruschke²

¹Environmental Change Institute, University of Oxford, Oxford, United Kingdom; ²Rosby Centre, Swedish Meteorological and Hydrological Institute (SMHI), Norrköping, Sweden

Introduction

In the summer of 2018 persistent soaring temperatures and droughts from Greece to Finland led to health warnings, serious harm to crops, and numerous wildfires. Specifically, May and July 2018 (Figure 1) in Sweden were the warmest May and July on the record, respectively. Furthermore, Sweden experienced extensive drought and large wildfires reaching even north of the Arctic Circle. This project models these extreme summer events in Europe with the state-of-the-art climate model EC-Earth3.3 [1]. We generate extensive ensembles for probabilistic event attribution to assess to what extent anthropogenic forcing factors modifies the probability and/or magnitude, and hence the risk of such class of extreme events to occur [2].

Methods

At the base of probabilistic extreme event attribution is the comparison of historical or actual probability distribution of a variable or variables with the counterfactual or natural (or preindustrial), i.e., a world without anthropogenic climate change, probability distribution. Specifically, we need large or very large model ensembles (more than 100 members) of climate simulations to estimate characteristics of extremes and to determine risk indicators such as probability ratio (PR) or intensity change that are of interest to scientific community and various stakeholders. We executed very large ensembles of 4-month EC-Earth3.3 (T255L91 IFS c36r4 + ORCA1L75 NEMO3.6 used for CMIP6) simulations (on HPC system Beskow at KTH-PDC) initialized on 1 May 2018. They are produced in the following manner:

- 1) Generation of actual (using observed/historical greenhouse gasses and aerosol forcing fields) ensemble simulations using ECMWF atmospheric and oceanic reanalyses for observation-based initial conditions (IC).
- 2) Generation of associated counterfactual ensemble simulations (in pre-industrial conditions). This is a critical element the nonparametric event attribution. To get counterfactual ocean and sea ice IC we have extracted excess ocean heat content from the present-day IC based on the difference of present day (early 21st century) ocean-sea-ice state and the last 100 years of long-term preindustrial simulation of EC-Earth3.3.

Results

Monthly SAT averaged over the rectangular region in northern Europe marked in Figure 1 has been exceptionally high in May and July 2018. The preliminary analysis of actual (present-day) vs counterfactual (pre-industrial) ensembles of EC-Earth3.3 simulations show PR = 49.3 (95% Confidence Interval: 19.9, 338.3) for May 2018 (+3.25°C anomaly) and PR = 29.8 (95% CI: 9.4, 127.6) for July 2018 (+2.29°C anomaly). In other words, May (July) 2018 high temperature in the specified region has become almost 50 (30) times more likely, at present, due to the climate change (with respect to pre-industrial climate conditions). On the other hand, the concurrent low precipitation conditions in the same region

show PR = 0.09 (95% CI: 0.01, 0.34) for May 2018 and PR = 0.54 (95% CI: 0.20, 1.05) for July 2018: Meaning that such meteorological droughts have become significantly less likely due to the climate change.

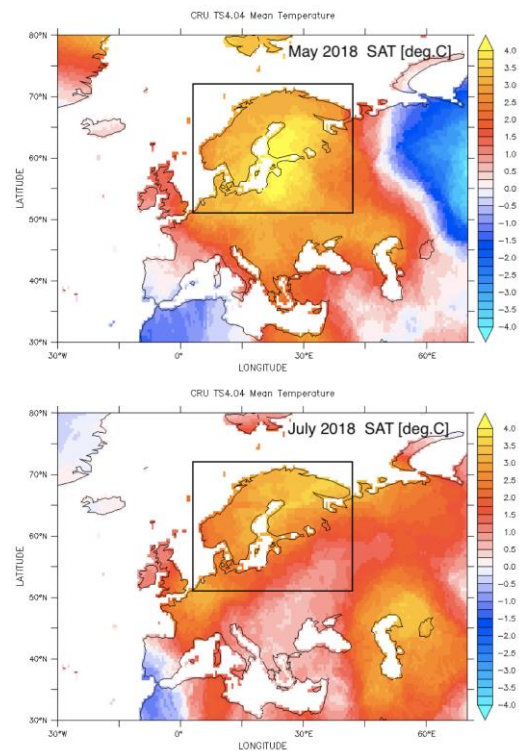


Figure 1 – Monthly mean surface air temperature (SAT) anomaly (with respect to the 1981-2010 climatology) in May and July 2018 (CRU TS v4.04 SAT data [3]).

Conclusions

This study shows that examined concurrent extreme events in northern Europe can have complex relationship with the climate change. Anthropogenic factors have astoundingly increased the likelihood of such heatwaves, but they are making probability of coocurred droughts much less likely (meaning there were results of strong internal variability).

References

- [1] <http://www.ec-earth.org/>. [2] Stott, P.A., et al., WIREs Clim Change, 7: 23-41. doi:10.1002/wcc.380, 2016. [3] Harris, I., et al., Sci Data 7, 109, doi:10.1038/s41597-020-0453-3, 2020.

Acknowledgements

The work has been performed under the Project HPC-EUROPA3 (INFRAIA-2016-1-730897), with the support of the EC Research Innovation Action under the H2020 Programme; in particular, the author gratefully acknowledges the support of Torben König, Tim Kruschke and SMHI in Norrköping, and the computer resources and technical support provided by PDC at KTH in Stockholm.

Comparison between METIS, SCOTCH, ParMETIS and PT-SCOTCH for 3D frequency-domain wave modelling using MUMPS

Y. Li¹, R. Brossier¹, L. Métivier^{1,2}, J. de la Puente³

¹ISTerre, Univ. Grenoble Alpes, France; ²CNRS, LJK, Univ. Grenoble Alpes, France; ³Barcelona Supercomputing Center, Spain

Introduction

Frequency-domain FWI has been investigated using the acoustic approximation. However, the acoustic approximation can no longer be used for the inversion of the land data because the anelastic and visco-elastic effects dominate. Thus, we investigate the large-scale 3D frequency-domain anisotropic visco-elastic wave modeling in this research.

Spectral element method is used to discretize the wave equation and we solve the linear system by the parallel direct solver MUMPS. Comparison between sequential matrix reordering algorithms (METIS and SCOTCH) and their parallel counterparts (ParMETIS and PT-SCOTCH) is conducted to investigate the performance of LU decomposition.

Methods

The 3D frequency-domain elastic wave equation reads:

$$\rho\omega^2 u_j + \frac{\partial}{\partial x_i} \left(c_{ijkl} \frac{\partial u_k}{\partial x_l} \right) + f_j(\omega, r_s) = 0, i, j, k, l = 1, 2, 3,$$

where ρ is the density, ω is the angular frequency, u_j is the displacement vector, c_{ijkl} is the elastic modulus tensor, $f_j(\omega, r_s)$ is the point source force vector located at r_s . A fifthorder spectral element method is used to discretize the weak form of the wave equation. We have

$$Au = f,$$

where $A = \omega M + K$, M is the diagonal mass matrix, K is the stiffness matrix, u is the discretized displacement vector, and the right-hand side f is the discretized source. We use the MULTifrontal Massively Parallel sparse direct Solver (MUMPS [1]) to solve this system. The sequential algorithm METIS [2] and SCOTCH [3] and their parallel counterparts ParMETIS and PT-SCOTCH to perform the matrix reordering to decrease the fill-in effect during the LU decomposition.

Results

A subset of the SEAM Phase II Foothills model is used to perform the modeling. Figure 1 shows the V_p , V_s and model.

The parameter settings are summarized in Table 1.

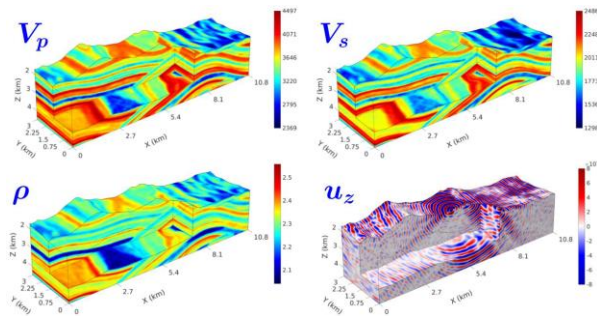


Figure 1 - Subset of the 3D SEAM Phase II Foothills model for V_p , V_s and ρ , and the real part of u_z .

N_e	N_{PML}	$ e $ (m)	f (Hz)	DOFs	N_{NNZ}
$30 \times 72 \times 20$	2	100	7	11,449,395	3,872,156,500

Table 1 - Parameter settings: N_e , number of elements in each dimension; N_{PML} , number of elements in PML; $|e|$, element size; f , modeled frequency; DOFs, the number of degrees of freedom; N_{NNZ} , number of nonzeros in the matrix.

We use 10 fat nodes (384 Gb per node, 60 MPIs, 8 OpenMP) for METIS and SCOTCH and 100 normal nodes (96 Gb per node, 200 MPIs, 24 OpenMP) for ParMETIS and PT-SCOTCH. The results are summarized in Table 2. METIS generates the most efficient reordering for the following factorization in terms of both memory cost and flops. ParMETIS and PTSCOTCH may reduce the reordering time, but not as efficient as METIS for the LU decomposition. PTSCOTCH failed because of the large memory cost during the factorization.

Method	$M_{allocated}$ (Mb)	T_A (s)	T_F (s)	T_S (s)
METIS	1,513,578	1261.5	785.8	1.6
SCOTCH	1,570,540	1585.7	872.8	1.7
ParMETIS	3,500,585	511.6	5364.7	7.7
PT-SCOTCH	out of memory	-	-	-

Table 2 - Memory cost $M_{allocated}$, analysis time T_A , factorization time T_F and solving time T_S for different reordering methods.

Conclusions

For 3D frequency-domain wave modelling, METIS generates the most efficient matrix reordering for the LU factorization in terms of both memory cost and flops. But the bottleneck is the memory cost of METIS has reached the limit of one single computing node because it is sequential. Parallel reordering methods may reduce the analysis step time, but the memory cost of the following factorization is much larger. Therefore, the parallel reordering methods are currently not suitable for large-scale modelling. Further research will focus on investigating more efficient parallel reordering algorithms.

References

- [1] MUMPS-team, MUMPS - MULTifrontal Massively Parallel Solver users' guide - version 5.2.1. ENSEEIHT-ENS Lyon, 2019.
- [2] Karypis, G., METIS - A software package for partitioning unstructured graphs, partitioning meshes, and computing fillreducing orderings of sparse matrices - version 5.1.0. University of Minnesota, 2013.
- [3] Pellegrini, F., PT-SCOTCH and libPTSCOTCH 6.0 user's guide - version 6.0.5. Université Bordeaux, 2018.

Acknowledgements

This work was partially funded by the SEISCOPE consortium. The work has been performed under the Project HPC-EUROPA3 (INFRAIA-2016-1-730897), with the support of the EC Research Innovation Action under the H2020 Programme; in particular, the author gratefully acknowledges the support of Josep de la Puente, Department of Computer Applications in Science and Engineering and the computer resources and technical support provided by Barcelona Supercomputing Center.

Unveiling forest degradation in the tropics: new approaches using 3D terrestrial LiDAR

Y. Mendes de Moura¹, E. Maeda²

¹Royal Society, Newton International Fellow, University of Leicester, United Kingdom; ²Department of Geosciences and Geography, University of Helsinki, Finland

Introduction

Tropical forests play a major role in the global carbon (C), nutrients, and energy cycles (Gloor, 2019). Despite their importance, tropical forests have been extensively degraded in recent decades. Forest degradation is key to understand the full picture of the carbon cycle in the tropics. However, our knowledge of the carbon budget in degraded tropical forests is still very poor. Degradation is primarily visible through changes in forest structure, but there is a huge lack of this information across the tropics. Recently, significant advances have been made in methods for quantifying canopy structure from Light Detection and Ranging (LiDAR). The objective of this study was to develop methods and techniques for processing Terrestrial Laser Scanning (TLS) using high-performance computing to derive robust structural metrics over degraded forests in the Amazon.

Methods

We used Ultra High Performance High 3D laser scanner collected with a RIEGL VZ-400i TLS (RIEGL Laser Measurement Systems GmbH), which uses on-board waveform processing. This instrument records multiple return LiDAR data, which improves vertical sampling (Lovell et al., 2003) with a range of up to 800 meters. We used three steps (following Calders et al., 2018) for stand reconstruction based on TLS cloud points:

- Filtering: identification and removal of spurious points in the TLS;
- Down-sampling: based on the point cloud we use voxel grid aggregation;
- Stem identification and stem segmentation: individual stems were identified based on the segmentation of height slice above the Digital Terrain Model (DTM).

We used RiSCAN PRO 2.0 and CloudCompare and TreeSeg, an open-source software that was installed at CSC Puhti Supercomputer. This software built upon the Point Cloud Library and full details can be found in Burt et al., 2018.

Results

This work has contributed for delineating a data processing pipeline necessary for extracting key forest parameters. We have initiated the analysis of the canopy structure in five transects located in the central Amazon forest. At a tree level, the methods tested during this project showed promising results for identifying changes in canopy height, tree stem density, and diameter at breast height. Nonetheless, our results demonstrate that some forest attributes that requires a precise segmentation of trees cannot be extracted easily in tropical ecosystem. For instance, measuring precise tree crown diameter is challenging, given that tree canopies are largely intersected in dense forests.

A promising alternative approach is the assessment of 3D canopy structure, that is, the vertical and horizontal distribution of plants within the canopy. Our initial assessments have shown that forest degradation is likely to significantly change the distribution of above ground biomass within the canopy, leading to measurable changes in canopy structure.

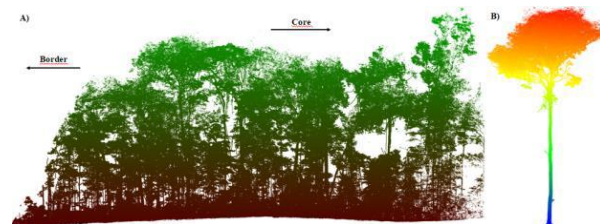


Figure 1 – A) Sample of filtered and down-sampled point cloud data from TLS showing structural differences from the border and the core of a fragment of forest in the Amazon region. B) Example of a tree segmentation and separation from the cloud point. A full visualization of 3D model is available on the link: <https://www.youtube.com/watch?v=bzyCiv-AV3E>

Conclusions

The methods used in this study for stand reconstruction seems very promising, especially for structural-complex environments (e.g. tropical ecosystems). The use of High Performance computing for highly dense cloud points, as those derived from TLS, is essential for a robust and time-effective generation of results. Future work aims to provide a full quantitative analysis and structural metrics derived from TLS, including carbon estimates for tropical ecosystems.

References

- [1] Gloor, *Nature Climate Change*, 9(5), 355-356, 2019.
- [2] Lovell et al., *Canadian Journal of Remote Sensing*, 29(5), 607-622, 2003.
- [3] Calders et al., *Remote Sensing*, 10(6), 933, 2018.
- [4] Burt et al., *Methods in Ecology and Evolution*, 10(3), 438-445.

Acknowledgements

The work has been performed under the Project HPC-EUROPA3 (INFRAIA-2016-1-730897), with the support of the EC Research Innovation Action under the H2020 Programme; in particular, the author gratefully acknowledges the support of Dr Eduardo Maeda, Academy of Finland Research Fellow, Department of Geosciences and Geography, Helsinki Institute of Sustainability Science (HELSUS) and the computer resources and technical support provided by CSC - IT CENTER FOR SCIENCE LTD.

Improved Elmer/ice calving model: integrated 3D remeshing

*E. van Dongen*¹, *J. Todd*²

¹ETH Zurich, Switzerland; ²University of St Andrews, Scotland, United Kingdom

Introduction

Warming in recent decades has caused glaciers and ice sheets to shrink substantially, and thus to contribute to the observed global sea-level rise. Iceberg calving – the breaking off of icebergs at the edge of glaciers into the sea – is responsible for approximately half of the ice mass loss of the Greenland ice sheet. Calving mechanisms are still not entirely understood. An improved understanding of iceberg calving will help to better constrain the future contribution of ice sheets to sea level rise.

The current implementation of 3D iceberg calving in Elmer/Ice is limited by 2D external remeshing, such that the 3D model must first be turned into a representative footprint, extruded and deformed to match potentially non-vertical regions of the calving terminus. For reasons of model flexibility, robustness and efficiency, it is desirable to be able to remesh arbitrarily in 3D, with no dependence on vertically structured meshes.

Methods

In a previous HPC-Europa3 Transnational Access visit by Joe Todd to Thomas Zwinger and Peter Råback at CSC in Finland, an interface of Elmer with MMG3D (<http://www.mmgtools.org/>) was developed. The remeshing routine developed then, was now integrated in the existing 3D iceberg calving model in Elmer/Ice. Based on the stress state modelled by Elmer/Ice, a level-set function is calculated which is used by MMG3D to cut the part of the mesh where calving is predicted to occur. Also the partitioning and treatment of domain edges had to be updated for the new remeshing method, such that boundary element info is properly transferred.

Besides glacier retreat by calving, a transient glacier dynamics model needs to be capable of modelling glacier advance as well. Therefore, the existing routine *GlacierFrontAdvance* had

to be extended to include migrating margins. A functionality was introduced that ensures that an advancing glacier remains aligned with the valley walls, by providing the valley geometry as input to Elmer/Ice.

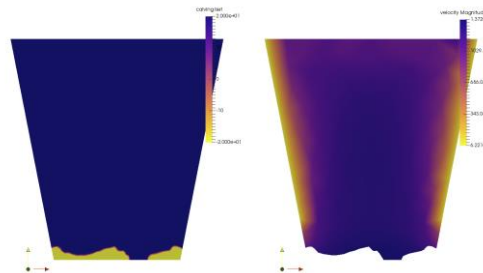


Figure 1 – Top view of the calculated level-set (left) and resulting geometry with velocity (right) for a conceptual glacier geometry.

Outlook

Although multistep calving simulations are now possible using the new remeshing routine, some development remains to be done. For example, the mesh quality needs to be ensured, particularly in case no calving event takes place. Besides that, ideally the remeshing would be done in parallel whereas it is limited to serial now. Especially for large-scale, multiple glacier simulations, remeshing in parallel is essential.

Acknowledgements

The work has been performed under the Project HPC-EUROPA3 (INFRAIA-2016-1-730897), with the support of the EC Research Innovation Action under the H2020 Programme; in particular, the author gratefully acknowledges the support of Joe Todd and the computer resources and technical support provided by EPCC.

Serpent neutronics model of Wendelstein 7-X

S. Äkäslompolo^{1,2}, J. Leppänen³, the Wendelstein 7-X team

¹Max Planck Institute for Plasma Physics, Germany; ²Current affiliation: Aalto University, Finland; ³VTT Technical Research Centre of Finland Ltd

Introduction

Wendelstein 7-X stellarator (W7-X) is a large-scale, magnetic confinement fusion experiment in Germany. In the reactor, gas is heated into the temperatures of millions of degrees becoming ionized gas or plasma. The very hot plasma is insulated from the walls of the reactor by using a strong and carefully shaped magnetic field produced with superconducting coils. In the future, the experiment will use deuterium gas, which will result in a small but measurable amount of fusion. Certain fusion reactions produce neutrons with 2.45 MeV or 14.1 MeV energy. The neutrons will occasionally collide with the nuclei of the material and change their direction and speed (scatter) and are eventually absorbed. The measured neutron flux can be used to assess the performance of the machine, especially its capability to confine the so-called fast ions.

In the HPCE3 project a computational model of the neutron transport was prepared with the Serpent Monte Carlo code [1]. The model must incorporate the relevant structures in and near the experiment to accurately predict the scattering of neutrons and thus predict the signal of any neutron detectors. The main deliverable of the project is the neutron transport part of the instrument function of the planned Scintillating Fibre (ScFi) neutron detector [2].

Technical details of the model

The Serpent model of W7-X includes i.a. the vacuum vessel, superconducting coils and plasma facing components. The detector is housed in a collimator box made of borated polyethylene and an aluminium cylinder is used as a proxy for the detector itself. The geometry is included mainly in unstructured .STL-formatted meshes and represents the key components in one period of the approximately 5-fold symmetric device. The code replicates the single period to form a closed torus.

Neutron flux as a function of energy has been modelled in the detector. The Serpent code was expanded by including support for anisotropic response functions for track-length detectors. This was done to account for the intrinsic directionality of the ScFi detector.

Instrument function for ScFi neutron detector

The instrument function translates a given fusion rate in the experiment to the measured signal from the detector. The Serpent model transforms the fusion rate as a function of neutron birth location to the neutron flux inside the neutron detector. The neutron flux can be translated to the measured signal using a calibration factor measured in a separate, dedicated facility. The Serpent code was modified to enable collection of neutron flux as a function of the birth location of the neutrons.

Results

The main result is the identification of the main components responsible for scattering neutrons in W7-X: the coils and coil-casings (figure 1). The modelling shows that the coils shadow neutron flux from the detectors, while backscattering from massive components is negligible. This is understandable due to the model following high energy (>0.1 MeV) neutrons only.

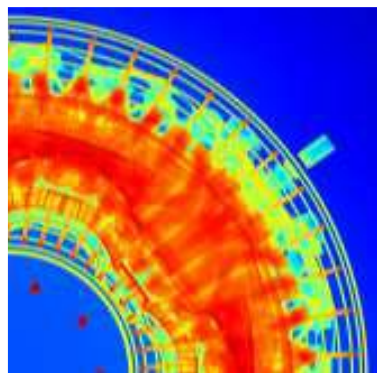


Figure 1 - The total reactivity of high-energy neutrons in W7-X as a vertical projection of all reactions. A few example coils are indicated with black arrows and the collimator box with a yellow arrow. The simplified water-cooling manifold is also visible.

Future work

Fine-tuning of an effective weight-window map for variance reduction is still on-going at the time of writing this report. When the variance reduction is working as expected, the final simulations can produce the sought-after instrument function. A further upgrade of Serpent can facilitate calculating the response function as a function of neutron initial velocity.

A more complete report of the results is expected in the 31st Symposium on Fusion Technology and in the proceedings thereof.

References

- [1] Leppänen, J., et al. *Ann. Nucl. Energy*, 82 142-150, 2015.
- [2] Sailor, W.C., et al. *Rev. Sci. Instr.* 66, 898 1995.

Acknowledgements

The work has been performed under the Project HPC-EUROPA3 (INFRAIA-2016-1-730897), with the support of the EC Research Innovation Action under the H2020 Programme; in particular, the author gratefully acknowledges the support of VTT Technical Research Centre of Finland Ltd. and the computer resources and technical support provided by CSC – IT CENTER FOR SCIENCE LTD.

This work has been carried out within the framework of the EUROfusion Consortium and has received funding from the Euratom research and training programme 2014-2018 and 2019-2020 under grant agreement No 633053. The views and opinions expressed herein do not necessarily reflect those of the European Commission.

Inner and outer vacuum vessel

Modelling of TJ-II plasmas with Monte Carlo orbit-following code ASCOT

J. Kontula¹, S. Mulas², M. Mantsinen³, T. Kurki-Suonio³, A. Cappa²

¹Aalto University, Finland; ²CIEMAT, Spain; ³BSC and ICREA, Spain

Introduction

Nuclear fusion is a promising alternative for baseload power generation. Stellarator-type fusion reactors are capable of steady-state operation, making them attractive for power plant operation. The experimental fusion device TJ-II, located at the Spanish National Fusion Laboratory CIEMAT, is one of the leading stellarator facilities in Europe. One of the primary challenges facing stellarator reactors is the behaviour of energetic ions. In TJ-II, fast ions are produced in plasma heating by neutral beam injection (NBI). The NBI ions carry an electric current which could disturb the carefully constructed magnetic equilibrium of the device.

In this work, we used the ASCOT code to examine the properties of NBI ions in TJ-II. The objective was to allow for calculation of both the full phase space distribution function of the NBI ions, as well as the beam-driven current. To allow for experimental validation of the ASCOT fast ion distribution function calculations, the possibility of using synthetic diagnostics, namely the FIDASIM code, to model the TJ-II neutral particle analyser was examined.

Methods

The fast particle simulations in this work were done using the ASCOT Monte Carlo orbit-following code [1]. ASCOT is especially suitable for fast ion simulations in stellarators due to its non-axisymmetric nature. ASCOT also fully utilizes the capabilities of modern HPC environments with hybrid OpenMP and MPI parallelization plus vectorization. It also includes the NBI ionization code BBNBI, making it possible to simulate the particle injection in full. The 3D wall and injector geometry of TJ-II were imported to the ASCOT format. Tools for converting the kinetic profiles and magnetic equilibria to ASCOT inputs were also written. For calculating the electron response to the fast ion current, a model based on classical collisional theory was implemented [2].

Results

The fast ion current from the NBI beams was calculated in two different experiments. Qualitative agreement between ASCOT and experimental current measurements was achieved in both cases. Quantitative agreement required accounting for atomic interactions using the FAFNER code [3]. During these simulations, it was discovered that the NBI particles can make excursions of up to 20% of the plasma width during one gyro orbit, so the plasma density and temperature vary significantly during single orbits as well. This makes the often-used guiding-centre formalism unsuitable for accurate simulation of fast ions in TJ-II.

To gain more understanding of fast ion confinement in TJ-II, a large simulation scanning particle losses from the entire phase space was conducted. The particle power losses have a distinct pattern in this phase space, as shown in Figure 1. This loss mapping serves as a basis for further fast ion loss studies, where the simulation resolution can be improved by focusing on regions with a high particle loss fraction.

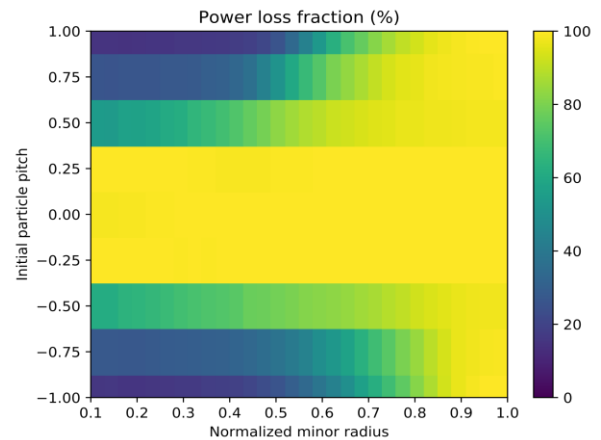


Figure 1 - Fast ion power loss fraction as a function of the initial particle pitch (direction) and normalized minor radius. The power loss fraction is highest for particles with pitch between -0.4 and 0.4, or those born outside 80% of the minor radius. NBI particles in TJ-II are typically born at the well-confined region with pitch > 0.8.

Conclusions

In this work, we investigated the properties of NBI-injected ions in TJ-II with the orbit-following code ASCOT. The commonly used guiding-centre formalism was found to insufficiently capture the behaviour of fast ions in TJ-II. The full phase space of TJ-II was mapped with regards to fast ion confinement. This mapping can help in optimizing future simulations as well as designing NBI injectors.

The accuracy of experimental comparisons was limited by the lack of an atomic reaction module in the present ASCOT version. In TJ-II, charge-exchange reactions of the NBI ions can account for a significant portion of the fast ion losses. The development of an atomic reaction module for ASCOT is underway and the model will be used for further simulations.

During the work, ASCOT was established as a working simulation tool for fast ions in TJ-II. This opens up avenues for further research into fast ion behaviour. Validation of the current drive model is ongoing, and experimental comparison will continue by comparing the fast ion distribution from ASCOT to measurements made using the FIDA diagnostic.

References

- [1] Varje J. et al., Submitted to Comput. Phys. Comm., (2019).
- [2] S. P. Hirshman, Physics of Fluids 23.6:1238, 1980.
- [3] Lister, G.G., IPP—4/222, 1985.

Acknowledgements

The work has been performed under the Project HPC-EUROPA3 (INFRAIA-2016-1-730897), with the support of the EC Research Innovation Action under the H2020 Programme; in particular, the author gratefully acknowledges the support of ICREA Research Professor Dr. Mantsinen (Fusion) and the computer resources and technical support provided by BSC.

Molecular dynamics simulations on hydrogen embrittlement

B. Bal¹, C. Schön²

¹Department of Mechanical Engineering, Abdullah Gül University, Turkey; ²Max Planck Institute for Solid State Research, Stuttgart, Germany

Introduction

Hydrogen embrittlement (HE) is a failure mechanism in metallic materials. Due to HE, the fracture mode of metals changes from ductile to brittle. There have been lots of studies, both experimentally and numerically, on HE, the exact mechanism of HE is still unclear[1]. In this study, the effect of hydrogen on dislocation mobility, microstructural activities and corresponding macroscopic response is studied via Molecular Dynamics (MD) modelling.

Methods

Molecular dynamics (MD) simulations were performed using LAMMPS (Large-scale Atomic/Molecular Massively Parallel Simulator) on α -Fe crystals. The interatomic interactions among Fe and H atoms were described by using an EAM (embedded atom method) potential. Periodic boundary conditions are used. Prior to loading, the energy was minimized for each simulation cell and the system temperature is equilibrated via NVE ensemble simulations for 50 ps by rescaling the temperature of the atoms to 300 K in each step, in order to let the hydrogen atoms, diffuse through the system.

Results

It is showed that atomic hydrogen decreases the mobility of edge dislocations. In addition, atomic hydrogen can shield the stress field of dislocation and enhance localized deformation. In addition, hydrogen can pin dislocations and create additional hardening. Furthermore, coexistence of several HE mechanisms are observed in MD simulations. Finally, hydrogen inhibits the formation of new grain boundaries.

Conclusions

Effect of hydrogen on dislocation level is studied. The influence of hydrogen on interaction between grain boundary and dislocation will be discussed in more detail as a future work.

References

[1] Dwivedi S.K et al., Int. J. Hydrogen Energy, 43:21603-21616, 2018

Acknowledgements

The work has been performed under the Project HPC-EUROPA3 (INFRAIA-2016-1-730897), with the support of the EC Research Innovation Action under the H2020 Programme; in particular, the author gratefully acknowledges the support of Christian Schön.

Performance analysis of parallel simulation code for cardiovascular hemodynamic flows

N. Mirkov¹, S. Kenjereš²

¹University of Belgrade, Vinča Institute of Nuclear Sciences, Belgrade, Serbia; ²Department of Chemical Engineering, Faculty of Applied Sciences, Delft University of Technology, Delft, the Netherlands

Introduction

Engineering modelling approaches for simulating hemodynamics play critical role in diagnosis and treatment of cardiovascular diseases. Nonstationary nature of flow instabilities and shear stress fields on vessel wall as well as pulsatile boundary conditions show the necessity of highly accurate time-resolving simulations. There is obvious potential for improvement of existing modelling practices by introducing higher order accurate time-stepping algorithms in hemodynamic flow simulation codes. The use of higher order in time computational algorithms would be able to resolve transient effects of instabilities in blood flow and resolve to a higher accuracy oscillatory behaviour of wall shear stress on the blood vessel walls. Newly developed computational tool has goal of improving accuracy prediction of said parameters responsible for plaque formation and improve diagnostic capability of hemodynamic simulations.

Methods

Our approach in simulation of cardiovascular hemodynamic flows relies on discretized solution of Navier-Stokes equations in fixed or in moving domains, with included non-Newtonian model for blood rheology which takes into account shear-thinning of the whole blood caused by the red blood cell aggregation and dispersion as function of shear rates [1]. The code used in the project is *freeCappuccino* [2,3], a parallel, open-source unstructured CFD code based on Finite Volume Method, developed and maintained by the visiting researcher (N. Mirkov, University of Belgrade). The code is hosted on GitHub platform (www.github.com/nikola-m/freeCappuccino).

Results

We present one of the studied cases, a high fidelity numerical simulation of a phantom artery, a 3D configuration with geometrical complexity present in artery stenosis which can be studied both experimentally and numerically. This model would serve validating proposed novel medical protocol for estimating wall shear stresses on arteries using 4D MRI. Using magnetic resonance imaging is not typical for engineering flow measurements but is quite common in medical application, so it seems necessary to compare measured results to those of high-fidelity time accurate simulation. In the initial stage a multiblock structured mesh generation is undertaken to correctly represent given geometry while preserving good mesh quality needed for Large Eddy Simulation (LES). The mesh resolution was estimated based on initial stationary, RANS simulation. The case has relatively small Reynolds number of $Re=4410$ and it was concluded that LES with model that would take into account the wall effects would be a proper modelling choice. Two configurations were chosen, one with prescribed inlet conditions, and other based on constant feeding from precursor simulation.

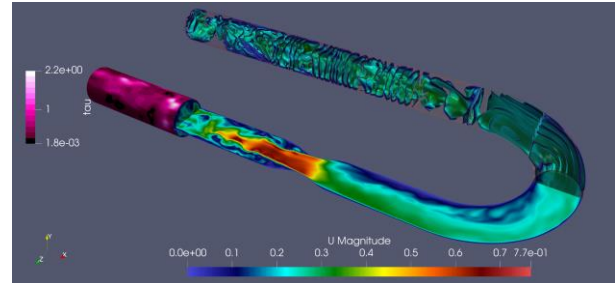


Figure 1 – Computational study of flow in phantom stenosis, pressure isosurfaces before the bend, velocity magnitude in stenosis region showing flow separation and instantaneous wall shear stress (purple) on a segment of a vessel.

High temporal accuracy and small time steps allowed for studying flow development on a timescale not resolved by measurement and help understanding effects that lead to certain observed phenomena. In Fig. 1 we observe flow complexity of the studied case. This is especially evident in the region behind stenosis where transient character of wall shear stress is observed due to flow instabilities developed at stenosis.

Conclusions

Our objective was to deliver improved higher order accurate time-stepping algorithm, distinguished by scalable parallel implementation that would be capable of performing validated simulations of higher accuracy and improved scalability, overcoming several of the limitations of existing software. We feel that increase in extension of time-scales, domains and fidelity for cardiovascular hemodynamic simulation in realistic geometries using developed algorithm will be valuable for the experts in the field. We expect further improvements in automation of the process from extracting the geometry to final simulation results which will speed up the whole procedure.

References

- [1] Kenjereš S, Flow Turbulence Combustion, 96:837–860, 2016.
- [2] Mirkov N et al. In book: Experimental and Numerical Investigations in Materials Science and Engineering, Lecture Notes in Networks and Systems 54:137-147, 2019.
- [3] Mirkov N et al., Journal of Computational Physics, 287:18-45, 2015.

Acknowledgements

The work has been performed under the Project HPC-EUROPA3 (INFRAIA-2016-1-730897), with the support of the EC Research Innovation Action under the H2020 Programme; in particular, the author gratefully acknowledges the support of Prof. Saša Kenjereš, TU Delft, the Netherlands and the computer resources and technical support provided by SURFsara, Amsterdam, the Netherlands.

Three-dimensional direct numerical simulations of a shear-thinning viscoelastic flow past a stationary sphere

C. Fernandes

Institute for Polymers and Composites, University of Minho, Campus de Azurém, Guimarães Portugal

Introduction

Many industrial operations comprise processing of concentrated particle-laden complex fluids. The research work involved in this project aims, in long term, the development of a 3D numerical code able to cope with the transient dynamics of viscoelastic-based-fluid suspensions. Therefore, an accurate expression is needed to rapidly evaluate the drag coefficient of spherical particles translating in a viscoelastic matrix. To this end, we employed 3D direct numerical simulations. The numerical studies that are being performed, using OpenFOAM [1], are computationally demanding and, naturally benefit from being run in HPC systems. The work developed with the selected host (CINECA) allowed to study the scalability of the developed solver. Additionally, a parametric study to measure the drag coefficient of a sphere in a shear-thinning viscoelastic matrix-based fluid was performed.

Methods

The work developed within this project started with the analysis of the scalability and efficiency of the code already available to simulate systems comprising rigid particles in viscoelastic fluids (Oldroyd-B). For that purpose, the Intel software utility VTune [2] was employed to measure the bounded memory. This study allowed to choose the most efficient computational setup to be used on the envisaged parametric experiments, which was performed using the open-source Dakota [3] optimization software in the Galileo cluster environment, where approximately 1000 simulations were conducted.

Results

The viscoelastic numerical solver was first evaluated in terms of memory performance for configurations with a total of 36, 72 and 108 cores, which were run with 36, 18, 12 and 9 tasks per node and with exclusive or non-exclusive access to the node. Figure 1 shows the memory bound results obtained for the case with a total of 72 cores with exclusive access to the nodes. The results obtained for the other cases were similar and allowed to conclude that with 18 tasks per node the memory access is lesser than the bound threshold.

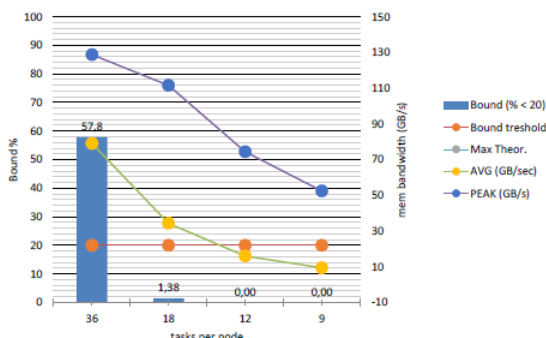


Figure 1 – Memory bound study for a total of 72 tasks per simulation.

Subsequently, and as the main purpose of the work was to perform a massive parallel computational parametric study, we have computed the computational cost/hour (=Number Nodes*Number Cores*Simulation Wall Time/3600) of the above-mentioned configurations (see Figure 2). As shown in the figure the most economical configuration is to use 72 total tasks in non-exclusive deploy, with 12 or 9 task per node. Additionally, we have measured the speedup ratio for this two configurations, and found out that the latter is nearer from the ideal speedup, being 1.3 and 1.8 respectively.

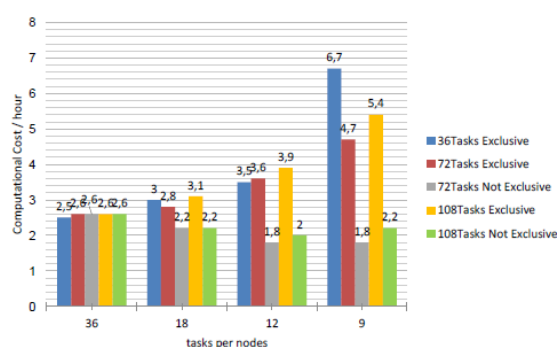


Figure 2 – Computational cost/hour study.

Conclusions

A solver able to compute the drag coefficient on rigid spherical particles inside a viscoelastic fluid matrix was analysed in terms of scalability and efficiency. The scientific host experience on computational analysis was essential to do the diagnostic of the code. The already available case study for the computation of the drag coefficient on a single sphere in an unbounded domain filled with an Oldroyd-B fluid was used on the envisaged performance analysis. The studies performed allowed to reach the best computational configuration to be used on a parametric study for the calculation of the drag coefficient of a sphere immersed in a shear-thinning viscoelastic fluid matrix.

References

- [1] OpenFOAM, The open source CFD toolbox, 2004. <https://www.openfoam.com/>
- [2] Intel VTune Profiler. <https://software.intel.com/content/www/us/en/develop/tools/vtune-profiler.html>
- [3] Dakota, Explore and predict with confidence. <https://dakota.sandia.gov/>

Acknowledgements

The work has been performed under the Project HPC-EUROPA3 (INFRAIA-2016-1-730897), with the support of the EC Research Innovation Action under the H2020 Programme; in particular, the author gratefully acknowledges the support of Ivan Spisso, Gianfranco Marras and the computer resources and technical support provided by CINECA. Additionally, the author would like to acknowledge Miguel Nóbrega for his guidance at IPC, University of Minho.

Data-driven analysis of high-fidelity multi-stage compressor simulation data

P.J. Przytarski¹, A.P.S. Wheeler¹, D. Lengani², D. Simon²

¹Whittle Laboratory, University of Cambridge, United Kingdom; ²DIME, Università di Genova, Italy

Introduction

The flow dynamics within multi-stage turbomachinery flows such as those found in gas turbines are still not fully understood. Such flows are rich in turbulent phenomena driven by high levels of unsteadiness. Understanding of physical mechanisms responsible for loss generation and the impact of unsteadiness on them is needed to achieve higher engine efficiencies¹. To investigate such flows, researchers are employing high-fidelity techniques such as direct numerical simulations (DNS) which attempt to resolve all scales of turbulence within the flow to accurately capture its physics. As a result, DNS studies are expensive and cannot be done routinely. On the other hand, DNS studies give access to unprecedented resolution and a wealth of data but extracting knowledge and distilling it into physical understanding is challenging. This is because the size and complexity of the data limits how it is used². Typically, data is reduced and analysed using statistical and spectral analysis. As a result several time-averaged quantities (e.g. total pressure loss, pressure distribution, turbulence production, etc.) are computed and a spectral signature of the flow at certain points of interest can be found. However, these approaches mean that large portion of information carried by the flow is ignored. This problem can be addressed using data-driven flow decomposition. Such approaches received much attention in recent years thanks to their ability to identify and isolate dynamics present in the flow-field and represent them in a form of decomposed modes and their temporal evolutions. This approach is pursued here to analyse massive amounts of unsteady flow-field data representative of a flow within a multi-stage compressor. Further, this approach is used to perform data-driven assisted scale separation and study the direction and magnitude of energy transfers within the compressor.

Methods

For this study the data was generated with an in-house DNS code using an idealised repeating-passage compressor model for NACA65 compressor blade profile. The details of the code and model can be found in Przytarski and Wheeler¹. The dataset consisted of 500 3D snapshots of data. Each snapshot was made up of 130M grid points with 3 velocity components (u, v, w) available at each grid point. This amounted to approximately 195B data points and just over 1.5TB. To perform data-driven flow decomposition, the Proper Orthogonal Decomposition (POD) procedure³ was selected and implemented following the method of “snapshots”⁴. To allow for full flow decomposition the POD procedure was parallelised in Fortran90 using MPI. The limiting factor of the procedure was the amount of virtual memory available, but the advantage of the developed code was that it did not require any pre-processing or modification of the raw available flow-field data. To bring the costs down, data was also processed in batches whenever possible. The code was tested up to 175 processors and with an excess of 2TB processed. Supplementary parallel Fortran90 codes were also developed and used to allow for the efficient estimation of turbulence quantities associated with each mode as well as

computation of energy transfers between different mode families.

Results

The POD decomposes the data into orthogonal modes and its time signatures. Figure 1 demonstrates how this procedure performed based on the data used here. Given raw flow-field data POD was able to identify known physical dynamics, e.g. related to periodic wakes (mode 1). In addition, it was able to help discover new dynamics (not shown here) and confirm existence of different types of competing transition mechanisms on compressor blades (mode 64). Select modes were then used to partially reconstruct the flow-field and investigate the impact of wake periodic modes and modes related to multi-stage effects on boundary layers. Quantifying their impact is of crucial importance as suction-side boundary layer is responsible for 50% of loss generated within the passage.

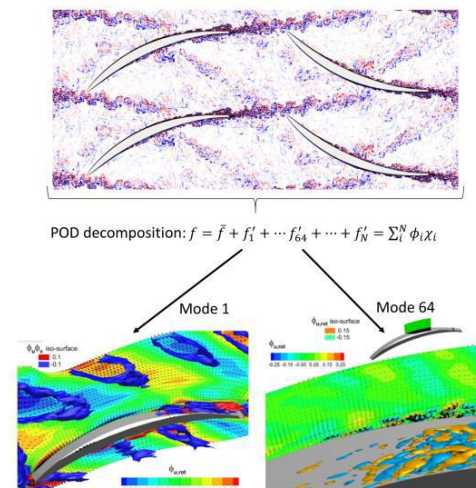


Figure 1 – An example of raw unsteady flow-field data and example dynamics obtained with a POD procedure.

Conclusions

Parallel POD procedure was developed and used to analyse complex high-fidelity data representative of the multi-stage compressor. The results showed here highlight the capability of data-driven approaches in efficiently identifying dynamics present within the turbomachinery flows.

References

- [1] Przytarski PJ, Wheeler APS, The effect of gapping on compressor performance, *Journal of Turbomachinery*, 2020.
- [2] Durasaimy K et al., Turbulence modelling in the age of data, *Annual Review of Fluid Mechanics*, 2019.
- [3] Lumley JL, The structure of inhomogenous turbulent flows, *Atmospheric Turbulence and Wave Propagation*, pp 166-178, 1967.
- [4] Sirovich L, Turbulence and the dynamics of cohere structures, part I-III, *Q. Appl. Math.*, 1987

Acknowledgements

The work has been performed under the Project HPC-EUROPA3 (INFRAIA-2016-1-730897), with the support of the EC Research Innovation Action under the H2020 Programme; in particular, the author gratefully acknowledges the support of Davide Lengani from the University of Genova and the computer resources and technical support provided by CINECA.

Numerical model development for convective cooling of electrical devices

J. Vencels¹, J. Keränen², A. Karvinen², P. Råback³

¹EOF Consulting LLC, Latvia; ²VTT Technical Research Center of Finland Ltd, Finland; ³CSC - IT Center for Science Ltd, Finland

Introduction

In this project we developed a numerical model for convective cooling of electrical devices using Elmer FEM, OpenFOAM and EOF-Library software packages.

Electrical components of motors require numerical solvers for electromagnetic fields and are typically modelled using the finite element method (FEM), while turbulent flows and conjugate heat transfer (CHT) are solved using the finite volume method (FVM). In industry these problems are computed as independent physics processes. This saves simulation time and reduces the complexity of the problem, but also is less accurate compared to the coupled Multiphysics problem. The need for smaller, lighter and more energy efficient electrical devices makes cooling more challenging; therefore, more accurate models are needed [1].

Methods

We use EOF-Library, an open-source coupler for Elmer FEM and OpenFOAM. It enables accurate internal field interpolation and communication between the two software packages. The coupling is based on the Message Passing Interface (MPI), which results in low latency, high data bandwidth and parallel scalability.

The reader can refer to [2] for a more detailed overview.

The modelled mock-up problem is a 3D slice of simplified stator in a permanent magnet motor. An illustration is shown in Figure 1. The alternating current passes copper coils and generates Joule heat. On the outer side of the cover liquid coolant flows and removes it. The electrical properties for copper are temperature-dependent - resistivity increases by 0.4% per 1 °C and thus partially reduces the efficiency of the motor. Electromagnetics and fluid dynamics need to be recomputed until the steady-state solution is found.

Simulations with and without coupling were conducted.

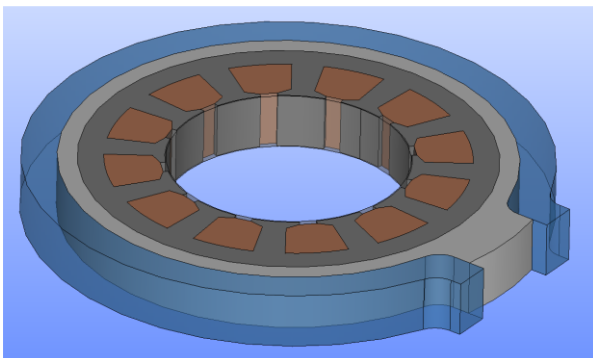


Figure 1 – 3D slice of simplified stator in electrical motor mock-up that includes coils, magnetic iron, an aluminium cover and cooling fluid.

Results

The temperature distribution and fluid streamlines for the coupled solution are shown in Figure 2. In a worst-case scenario, the temperature difference between the uncoupled and coupled simulations was 12°C, which indicates a margin of error of approximately 20%.

Fluid dynamics and CHT (solved using OpenFOAM) were the most-time consuming parts of the problem consuming 90% of the total simulation time which was 14 CPU hours. It means that Elmer and EOF-Library with 10% of the total simulation time would significantly improve the accuracy of the model.

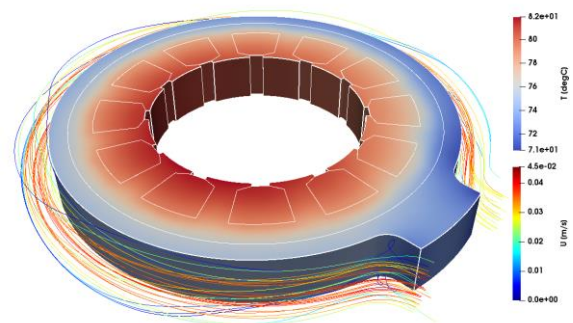


Figure 2 – Simulation results - temperature distribution in rotor and flow streamlines.

Conclusions

The practical applications of such a numerical model extend far beyond the design of electrical motors; other uses include designing transformers, electrical heating devices and flow sensors.

References

- [1] Innovative motor designs for electric cars come to life. Multiphysics Simulation 2017
<https://spectrum.ieee.org/computing/software/innovativemotor-designs-for-electric-cars-come-to-life>
- [2] Vencels, J., Råback, P. and Geža, V.. "EOF-Library: Opensource Elmer FEM and OpenFOAM coupler for electromagnetics and fluid dynamics." SoftwareX (2019)
<https://doi.org/10.1016/j.softx.2019.01.007>

Acknowledgements

The work has been performed under the Project HPC-EUROPA3 (INFRAIA-2016-1-730897), with the support of the EC Research Innovation Action under the H2020 Programme; in particular, the authors gratefully acknowledge the support of VTT and the computer resources and technical support provided by CSC.

Practical parallelization of MPI applications

I. Colonnelli, B. Cantalupo, V. Cesare, A.R. Martinelli, M. Aldinucci

Università degli Studi di Torino

Introduction

In collaboration with MSc students of the Parallel Computing course at the University of Torino, we distilled a general and systematic methodology for loop parallelization of legacy scientific applications. Legacy applications were commonly designed with a purely sequential programming mindset, relying on global variables, aliasing, random number generators, and stateful functions. The proposed methodology aims to give students a way to achieve the first version of a parallel fault-tolerant code, with a limited re-designing effort.

In this work, we tested the proposed methodology with the message passing model (via MPI), applying it to a sequential code in the domain of Molecular Dynamics (MD). This report is part of a broader analysis, which demonstrated that the same methodology works also in the shared memory model (via OpenMP) and in the general-purpose GPU computing model (via OpenACC) [1].

Methods

The proposed methodology consists of four main steps: 1) Identify all parallelizable loops in the code, according to a depth-first search strategy; 2) Evaluate the potential performance gain obtainable by modifying each parallelizable loop, filtering out those that are not worth the parallelization effort; 3) Make each of the remaining candidate loops self-contained to remove true data dependencies among different iterations; 4) Rely on non-parallelizable loops to implement a checkpointing logic to support stop-resume behaviour.

According to the Owner Computes Rule, each process of a multi-process application retains a partition of the data to be locally written and a copy of all the (potentially replicated) input data needed to compute the results. All the sequential loops whose iterations (or ranges of them) admit a partition of write-accessed data can be turned into parallel Single Program Multiple Data (SPMD) processes owning these partitions. These processes can then periodically exchange data, either locally or globally, depending on the data dependency patterns of the application. This approach is quite general but not very scalable. Any computation stencil is admitted, including ones whose extent is potentially all the data (or randomly selected inputs from the whole data).

As an example, we parallelized a Simple MD application, where several second-level loops are parallelized by partitioning iteration blocks into MPI processes that globally Allgather (or reduce) all the data produced in the previous super-step. According to the proposed methodology, these loops are the outermost parallelizable loops. The pseudocode of the parallelized application is reported in Figure 1.

Results

data in further processing was tested on data in OpenFoam format, which were divided into 6 domains. The data were at first read in Vistle and then the streamlines were computed. The result of computation is in Figure 1.

Algorithm 4: Parallel SimpleMD (SPMD).

```

Data: nparticles, number of iterations T
1 rank ← getRank()
2 if rank == 0 then
3   particles ← generate_particles(nparticles)
4 broadcast(particles, 0)
5 nprocs ← getNumberProcesses()
6 nparticlesloc ← nparticles/nprocs // nparticlesloc ← nparticles for seq.
7 force ← init_forces(particles)
8 for t ← 1 to T do
9   for i ← 0 to nparticlesloc-1 do
10    k ← rank × nparticlesloc + i // k ← i for seq.
11    update_position(particles[k], force[k])
12 Allgather(particles, nparticlesloc)
13 for i ← 0 to nparticlesloc-1 do
14    k ← rank × nparticlesloc + i // k ← i for seq.
15    force[k] ← 0
16    for j ← 0 to nparticles-1, j ≠ k do
17      force[k] ← force[k] + compute_force(particles[k], particles[j])
18    update_velocity(particles[k], force[k])
19 Allgather(particles, nparticlesloc) // can be optimised using
   "triangular_pattern(particles)"
20 Ep ← 0
21 for i ← 0 to nparticlesloc-1 do
22    k ← rank × nparticlesloc + i // k ← i for seq.
23    for j ← k + 1 to nparticles-1 do
24      Ep ← Ep + potential_difference(particles[k], particles[j])
25 Ek ← 0
26 for i ← 0 to nparticlesloc-1 do
27    k ← rank × nparticlesloc + i // k ← i for seq.
28    Ek ← Ek + kinetic_energy(particles[k])
29 TotalEnergy ← Ep + Ek
30 reduce(TotalEnergy, sum, 0)

```

Figure 1 – Pseudocode of the parallelized Simple MD application. Parallelization-specific directives are written in red. Comments are written in blue.

Results

For the experimental evaluation, we ran the serial and parallel versions of the code on up to 6 nodes of the BSC MareNostrum4 supercomputer. Each node comes with 2 Intel Xeon Platinum 8160 sockets (24cores, 2.1GHz each) and 96GB RAM. Nodes are interconnected with a 100 Gb/s Intel Omni-Path technology. We ran 10k iterations (T) on 15k particles (nparticles). The sequential version took more than 5 hours to complete, while the parallel code with 240 processes finished in less than 3 minutes, achieving a maximum speedup of 111. Scaling to more than 5 nodes resulted in an evident performance degradation, meaning that the additional computing power could not compensate for the overhead induced by heavy Allgather communications.

References

[1] Aldinucci M et al., Practical parallelization of scientific applications with OpenMP, OpenACC and MPI, Journal of Parallel and Distributed Computing, Volume 157, 2021, Pages 13-29, ISSN 0743-7315, doi: 10.1016/j.jpdc.2021.05.017.

Acknowledgements

The work has been performed under the Project HPC-EUROPA3 (INFRAIA-2016-1-730897), with the support of the EC Research Innovation Action under the H2020 Programme; in particular, the author gratefully acknowledges the support of Eduardo Quiñones Moreno, from Barcelona Supercomputing Center (BSC), and the computer resources and technical support provided by the BSC.

Native communication support for the PCJ library

Ł. Górski

Interdisciplinary Centre for Mathematical and Computational Modelling, University of Warsaw, Poland

Introduction

PCJ library is Java-based solution that enables parallel programming in the PGAS programming model on the JVM. The library has already been acknowledged by HPC community, receiving HPC Challenge Benchmark Class II Award for Code Productivity in 2014 [1]. It was successfully used to run jobs spanning thousands of computational nodes [2]. Currently, the implementation of its internode communication routines relies on native Java socket-based conduit. The aim of this work was to develop, optimize and test MPI-based conduit for the PCJ library.

Methods

The initial tests (e.g. comparison using the RandomAccess code, which is a communication-intensive workload) have proven that C/MPI-based reference HPC Challenge implementation is better-performant than PCJ-socket based one (cf. fig. 1). Therefore, the aim of this project was to implement MPI-based conduit for Java/PCJ. This work involved test runs that used a number of well-known benchmarks (e.g. FFT, RandomAccess code, parts of HPC Challenge Benchmark suite [1]) as well as microbenchmarking (including the ping-pong test). The benchmarking performed at HLRS was done to assess the performance of various implementations of MPI-based PCJ communication conduit. All the tests were ran using Cray XC 40 (Intel Xeon E5-2680, 128 GB RAM per node).

Results

The tests ran using the more complex benchmarks have proven that the initial implementation of PCJ-MPI communication routine, prepared before the computing time at HLRS was granted, had to be revised. Further work therefore included library micro-benchmarking and the development of various new communication conduit implementations. The best results were achieved using non-blocking MPI communication routines (cf. fig. 2 for ping-pong test results).

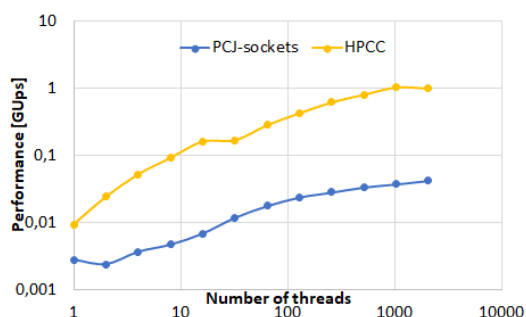


Figure 1 – Socket-based PCJ vs C-MPI code performance as measured by HPCC RandomAccess benchmark; data size was 2²⁷.

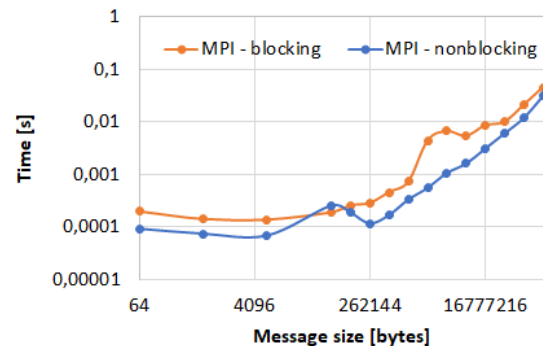


Figure 2 – Performance of two selected PCJ-MPI communication conduit implementations using the ping-pong test

Conclusions

The work funded under HPC-Europa3 scheme allowed to develop a better-performant MPI-based communication conduit for the PCJ library. The solution described herein integrated seamlessly with existing PCJ library API and the client codes do not need to be modified to accommodate this new conduit. MPI-based communication is enabled by passing a switch to JVM (-Dpcj.communication.conduit=mpi), which is typically done when invoking the JVM from the command line.

Further work should involve further communication optimizations, as well as the analysis of new conduit's performance on other systems and using various interconnects. Also, different thread support levels as defined by MPI standard should be taken into account, as the current implementation of MPI-based conduit achieves the best performance using MPI_THREAD_MULTIPLE level, which decreases when using MPI_THREAD_SERIALIZED and MPI_THREAD_FUNNELLED is currently unsupported.

References

- [1] „HPC Challenge Website,” 30 01 2020. [Online]. Available: <https://www.hpchallenge.org/>.
- [2] M. Nowicki, Ł. Górski i P. Bała, „Performance evaluation of parallel computing and big data processing with Java and PCJ library,” In: Cray Users Group, Stockholm, 2018.

Acknowledgements

The work has been performed under the Project HPC-EUROPA3 (INFRAIA-2016-1-730897), with the support of the EC Research Innovation Action under the H2020 Programme; in particular, the author gratefully acknowledges the support of Alexey Cheptsov, HLRS and the computer resources and technical support provided by HLRS.

Enhancing resource management through prediction-based policies¹

A. Navarro², A. Lorenzon³, E. Ayguadé², and V. Beltran³

²Barcelona Supercomputing Center, Barcelona, Spain; ³Federal University of Pampa, Alegrete, Brazil

Introduction

High-performance computing (HPC) systems are widely used to execute applications from many domains, such as financial computing, medical applications, and video and image processing. These systems are usually based on many-/multi-core architectures with heterogeneous memory and computing devices. Often, this implies the existence of complex memory hierarchies and technologies that evolve each year. Hence, application developers need productive and efficient tools to keep pace with the growing power of HPC systems. Task-based programming models have emerged as a promising alternative to develop complex applications on those systems. These models provide high-level abstractions to increase the productivity of application developers, and they rely on runtime systems to cope with system complexity. The main goal of a runtime system is to dynamically schedule application tasks to cores to optimize performance. However, these runtime systems must also cope with application phases with low parallelism that leave some of the cores without any task to execute.

In this work, we propose a novel resource management policy that can simultaneously optimize performance and energy efficiency. Our policy relies on the information provided by our monitoring and prediction framework to dynamically predict the number of cores that are required for each application phase. The main contributions of this work are: (i) the creation of the monitoring and prediction infrastructure, which is capable of making precise workload predictions for task-based programming models; (ii) the design of prediction-based resource managing policies; and (iii) the enhancing of existent resource-sharing policies through predictions.

Methods

The main benefits of our policy are twofold. If we compare our prediction policy to the idle or passive policies defined in the state-of-the-art, a common feature is that they are both highly reactive to changes in the available workload. However, predictions occur at a specific rate. This allows our policy to avoid the overhead of continuously waking and idling threads in fine-grained or irregular applications. This benefit can also be seen as a middle ground between idle and busy policies. The rate at which predictions are inferred

avoids multiple idling and resuming operations which, in the long run, adds up to avoid substantial overhead.

Another primary benefit of our policy is the adaptiveness to the granularity of tasks. Managing resources by only considering the number of ready tasks is enough in some scenarios. Nonetheless, for applications with fine-grained tasks, it would end up utilizing an excessive amount of CPUs for their workload. With the prediction policy this is resolved, as it takes into account the predicted granularity of tasks.

Results

Our evaluation comprises four different implementations: GCC OpenMP, Intel OpenMP, OmpSs-2 using its linear regions dependency system, and OmpSs-2 using its improved discrete dependency system. For the OpenMP implementations, we evaluate all their available thread-waiting policies: active, passive, and a hybrid between both. For the OmpSs-2 counterparts, we evaluate their current resource managing policies, busy and idle, and our prediction policy.

The main results achieved are: (i) We equal -- and sometimes beat -- the performance of state of the art policies that prioritize performance. (ii) Our policies also equal and, in some scenarios, beat the energy efficiency of state of the art policies that prioritize energy efficiency. (iii) Enhancing resource-sharing techniques through predictions simultaneously improves performance and energy efficiency.

Conclusions

We showcase (i) a prediction-based CPU managing policy that maintains performance while improving energy efficiency, and (ii) a prediction-based resource sharing mechanism which enhances both performance and energy efficiency when compared to its predecessor.

Acknowledgements

The work has been performed under the Project HPC-EUROPA3 (INFRAIA-2016-1-730897), with the support of the EC Research Innovation Action under the H2020 Programme; in particular, the author gratefully acknowledges the support of Vicenç Beltran (Dept. Computer Sciences - Runtime systems for parallel programming models) and the computer resources and technical support provided by BSC.

¹ Full paper accepted for publication in the 26th International European Conference on Parallel and Distributed Computing

Efficiently exploiting distributed large many-core systems

M. Maronas¹, M. Bull²

¹Barcelona Supercomputing Center (BSC), Spain; ²Edinburgh Parallel Computing Center (EPCC), United Kingdom

Introduction

Next generation computing systems will be compound by an enormous number of nodes, each of them containing many processors. Moreover, some (or even all) of the nodes may be heterogeneous, combining traditional computing resources with GPUs or many-core processors. This kind of systems challenge non-expert programmers. Scientists will need deep knowledge in hardware/software to adequately exploit the computing resources when writing their applications.

In order to alleviate the abovementioned requirements from non-expert users, an environment formed by a wide variety of tools, libraries and models appeared. At BSC's Programming Models group, we are working on that environment developing different software pieces and models. Two of those are the OmpSs-2 programming model for shared memory environments, built on top of the Mercurium C/C++ and Fortran source-to-source compiler and the Nanos6 runtime library; and the Task-Aware MPI (TAMPI) library.

Methods

The objective of this project is to benchmark OmpSs2+TAMPI applications in order to identify possible bottlenecks and improve them, as well as compare its performance with the state of the art (OpenMP+MPI).

For that purpose, the first step is porting applications to the OmpSs2+TAMPI environment. After that, we must perform a careful analysis to identify bottlenecks. After identifying the bottlenecks, we have to improve the application/environment to obtain the best performance. Finally, it is important to compare the performance with the state of the art.

The analysis of the application includes an exhaustive exploration of all the parameters that may affect the application. Some of those can be number of MPI processes per node, application size, task size, etc.

Results

Up to now, we have ported the HPCCG benchmark from its original implementation using pure MPI and a hybrid version using OpenMP+MPI to OmpSs-2+TAMPI.

Our evaluation shows that our approaches (OSS_TF and OSS_T) are outperforming the pure MPI version (MPI) by far. This can be seen in both Figures 1 and 2. As well, it is competitive with the hybrid OpenMP+MPI (OMP) version in most scenarios, even outperforming it, as shown in Figure 1. However, in scenarios where the whole data set fits in cache,

Figure 1, OpenMP is able to exploit data locality at L2 level, while OmpSs-2 is only able to exploit data locality at L3 level. This fact gives OpenMP+MPI version a boost of performance.

For both figures, there are some cases where MPI does not have a bar because it is not possible to run the experiment with that size for that version.

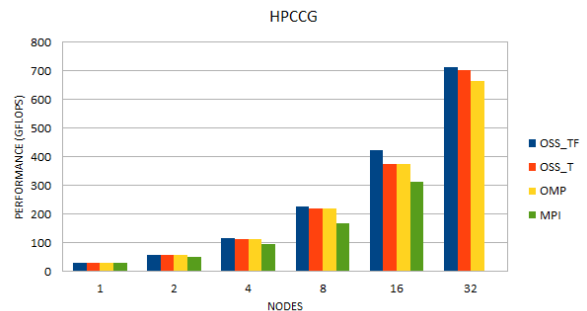


Figure 1 -Scenario where the whole data set does not fit in cache.

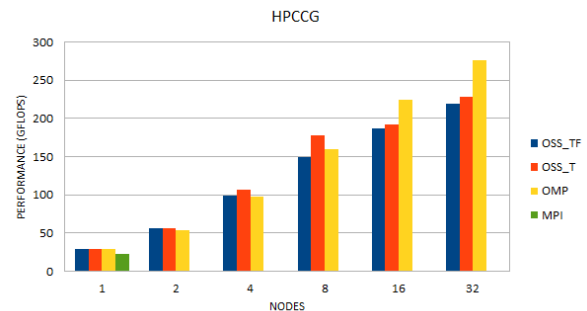


Figure 2 -Scenario where the whole data set fits in cache.

Conclusions

Our evaluation shows that programming models are good options to exploit the resources of huge and complex systems. As well, OmpSs-2+TAMPI are competitive with state-of-the-art alternatives even outperforming them in some scenarios.

Acknowledgements

The work has been performed under the Project HPC-EUROPA3 (INFRAIA-2016-1-730897), with the support of the EC Research Innovation Action under the H2020 Programme; in particular, the author gratefully acknowledges the support Mark Bull and EPCC and the computer resources and technical support provided by EPCC.

Model-based selection of optimal MPI broadcast algorithms for multi-core clusters

E. Nuriyev¹, J.A. Rico-Gallego², A. Lastovetsky¹

¹University College Dublin, Dublin, Ireland; ²University of Extremadura, Caceres, Spain

Introduction

The Message Passing Interface (MPI)[1] offers portable and scalable performance on high performance computing (HPC) platforms. Therefore, it has been dominantly used since its invention in HPC applications. Collective routines involve a group of processes communicating in an isolated context, and those collectives rely on the semantics of collective operations such as broadcast, gather, reduce and so forth. Significant research efforts have been invested in the design and implementation of efficient collective algorithms aimed to improve the performance of collective operations [2]. For example, Open MPI 3.1 [3] employs six different algorithms to implement MPI_Bcast. Unfortunately, there is no single collective algorithm optimal in all situations. Thus, there is a problem of selection of the optimal algorithm for each call of a collective routine, which normally depends on the platform, the number of processes, the message size and so forth.

Methods

Our method can be summarized as follows:

- We propose and implement a new analytical performance modelling approach for MPI collective algorithms, which derives the models from the code implementing the algorithms.
- We propose and implement a novel approach to estimation of the parameters of analytical performance models of MPI collective algorithms, which estimates the parameters separately for each algorithm and includes the modelled collective algorithm in the communication experiment, which is used to estimate the model parameters.

Results

In our collective experiments, we use up to 10 nodes in MareNostrum4. MPI programs use the one-process-per-CPU-core configuration, and the maximal total number of processes is 480 for MareNostrum4. They utilize all CPU-cores in the nodes used in experiments. The default serial mapping of MPI processes to cores is used in all programs. The message segment size, m_s , for segmented broadcast algorithms is set to 8KB and is the same in all experiments. This very segment size is commonly used for segmented broadcast algorithms in Open MPI. Selection of optimal segment size is out of the scope of this paper.

Figure 1 shows the results of our experiments in MareNostrum4 clusters for MPI_Bcast.

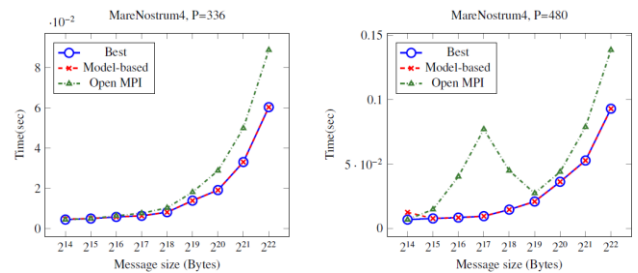


Figure 1 – Present performance of MPI_Bcast on MareNostrum4 cluster. Blue, red and green surfaces present the best performance of MPI_Bcast, model-based estimation and Open MPI decision function respectively.

Conclusions

We proposed a model-based approach to automatic selection of optimal algorithms for the MPI broadcast operation on multi-core clusters, which proved to be both efficient and accurate. We took into account the topology of the communication channels to build performance models. Communication experiments are designed to estimate algorithmic and channel-specific model parameters.

We also developed this approach into a detailed method and applied it to Open MPI 3.1 and its MPI_Bcast operations. We experimentally validated this method on MareNostrum4 cluster and demonstrated its accuracy and efficiency. These results suggest that the proposed approach, based on analytical performance modelling of collective algorithms, provides the solution of the problem of accurate and efficient runtime selection of optimal algorithms for MPI collective operations.

References

- [1] A Message-Passing Interface Standard. <https://www.mpi-forum.org/>
- [2] R. Rabenseifner Rolf, Traff, Jesper Larsson. "More Efficient Reduction Algorithms for Non-Power-of-Two Number of Processors in Message-Passing Parallel Systems". Recent Advances in Parallel Virtual Machine and Message Passing Interface, Springer Berlin Heidelberg, Berlin, Heidelberg, 2004, pp. 36–46.
- [3] <https://www.open-mpi.org/>.

Acknowledgements

The work has been performed under the Project HPC-EUROPA3 (INFRAIA-2016-1-730897), with the support of the EC Research Innovation Action under the H2020 Programme; in particular, the author gratefully acknowledges the support of Computer Systems Engineering and Telematics, University of Extremadura, School of Technology and the computer resources and technical support provided by BSC.

Adversarial risk analysis for obfuscation attacks (extension)

A. Redondo¹, J. Brynielsson²

ICMAT-CSIC, FOI-KTH

Introduction

Obfuscation techniques are used by attackers to create malware hard to detect. These techniques have two main forms: metamorphism and polymorphism [1].

Metamorphism methods used to be more advance obfuscating the code making substitutions, transportations, dead code insertion or register renaming from which the attacker is able to modify the data extracted from the binaries. In this manner, the attacker could perform poison attacks that makes the algorithm learn wrong data or evasion attacks to cause the algorithms misclassification.

Methods

We approach the problem through a framework based on hybrid analysis which combine static and dynamic features extraction from the binaries perceiving their behaviour. The framework combines the extraction of static features such as operation codes, registers, API calls, entropy, files read, written, deleted, copied, moved, recreated, opened, length of file operations among others [2] and the extraction of dynamic features executing malware in a controlled environment Cuckoo Sandbox [3]. Once we have extracted the malware features, we perform poison attacks which affect the training set and evasion attacks tailored to the test set. Then, we make use of Adversarial Risk Analysis for Obfuscation Attacks (AROA) based on [4] to model the adversary behaviour when perform attacks in order to improve the detection accuracy.

Results

We made large scale of experiments using 1000 features extracted from binaries performing poison attacks and evasion attacks. The attacks performed simulates the attacks of a metamorphic engine called metame [5] which used to attack at least 4 features.

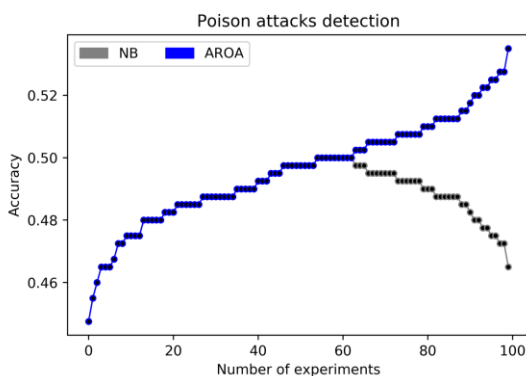


Figure 1 – Accuracy NB vs AROA through poison attacks.

The results obtained detecting poison attacks are shown in Figure 1. The plot describes the accuracy obtained through

the NB algorithm and AROA model in 100 experiments. We note that AROA obtains slightly 9% higher accuracy than NB in this type of attacks.

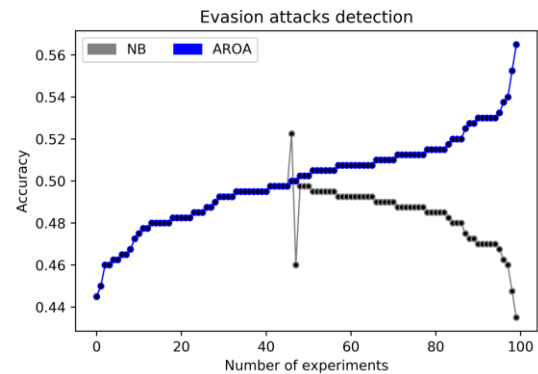


Figure 2 – Accuracy NB vs AROA through evasion attacks.

In the case of detecting evasion attacks, see Figure 2, AROA acquired 12% higher accuracy than NB. We observe that NB shows some fluctuations altering the accuracy with unbalanced results, on the other hand, AROA presents a stable behaviour contributing with the same accuracy in those cases.

Conclusions

We explore the performance between NB and AROA model detecting obfuscated malware when the adversary perform poison and evasion attacks. AROA obtains better results than NB getting 12% higher accuracy in the best case. In addition, AROA presents stable behaviour during the detection process in which NB shows variations in several cases. We think this approach could contribute to progress in the field to detect malware obfuscated.

References

- [1] You, I., & Yim, K. Malware obfuscation techniques: A brief survey. In *Broadband, Wireless Computing, Communication and Applications (BWCCA)*, 297-300, 2010.
- [2] Baldangombo, U., Jambaljav, N., & Horng, S. J. A static malware detection system using data mining methods, 2010.
- [3] Cuckoo Sandbox, <https://cuckoosandbox.org/>,
- [4] Naveiro, R., Redondo, A., Insua, D. R., & Ruggeri, F. (2019). Adversarial classification: An adversarial risk analysis approach. *International Journal of Approximate Reasoning*, 113, 133-148.
- [5] Metame, <https://github.com/aOrtega/metame/>.

Acknowledgements

The work has been performed under the Project HPC-EUROPA3 (INFRAIA-2016-1-730897), with the support of the EC Research Innovation Action under the H2020 Programme. In particular, the author gratefully acknowledges the support of Joel Brynielsson from Department of Theoretical Computer Science, the computer resources and technical support provided by KTH-PDC and Virus Total for providing the corresponding malware files to the study.

Perturbation response scanning and clustering, methods for investigating dynamics of proteins

F. Jalalypour, C. Atilgan

Faculty of Engineering and Natural Sciences, Sabanci University, Istanbul, Turkey

Introduction

Experimental methods such as X-ray crystallography, and nuclear magnetic resonance spectroscopy (NMR) can capture native states of a protein. However, conformations obtained under specified conditions such as modified pH or a variety of salt concentrations are harder to obtain via conventional methods. Subjecting experimental structures to classical molecular dynamics (cMD) simulations may help achieve a biologically relevant conformational ensemble to study the time-resolved characteristics of proteins under various conditions to elucidate the relationship between structure and dynamics. Here, we combined Perturbation Response Scanning (PRS) method with MD simulations to study dynamics of calmodulin (CaM) as a model system under various conditions. PRS provides a valuable source of detailed information including key residues/areas (allosteric sites) and directionality of a transition (collective variable) [1]. Previously, using PRS, we have perturbed the protein structure and selected the corresponding force which results in the response giving the highest overlap to reach a target state [1]. As a new approach, regardless of a target state, PRS responses are classified using a clustering algorithm and cluster centroids are utilized to predict new structures. These structures are then compared to the initial state to identify residues whose perturbation displaced the structure the most. This approach might predict new allosteric sites as well as conformations that cannot be captured via crystallography, NMR and other common methods.

Methods

PRS is a computational technique used to generate the displacement of all residues in a protein as a response to a perturbation inserted at selected locations. PRS is able to identify key residues responsible for the transition between two endpoints [1]. PDB codes 3CLN and 1PRW are selected as open (initial) and closed (target) states, respectively. 400 ns simulations of the open form in physiological (pH=7.4) and acidic (pH=5.5) environments are performed using the NAMD software and subjected to PRS. Protonation state of residues are determined using H++2 and PROPKA web servers [3,4]. The results are compared to previous studies to investigate the reproducibility and repeatability. Additionally, predicted collective variable sets generated by perturbing each residue are clustered sequentially using k-Means algorithm to identify residues with a significant role in the protein displacements and conformational modulations. Finally, highlighted residues are mutated in silico and studied via a separate MD simulation to evaluate their effect on protein dynamics. The scripts have been implemented using the Statistics and Machine Learning Toolbox of MatLab.

Results

PRS highlighted residues 106, 105, 26, 118, and 115 as effective residues in the transition from open to closed form of CaM under physiological conditions. These results are consistent with those from our previous study1. Applying PRS on CaM system in acidic condition highlighted residues 30, 31, 101, and 118 to be effective in the open to closed transition which indicates that protonation modifies the dynamics of protein. Finally, as a new approach,

displacement vectors generated from PRS calculation using the wild type (WT) CaM simulation (pH=7.4) are clustered and centroids are recorded. Each centroid represents the average displacement vector of a residue and is utilized to construct the final structure. Predicted structures are compared to the initial structure by measuring the RMSD. The highest RMSD between predicted and initial structures (PDB code 3CLN) were 4.54 and 4.31 Å obtained by perturbing residues 75 and 42, respectively (Fig 1. B). To evaluate the effect of residue 75, K75A mutated CaM is subjected to an MD simulation. To compare results, RMSD values and Bending-Torsional angles are calculated for each frame of simulation according to ref 1 (Figure 1). Results show that RMSD values are relatively similar for WT type and protonated CaM (Fig1. A). However, protonation altered the position and orientation of the domains, but not the linker shape. Mutated CaM tends to bend and form the structure similar to the closed form (Fig1. C).

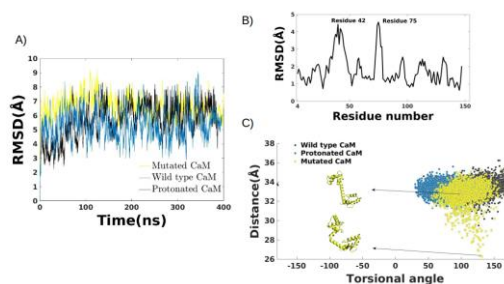


Figure 1 - A) RMSD of WT, protonated, and mutated CaM from the initial state for 400 ns trajectories. B) RMSD values between clustering predicted conformations compared to the initial state. C) bending-torsional angles plotted according to ref 1: WT (black) protonated (blue) and mutated (yellow) CaM.

Conclusions

We have proposed to further develop our methodology to study dynamics of proteins that cannot be captured via crystallography, or not yet detected via NMR and other common methods. The centroids may be considered as predicted B-factors which describe the fluctuation of residues. This approach might also be utilized to predict new solution conformations that have not yet been captured experimentally. Residue 75 is highlighted by new method; it has been reported in several experimental studies [5,6] as a key residue having a significant role in CaM dynamics. Its mechanism of function is not clear yet and will be studied as future work.

References

- [1] Jalalypour et al, Journal of Chemical Theory and Computation, 16(6), 3825-3841, 2020. [2] Gordon et al, Nucleic Acids Research, 33(2), 368-371, 2005. [3] Li et al, Proteins: Structure, Function, and Bioinformatics, 61(4), 704-721, 2005. [4] Olsson et al., Journal of Chemical Theory and Computation, 7(2), 525-537, 2011. [5] Medvedeva et al, Biochimica et Biophysica Acta-Protein Structure and Molecular Enzymology, 1544(1-2), 143-150. 2001. [6] Medvedeva et al, FEBS letters, 450(1-2), 139-143. 1999.

Acknowledgements

The work has been performed under the Project HPC-EUROPA3 (INFRAIA-2016-1-730897), with the support of the EC Research Innovation Action under the H2020 Programme; in particular, the author gratefully acknowledges the support of Aatto Laaksonen, Stockholm University and the computer resources and technical support provided by KTH. We thank Prof. Erik Lindahl for the helpful discussions.

Delineating the role of adaptive immunity in coeliac disease comorbidities, the role of MALT1

T. Katsila¹, C. De La Torre²

¹Institute of Chemical Biology, National Hellenic Research Foundation, Athens, Greece; ²Proteomics Unit, Josep Carreras Leukaemia Research Institute, Barcelona, Spain

Introduction

Coeliac disease is a complex chronic immune-mediated disorder of the small intestine. Nowadays, the information pathobiology of the disease is unclear and makes it difficult to differentially diagnose and/or stratify patients, making evidence-informed clinical decisions. In addition, coeliac disease, as a chronic inflammatory disease (also in its undiagnosed or long-term untreated form), promotes comorbidity with autoimmune diseases and malignant tumours [1].

Focusing on Th1 cell immunity, herein, we mined information from databases and data repositories to define a. a candidate coeliac-disease (severe phenotype) molecular signature, b. candidate coeliac disease comorbidity biomarkers and c. triangulate coeliac-disease comorbidity to viral stimuli. Among the candidate proteins of interest MALT1 was selected to study its protein flexibility using molecular dynamics simulations and explore its plasticity for potential targeting with small molecules.

Methods

A monomer from the crystal structure of MALT1 (PDB ID 6H4A) [2] was used for preparation of the starting model, MD simulations were performed using GROMACS version 2018.5 and the AMBER99SB-ILDN force field. The complex was inserted in a pre-equilibrated box containing water implemented using the TIP3P water model. The MALT1-water system consisted of the protein embedded in a pre-equilibrated box of 10 x 10 x 10 nm with ~90 Na and ~90 Cl ions in a total of ~170,000 atoms (Figure 1A). The system was energy-minimized and subsequently subjected to a 30ns MD equilibration, with an isothermal-isobaric ensemble using isotropic pressure control, and positional restraints on protein and ligand coordinates.

The resulting equilibrated system was replicated 2 times and two independent simulations of 1 μ s were produced at a constant temperature of 300 K, using separate vrescale thermostats for the protein and solvent molecules. A time step of 2 fs was used, and all bonds were constrained using the LINCS algorithm. Lennard-Jones interactions were computed using a cut-off of 10 Å and electrostatic interactions were treated using particle mesh Ewald. Analysis for potential binding cavities on trajectories was performed using trj_cavity [3].

Results & conclusions

Both trajectories of the protein were considerably stable, with a median rmsd value of ~3.5 Å and ~3.3 Å, in relation to the starting conformation. Non-significant fluctuations were observed (Figure 1B), given the fact that the initial conformation comes from a crystallographic structure. The allosteric binding site, as described initially (Quancard et al, 2019) was found to have a reduced size of less than 82% in Å² in 50% of the sampled conformations in the absence of

the cocrystallized ligand. Further analysis using trj_cav in all trajectory snapshots identified two extra potential allosteric sites which appeared in 40% and 36% of all snapshots. These two potential allosteric cavities are currently being investigated to be targeted using virtual screening methodologies in order to identify novel chemical compounds that may bind and interfere with activation of the protein.

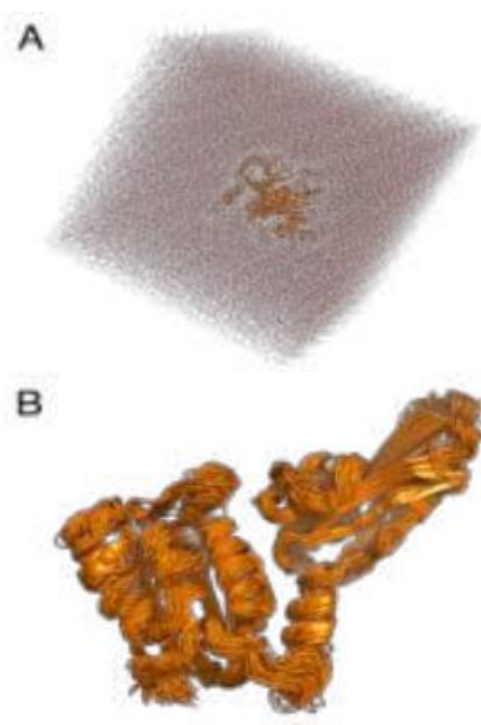


Figure 1 - A) System of the monomer (protein and water box) that was studied, B) Snapshots of the MALT1 backbone of during the MD simulations.

References

- [1] Trynka N et al., Nature Genetics, 43(12):1193, 2011.
- [2] Quancard, J et al., Nat Chem Biol, 15:304, 2019.
- [3] Paramo T et al., J Chem Theory Comput, 10(5):2151, 2014.

Acknowledgements

The work has been performed under the Project HPC-EUROPA3 (INFRAIA-2016-1-730897), with the support of the EC Research Innovation Action under the H2020 Programme; in particular, the author gratefully acknowledges the support of Carolina de la Torre, Proteomics Unit, Josep Carreras Leukaemia Research Institute, 08916 Badalona, Barcelona, Catalonia, Spain and the computer resources and technical support provided by BSC.

The Na, K-ATPase acts upstream of phosphoinositide PI(4,5)P2 facilitating unconventional secretion of fibroblast growth factor 2

C. Legrand¹, R. Saleppico¹, J. Sticht^{2,3}, F. Lolicato^{1,4}, H-M Müller¹, S. Wegehingel¹, E. Dimou¹, J. P. Steringer¹, H. Ewers², I. Vattulainen⁴, C. Freund¹, W. Nickel¹

¹Heidelberg University Biochemistry Center, Germany; ²Institute for Chemistry and Biochemistry, Freie Universität Berlin Germany; ³Core Facility BioSupraMol, Freie Universität Berlin, Germany; ⁴Department of Physics, University of Helsinki, Finland

Introduction

FGF2 is a tumor cell survival factor exported from cells by an ER/Golgi-independent secretory pathway [1]. This unconventional mechanism of protein secretion is based on the direct translocation of FGF2 across the plasma membrane [2,3]. The Na, K-ATPase has previously been shown to play a role in this process. However, the underlying mechanism has remained elusive. Here, we define structural elements critical for a direct physical interaction between FGF2 and the $\alpha 1$ subunit of the Na, K-ATPase. Our findings reveal the Na, K-ATPase as the initial recruitment factor for FGF2 at the inner plasma membrane leaflet required for efficient membrane translocation of FGF2 to cell surfaces.

Methods

Protein-protein global and local docking studies were performed using the Rosetta 2018 package [4]. After the filtering procedure, 33 potential protein-protein energy favourable interfaces were found. These were clustered based on the RMSD value for FGF2 using the Gromos [5] algorithm. To test the stability of the interface between FGF2 and $\alpha 1$ -subCD3, the central structure of all clusters was simulated in three replicates for 200 ns. The atomistic molecular dynamics (MD) simulations were performed using the CHARMM36m [6] force field for lipids and proteins, the CHARMM TIP3P force field for water, and the standard CHARMM36 force field for ions. The GROMACS 2018.3 simulation package [7] was used in all simulations. For FGF2, we used its truncated structure (PDB ID: 1BFF [8]) from residue 26 to 154 in its monomeric form and the modelled version of human $\alpha 1$ -subCD3. The N- and C-terminal groups were modelled as charged residues.

Results

To analyse the protein-protein interface between FGF2 and the cytoplasmic domain of Na, K-ATPase and to evaluate a potential role of K54 and K60 as residues in FGF2 that are in direct contact with $\alpha 1$ -subunit, we conducted both in silico molecular docking studies and atomistic MD simulations. The most representative docked structures of the most significantly populated clusters were refined employing MD simulations as explained in Methods. The ultimate goal of this approach was to find the most stable FGF2/ $\alpha 1$ -subCD3 interface and characterize the network of interactions it involves. The in silico results shown in Fig. 1 suggest the WT1 structure to be the most energetically stable protein-protein interaction surface between FGF2 and $\alpha 1$ -subCD3. It depends on K54 and K60 and is characterized by many electrostatic interactions that are stable throughout the simulations time.

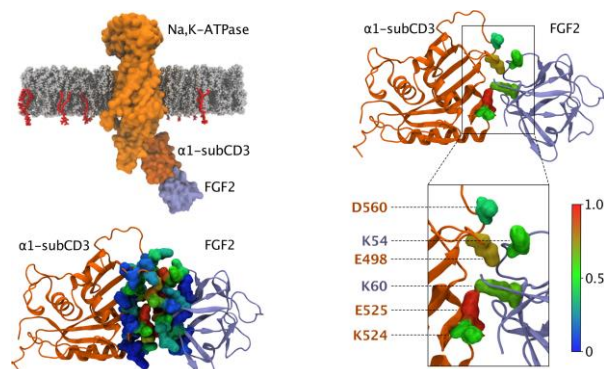


Figure 1 - Characterization of the molecular interface between FGF2 and $\alpha 1$ -subCD3 based on in silico docking studies and atomistic molecular dynamics simulations.

Conclusions

In the current study, we define a sub-domain in the cytoplasmic part of $\alpha 1$ that forms the binding surface for FGF2. Employing a chemical crosslinking approach, we identified a physical 1:1 complex of FGF2 and this minimal $\alpha 1$ domain as the main crosslinking product. Using NMR spectroscopy, we identified two lysine residues (K54 and K60) on the molecular surface of FGF2 that are involved in binding to $\alpha 1$. Using both docking studies and MD simulations, we validated the role of K54 and K60 in a thermodynamically relevant model system. Our findings reveal the Na, K-ATPase as the initial recruitment factor for FGF2 at the inner plasma membrane leaflet required for efficient membrane translocation of FGF2 to cell surfaces.

References

- [1] Dimou, E. et al. *Curr. Biol.* 28, R406–R410, 2018.
- [2] Steringer, J. P., et al., *Semin. Cell Dev. Biol.* 83, 3–7, 2018.
- [3] Steringer, J. P. et al., *Elife* 6, e28985, 2017.
- [4] Gray, J. J. et al., *J. Mol. Biol.* 331, 281–299, 2003.
- [5] Daura, X. et al., *Angew. Chem. Int. Ed. Engl.* 38, 236–240, 1999.
- [6] Huang, J. et al., *Nat. Methods* 14, 71–73, 2017.
- [7] Abraham, M. et al., *SoftwareX* 1, 19–25, 2015.
- [8] Huang, J. et al., *Nat. Methods* 14, 71–73, 2017.
- [9] Kastrup, J. S., et al., *Acta Crystallogr. D Biol. Crystallogr.* 53, 160–168, 1997.

Acknowledgements

The work has been performed under the Project HPC-EUROPA3 (INFRAIA-2016-1-730897), with the support of the EC Research Innovation Action under the H2020 Programme; in particular, the author gratefully acknowledges the support of Prof. Walter Nickel and Heidelberg University Biochemistry Center and the computer resources and technical support provided by HLRS, Stuttgart, Germany.

Dynamic causal model of auditory steady state responses

F. Van De Steen¹, G. Arcara², G. Pellegrino², D. Marinazzo^{1,2}

¹Department of Data Analysis, Ghent University, Belgium; ²IRCSS San Camillo Venice, Italy

Introduction

Steady state evoked responses (induced oscillations in brain rhythms). Among their many applications, relevant to this project are motor research [1], and predictors for successful rehabilitation [2]. Steady state evoked potentials are easy to elicit, and their properties can then be associated to several clinical or cognitive variables, mostly in a frequentist approach. This entails the inherent risk of reverse inference and privileging specificity to sensitivity. Dynamic Causal Modelling (DCM, (Friston, Harrison, and Penny 2003) combines a generative model of brain activity with a Bayesian inference based on the trade-off between accuracy and complexity.

Methods

To study the spectral effects of auditory steady state responses, we will use dynamic causal modelling (DCM) for cross-spectral [3]. As a proof of principle, we looked at the intrinsic connections of auditory A1. In DCM, a biophysical model of how neural populations within and/or between different regions interact is combined with a forward model, which provides a mapping from hidden neural activity to observed measurements. Here, we used the so-called canonical micro circuitry (CMC; [4]) to model neural dynamics. The CMC comprises four neural subpopulations (per modelled region) corresponding to superficial and deep pyramidal cells, spiny stellate cells and inhibitory interneurons. Dynamics and coupling between the neural populations are described by four pairs of ordinary differential equations. Because we used source reconstructed activity of A1, the source was treated as local field potentials (LFP's). The forward model is a simple linear mapping from the hidden states to LFP where it is assumed that the superficial cells contribute the most to the LFP. However, contribution from deep pyramidal cells and spiny stellate cells are allowed by putting prior weights of mean 0 and variance. Group analysis of intrinsic connection was performed using a Hierarchical Bayesian linear model. More specifically, we used the parametric empirical Bayesian (PEB) framework to derive the average posterior distribution of intrinsic connectivity modulations [5]. Once the PEB model was estimated, we used Bayesian model reduction (BMR) combined with a greedy search algorithm and Bayesian model averaging (BMA) to obtain posterior BMA's of intrinsic connectivity parameters. All these models were simulated and inverted on the High Performance Computer platform at CINECA.

Results

The BMA of the intrinsic connectivity modulations are shown in Figure 1, right. We observe three connections in which the 90% Bayesian credible intervals fall outside the group mean of 0. The self-inhibition (sp to sp) of the superficial pyramidal

cells, the inhibitory connections from sp to ss and from ii to ss.

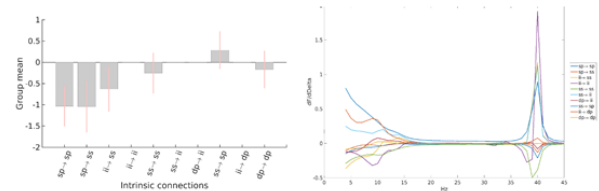


Figure 1 - Left: The Bayesian Model Averages (BMAs) are shown for the 10 intrinsic connectivity modulations. Grey bars denote the posterior mean and pink bars denote the 90% Bayesian credible interval around the mean. Right: sensitivity analysis averaged across subjects for each of the 10 intrinsic connectivity modulators. A clear effect can be seen in the low frequency ranges (5-15Hz) and around the stimulation frequency (40Hz).

Conclusions

Apart from the two most salient characteristics and advantages of DCM (a biophysically inspired model with a robust inference structure), three further aspects are relevant in this context:

- since in MEG and EEG the data are the distribution of electrical activity on the scalp, models with different regions can be compared between them.
- DCM spectral analysis does not separate in specific bands. This is important both theoretically and practically, see the right panel of the figure above, in which modulations are evident also at lower frequencies following a stimulation at 40 Hz.
- DCM also performs a parametrization of the spectra in terms of background aperiodic activity and spectral modulations.

These results open a first avenue for the biophysical modelling of auditory steady state response and the interpretation of their origin and modulation in different pathophysiological conditions.

References

- [1] Pellegrino et al. *Human Brain Mapping* 40 (9) 2736–46. 2019.
- [2] Pellegrino et al. *NeuroImage. Clinical* 24 102092. 2019.
- [3] Moran et al. *NeuroImage* 55 (4): 1694–1708. 2011.
- [4] Bastos et al. *Neuron* 76 (4): 695–711. 2012.
- [5] Friston et al. *NeuroImage* 59 (1): 439–55. 2012.

Acknowledgements

The work has been performed under the Project HPC-EUROPA3 (INFRAIA-2016-1-730897), with the support of the EC Research Innovation Action under the H2020 Programme; in particular, the author gratefully acknowledges the support of San Camillo IRCSS and the computer resources and technical support provided by Cineca.

Modelling Src conformational transitions by means of classical molecular dynamics and essential dynamic sampling

M. Montagna¹, J. Alba², M. D'Abramo²

¹Institute for Materials Science, TU Dresden, Germany; ²Chemistry Department, Sapienza University of Rome, Italy

Introduction

The Src-family protein kinases [1] are a class of enzymes with implications in many crucial processes regulating cell functions such as growth, differentiation and proliferation. Src is formed by a myristoylated SH4 domain which anchors the kinase to the cell membrane the structural SH3 and SH2 domains and the kinase domain (KD), which contains the active site. They play a crucial role catalysing the transfer of a phosphate group from a triphosphate donor to a protein tyrosine residue (phosphorylation) [2]. In this way, they can activate T cell and B cell receptors [3], which are involved in pathologies like cancer and autoimmune diseases.

The Src enzymatic activity is regulated by the switch between two conformations, called open and closed state, with a three-dimensional rearrangement modulated by phosphorylation and interaction with other proteins. A detailed picture of the structural molecular changes involved in Src kinases activation/deactivation mechanism could represent an important achievement in drug design for the therapeutic treatment diseases. Furthermore, a new mutation (E527K) has been recently identified in Src protein, as a possible cause of an immunological disease. In this work, the open and closed state have been characterized in wild type (WT) and mutant proteins in order to identify possible structural significance differences between them.

Methods

We have performed MD simulations using Gromacs soWware and Amber99sb force field. The two proteins, namely Src WT and E527K, were solvated separately in a cubic box. The systems have been initially equilibrated in the NPT ensemble and then evolved in the NVT ensemble, keeping the temperature constant at 300 K. Water molecules were described using the TIP3P model.

The long-range coulomb interactions were treated using Particle Mesh Ewald approach. All the simulations were performed with an integration time step of 2 ps, saving the trajectory each 1000 steps.

Results

The root mean square deviation (RMSD) and the root mean square fluctuation (RMSF), of Src and E527K, have been calculated and compared in order to identify possible structural differences. Concerning the RMSD, the same behaviour has been observed in the open/closed conformations, in case of WT and its mutant. With respect to the RMSF, we have identified a slight reduction of the Kd and SH2 domain residue fluctuations in case of E527K. The principal component analysis (PCA) was performed using the covariance matrix of C-alpha fluctuations as obtained by the simulations, in both the conformational states. By the MD trajectory projections in the essential 2D subspace of the two

main eigenvectors, we are able to discriminate between the open and the closed forms for both the proteins. As expected, the open form is characterized by a greater structural variability, due to the higher mobility of Kd, able to explore a wider region of the essential subspaces (see Fig.1). This behaviour is verified for both the proteins.

Essential dynamic sampling (EDS) has been performed and analysed in the case of WT Src on the two different mechanisms related to the activation (close-toopen) and to the deactivation (open-to-close) pathways.

The results suggest that the activation pathway is mainly driven by the conformational change of the A-loop chain while the deactivation process (open-to-close) is governed by the C-helix rearrangement.

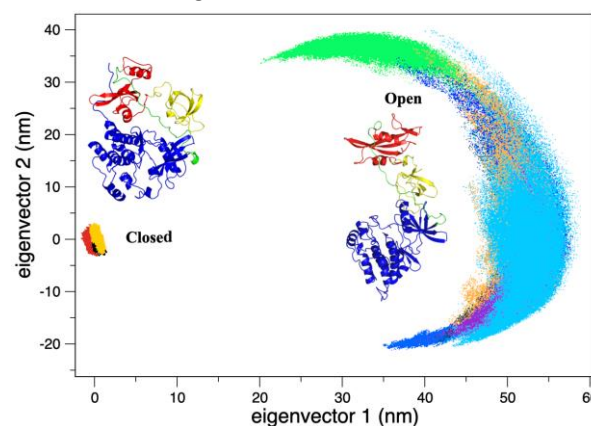


Figure 1 - PCA of the open and closed states for WT.

Conclusions

In this study, we have investigated and characterized the closed and open state of the WT and E527K mutant.

We did not observe significant changes in structural features except a slight reduction of the Kd and SH2 mutant flexibility that we are now investigating in more detail.

References

- [1] Parsons S.J. et al., *Oncogene*, 23(48), 7906-7909 (2004).
- [2] Palacios E.H. et al. *Oncogene*, 23(48), 7990-8000 (2004).
- [3] Nika K. et al., *Immunity*, 32(6), 766-777 (2010).

Acknowledgements

The work has been performed under the Project HPC-EUROPA3 (HPC17XDABL), with the support of the EC Research Innovation Action under the H2020 Programme; in particular, the author gratefully acknowledges the support of Prof. D'Abramo, Chemistry Dept. Univ. La Sapienza (Rome) and the computer resources and technical support provided by CINECA center.

Dynamical clustering of the inferior olive

M. Negrello

Erasmus Medical Center, Rotterdam, The Netherlands

Introduction

Despite being at the core of the brain, and at the core of brain function, not much is known about many of the processing capabilities of the mesencephalic nuclei. In terms of neuro-architecture they are generally simpler than cortices, with fewer cell types and more homogeneous connectivity.

We have undertaken to discover the capabilities of the inferior olivary nucleus of the cerebellum, known to be essential to limb coordination, motor timing and smooth movements via large scale parameter explorations of inferior olive neural network models.

Through dynamical systems modelling and anatomical measurement, we believe to have uncovered fundamental operational potentialities of the inferior olivary nucleus, one of the three main components of the cerebellar system. Due to its cellular properties and arrangement, the inferior olive can transiently store and maintain phase differences in subpopulations of the nucleus, in dynamically organized clusters.

Methods

IO model cells used in this experiment were previously described by De Gruijl et al. (2012). In short, the single model IO cell is composed by a three-compartment HH-type model including axon hillock, soma and dendrites, with a total of 12 ion channels, in addition to Calcium dynamics. The model faithfully reproduces most IO spiking phenomenology, including tuneable oscillations, high threshold plateaus and spikelets for a wide range of parameters. For the paired excitation and inhibition paradigm, post-synaptic potentials were emulated via AMPA and GABA synaptic mechanisms delivered respectively to soma and dendrite. Time course of synaptic activation was tuned to values derived from the literature (GABA: Best and Regehr 2009, AMPA: O'Donnel et al., 2011). In addition, conductance of ion channels for the model cells used in this study were varied to achieve a range

of IO cell behaviours, including robust oscillators, dampened oscillators and non-oscillating cells (De Jeu et al., 2012). The model networks used here are comprised of a topographical grid of 1000 coupled cells, from a reconstruction of the inferior olive, for instance, the rostral portion of the dorsal lamella of the principle olive of the mouse. It is available online at <https://github.com/MRIO/OliveTree>.

Results

The results support our observation that the inferior olive can produce chimera states between its coupled oscillators for a wide range of the parameter space, confirming our predictions and increasing the statistical confidence.

Conclusions

Through a large-scale model of the inferior olive we have uncovered a fundamental principle of operation of this system, namely, multi-scale dynamical clustering. From physics it is known that systems of oscillators with weak coupling and input forcing may produce the so called 'chimera states', when different subsets of oscillators may simultaneously produce coherent or disorganized sets. The phenomenon happens when single coupled oscillators will pledge allegiance to clusters depending on momentary phase-relationships between neighbouring cells. Clusters can thus grow and shrink depending on two properties: phase response to stimulus and strength of coupling.

References

[1] M. Negrello, P. Warnaar, V. Romano, C. B. Owens, S. Lindeman, E. Iavarone, J. K. Spanke, L. W. J. Bosman, and C. I. D. Zeeuw. Quasiperiodic rhythms of the inferior olive. *PLOS Computational Biology*, 15(5):e1006475, 2019.

BCPNN for text prediction

V. Skorniakov

Vilnius University, Faculty of Mathematics and Informatics, Institute of applied mathematics, Lithuania

Introduction

Though there are prevailing theoretical models of memory based on the possible hypothetical structure of human brain cortex [1], a lot remains to be done on the level devoted to mathematical simulative counterparts resembling known stylized facts and allowing to gain more insight into the human brain functioning (HBF) phenomena.

During my visit, I have worked on the text prediction task and took initial steps towards investigation of the performance of the Bayesian confidence propagation neural network (BCPNN) model previously developed by my host and co-authors (e. g., [2] and references therein) and successfully applied for many other HBF related investigations.

Methods

I had an opportunity to make use of an existing c++ code developed by the host and designed to train BCPNN to predict one letter ahead given fixed length window of preceding letters. My method of investigation was to perform a greedy search over parameter space defining BCPNN and to investigate changes of BCPNN's prediction accuracy in response to variation of these parameters. The set of varying parameters included: i) the size of training set; ii) the size of preceding letters' window; iii) the number of training epochs used to train BCPNN.

Results

Main observations gained during analysis were as follows.

- In most cases, keeping other parameters fixed, training (trAcc) and testing (teAcc) accuracies decreased when window size increased (fig. 1, upper panel). The decrease of both usually resembled linear pattern with the same slope and different intercepts with that of teAcc being smaller.
- Number of training epochs had least impact and, with other parameters fixed, usually did not result in significant fluctuations neither of trAcc, nor of teAcc.
- As expected, increasing number of training patterns resulted in increasing accuracies. However, though the "saturation" pattern seen in fig. 1 (lower panel) remained quite similar in most cases, it is notable that both trAcc and teAcc deflated with an increase of window size which coincides with findings stated in a).

Conclusions

On the conceptual level, presented findings reflect HBF: though longer learning improves memorizing, too large patterns are more difficult to store in memory. Keeping in mind biologically plausible structure of BCPNN, they show it being a prominent tool for modelling HBF mentioned in the

introduction and support further investigations in that direction.

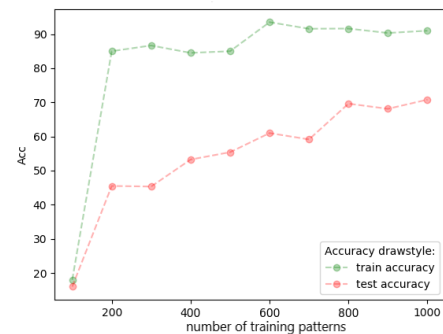
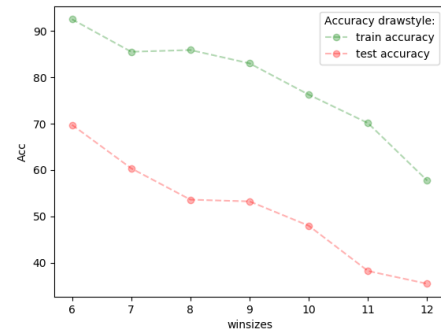


Figure 1 - Top: number of training patterns 800; bottom: window size 6.

References

- [1] Lansner, Anders. "Associative Memory Models: From the Cell-Assembly Theory to Biophysically Detailed Cortex Simulations." *Trends in Neurosciences*, vol. 32, no. 3, Mar. 2009, pp. 178–86.
- [2] Sandberg, A., et al. "A Working Memory Model Based on Fast Hebbian Learning." *Network: Computation in Neural Systems*, vol. 14, no. 4, Jan. 2003, pp. 789–802.

Acknowledgements

The work has been performed under the Project HPC-EUROPA3 (INFRAIA-2016-1-730897), with the support of the EC Research Innovation Action under the H2020 Programme. I gratefully acknowledge KTH PDC centre for providing the computer resources and technical support. My special thanks go to my host Anders Lansner from KTH Royal Institute of Technology, Division of computational science and technology for his careful supervision, advices, and ability to use redundant computational resources for statistical task which I plan to acknowledge in my forthcoming work. I also would like to thank Anders' department colleague Pawel Herman.

Investigating the dynamical steps of arrestin-GPCR pre-complex formation & sharing and analysing MDs of GPCRs at GPCRmd

J.K.S. Tiemann¹, T.M. Stępniewski², M. Torrens-Fontanals², P.W. Hildebrand¹, J. Selent²

¹University Leipzig, Leipzig, German; ²Pompeu Fabra University-Hospital del Mar Medical Research Institute (IMIM), Barcelona, Spain

Introduction

G protein-coupled receptors (GPCRs) are pharmacologically highly relevant transmembrane receptors. Although they bind a high variety of extracellular molecules, ligands or peptides, only a few proteins couple intracellularly for further signal transduction. One of those transducer proteins is arrestin, which plays, beyond its major function of receptor desensitization, an important role in cancer treatment, immune system-related diseases, or the central nervous/cardiovascular system. Therefore, understanding the initial engagement of arrestin to GPCRs is of major interest.

So far, the dynamic transition from initial arrestin-receptor interactions to a pre-complex and finally the high-affinity complex is only partly understood [1-2]. To transit from pre-complex to high-affinity complex, major structural changes have to occur. These changes happen in a dynamic equilibrium and are so far not possible to observe step wise using experimental techniques. Molecular Dynamics (MD) simulations provide a unique opportunity to investigate those dynamic processes. Here, we aim to study the initial encounter between visual arrestin and the GPCR Rhodopsin and thereby enlighten the sparse knowledge about the dynamics of this transient intermediate process.

MD simulations provide a powerful technique to investigate such dynamic processes, which is also reflected in the rising number of easy-usable setup and analysis tools.

Nevertheless, MDs are expensive and complex, containing information beyond the scope of most studies. Yet, MD trajectories are rarely shared in a dynamic way, reducing the benefits like re-usage and a better understanding of dynamic processes [3-4]. A second aim of this study was to foster the development of GPCRmd, an online platform to visualize, analyze and share GPCR MD data.

Methods

MD simulations is a widely established technique to investigate the function of proteins in the 4D space. Due to recent technological advances, it is now possible to simulate huge systems for longer timescales (μ s-ms) with increased speed and accuracy. Classical MD and adapted sampling was used in this study to sample the conformational space of arrestin and rhodopsin and further to evaluate docking poses.

Besides, until recently it was not possible to visually share MD trajectories and their dynamics in an easy, interoperable and intuitive way. In order to make GPCR MD simulations available, understandable and intuitively usable by everyone, MDsrv was integrated for visual streaming of simulations [5].

Results

The performed (solo/peptide) MD simulations demonstrate an increased flexibility beyond the ionic lock of arrestin C-tail when the phosphorylated rhodopsin C-tail is present. Additional simulations designed to understand how arrestin approaches Rhodopsin did not yet reveal a clear pattern.

Also, we present the GPCRmd, the first user-friendly, intuitive and comprehensive platform of GPCR MD simulations, now available at <http://www.gpcrmd.org> and as a preprint at [6].

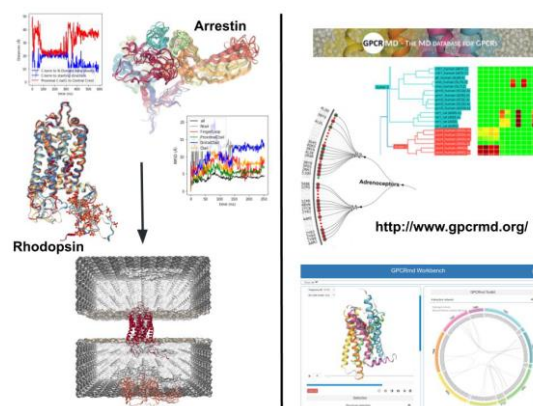


Figure 1 - (Left) Collective variables and observed dynamics of arrestin (right top) and rhodopsin (middle left) were obtained, analyzed, and clustered to generate an initial complex system (center, down). (Right) Snapshots of GPCRmd showing receptor-dynamic comparison, an interactive search-tree and the workbench.

Conclusions

The increased flexibility of Arrestin C-tail, which has previously not been observed in computational and experimental studies, provides new insights and hypothesis into pre-complex formation. Additional simulations are currently carried out to ensure coverage of the obtained observations. With regard to the complex simulations, no well-defined states have been detected rather an interconversion of substates, suggesting that longer simulations or different approaches are required. Making MD simulations available in a comprehensive and intuitive manner allows researchers despite their background knowledge all over the world to explore the functional dynamics of proteins [4]. By providing such a database, we hope to reduce redundancy, increase re-usage and a better understanding of protein dynamics.

References

- [1] Lally, C. C. M., et al., Nature Communications, 8: 14258, 2017.
- [2] Latorraca, N. R., et al., Nature, 557(7705): 452–456, 2018.
- [3] Abraham, M. et al., J. Chem. Inf. Model, 59 (10): 4093-9, 2019.
- [4] Hildebrand P. W., et al. Trends Biochem Sci, 44(11): 902-13, 2019.
- [5] Tiemann, J. K. S., et al., Nature Methods, 14(12): 1123-4, 2017.
- [6] Rodríguez-Espigares, I, et al. bioRxiv, 839597: 2019.

Acknowledgements

The work has been advanced under the Project HPC-EUROPA3 (INFRAIA-2016-1-730897), with the support of the EC Research Innovation Action under the H2020 Programme; in particular, the author gratefully acknowledges the support of Jana Selent at Pompeu Fabra University and the computer resources and technical support provided by BSC. We acknowledge funding and resources by the Deutsche Forschungsgemeinschaft (Sfb740/B6) and the GCS Supercomputer SuperMUC at Leibniz Supercomputing Centre.

Understanding the structural and electronic properties of photoactive tungsten oxide (WO₃) nanoparticles from DFT and GW approaches

V. Díez-Cabanes¹, Á. Morales-García², F. Illas², M. Pastore¹

¹Université de Lorraine & CNRS, Laboratoire de Physique et Chimie Théoriques (LPCT), Nancy, France; ²Departament de Ciència de Materials i Química Física & Institut de Química Teòrica i Computacional (IQTCUB), Universitat de Barcelona, Barcelona, Spain

Introduction

Tungsten trioxide (WO₃) derived nanostructures have emerged recently as feasible semiconductors for photocatalytic purposes due to their visible light harvesting that overcomes the drawbacks presented by TiO₂ derived nanoparticles (NPs). However, applications are still limited by the lack of fundamental knowledge at nanoscale due to the poor knowledge of the physical processes that affect to their photoactivity. In this context, theoretical modelling can provide reliable structure-property relationships by considering NPs with different phases and morphologies and by employing high accurate and unbiased methods such as the GW formalism,[1] thus paving the way to establish relevant rules for the design of photoactive WO₃ nanostructures.

Methods

Our set of studied nanostructures comprises NPs sizing from ~0.4 to ~5 nm (containing up to 1680 atoms), well representing the size range of the smallest synthesized NPs found in the literature, exhibiting cubic, rectangular, octahedral, spherical, hexagonal nanosheet and cuboid nanowires morphologies (see Figure 1); which were generated by considering the bulk phases with their experimentally determined preferential exposed facets. The electronic properties of the obtained NPs were estimated at the Density Functional Theory (DFT) and GW levels of theory by using an all-electron basis set and including relativistic effects, as it is implemented in the FHI-AIMS program package [2].

Results

The first addressed issue was the relative stability for the different NP morphologies as the size of the NP increases. We found that cubic/nanosheet NPs are energetically favoured for medium and large size monoclinic/hexagonal phase NPs, while, for small NPs ($n < 50/125$), rectangular/nanowire NPs displayed a larger stability. In all the cases the NPs energies reached an asymptotic dependency with their size for a few hundred of units. Then, we investigated their optoelectronic properties, showing that the proper description of the ionization potentials/electron affinities (IPs/EAs) can be achieved only through a GW approach. Afterwards, for a representative subset of NPs, a linear correlation emerges between DFT and GW calculated values of IP/EA indicating that the error in the DFT energies is systematic. Next, by making use of these correlations we were able to obtain electron IP/EA energies of GW quality for all the set of NPs studied in this work. The high localization of the highest occupied levels on few oxygen atoms of the NP was found to be at the origin of the almost independent behaviour of the

IP energies with respect the size and morphology of the NP. On the other hand, a large delocalization over the whole NP of the LUMO on the 5d W orbitals induced a large dependence of EAs upon size and morphology, with a sizeable drop in magnitudes when moving to small NP sizes ($n < 100$).

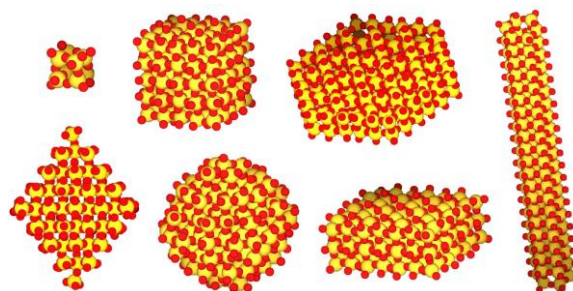


Figure 1 - cubic (WO₃)₈ and (WO₃)₁₂₅, hexagonal nanosheet (WO₃)₁₄₇ and nanowire (WO₃)₁₂₆, octahedral (WO₃)₁₂₉, spherical (WO₃)₁₄₇ and rectangular (WO₃)₁₄₇ NPs (from the top left to the bottom right).

Conclusions

In this work we have established a solid theoretical protocol, based on combining DFT and state-of-the-art GW calculations to investigate the intertwined role played by the size and morphology of realistic WO₃ NPs on the relevant optoelectronic properties which drive its photocatalytic behavior. The present results indicate that the photocatalytic efficiency of WO₃ nanostructures for water oxidation can be substantially improved by quantum confinement effects when moving towards nanocrystals with a range of $100 < n < 150$ units of WO₃ and choosing the proper morphology.

References

- [1] Reining L Wiley Interdiscip. Rev. Comput. Mol. Sci., 8(3):1–26, 2018.
- [2] Blum V et al., Comput. Phys. Commun., 180(11):2175–2196, 2009.

Acknowledgements

The work has been performed under the Project HPC-EUROPA3 (INFRAIA-2016-1-730897), with the support of the EC Research Innovation Action under the H2020 Programme; in particular, the author gratefully acknowledges the support of the IQTCUB and the computer resources and technical support provided by the Barcelona Supercomputing Centre (BSC).

DFT study of a relaxed amino acid, glutamine, on TiO₂ surfaces

D. Jovanović^{1,2}, J.C. Schön³, J. Zagorac^{1,4}, A. Zarubica², D. Zagorac^{1,4}, B. Matović^{1,4}

¹Institute of Nuclear Sciences Vinča, Materials Science Laboratory, University of Belgrade, Serbia; ²Faculty of Science and Mathematics, Department of Chemistry, University of Niš, Serbia; ³Max Planck Institute for Solid State Research, Stuttgart, Germany; ⁴Center for Synthesis, Processing and Characterization of Materials for Application in the Extreme Conditions-CextremeLab, Belgrade, Serbia

Introduction

Linking inorganic systems with organic ones is a highly important avenue for finding new drugs and treatment methods. Several amino acids have roles in supporting cancer growth, and one of the inorganic materials that can show antitumor properties is titanium dioxide. [1] Doping TiO₂ enhanced interactions with biological systems: Cu / Ag / Au doped TiO₂ particles showed toxic effects on cervical cancer cell lines [2], and on human colon carcinoma [3]. Adding nanoparticles of silver improves the pathophysiological effects of photocatalytic systems, and similarly, the cytotoxic activity of Cu dopant in TiO₂ results in a high bactericidal activity even under very weak UV light.[4] Recent studies have shown that tumour cells have altered metabolic pathways involving glutamine which were recently identified as alternatives to glucose for fuelling the tricarboxylic acid (TCA) cycle in cancer cells [5], thus in this study we choose to investigate interactions between Glutamine (L) molecule and anatase (TiO₂ modification) undoped and doped surfaces.

Methods

We first locally optimized 2D slab structures of undoped and doped anatase 001 and 101 surfaces, then similarly optimized a single molecule of glutamine in vacuum. Next, we placed the pre-optimized glutamine molecule in various orientations (rotations of 0°, 90° and 180° relative to the previous position of a molecule) to the central position onto the relaxed substrate surfaces 3 × 3 supercell slabs), and then performed ab initio relaxations of the molecule on the substrate slabs. We employed the DFT method with exchange correlation LDA with a Perdew-Zunger correlation functional (CRYSTAL 17 code) and a GGA-PBE functional, as implemented in the Quantum Espresso code.

Results

The results suggest that the particular conformation of a Glutamine (L) molecule on pristine anatase slab 001 and 101 surfaces shows a noticeable deformation due to the interaction between the molecule and the slab contributing to the total energy of the system, for both types of surfaces (Figures 1). However, the same conformation of the Glutamine molecule did not show such a deformation when interacting with a Au doped 001 anatase surface (Figure 2).

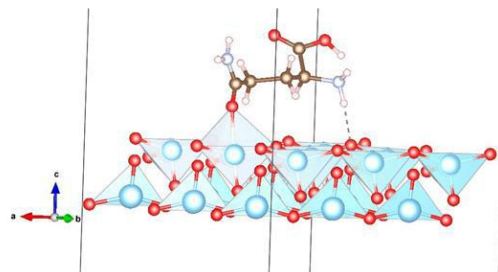


Figure 1 - An interaction of Glutamine (L) molecule and relaxed pristine anatase slab surface 101 after.

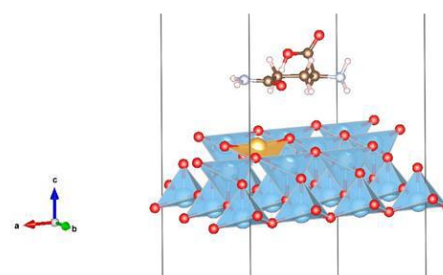


Figure 2 - An interaction of Glutamine (L) molecule on Au doped anatase slab surface 001.

Conclusions

Comparison of the optimized conformations, electronic structure and properties of the amino acid in vacuum and on the surface, yield useful insights into various biological processes. In the future we will investigate potential significant interactions with other Glutamine (L) conformations and with another substrate dopants.

References

- [1] Hamadani M et al., *Mat. Sci. Semicond. Proc.*, 41:168–176, 2016.
- [2] Garg A et al., *New J. Chem.*, 41:9931–9937, 2017.
- [3] Xu J et al., *Int. J. Photoenergy*, 2007:ID 97308, 2007.
- [4] Skorb EV et al., *Appl.Catal. B.*, 84:94–99, 2008.
- [5] DeBerardinis RJ et al., *Cell Metab.*, 7:11–20, 2008.

Acknowledgements

The work has been performed under the Project HPC-EUROPA3 (INFRAIA-2016-1-730897), with the support of the EC Research Innovation Action under the H2020 Programme; in particular, the author gratefully acknowledges the support of Prof. Christian Schön, Nanoscale Science Department, Max Planck Institute for Solid State Research, Stuttgart, Germany and the computer resources and technical support provided by HLRS.

Multiscale modelling of gas separation with poly(2,6-dimethyl-1,4-phenylene oxide) (PPO)

E. Ricci¹, N. Vergadou²

¹Department of Civil, Chemical, Environmental and Materials Engineering, University of Bologna, Italy; ²Institute of Nanoscience and Nanotechnology, NCSR Demokritos, Athens, Greece

Introduction

In this project, a coarse-graining strategy was applied for the efficient generation of molecular models of a polymeric membrane material: poly(2,6-dimethyl-1,4-phenylene oxide) (PPO), which is a promising candidate for hydrogen recovery and natural gas treatment.

Methods

Molecular models of polymeric structures with high molecular weight (M_w), cannot be sufficiently equilibrated through Molecular Dynamics (MD) simulations at the atomistic level. To overcome this limitation a coarse-grained (CG) representation is adopted,^[1] in which the repeating unit of PPO is mapped to 4 CG beads (Figure 1a). The interactions of the coarse-grained moieties are described through an optimized force field, based on the properties of the underlying atomistic representation [1].

Atomistic packing model, consisting of 36 chains of 30 repeating units, was generated using the Rotational Isomeric State model, as modified by Theodorou and Suter [2], and mapped to the CG representation using the VMD software [3] (Figure 1b). MD simulations at the CG level were carried out in the NPT and NVT ensembles at 600 K. All-atom (AA) simulations were carried out at the same conditions, using the pcff force field, in order to compare the results obtained with the CG representation and assess their accuracy. Thermodynamic and structural properties, such as chain dimensions, torsion angles distributions, and radial distribution functions (RDF) were evaluated.

Results

The specific volume of the CG system was 0.99 cm³/g, very close the atomistic value of 0.98 cm³/g. The chain dimensions at the CG level were in good agreement with the AA ones: the average radius of gyration of the CG chains was 15.6 ± 3.0 Å, while for the AA ones it was 14.7 ± 2.5 Å. Very good agreement was observed also in the position of the peaks in the RDF. The CG RDF showed slightly less sharp feature than the corresponding AA one. Torsion angle distributions were matched.

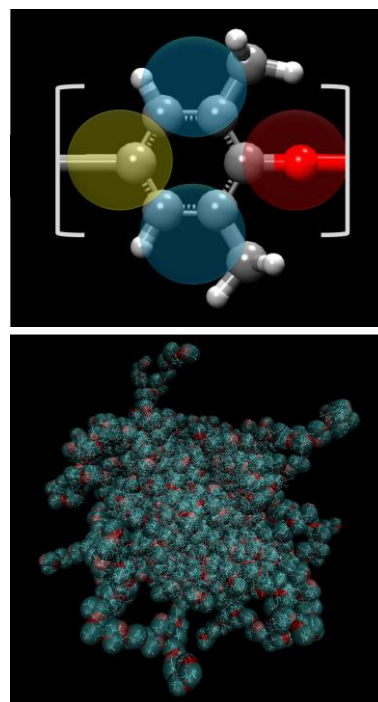


Figure 1 - (a) Mapping scheme for PPO. (b) Simulation box mapped to the CG representation.

Conclusions

The CG model adopted allowed halving the simulation times, while retaining good accuracy in the representation of the structural features of the polymer. This model constitutes a promising strategy for the efficient equilibration of PPO polymer chains, which can be subsequently back-mapped to the atomistic level for the modelling of gas-polymer properties.

References

- [1] Wang, H. et al., *Mol. Simul.*, 42:312-320, 2016.
- [2] Theodorou D.N. et al., *Macromolecules*, 19:139-154, 1986.
- [3] Humphrey, W., et al. *J. Molec. Graphics*, 14:33-38, 1996.

Acknowledgements

The work has been performed under the Project HPC-EUROPA3 (INFRAIA-2016-1-730897), with the support of the EC Research Innovation Action under the H2020 Programme; in particular, Eleonora Ricci gratefully acknowledges the support of Niki Vergadou of the NCSR Demokritos and the computer resources and technical support provided by GRNET.

Structure and energetics of dye-sensitized NiO interfaces in water from ab-initio MD and GW calculations

A. Segalina¹, S. Lebegue¹, D. Rocca¹, S. Piccinin² and M. Pastore¹

¹Université de Lorraine & CNRS, LPCT, Nancy, France; ²CNR-IOM DEMOCRITOS SISSA, Trieste, Italy

Introduction

P-type dye-sensitized solar cells (DSCs) offer the possibility to directly convert sunlight into electrical energy at a low cost. However, these devices have rather poor power conversion efficiencies (~2.5%) compared to the n-type DSCs (~14%) for reasons that are not yet clarified (slow hole injection, fast back recombination pathways). P-type DSCs are based on the hole injection from the HOMO of the photoexcited dye (e.g. C343) into the valence band of a semiconductor (e.g. NiO) and the driving force (the difference between the VB energy and the HOMO energy) has a key role on the overall efficiency of the DSCs. As far as dye-sensitized NiO is concerned, relatively few computational works, based on density functional theory (DFT) calculations, have been reported [1-2]. A common outcome of these studies is that the interfacial energetics, dictating the driving force for hole injection from the dye to the NiO VB, turns out to be extremely sensitive to the dye anchoring mode and solvation effects [1-2]. In this framework, we carry out a theoretical characterization of the C343-sensitized NiO surface in water, by combining ab-initio molecular dynamics (MD) simulations with GW calculations along the MD trajectory, to reliably describe the structure and energetics of the interface when explicit solvation and finite temperature effects are accounted for.

Methods

To build the surface slab, we cleaved the bulk structure along the (100) direction and we considered 6 layers in a (2×2) supercell. For the dye we considered the original C343 molecule, bearing the carboxylic acid as anchoring group. DFT calculations have been performed using the PBE exchange and correlation functional and adding a Hubbard term on the Ni(d) states ($U=4.6$ eV). DFT (PBE+U) and GW ($G_0W_0@PBE+U$) calculations were performed with the Vienna ab initio simulation package (VASP) using the pseudopotentials constructed by the projector augmented wave (PAW) method and a plane waves basis set. We used a plane-wave cut-off of 650 eV and the Brillouin zone was sampled at the Γ -point. Regarding the GW calculations, the cut-off for the dielectric function was set at 200 eV. MD simulations of the C343@NiO(100) interface in explicit water were performed with the CP2K code using GTH norm conserving pseudopotentials, MOLOPT-DZVP-SR basis set, 500 Ry cut-off for charge density and sampling the Brillouin zone at the Γ -point. The MD simulations have been carried out using the PBE+U approach in combination with Grimme's van der Waals corrections. The simulation box, having dimensions $8.35 \times 8.35 \times 33.40 \text{ \AA}^3$, consists of the C343@NiO interface and 42 water molecules. The MD run was conducted in the NVT ensemble for 30 ps by imposing the temperature to 360 K through the canonical sampling velocity rescaling thermostat.

After equilibration (the first 3 ps of the MD simulation) we extracted 20 configurations equally spaced in time, to perform single point PBE+U and $G_0W_0@PBE+U$ calculations with the same set up discussed above.

Results

The time evolution of the calculated driving force is plotted in Figure 1. We find that the driving force for hole injection is always significantly larger at GW level (average value of 0.62 ± 28 eV) compared to the values obtained with PBE+U (average value of 0.36 ± 0.32 eV) and in quantitative agreement with the experimental estimation in the range 0.6-1.0 eV [3-4]. More in detail, the GW driving force is always positive, i.e. favourable for hole injection and oscillates between 1 eV and 0.1 eV. To conclude, GW calculations coupled to AIMD simulations in explicit solvent, are capable to deliver, in quantitative agreement with experiments, the interfacial energy-level alignment required for the functioning of p-type photocathodes.

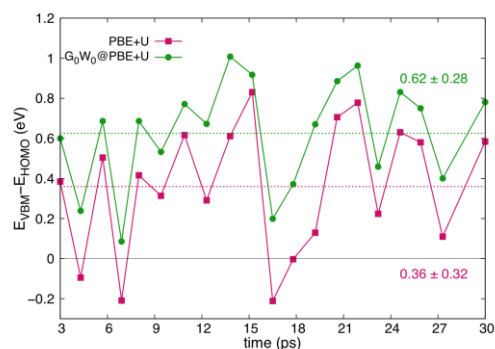


Figure 1 - Calculated differences between the VBM of the NiO and the HOMO of the Dye along the MD production run in eV considering both the PBE+U and the $G_0W_0@PBE+U$ methods.

References

- [1] Piccinin, S. et al. J. Phys. Chem. C 2017, 121, 22286–22294. [2] Pavone, M. et al. Phys. Chem. Chem. Phys. 2015, 17, 12238–12246. [3] Mori, S. et al. J. Phys. Chem. C 2008, 112, 16134–16139. [4] Morandeira, A. et al. J. Phys. Chem. B 2005, 109, 19403–19410.

Acknowledgements

The work has been performed under the Project HPC-EUROPA3 (INFRAIA-2016-1-730897), with the support of the EC Research Innovation Action under the H2020 Programme; in particular, the author gratefully acknowledges the support of Simone Piccinin of CNR-IOM DEMOCRITOS & SISSA and the computer resources and technical support provided by CINECA.

Molecular dynamics simulations of graphene oxide-based nanocomposites targeted for the removal of water pollutants

I. Tanis¹, K. Karatasos²

¹CEA, DAM, DIF, Arpajon 91297, France; ²Aristotle University of Thessaloniki, Department of Chemical Engineering, Greece

Introduction

Given the continuous growing world population together with the greater energy needs, addressing the lack of water is one of the most important challenges of our time [1]. Among different water treatment methodologies, membrane-based separation techniques have a key role in water purification and desalination due to their low energy consumption, the simplicity of their operating conditions and their environmental friendliness. According to pertinent studies, porous membranes constructed by graphene oxide (GO) sheets appear as appealing candidates for the production of molecular sieving membranes for desalination and water purification [2]. The performance of GO membranes can be further improved by properly spacing and bonding the GO nanosheets through the inclusion of different-sized linkers such as linear or hyperbranched polymers, such as poly(ethylene imine) (PEI). Motivated by the aforementioned studies, the purpose of the present collaboration is to examine by MD simulations aqueous dispersions of PEI-GO nanocomposites, targeted for the removal of methylene blue (MB), a water soluble organic dye, from water.

Methods

To examine the effect of the presence of PEI on the adsorption capacity of the GO sheets, molecular models of GO with or without the presence of HBP, were prepared. The latter was either chemically attached to the GO surface or dispersed in GO sheets. In order to allow for a reasonable degree of interdiffusion between the two components of the mixture, we considered GO-based nanocomposites with a number of PEI molecules per GO, chosen to allow a desired coverage of the surface of the latter. In total, three atomistic models were created, the average size of each amounted to about 300000 atoms. Molecular dynamics simulations were conducted at a temperature of 300K. All simulations were performed via the NAMD simulation package [3]. By the aid of the allocation of 200000 CPU hours in the GRNET cluster (Athens), production runs of at least 300ns for all systems, were produced. By monitoring the average GO-PEI, PEI-PEI, MB-MB, GO-MB, PEI-MB and GO-PEI distances, it was found that a timescale of maximum 80 ns was sufficient for the systems to reach equilibrium.

Results

Preliminary analysis based on the calculation of radial distribution functions between GO-MB centers of mass together with the calculation of the distribution of dye molecules along the axis perpendicular to GO plane, demonstrates an affinity between GO and MB. Further analysis of thermodynamic properties allowed for the

calculation of the free energies of binding between the nanocomposites and MB via the MM-PBSA method. Results revealed a higher affinity between GO and MB in the case of pure GO with respect to their GO-PEI counterparts. Analogous behaviour is extracted by the aid of the calculation of the potential of mean force (PMF) between GO and MB. The latter was extracted through the corresponding radial distribution functions.

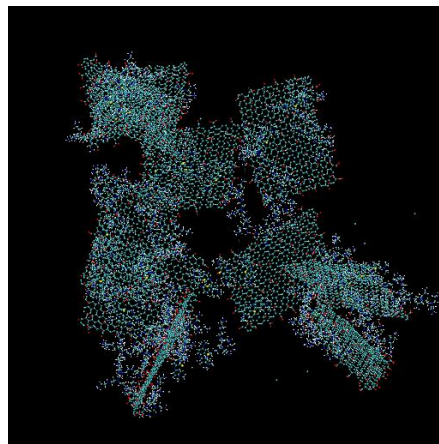


Figure 1 - Equilibrated configuration of a GO-based nanocomposite loaded with MB. Water molecules are omitted for clarity.

Conclusions

The outcome of this study can open the way for the examination of further factors affecting the performance of such systems, as, for example, the size and the concentration of the polymer component. In addition, this work can be beneficial for the design of analogous systems targeted for both water purification and desalination operations. Finally, the outcome of this study will be the subject of a manuscript that is about to be submitted for publication shortly.

References

- [1] Werber, J. R. et al, *Nature Rev. Materials*, 1, 16018, 2016.
- [2] Goh, P.S. et al, *Desalination* 356, 115, 2015.
- [3] Phillips J.C. et al, *J. Chem. Phys.*, 153, 044130, 2020.

Acknowledgements

The work has been performed under the Project HPC-EUROPA3 (INFRAIA-2016-1-730897), with the support of the EC Research Innovation Action under the H2020 Programme; in particular, the author gratefully acknowledges the support of Kostas Karatasos, (Dept. of Chemical Engineering, Aristotle University of Thessaloniki, Greece) and the computer resources and technical support provided by ARIS cluster (GRNET center, Athens).

An efficient parallel code for solving fractional partial differential equations in complex geometries

J.A. Acebrón¹, G. Pagnini²

¹*Department of Information Science and Technology, ISCTE - University Institute of Lisbon, Portugal;* ²*Basque Center for Applied Mathematics (BCAM), Bilbao (Spain)*

Introduction

In these days, there is a renewed interest in Fractional partial differential equations (fPDEs). Relevant applications in Science and engineering include, for instance, control, biological tissues, materials for civil engineering, neurosciences, complex (heterogeneous and random) media, plasma physics, seismology and, earthquakes modelling.

While solving purely initial-value problems seems to be to some extent tractable, the case of boundary/value problems on a smooth bounded domain $\Omega \subset \mathbb{R}^n$ is quite different, and it was observed that the results depend strongly on the definition of the fractional derivative used so far [1]. One of the most important differences among these variety of fractional derivatives are in the type of boundary data.

Essentially there are of two types: Those nonlocal boundary conditions (also called extended boundary conditions) which are imposed on the complement Ω^c of the domain, and the local boundary conditions which are given only on $\partial\Omega$. The latter coincides with the type of boundary conditions typically imposed for classical partial differential equations, and moreover, under computational point of view, it has been found to be the more advantageous for dealing with large scale problems. In fact, note that the nonlocal boundary conditions require in practice to be able to tackle the unbounded region Ω^c , which can be computationally very costly for solving numerically those large-scale problems. Therefore, in this project we focus exclusively on the case of local boundary conditions.

During this three-weeks research stay, we started a collaboration within the goal of developing efficient algorithms capable of solving fractional differential equations (fPDEs) in complex geometries using a Monte Carlo method.

Methods and Results

We described in the following the most relevant results obtained during the stay. In addition, the methods used to accomplish such a goal are summarized:

A promising numerical method for solving fPDEs in bounded domains was recently proposed in [2] by using the so-called spectral fractional derivative. The spectral fractional derivative is a nonlocal operator, which is defined mathematically as the spectral decomposition of the standard Laplace operator. The main idea of the numerical method consists in exploiting the integral formulation of the fractional operator using the classical heat-semigroup formalism. One of the main advantages of this formalism rests on the fact that classical methods, such as the well-known finite element method, could be adopted to solve as well fPDEs by adapting it conveniently to this different

mathematical framework. This in practice will allow to potentially solve fPDEs in arbitrary complex geometries and boundary conditions.

An alternative to this deterministic method does exist, and this is what it was explored in this project, and consists in probabilistic methods based on Monte Carlo simulations. The main advantages of the probabilistic methods are mainly due to its special computational features, such as simplicity to code and parallelization. This in practice allows to develop parallel codes with extremely low communication overhead among processors, having a positive impact in parallel features such as scalability and fault-tolerance.

To solve numerically fPDEs in bounded domains we used the aforementioned heat-semigroup formalism. Moreover, to apply such a formalism the action of a matrix exponential over a vector has to be computed, and we know that this can be done very efficiently and in parallel using the novel algorithm based on a multilevel Monte Carlo method described in [3]. Since the solution is computed through an expected value of a given finite sample, whose elements are independent from each other, it becomes easily to parallelize. The parallelization was done mainly porting an existing sequential code to OpenMP, and some benchmarks were already run to test the scalability of the algorithm, showing in general a good scalability of the code.

Conclusions

It was developed a probabilistic method based on a Monte Carlo method capable to solve fPDEs in complex geometries.

The method is based on the classical heat-semigroup formalism, and the computation of underlying the matrix exponential is done very efficiently using a multilevel Monte Carlo method.

References

- [1] Duo, S., Wang, H. and Zhang, Y., "A comparative study on nonlocal diffusion operators related to the fractional Laplacian", *Discrete and Continuous Dynamical Systems B* 24 2311-256, 2019.
- [2] Cusimano, N. del Teso, F., Gerardo-Giorda, L.D and Pagnini, G.D., "Discretizations of the spectral fractional Laplacian on general domains with Dirichlet, Neumann, and Robin boundary conditions", *SIAM J. Numer. Anal.*, 56: 1243-1272, 2018.
- [3] J.A. Acebrón, J.R. Herrero, and J. Monteiro, "A highly parallel algorithm for computing the action of a matrix exponential on a vector based on a multi-level Monte Carlo method", *Comput. Math. Appa.* In press (2020).

Acknowledgements

The work has been performed under the Project HPC-EUROPA3 (INFRAIA-2016-1-730897), with the support of the EC Research Innovation Action under the H2020 Programme; in particular, the author gratefully acknowledges the support of Dr. Gianni Pagnini, BCAM and the computer resources and technical support provided by the BSC.

A parallel semi-implicit solver for viscous two-phase flows with surface tension

S. Chiocchetti, M. Dumbser

Laboratory of Applied Mathematics, University of Trento, Italy

Introduction

In this paper we provide some benchmark results concerning a parallel code for computing viscous two-phase flows with surface tension.

We employ a hyperbolic model for continuum mechanics that describes elastic solids, viscoplastic solids, viscous fluids and ideal fluids in a unified framework. In particular, in this work we focus on viscous, two-phase, compressible flows with low Mach number.

The governing equations consist of a system of 32 PDEs (see [1, 2]) including non-conservative products and highly nonlinear stiff relaxation source terms.

Methods

The numerical method extends the solver of Boscheri et al. [1] to handle viscous two-phase flows with hyperbolic surface tension effects.

In order to deal with low Mach number flows, and preserve certain involution constraints present in our PDE system, the governing equations are discretized in a Finite Volume fashion on a staggered grid. Some of the state variables are collocated (or rather stored as cell averages) at cell centers, some at cell edges, and some at cell corners. At each timestep, the update of the state quantities is carried out in four different phases.

First, convective fluxes are computed by means of a path-conservative MUSCL Finite Volume scheme. Then corner quantities are evolved using special gradient operators such that curl involutions are preserved exactly up to machine precision. In a third step, stiff source terms are evaluated with an exponential time integrator and finally momentum and energy fluxes due to acoustic waves are computed. This last step requires the solution of a sequence of linear systems, for which we employ the conjugate gradient algorithm.

Results

Most of the communication work in our MPI-parallel code is in the form of halo exchanges executed via (neighbour-to-neighbour) nonblocking communications, which can be easily masked by overlapping them with computations on the interior cells of each sub-domain. However, we also employ global all-to-all reduction routines for the computation of the global sum of residuals at each conjugate gradient iteration. These messages are very small in size (only a single scalar per conjugate gradient iteration must be communicated), but nonetheless such a global coupling introduced measurable overhead running on 32 768 or more CPU cores.

The results of a strong scaling test, from 64 to 65 536 CPU cores on the HPE Apollo (Hawk) machine at HLRS, can be seen in Figure 1. In general, good scaling has been obtained, also thanks to increased efficiency in cache use, given by partitioning the domain onto many CPU cores (for this test, the computational grid counts 225 cells in total). We can recognize these effects in the form of a mildly superlinear scaling (120%) up to 4 096 CPU cores. Speedup efficiency is above 90% up to 16 384 CPU cores and drops to 50% on 65 536 CPU cores. In a typical run, depending on the physical setup of problem (stiff or mild source terms, very low or moderately low Mach number) the time required for updating one cell is between 4 and 20 microseconds.

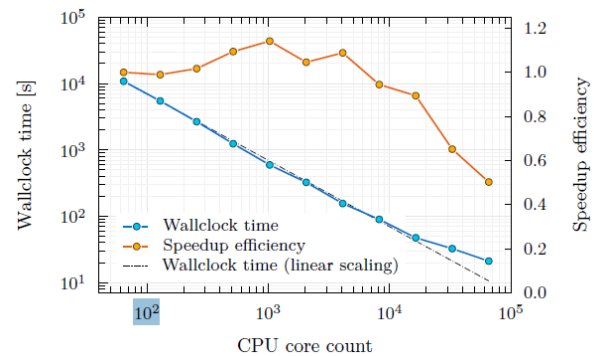


Figure 1 - Strong scaling from 64 CPU cores to 65 536 CPU cores on the HPE Apollo (Hawk) supercomputer at HLRS.

Conclusions

Satisfactory performance and scaling have been achieved, with global all-to-all communications currently constituting the main challenge to further scalability of our code.

References

- [1] W. Boscheri, M. Dumbser, M. Ioriatti, I. Peshkov, and E. Romenski. A structure-preserving staggered semiimplicit finite volume scheme for continuum mechanics. *JCP*, 424:109866, 2021.
- [2] S. Chiocchetti, I. Peshkov, S. Gavrilyuk, and M. Dumbser. High order ADER schemes and GLM curl cleaning for a first order hyperbolic formulation of compressible flow with surface tension. *JCP*, 426:109898, 2021.

Acknowledgements

The work has been performed under the Project HPC-EUROPA3 (INFRAIA-2016-1-730897), with the support of the EC Research Innovation Action under the H2020 Programme; in particular, the author gratefully acknowledges the support of Prof. Dr. rer. nat. Claus-Dieter Munz at IAG and the computer resources and technical support provided by HLRS in Stuttgart.

Predator-prey model with SEIR (Susceptible-Exposed-Infectious-Recovered) Epidemic disease

S.-M. Gurova

Institute of Information and Communication Technologies (IICT-BAS), Sofia, Bulgaria

Introduction

The predator-prey model with SEIR epidemic disease is described by a system of five nonlinear ordinary differential equations (ODEs), which depends on five functions [1] [2]. The first four of them introduce interaction in the SEIR epidemic model: $S(t)$ – susceptible prey, $E(t)$ - exposed prey, $I(t)$ -infected prey and $R(t)$ -recovered prey. The fifth function $P(t)$ – predator population, is used to present the interaction between a predator and a prey, which is given by Lotka-Volterra type [3]. The different coefficients of the system can be grouped as follows: (i) migration coefficients; (ii) natural mortality coefficients; (iii) mortality by disease and predation and (iv) specific coefficients describing infection rate, incubation rate, recovery rate and etc. The main aim of our work is to investigate how the solution of the above system depends on the coefficients in the four groups.

Methods

The Euler's method is used to solve the system describing predator-prey interaction with SEIR epidemic disease in the prey. This numerical method is one of the most popular approaches for solving systems with nonlinear ODEs.

Results

A parallel version using MPI of the sequential program written in C++ code was created. As a preproduction process all 21 coefficients grouping in the above 4 groups were discretized with a fix step in a given interval. Thus, a huge number of equilibrium points (more than 60000) was received. Using these points, the system was solved applying Euler method for different initial data. To receive a good approximation of the solutions in the time interval from 0 to 240 days, 24000 iterations have been done. Finally, a total of 69230 output files are received. They contained a solution of the system in a fixed equilibrium point that described population changes in the considered time interval. The developed parallel algorithm was tested on two HPC systems: ARGO (The Department of Informatics and Telecommunications of the University of Athens) and ARIS (GRNET) and it shows good parallel efficiency. To improve scalability of the algorithm a parallel I/O is used. The obtained results allow to select thus equilibrium points in which the dynamics of population is stable, and the disease is controlled. Using two combinations of input parameters, the following two figures are created that show the dynamics of the five populations and the impact of one population on the other in cases where we have 1) instability and the existence of epidemic (fig.1); 2) stability and infection is controlled (fig.2).

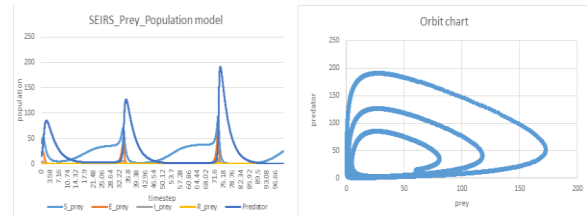


Figure 1 - The unstable case

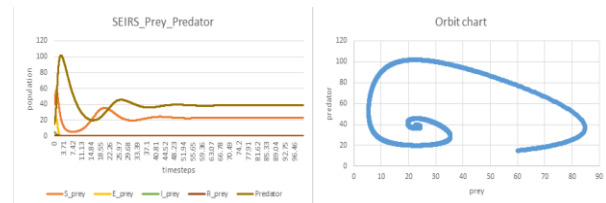


Figure 2 - The stable case

Conclusions

Using the parallel implementation of our algorithm allows us to receive a large number of solutions of the system describing predator-prey interaction with SEIR epidemic disease in the prey. These solutions depend on the coefficients in the four groups and also on the various number of initial conditions. Using these results, we can select equilibrium points in which the dynamics of population is stable and the disease is controlled. The large number of solutions allows us to create a video demonstrating how the coefficients affect the predator-prey population in an epidemic environment.

References

- [1] S.-M. Gurova, "A predator-prey model with SEIR and SEIRS epidemic in the prey", AIP Conference Proceedings 2164, 080003 (2019); <https://doi.org/10.1063/1.5130826>, 2019.
- [2] F. Etbaigha, A. R. Willms, Z. Poljak, An SEIR model of influenza A virus infection and reinfection within a farrow-to-finishes wine farm, 2018, <https://doi.org/10.1371/journal.pone.0202493>.
- [3] J. Chattopadhyay, O. Arino, A predator-prey model with disease in the prey, Nonlinear Analysis: Theory, Methods & Applications, vol. 36, Issue 6, pp. 747-766, 1999.

Acknowledgements

The work has been performed under the Project HPC-EUROPA3 (INFRAIA-2016-1-730897), with the support of the EC Research Innovation Action under the H2020 Programme; in particular, the author gratefully acknowledges the support of prof. Yiannis Contronis from Department of Informatics and Telecommunications, National and Kapodistrian University of Athens and the computer resources and technical support provided by GRNET HPC.

Local nearrings

I. Raievska, M. Raievska

Institute of Mathematics of NAS of Ukraine, Ukraine

Introduction

We study algebraic structures called nearrings, which are interesting examples of generalised rings (i.e. addition need not to be commutative, and only one distributive law is assumed) with applications in a non-commutative homological algebra, algebraic topology, functional analysis and in categories with group objects. The classification of nearrings up to certain orders is a challenging problem, and requires extensive computations, which we will implement using the computational algebra system GAP [1].

Methods

A nearring with identity is called local if the set of all its non-invertible elements is a subgroup of its additive group.

For the researchers in nearrings, the list of all 698 local nearrings of order at most 31 up to isomorphism is provided by the GAP package SONATA [2]. However, classifying nearrings of order 32 is a significant challenge.

Motivated by this, we have implemented algorithms to compute all local nearrings of further orders, in a new GAP package called LocalNR [3]. The current version of this package contains all 37,441 local nearrings of order at most 361, except those of orders 32, 64, 128, 243 and 256.

We have already calculated some classes of local nearrings of orders 32 (with 14927685 nearrings), 64 (with 1115947 nearrings) and 243 (with 705105 nearrings), but to reach further progress we need to parallelise LocalNR code and use HPC facilities to run large scale calculations.

GAP provides a programming language, also called GAP, a library of mathematical algorithms implemented in this language, and various libraries of mathematical objects, such as, for example, the 423164062 groups of order not greater than 2000 (excluding 49487365422 groups of order 1024).

Results

There exist 267 non-isomorphic groups of order $64 = 2^6$, of which 5 groups are of exponent 32 and 27 groups are of exponent 16. Among them, only 2 groups of exponent 32 and 8 groups of exponent 16 are additive groups of local nearrings (see, for example, [5]).

Let $[n, i]$ be the i -th group of order n in the SmallGroups library in GAP. We denote by C_n and D_n the cyclic and dihedral groups of order n , respectively. We have the following assertions [4].

Proposition 1. The following groups of exponent 32 are the additive groups of local nearrings of order 64:

IdGroup	Structure Description	Number of LNR
[64, 50]	$C_{32} \times C_2$	257
[64, 51]	$C_{32} \times C_2$	257

Theorem 1. The following groups of exponent 16 are the additive groups of local nearrings of order 64:

IdGroup	Structure Description	Number of LNR
[64, 26]	$C_{16} \times C_4$	11467
[64, 27]	$C_{16} \times C_4$	11467
[64, 29]	$(C_{16} \times C_2) \times C_2$	28185
[64, 30]	$(C_{16} \times C_2) \times C_2$	4433
[64, 44]	$C_4 \times C_{16}$	28500
[64, 45]	$C_8, D_8 = C_4, (C_8 \times C_2)$	1920
[64, 183]	$C_{16} \times C_2 \times C_2$	exact number is unknown
[64, 184]	$C_2 \times (C_{16} \times C_2)$	exact number is unknown

Conclusions

At the moment we use serial codes. We are interested in its parallelisation for constructing local nearrings of bigger orders. Parallelising GAP is fundamentally different from commonly used approaches to numerical calculations such as e.g. OpenMP or MPI, due to different type of objects GAP operates with. To parallelise GAP calculations, we will use the GAP package SCSCP (<https://gap-packages.github.io/scscp/>), which provides a framework for distributed parallel computation in GAP.

References

- [1] The GAP Group, GAP - Groups, Algorithms, and Programming, Version 4.10.2; 2019, <https://www.gap-system.org>
- [2] Aichinger E., Binder F., Ecker Ju., Mayr P. and Noebauer C. SONATA - system of near-rings and their applications, GAP package, Version 2.9.1, 2018, <https://gap-packages.github.io/sonata/>
- [3] Sysak Ya., Raievska I., Raievska M. LocalNR - library of local nearrings, GAP Package, Version 1.0.2, 2020, <https://gap-packages.github.io/LocalNR>
- [4] Raievska Iryna, Raievska Maryna. The additive groups of local nearrings of order 64, <http://www.iapmm.lviv.ua/chyt2020/abstracts/Raievska.pdf>
- [5] <https://www.imath.kiev.ua/~algebra/LocalNR/>

Acknowledgements

The work is part of research projects entitled "LocalNearRing" and "NearRingsWithIdentity". The work has been performed under the Project HPC-EUROPA3 (INFRAIA2016-1-730897), with the support of the EC Research Innovation Action under the H2020 Programme; in particular, the authors gratefully acknowledge the support of Dr. Alexander Konovalov of the School of Computer Science at the University of St Andrews and the computer resources and technical support provided by EPCC at the University of Edinburgh.

Nearrings with identity

I. Raievska, M. Raievska

Institute of Mathematics of NAS of Ukraine, Ukraine

Introduction

Nearrings naturally arise in the study of systems of nonlinear mappings, and have been studied for many decades.

However, it is not true that any finite group is the additive group of a nearring with identity. Therefore, it is important to determine such groups and to classify some classes of nearrings with identity on these groups, for example, local nearrings.

The classification of all nearrings up to certain orders (i.e. producing their complete and irredundant list up to equivalency) is an open problem. It requires extensive computations, and the most suitable platform for their implementation is the computational algebra system GAP [1].

Methods

The initial idea for the project was motivated by the need of having a database of examples of moderately sized nearrings with identity to search for examples and counterexamples. As an existing example the GAP package SONATA [2] was an inspiration on how such a project could be established. Unfortunately, the number of nearrings with identity is so much bigger, and most of them bare so little structure, that new techniques to store and handle such nearrings had to be developed. Of course, the first step was to actually construct some classes of nearrings.

We have implemented algorithms to compute all local nearrings of further orders, in a new GAP package called LocalNR [3]. The current version of this package (not yet redistributed with GAP) contains all local nearrings of order at most 361, except those of orders 32, 64, 128, 243 and 256. We have already calculated some classes of local nearrings of orders 32, 64 and 243.

Results

There exist 15 non-isomorphic groups of order 625, of which 11 groups are additive groups of local nearrings (see, for example, [4]). Let $[n, i]$ be the i -th group of order n in the

SmallGroups library in GAP. We denote by C_n the cyclic group of order n , respectively. We have the following assertion.

Theorem 1. The following groups and only they are the additive groups of local nearrings of order 625:

IdGroup	Structure Description
625, 1	C_{625}
625, 2	$C_{25} \times C_{25}$
625, 3	$(C_{25} \times C_5) \rtimes C_5$
625, 5	$C_{125} \rtimes C_5$
625, 6	$C_{125} \rtimes C_5$
625, 7	$(C_5 \times C_5 \times C_5) \rtimes C_3$
625, 8	$(C_{25} \rtimes C_5) \rtimes C_5$
625, 11	$C_{25} \times C_5 \times C_5$
625, 12	$C_5 \times ((C_5 \times C_5) \rtimes C_5)$
625, 13	$C_5 \times (C_{25} \rtimes C_5)$

Conclusions

Presently, serial codes from the LocalNR package are used for constructing nearrings and extending its data library. We are interested in its parallelisation for constructing nearrings with identity of bigger orders.

References

- [1] The GAP Group, GAP - Groups, Algorithms, and Programming, Version 4.10.2; 2019, <https://www.gap-system.org>
- [2] Aichinger E., Binder F., Ecker Ju., Mayr P. and Noebauer C. SONATA - system of near-rings and their applications, GAP package, Version 2.9.1, 2018, <https://gap-packages.github.io/sonata/>
- [3] Sysak Ya., Raievska I., Raievska M. LocalNR - library of local nearrings, GAP Package, Version 1.0.2, 2020, <https://gap-packages.github.io/LocalNR>
- [4] <https://www.imath.kiev.ua/~algebra/LocalNR/>

Acknowledgements

The work is part of research projects entitled "LocalNearRing" and "NearRingsWithIdentity". The work has been performed under the Project HPC-EUROPA3 (INFRAIA2016-1-730897), with the support of the EC Research Innovation Action under the H2020 Programme; in particular, the authors gratefully acknowledge the support of Dr. Alexander Konovalov of the School of Computer Science at the University of St Andrews and the computer resources and technical support provided by EPCC at the University of Edinburgh.

Modifying ground state chemistry of molecules by ultra strong coupling to plasmonic resonances

T.J. Antosiewicz

Faculty of Physics, University of Warsaw, Warsaw, Poland.

Introduction

To alleviate limitations on equal treatment of the plasmonic cavity strongly coupled to a molecule, that is typically present in cavity quantum electrodynamics [1,2], we use density functional theory (DFT). This way the matter subpart in the unified light-matter polaritons is treated accurately and is expected to show characteristic changes in the strong coupling regime. We use DFT to calculate ground state energy modifications (GSEM) in the ultra-strong coupling regime.

Methods

We use real-time-propagation time-dependent DFT (TDDFT) approach [3] based on the localized basis sets [4] as implemented in the open-source GPAW package [5]. Calculations were carried out using the Perdew-Burke-Ernzerhof (PBE) [6] exchange-correlation functional in the adiabatic limit. The spectra are calculated using the δ -kick technique [3] in the linear-response regime and employing the dipole approximation for light-matter interaction. We use the default projector augmented-wave (PAW) [7] data sets and double- ζ polarized (dzp) basis sets in GPAW. Additional contributions from van der Waals interactions are evaluated using the DFT-D3 dispersion correction [8].

Results

Modelled systems consist of Na, Mg, and Al nanoparticle dimers of a few hundred atoms to span a broad energy range to probe the possibility of ultra-strong coupling to co-resonant molecules. By fitting the coupled spectra, we obtain the coupling strengths g and then calculate the GSEM as $\Delta_e = g^2/2\omega$. Shown in Fig. 1a, they demonstrate that across a broad energy range single-molecule ultra-strong coupling results in GSEM of up to 30-60 meV, what is comparable to or larger than $k_B T$ at room temperature. This is an increase of the GS energy, which is dependent on the orientation and position of the molecule. In Fig. 2b,c, as an example, we plot the GSEM as function of rotation and position of tetracene in the gap of a Mg_{201} dimer.

Conclusions

GSEM Δ_e obtained from single mode cavity quantum electrodynamics theory, show that in the ultra-strong coupling regime the GS energy increases by 30-60 meV, practically irrespective of the plasmonic cavity and molecule, provided that the molecule's transition dipole moment is big enough. This increase in energy means that energy is required to assemble the strong coupled system [9], making it potentially unstable. However, total energy calculations with PBE and van der Waals dispersion corrections show that for these systems their energy modifications with geometry are on the order of up to 0.4 eV, i.e. one order of magnitude more than GSEM from ultra-strong coupling. This means that such strongly coupled systems will be stable and may benefit from polariton contributions to chemistry.

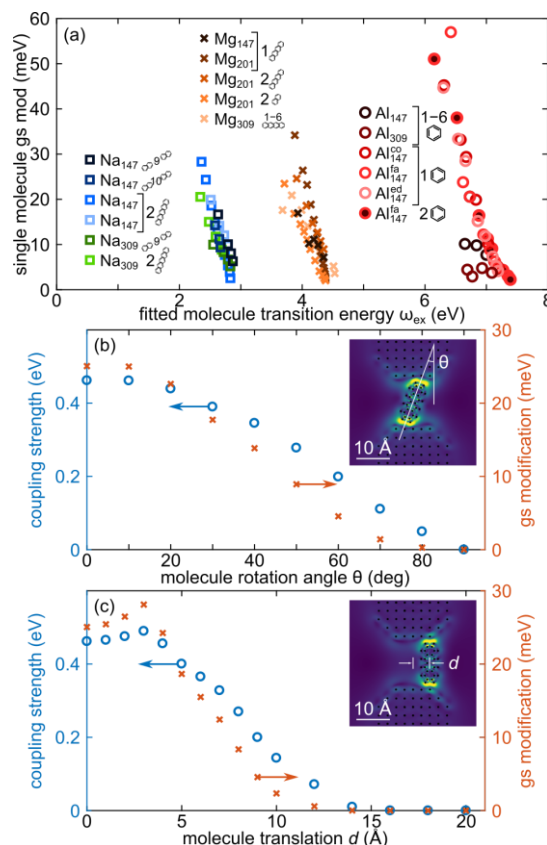


Figure 1 – (a) GSEM in the ultra-strong coupling regime for various studied systems. (b,c) Exemplary GSEM of Mg_{201} dimer coupled with tetracene as function of molecule (a) rotation and (b) position.

References

- [1] Jaynes, ET et al., Proc. IEEE 51, 89 (1963).
- [2] Garraway, BM, Philos. Trans. Royal Soc. A 369, 1137 (2011).
- [3] Yabana, K, Bertsch, GF, Phys. Rev. B 54, 4484 (1996).
- [4] Kuisma, M et al., Phys. Rev. B 91, 115431 (2015).
- [5] Mortensen, JJ et al., Phys. Rev. B 71, 035109 (2005).
- [6] Perdew, JP et al. PRL 77, 3865 (1996) & 78, 1396 (1997).
- [7] Blöchl, PE, Phys. Rev. B 50, 17953 (1994).
- [8] Grimme S et al. J. Phys. Chem. 132, 154104 (2010).
- [9] Baranov, DG et al. Nat. Commun. 11, 2715 (2020).

Acknowledgements

The work has been performed under the Project HPC-EUROPA3 (INFRAIA-2016-1-730897), with the support of the EC Research Innovation Action under the H2020 Programme; in particular, TJA gratefully acknowledges the support of Paul Erhart of the Department of Physics at Chalmers University of Technology and the computer resources and technical support provided by the Swedish National Infrastructure for Computing at PDC, Stockholm.

Initial stage of the spinodal instability

M. Attems

Instituto Galego de Física de Altas Enerxías (IGFAE), Universidade de Santiago de Compostela, 15782 Galicia, Spain.

Introduction

The holographic real-time approach allows to study the dynamics of near critical phase transitions. The dynamical signatures of a first order phase transition are relevant for the experimental searches with hot deconfined plasma at the Relativistic Heavy Ion Collider (RHIC) at Brookhaven National Laboratory, USA. The spinodal instability is a prime signature of the supposed first-order phase transition which the Quark-Gluon-Plasma may undergo near the supposed critical point in the quark matter phase diagram. Understanding the dynamical properties of extreme phases of nuclear matter is the core of the study.

Methods

The typical tool to study Quantum Chromo-Dynamics is lattice gauge theory. While its methods are well tested for systems in equilibrium, they are not yet applicable to non-equilibrium systems like instabilities. The gauge/gravity correspondence [1], on the other hand, provides access to time dependent non-equilibrium transport properties of plasmas such as viscosity, ratio of transverse over longitudinal pressure and other quantities characterizing the plasma transport coefficients. The holographic gauge/gravity duality relates general relativity in D-dimensional spacetime with Anti-de Sitter geometry to particle physics in $(D - 1)$ dimensions, thus offering a powerful toolkit for studying strongly-coupled gauge theories via gravity. Indeed, the spinodal instability of a plasma with a first order phase transition is modelled, in the dual gravity picture, by the Gregory-Laflamme type of instability, which affects black holes in higher dimensions by the addition of a weakly coupled tuned scalar potential. Solving the gravitational dynamics offers the opportunity to study the non-equilibrium physics of the spinodal instability and its evolution at strong coupling.

Solving Einstein equations in the characteristic formulation involves evaluating ordinary differential equations, which are polynomials with more than 50k terms. In particular the combined use of MPI for each domain and OpenMP inside each decomposition increases the computational speed. For the forward time-stepping of the evolution, depending on the required numerical resolution either fast Adams-Bashforth or the more precise higher-order Runge-Kutta methods are chosen. Using a characteristic evolution brings several optimizations: The initial data is free which implies the absence of elliptic constraints on the data. There are no second time derivatives, which means a smaller number of basic variables, compared to other approaches like Cauchy evolution. The equations have a convenient hierarchical structure in which variables are integrated in turn in terms of characteristic data from prior members of the hierarchy.

Results

The spinodal instability typically cools down regions in the unstable temperature band to the stable temperature and by doing so it pushes local energy density to specific regions. In

Figure 1 we show the time evolution of the spinodal instability plotting the local energy density. One sees, starting of a homogeneous plasma, the unstable growth of five peaks corresponding in this case to the small initial excitation. In [2,3], we classified as first the four generic dynamical stages of the spinodal instability. The fig.1 is a typical example of the linear stage, where the instabilities grow exponentially. The number of maxima and minima of the local energy density profile is given by the leading Fourier modes at that time. Additional evolution with different initial excitations are public on the dataset [3].

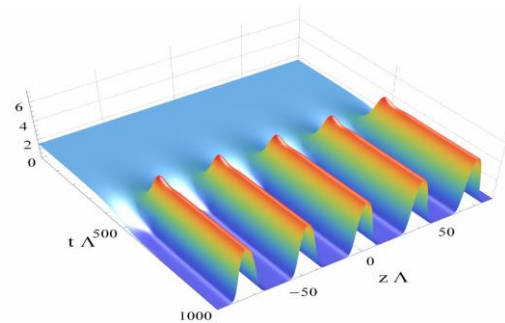


Figure 1 – Early time evolution of the local energy density with the excited unstable mode $n=5$ showing formation of peaks and cold stable domains.

Conclusions

We characterized several generic stages in the dynamics of the spinodal instability. In the first, linear stage the instability grows exponentially. Moreover, our work reveals a novel example of the applicability of hydrodynamics to a system with large energy gradients undergoing a first-order phase transition, where even with large spatial gradients the entire evolution (unstable growth, phase separation and final state) is surprisingly well described by second-order hydrodynamics. We have thus uncovered a new example of the unreasonably universal applicability of hydrodynamics.

References

- [1] Juan Martin Maldacena, *Int.J.Theor.Phys.* 38 (1999) 1113-1133, *Adv.Theor.Math.Phys.* 2 (1998) 231-252, hep-th/9711200 [hep-th].
- [2] Maximilian Attems et alii, *JHEP* 01 (2020) 106, doi:10.1007/JHEP01(2020)106, arXiv:1905.12544 [hep-th].
- [3] Maximilian Attems et alii. (Version v20190918) [Data set]. Zenodo. <http://doi.org/10.5281/zenodo.3445360>.

Acknowledgements

The work has been performed under the Project HPC-EUROPA3 (INFRAIA-2016-1-730897), with the support of the EC Research Innovation Action under the H2020 Programme; in particular, the author gratefully acknowledges the support of Aleksii Vuorinen and Niko Jokela of the Helsinki Institute of Physics, University of Helsinki and the computer resources and technical support provided by the Finish CSC - IT Center for Science.

Fighting bacteria: a computational exploration of chemical and physical interactions between sphere-shaped and rod-shaped bacteria

K. Bowal^{1,2}, *T. Idema*²

¹Department of Chemical Engineering and Biotechnology, University of Cambridge, Cambridge, United Kingdom; ²Department of Bionanoscience, Kavli Institute of Nanoscience, Delft University of Technology, Delft, The Netherlands

Introduction

Tackling issues such as antimicrobial resistance and microbe interactions requires a deep and fundamental understanding of microbial behaviour. In particular, interactions between microbial communities containing multiple species are complex and not yet well understood, even though they are known to influence microbial survival and disease development. For example, the presence of *Pseudomonas aeruginosa* and *Staphylococcus aureus* in chronic wounds or the airways of individuals with cystic fibrosis has been associated with shortened life spans and decreased lung function.

Understanding the movement and interactions of multispecies microbial communities is vital to develop and implement applications relevant to medical and industrial systems, such as infection treatment strategies.

This fundamental insight may also provide knowledge required to describe and design systems in which microbes perform a beneficial purpose, such as bioremediation and filtration.

Methods

In this work we use computational methods to probe the fundamental interactions of microbial communities.

We extend an existing agent-based model [1, 2] of self-propelling bacteria to incorporate molecule secreting and sensing as well as polydisperse bacteria shapes.

Results

Using this extended model, we study the collective dynamics of a bacterial community containing two species. The results are compared to recent experimental work by Limoli et al. [3] visualising the early interactions between a multispecies community of bacteria relevant to clinical situations, such as respiratory infections and chronic wounds. The most striking interaction is a 'fighting' process in which *P.aeruginosa*, rod-shaped bacteria, sense secreted products from *S. aureus*, sphere-shaped bacteria, and change their behaviour from collective movement to single-cell exploration with increased velocity. This transition results in a dynamic situation in which the *P.aeruginosa* surround and 'attack' the *S. aureus* groups and significantly inhibit growth of these sphere-shaped bacteria.

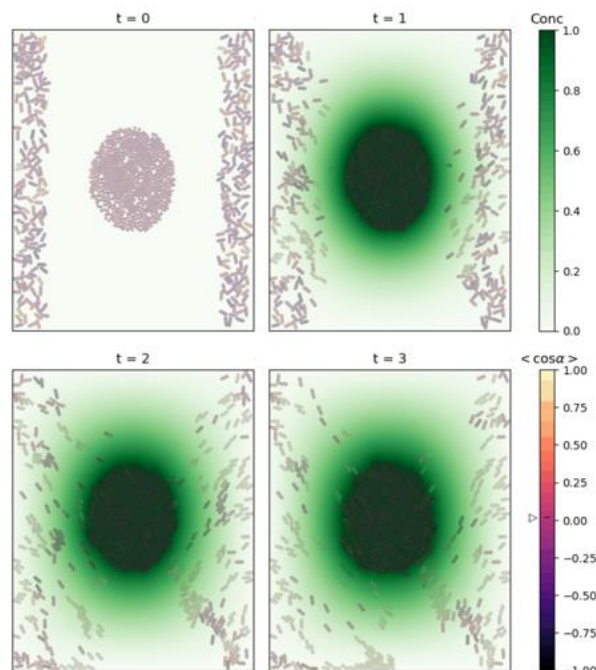


Figure 1 – Snap shots of two interacting bacterial colonies at four different time points. The central sphere-shaped cells are stationary and secrete a signalling molecule, the concentration of which is indicated by the green-white colouring. The outer rod-shaped cells are self-propelled and move in response to sensing the secreted signalling molecule. Each cell is coloured based on its local alignment angle.

Conclusions

This work provides a tool to probe the fundamental controlling mechanisms and resulting spatiotemporal patterns of diverse multispecies microbial communities. From the results, we can learn how we could rationally manipulate interspecies behaviour during infections.

Consequently, we might prevent bacteria with harmful effects (such as *P. aeruginosa* and *S. aureus* within the airways of cystic fibrosis patients) from engaging in physical interactions or bring species together who synergise to produce a beneficial effect.

References

- [1] Storck T et al., *Biophys. J.* 106(9):2037-2048, 2014.
- [2] van Holthe D et al, Preprint at <https://arxiv.org/pdf/2003.10509>, 2020.
- [3] Limoli D et al., *eLife*, 8:e47365, 2019.

Acknowledgements

The work has been performed under the Project HPC-EUROPA3 (INFRAIA-2016-1-730897), with the support of the EC Research Innovation Action under the H2020 Programme; in particular, the author gratefully acknowledges the support of Professor Timon Idema, Department of Bionanoscience, Kavli Institute of Nanoscience, Delft University of Technology and the computer resources and technical support provided by SURFsara.

Defect rotation controls the dynamics of Saturn rings

L.N. Carenza¹, G. Gonnella¹, D. Marenduzzo², G. Negro¹

¹Dipartimento di Fisica, Università degli Studi di Bari and INFN, Bari, Italy; ²SUPA School of Physics and Astronomy, University of Edinburgh, United Kingdom

Introduction

Active matter [1] identifies a novel kind of Soft Matter, in which the individual constituents inject energy continuously, thus driving the system far from thermodynamic equilibrium.

An important feature of active materials is the emergence of collective behaviours, consisting in the coherent motion of large groups of individual entities on scales much larger than the size of the constituents themselves. In this short report we present the result of a study concerning the properties of an active nematics shell suspended in a passive liquid crystal background. The energy injected by means of the active mechanisms, leads topological defects on the shell to rotate as observed in actual experiments [2]. Moreover, if homeotropic anchoring is imposed for the passive liquid crystal at the droplet interface a disclination line is formed around the droplet equator.

Methods

The physics of an active shell embedded in a passive liquid crystal can be described by introducing a small numbers of fields capable to capture the state of the systems. The active nematic tensor $Q_{\alpha\beta}$ is confined at the interface of a droplet identified by the scalar concentration field ϕ , while a second nematic tensor $P_{\alpha\beta}$ is confined outside the droplet. The equilibrium properties of the system are encoded in an adapted version of the Landau – DeGennes free energy [3].

The concentration field ϕ follows an advection-diffusion equation, while the two nematic fields $Q_{\alpha\beta}$ and $P_{\alpha\beta}$ evolve according to the Beris-Edwards equation. The dynamics of the order parameter is coupled to the underlying fluid by means of different stress contributions, including a phenomenological active stress term, which enter the Navier-Stokes equations that rules the evolution of the velocity field v . The dynamical equations are integrated by a well validated lattice Boltzmann approach. In order to investigate to the behaviour of the system in a full three-dimensional geometry we parallelized the code by means of an MPI approach. More details on the model and the numerical implementation can be found in [4].

Results

To investigate the physics of our system we scanned systematically the parameter space by varying the surface tension of the droplet, the anchoring of the two liquid crystals at the droplet interface and the intensity of activity.

Among the results of our study, we observed that by imposing tangential anchoring of the active nematics on the shell four semi-integer defects are formed. In the passive limit, they settle on the vertices of a tetrahedron, while they undergo a periodical rotational dynamic when active is switched on – a behaviour closely resembling the experimental observations in [2]. Moreover, by imposing homeotropic anchoring on the passive liquid crystal that is confined outside the droplet, we obtained the formation of a disclination line around the

droplet equator. The nematic tensor $P_{\alpha\beta}$ relaxes into this defect structure, commonly know as Saturn ring [3], when the activity is low and the viscosity of the underlying fluid is high for advective mechanisms to be relevant. Nevertheless, if viscosity is reduced and the flow generated by the active nematic tensor is strong enough, the disclination line may deform or exhibit a wiring dynamics as observed in experiments [1,2].

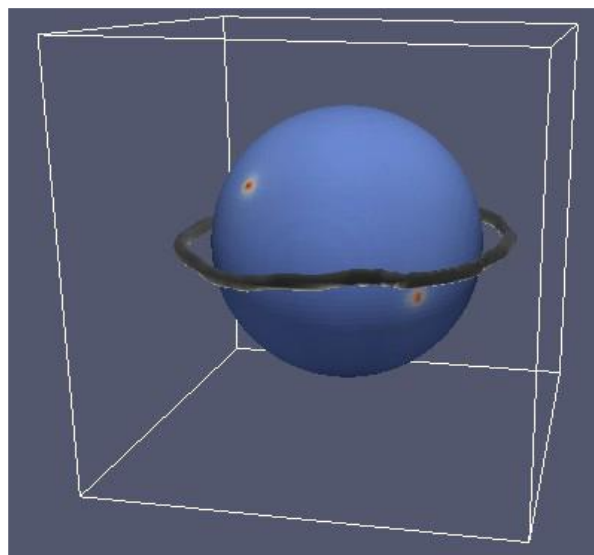


Figure 1 – Red spots on the active shell denote the position of the defects of the active nematics $Q_{\alpha\beta}$, while the Saturn ring is denoted with a black line surrounding the droplet equator.

Conclusions

Future research will focus on controlling the feedback dynamics between the active flow and the Saturn ring. Later, we will consider the case with multiple one active shells.

References

- [1] M.C. Marchetti, J.F. Joanny, S. Ramaswamy, T.B. Liverpool, J.J. Prost, M. Rao, and R.A. Simha. Hydrodynamics of soft active matter. *Rev. Mod. Phys.*, 85:1143, 2013.
- [2] P. Guillamat, Z. Kos, J. Hardoüin, M. Ravnik, and R. Sagués. Active nematic emulsions. *Science Advances*, 4:4, 2018.
- [3] L.N. Carenza and G. Gonnella and D. Marenduzzo and G. Negro. Rotation and propulsion in 3d active chiral droplets. *Proc. Natl. Acad. Sci.* 116, 22065 (2019).
- [4] L.N. Carenza, G. Gonnella, A. Lamura, G. Negro, and A. Tiribocchi. Lattice boltzmann methods and active fluids. *Eur. Phys. J. E*, 42(6):81, 2019.

Acknowledgements

The work has been performed under the Project HPC-EUROPA3 (INFRAIA-2016-1-730897), with the support of the EC Research Innovation Action under the H2020 Programme; in particular, the author gratefully acknowledges the support of prof. Marenduzzo of the School of Physics and Astronomy of the University of Edinburgh and the computer resources and technical support provided by EPCC.

Dynamics of equilibration and collisions in ultradilute quantum droplets

V. Cikojević^{1,2}, L. Vranješ Markić^{1,2}, M. Pi^{1,2}, M. Barranco^{3,4}, F. Ancilotto^{5,6}, J. Boronat²

¹University of Split, Faculty of Science, Split, Croatia; ²Departament de Física, Universitat Politècnica de Catalunya, Barcelona, Spain; ³Departament FQA, Facultat de Física, Universitat de Barcelona, Spain; ⁴Institute of Nanoscience and Nanotechnology (IN2UB), Universitat de Barcelona, Spain; ⁵Dipartimento di Fisica e Astronomia "Galileo Galilei" and CNISM, Università di Padova, Italy; ⁶CNR-IOM Democritos, Trieste, Italy

Introduction

The collision of liquid drops is one of the more fundamental and complex problems addressed in fluid dynamics, with implications in basic research and applications e.g. in microfluidics, formation of rain drops, ink-jet printing, or spraying for combustion, painting and coating [1–4]. Liquid drop collisions were also used as a model for nucleus-nucleus reactions [5] and nanoscopic ³He droplets collisions [6]. Some progress in the understanding of dynamical properties of quantum Bose-Bose droplets has been made in a recent experimental study of head-on collisions between pairs of 39 K- 39 K droplets [7], providing a new avenue of research. In Ref. [7], the authors discovered a highly compressible droplet regime, not present in the world of classical liquids, when the total atom numbers in colliding droplets are small. Thus, it is not clear whether the Weber number theory [8], describing the dynamics of classical liquid collisions, can apply to ultradilute droplets. Depending on the velocity of each droplet, the outcome of the experiment [7] was either merging or separation of the colliding droplets. In this work, we re-analyse that experiment by using a QMC-based functional which takes into account the effective range of the interactions and a two-component MF+LHY functional that enables the study of unequilibrated drops and an experimentally more realistic consideration of 3BL. Our results show the relevance of the non-optimal concentration ratio in the outcome of drop collisions, providing an alternative explanation to the experimental results without invoking 3BL.

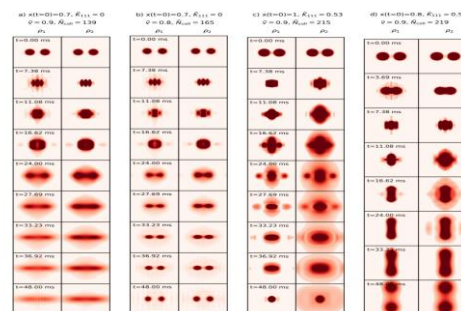
Methods

This project is using mainly Density Functional Theory. Main limitation for Quantum Monte Carlo methods we use is the number of particles, and the experimental number of particles in quantum Bose-Bose droplets is far from what can be simulated numerically. Under Density Functional Theory, problem is viewed as effectively single-particle one, and the effective Hamiltonian is obtained by variation of energy density with respect to density. In other words, problem is addressed calling upon a Hohenberg-Kohm-Sham 2nd theorem [1], guarantying that there exists a density functional for which the optimal density profile is one from the exact ground state solution of a Schrödinger equation.

Results

We lay out the basic equations of the extended LHY mean-field theory (MF+LHY). We present the details of our simulations. We discuss the effects of the non-optimal initial atom number ratio and 3BL on the stationary drop. We systematically compare the drops collisions results obtained within the effective single-component MF+LHY theory with those obtained using the QMC-based functional. We report results derived with the two-component framework. We investigate the influence on the collisions of both the initial

population imbalance and 3BL acting only on the $|F=1, m=0\rangle$ state.



Conclusions

If the droplets are not fully equilibrated when they enter the collision region, this affects the collision outcome because it introduces an important additional effect not previously considered, namely the halo of the expelled gaseous particles of the in-excess species that envelop the droplets and increase the tendency to merge. This effect has also been found in viscous droplet collisions [2]. Remarkably, the phase diagram changes even without the introduction of 3BL, as collisions between non-equilibrated droplets are shown to behave differently from equilibrated ones in terms of the optimal atom number ratio, leading to results that are in better agreement with experiment. We have focused here on zero temperature description, but it is plausible that thermally excited droplets [9] could produce similar shifts in the critical velocity.

References

- [1] N. Ashgriz and J. Y. Poo, *Journal of Fluid Mechanics* 221, 183–204 (1990).
- [2] J. Qian and C. K. Law, *Journal of Fluid Mechanics* 331, 59–80 (1997).
- [3] K.-L. Pan, P.-C. Chou, and Y.-J. Tseng, *Phys. Rev. E* 80, 036301 (2009).
- [4] V. Varma, A. Ray, Z. Wang, Z. Wang, and R. Ramanujan, *Scientific reports* 6, 1 (2016).
- [5] W. J. Swiatecki, *Nuclear Physics A* 376, 275 (1982).
- [6] M. Guilleumas, M. Pi, M. Barranco, and E. Suraud, *Zeitschrift für Physik D Atoms, Molecules and Clusters* 34, 35 (1995).
- [7] G. Ferioli, G. Semeghini, L. Masi, G. Giusti, G. Modugno, M. Inguscio, A. Gallellí, A. Recati, and M. Fattori, *Phys. Rev. Lett.* 122, 090401 (2019).
- [8] A. Frohn and N. Roth, *Dynamics of droplets* (Springer Science & Business Media, 2000).
- [9] J. Wang, H. Hu, and X.-J. Liu, *New Journal of Physics* 22, 103044 (2020).

Acknowledgements

The work has been performed under the Project HPC-EUROPA3 (INFRAIA-2016-1-730897), with the support of the EC Research Innovation Action under the H2020 Programme; in particular, the author gratefully acknowledges the support of UPC Barcelona and the computer resources and technical support provided by Barcelona Supercomputing Center

Numerical simulation of binary neutron stars

K.A. Cokluk^{1,2}, B. Giacomazzo², K. Yakut¹

¹Department of Astronomy and Space Sciences, University of Ege, İzmir, Turkey; ²Dipartimento di Fisica G. Occhialini, Università di Milano - Bicocca, Milano, Italy

Introduction

Since the first binary black hole (BH) merger observations detected by LIGO [1], a new window has been opened in astrophysics in the gravitational wave field and very important work has been done [2]. For the first time the GW signal from a binary neutron star merger, named GW170817, detected [3] accompanied by electromagnetic counterparts' observations [4]. Thus, the multi-messenger era has opened. It is crucial to study high-mass mergers of the type discussed in this study to study high-mass neutron stars and pulsars, obtain detailed information about a neutron star or possible black hole formed as a result the merger of two neutron stars. Additionally, working on this type of merger allows us to perform the internal structure of massive neutron stars.

Methods

In this work, we consider equal mass binary neutron star systems with total baryonic mass $3.2-3.8 M_{\square}$. For initial data of models, we use a seven-segment SLy piecewise polytropic equation of state described in [5] and compute using LORENE [6,7] code. For all model initial separation of components is chosen 40 km corresponding to approximately 3-3.5 orbits before merger. Einstein Toolkit [8, 9] (version of ET_2019_10) code is used to evolve BNS systems. We employ BSSN formulation provided by McLachlan thorn of ET for evolution of spacetime metric. Hydrodynamical values are evolved by using GRHydro package, HLLC Reimann solver and PPM reconstruction method. For grid structure we employ an adaptive mesh refinement approach provided by Carpet mesh refinement driver [10] so that we get finest grids to follow each NS during the simulations. The grid hierarchy consists of six refinement levels varying from coarsest levels $\Delta x_0 = 7.68 CU \approx 11.36 km$ to finest level which is $\Delta x_5 = 0.24 CU \approx 355 m$ where the outer boundary is $1024 CU \approx 1514 km$. After coalescence, we have chosen to add one finer refinement with $\Delta x_6 = 0.12 CU \approx 177 m$.

Results

The GW strain and the phase velocity for all models are shown in Figure 1. All GW signals become quasi-steady state before 1.5ms. The ringdown part of the waveform becomes less clear as the initial binary mass increases. For all models, the evolution of phase velocity is nearly identical, and both frequency and GW amplitude increase before the merger. It is because the remnant rotates faster due to increment of compactness after the merger that GW amplitude begins to decrease while frequency still grows.

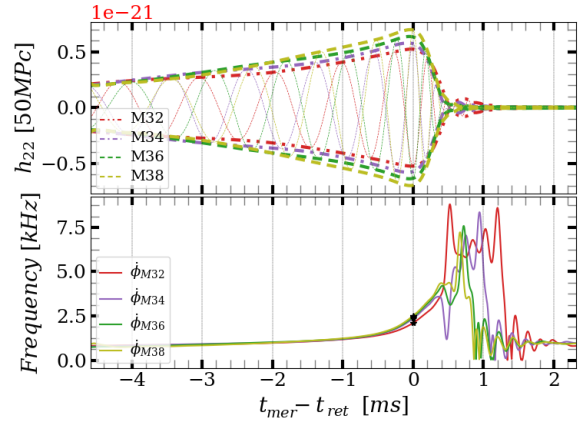


Figure 1 – upper: the dominant mode ($l,m=2,2$) of gravitational waveforms from $r=300M$ of our models. bottom: instantaneous frequency.

Conclusions

This study has performed a set of equal-mass and massive BNS system simulations with seven-segment piecewise polytropic SLy EOS. We started evolution before 3-3.5 orbits before the merger and followed systems 5ms after the merger. We reported that all models showed a prompt collapse of a BH within less than 1ms and formed a BH with mass range $M_{BH} = 2.82 - 3.26 M_{\square}$ and dimensionless spin range $\chi = 0.76 - 0.80$. Additionally, from the evolution of rest-mass density, we discussed the possible effect of initial binary mass on the matter around a BH after the merger. It suggested that for a given EOS and equal-mass systems, the matter outside of the horizon rapidly falls onto a BH. Moreover, we extracted the gravitational waveform of systems and discussed the evolution of frequency. It indicated massive binaries, and the merger frequency becomes higher. Detailed results are being prepared to publish referred journal.

References

- [1] Surname N et al., Journal, volume(issue):pages, year. [1] Abbott, B. P. et al. Physical Review Letters 116, 2016. [2] Barack, L. et al. Classical and Quantum Gravity 36, 2019. [3] Abbott, B. P. et al. Physical Review Letters 119, 2017. [4] Abbott, B. P. et al. The Astrophysical Journal 848, L12, 2017. [5] De Pietri, et al. Physical Review D 93, 2016. [6]ourgoulhon, E. et al. Physical Review D 63, 2001. [7] LORENE. <http://www.lorene.obspm.fr/>. [8] Einstein Toolkit. <http://einstein toolkit.org/>. [9] Loffler, F. et al. Classical and Quantum Gravity 29, 2012. [10] Carpet. <http://www.carpetcode.org>

Acknowledgements

The work has been performed under the Project HPC-EUROPA3 (INFRAIA-2016-1-730897), with the support of the EC Research Innovation Action under the H2020 Programme; in particular, KAC gratefully acknowledges the support of Bruno Giacomazzo, the University of Milano-Bicocca, Department of Physics "Giuseppe Occhialini" and the computer resources and technical support provided by HPC-CINECA.

Theoretical study of phase transitions in Sb_2Se_3 under compression

E. Lora da Silva^{1,2}, *S. Scandolo*³, *F.J. Manjon*²

¹NECL, IFIMUP, Department of Physics and Astronomy, Faculty of Science of the University of Porto, Porto, Portugal; ²Institute of Design and Manufacturing, MALTA Consolider Team, Technical University of Valencia, Valencia, Spain; ³The “Abdus Salam” International Centre for Theoretical Physics (ICTP), Trieste, Italy

Introduction

Since the identification of the tetradymite-like $R\text{-}3m$ phases of group-15 sesquichalcogenides (SCs) as 3D topological insulators [1], the family of A_2X_3 SCs have attracted a great deal of attention within the scientific community. From experimental data it has been evidenced that at room conditions the Sb_2Se_3 system crystallizes in the orthorhombic $Pnma$ phase, with first-order phase transitions occurring around 50 GPa,[2] i.e. to a disordered $Im\text{-}3m$ phase. On the other hand, several theoretical studies performed on the $R\text{-}3m$ structure of Sb_2Se_3 have suggested that the trigonal phase should undergo a topological quantum phase transition under compression [3]. In fact, it has experimentally been observed that such a topological transition can occur at 2 GPa [4].

Methods

The structural properties of the different crystalline phases of Sb_2Se_3 were calculated by using density-functional theory (DFT), with the Vienna *Ab-initio* Simulation Package (VASP) code [5]. The phonon properties were computed by using the supercell finite-displacement method implemented in the Phonopy package [6].

Results

Experimentally it is well-known that the $Pnma$ structural phase is the most stable polymorph for Sb_2Se_3 . However, we found from DFT enthalpy analysis, that the $R\text{-}3m$ phase is energetically more stable at low pressure values, up to at least 5 GPa. At around 5 GPa the $Pnma$ phase lowers the energy, becoming the most stable structure for Sb_2Se_3 ; at high-pressure (~ 21 GPa) the $Pnma$ phase is then surpassed by the disordered $Im\text{-}3m$ phase.

By probing the phonon dispersion curves of the $Pnma$ and $R\text{-}3m$ phases at 0 GPa, our calculations show that both systems are dynamically stable. These results suggest that the formation of the $R\text{-}3m$ phase for Sb_2Se_3 could therefore be feasible at close to ambient conditions. With respect to the disordered phase, we observe that only at 50 GPa is this phase dynamically stable. Moreover, by computing the $Pnma$ phonon dispersion curves at high pressure, we observe that negative frequencies start emerging at the zone-centre, therefore supporting the conclusions that a phase transition is likely to occur from the $Pnma$ to the disordered $Im\text{-}3m$ phase at high pressure. By further considering the disordered $Im\text{-}3m$ phase at 30 GPa, we observe that existing negative frequencies are localized at the high-symmetry M-point, consistent as being a zone-boundary instability. We have mapped out the anharmonic potential energy surfaces associated with the phonon instability, by generating

displaced supercells, which correspond to the phonon eigenvectors over a range of amplitudes. From this analysis we obtain a minimum energy configuration, in which the symmetry has lowered to $C2$ for this pressure range.

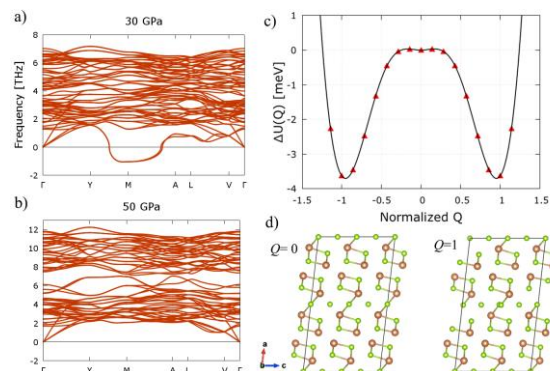


Figure 1 – Representation of the phonon dispersion curves of the disordered $Im\text{-}3m$ phase at 30 GPa (a) and at 50 GPa (b). Double-well potential-energy surfaces for the phonon instabilities associated with the M-point negative modes at 30 GPa (c). The crystal structures (d) represent the structure at $Q=0$ (left) and at $Q=1$ (right).

Conclusions

In summary, we have carried out a set of calculations to investigate the stability of possible phases, *viz.* $Pnma$, $R\text{-}3m$ and disordered $Im\text{-}3m$, of Sb_2Se_3 under hydrostatic pressures up to 60 GPa. We found that the disordered bcc-like $Im\text{-}3m$ phase is the most energetically stable phase at high pressure. By probing the low-pressure regions, we find that the $R\text{-}3m$ phase possess lower energy at 0 GPa than the $Pnma$, being surpassed by the latter at a moderate pressure range.

References

- [1] Chenurname Y. L. et al., Science, 325:178, 2009. Zhang H. et al., Nature Phys, 5:438, 2009.
- [2] Efthimiopoulos I. et al., Sci Rep, 3:2665, 2013.
- [3] Liu W. et al., Phys. Rev. B, 84:245105, 2011. Li W. et al., Phys. Rev. B, 89:035101, 2014.
- [4] Bera A. et al., Phys. Rev., Lett. 110:107401, 2013.
- [5] Kresse G. et al., Comput. Mater. Sci., 6:15, 1996.
- [6] Togo A., Phys. Rev. B, 78:134106, 2008.

Acknowledgements

The work has been performed under the Project HPC-EUROPA3 (HPC17R08HI), with the support of the EC Research Innovation Action under the H2020 Programme; in particular, the author gratefully acknowledges the support of ICTP and the computer resources and technical support provided by CINECA of the HPC centre.

Global simulations of Tayler instability in stellar interiors: The stabilizing effect of gravity

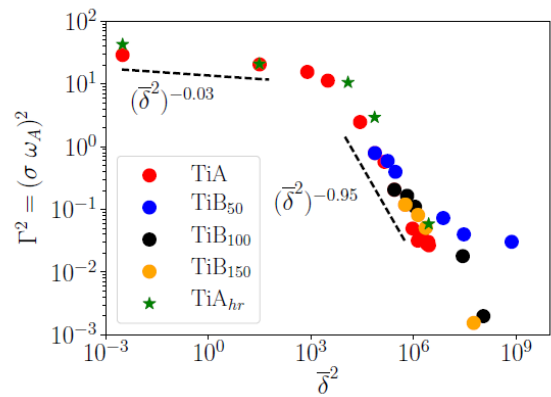
F. Del Sordo

Institute of Astrophysics, FORTH, Greece

Unveiling the evolution of toroidal field instability, known as Tayler instability, is essential to understand the strength and topology of the magnetic fields observed in early-type stars, in the isothermal core of the red giants, or in any stellar radiative zone. Here we want to study the nonlinear evolution of the instability of a toroidal field stored in a stably stratified stellar interior in spherical symmetry in the absence of rotation. In particular, we intend to quantify the suppression of the instability as a function of the Brunt-Vaisala (ω_{BV}) and the Alfvén (ω_A) frequencies. To do so, we use the MHD equations as implemented in the anelastic approximation in the EULAG-MHD code and perform a large series of high-resolution numerical simulations of the instability exploring the parameter space for the ω_{BV} and ω_A . We show that beyond a critical value gravity strongly suppress the instability, in agreement with the linear analysis. The intensity of the initial field also plays an important role, as weaker fields show much slower growth rates. Moreover, in the case of very low gravity, the fastest growing modes have a large characteristic radial scale, at variance with the case of strong gravity, where modes with small radial scale are excited too. In particular the number of growing radial modes ranges from $kr \approx 1$ to $kr \approx 18$ depending on the gravity and the magnetic field strength. In Figure 1 we show the dimensionless growth rate squared for the mode $m = 1$, as a function of δ^2 , which is the squared ratio of ω_{BV} and ω_A , for all the models we simulated (see Tables 1 and 2 in [1]). Our results illustrate that the anelastic approximation can efficiently describe the evolution of toroidal field instability in realistic stellar interiors. Moreover, the suppression of the instability as a consequence of increasing intensity of gravity, and hence of values of ω_{BV} , might play a role to explain the magnetic desert in Ap/Bp stars, which is the observational evidence that this kind of stars display only magnetic fields with intensity of at least the order of hundreds of Gauss. Since

weak fields are only marginally unstable in the case of strong gravity, we hypothesize that only very strong fields may escape from the interior of the stars, whilst weaker fields may be confined in the inner stellar region. In order to confirm this hypothesis further investigation and modeling will be needed.

The results of this HPC-EUROPA3 project have been published in [1].



References

[1] Global simulations of Tayler instability in stellar interiors: the stabilizing effect of gravity, MNRAS 490, 4281, 2020.

Acknowledgements

The work has been performed under the Project HPC-EUROPA3 (INFRAIA-2016-1-730897), with the support of the EC Research Innovation Action under the H2020 Programme; in particular, the author gratefully acknowledges the support of the School of Mathematics, University of Edinburgh and Birmingham Institute for Gravitational Wave Astronomy, University of Birmingham and the computer resources and technical support provided by EPCC.

Global simulations of Tayler instability in stellar interiors: The stabilizing effect of rotation

F. Del Sordo

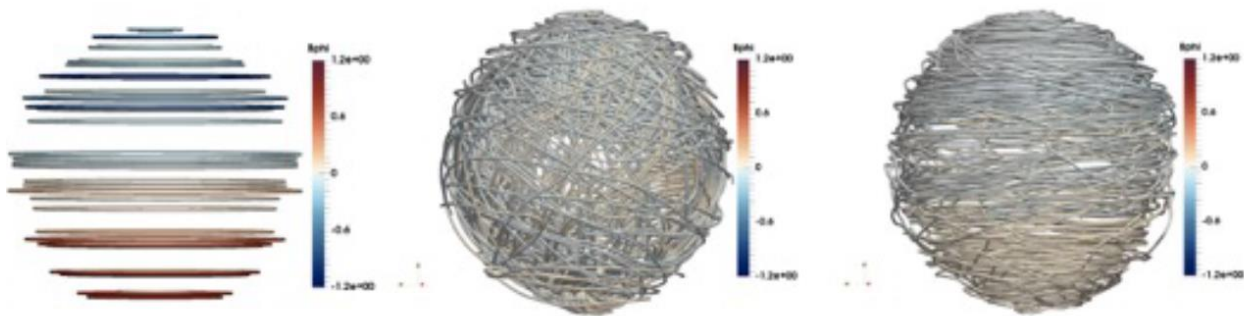
Institute of Astrophysics, FORTH, Greece

Unveiling the evolution of toroidal field instability, known as Tayler instability, is essential to understand the strength and topology of the magnetic fields observed in early-type stars, in the isothermal core of the red giants, or in any stellar radiative zone. Following up on our previous work (Guerrero, Del Sordo et al. MNRAS 490, 4281, 2019), here we want to study the nonlinear evolution of the instability of a toroidal field stored in a stably stratified stellar interior in spherical symmetry under the effect of rotation. In particular, we intend to quantify the suppression of the instability as a function of the rotation period P . To do so, we use the MHD equations as implemented in the anelastic approximation in the EULAG-MHD code and perform a large series of high-resolution numerical simulations of the instability exploring the parameter space for P . Combined with our previous work, that showed the stabilizing effect of gravity, this work is relevant for stellar astrophysics as it can explain the persistence of magnetic field in fully radiative stars as well as in the radiative cores of both solar-like stars and red giant stars.

We show that beyond a critical value of about 30 days, rotation strongly suppress the instability, in agreement with the linear analysis. The intensity of the initial field also plays an important role, as weaker fields show much slower growth rates. In Figure 1 we show the initial configuration of the field (left panel), the final configuration of the field in the absence

of rotation (center) and the final configuration in the presence of rotation with $P=10$ days. It is clear that the final configuration in the case of rotation preserves much better the initial topology of the field, hence showing a suppression of the instability. Also, it is important to underline that the final configuration in the non-rotating case is extracted after about 100 Alfvén travel times, whilst in the rotating case it is shown at about 15.000 Alfvén travel times. This illustrates even better the important role of rotation in the stabilization of toroidal magnetic fields. Our results confirm and extend the validity of our previous findings, in that the anelastic approximation can efficiently describe the evolution of toroidal field instability in realistic stellar interiors as well as in atmospheres. Further steps to be performed are the inclusion of differential rotation (which can lead to a dynamo effect) as well as the use of different stellar stratification profiles, in order to test the validity of our results to even more realistic cases.

The results of this HPC-EUROPA3 project are in the process of being submitted for publication to Monthly Notices of Royal Astronomical Society.



Expectations for the confirmation of Proxima c from a long-term radial velocity follow-up

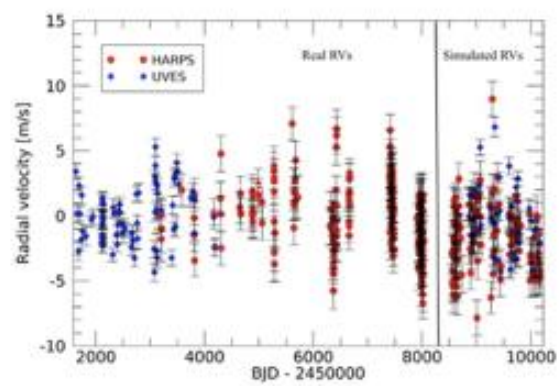
F. Del Sordo

Institute of Astrophysics, FORTH, Greece

Proxima c, a candidate second planet orbiting Proxima Centauri, was detected with the radial velocity (RV) method. The announced long orbital period ($5.21+0.26-0.22$ years), and small semi-amplitude of the induced Doppler signal (1.2 ± 0.4 m s⁻¹), make this detection challenging and the target worthy of a follow-up in the next years. We intend here to evaluate the impact of future data on the statistical significance of the detection. To do so, we simulate realistic radial velocities obtained with HARPS and UVES to be added to the published dataset, spanning up to one orbital period of Proxima c in the time range 2019-2023. We conceive 6 different scenarios. In Figure 1 an example of the produced dataset is depicted. Although the proposed scenarios are arbitrary, they are based on past observational campaigns and on what we deem affordable observing strategies to in-depth probe Proxima's planetary system. The longest time span we take into account is 2019-2023 so to include one additional orbit of Proxima c after the last published RVs. We also simulate time series over shorter periods, so to assess the potential of the RV technique before the full Gaia astrometric catalogue will be published, since Gaia astrometry is expected to confirm the existence of Proxima c. We analysed each dataset with models where the correlated noise is fitted with a quasi-periodic function (see [1]). We want to answer two questions: how will the results from a longer term follow-up look like if Proxima c exists? What if it does not exist? To answer, we conceived two sets of simulations. For the first, we assume that the orbits of Proxima b, Proxima c and the stellar activity pattern are well described by the parameters found in the discovery paper of Proxima c [2]. With a second set of simulations, we want to verify whether new RVs spanning 5 years may be sufficient to disprove the existence of Proxima c. To this purpose, we simulate datasets including only the signals due to Proxima b and stellar activity,

using the best-fit solution for the corresponding one-planet model derived in [2]. Our conclusion is that the detection significance of Proxima c increases depending on the amount of data collected, the number of instruments used, and the time-span covered, but on average we do not get strong statistical evidence. We predict that in the best-case scenario, in the next 5 years the detection of Proxima c can become significant at 4σ . If instead Proxima c does not exist, the detected signal may lower its significance to 2σ .

The results of this HPC-EUROPA3 project have been published in [1].



References

- [1]: Expectations for the confirmation of Proxima c from a long-term radial velocity follow-up, MNRAS 494, 1389, 2020.
- [2]: A low-mass planet candidate orbiting Proxima Centauri at a distance of 1.5 AU, Sci. Adv. 6, 7467, 2020.

Calculating the rotational period of Iota Horologii with a fractal approach

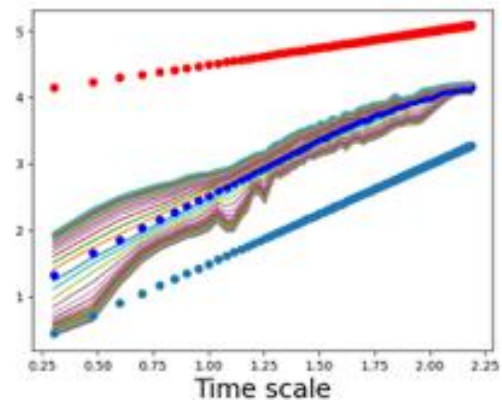
F. Del Sordo

Institute of Astrophysics, FORTH, Greece

A robust extraction of timescales characterizing planetary systems and stellar features, requires the use of state of the art techniques. Here we use a new approach, called MultiFractal Temporally Weighted Detrended Fluctuation Analysis (MF-TW-DFA, Agarwal, Del Sordo, Wettlaufer, 153 12 A, 2017) to analyse photometry. It quantifies a signal coming from a star as the combination of a deterministic dynamics and stochastic noise. This approach is based solely on temporal multifractality, and it is very flexible and versatile. It can distinguish the time scales over which a signal is affected by noisy dynamics without any a priori assumptions about the nature of these processes, and thereby examining an unfiltered time series of a stellar spectral signal. If a star hosts a planetary system, the time scales associated with stellar rotation and activity, as well as with planetary orbital motion, must be present. This method allows one to identify the dominant timescales of the observed system as agnostically as possible, also revealing the underlying nonlinear dynamics of the system. This approach is here used to analyse photometry of the young solar-like star Iota Horologii. It has mass and radius larger and it is 50% more luminous than the Sun. Iota Hor has been discovered to have quite short a magnetic cycle, of the order of 1.6 years. This is the shortest magnetic cycle ever measured for a solar-like star, so it makes the target very interesting. In order to understand it, it is important to correctly quantify its rotational period.

Previous studies have agreed on saying that Iota Hor rotates in about 7.7 days. Here the MF-TW-DFA is used on new data to test this hypothesis. The main outcome of the MF-TW-DFA is the fluctuation function, depicted in figure 1. It plots the fluctuation of the data around a temporally weighted mean value as function of logarithmic time. In such a way, it can identify the dynamics underlying some data. In the plot we can see the fluctuation function of a pure white noise (light

blue dots) and of pure red noise (red dots). The other lines represent the different moments of the fluctuation, and the 1st moment is displayed by the dark blue dots. The relevant time scales of a system can be seen where the fluctuation function presents some clear change of slope. Here the clearest knee is seen at 7.4 ± 0.1 days. This suggests a slightly shorter rotation period in contrast with those calculated previously. Also, we are able to further improve the accuracy, both because of the used technique and because of the analysed dataset a cadence of 1 hour. Here we report an accuracy of 0.1 days, instead of 0.2-0.6 previously proposed. We remark the importance of a good calculation of the rotation period in order to understand the magnetic cycles and activity of solar-like star, especially for those, like Iota-Hor, which also hosts a planetary system.



High-throughput materials discovery for sustainable battery materials

M.L. Evans

Theory of Condensed Matter Group, Cavendish Laboratory, University of Cambridge, United Kingdom

Introduction

It is becoming increasingly clear that rechargeable batteries have an important role to play in the effort towards decarbonising the global economy; humanity must outgrow its love affair with C=O bond formation and learn to love inorganic materials. Current battery technologies rely heavily on two elements, lithium and cobalt. Given the possible scale of demand for these materials, diversification of the chemistries we use in rechargeable batteries will be necessary to stabilise costs and improve sustainability.

In this project we apply high-throughput density-functional theory (DFT) calculations to screen prototype phases from open crystal structure databases, with the aim of finding new materials relevant to Li-, Na- and K-ion battery anodes. We have had previous success when combining this approach with high-fidelity crystal structure prediction on individual binary and ternary phase diagrams; by using this higher level approach across a wider materials space, new candidate phase diagrams could be suggested for more in-depth searches and for further experimental study.

Methods

Firstly, we identified the most useful material space to study in the manner described above. Initially, we shall consider all binary alloys of A_xB_y for $A=(\text{Li, Na, K, Mg, Ca})$, $B=(\text{Sc, Ti, V, Cr, Mn, Fe, Co, Ni, Cu, Zn}) + (\text{Al, Ga}) + (\text{Si, Ge, Sn}) + (\text{P, As, Sb}) + (\text{S, Se})$, i.e. all first-row transition metals, intermetallics, pnictogens and chalcogens. By using and extending the open-source *matador* [1] code, the unique prototype structures were geometry optimised in any other composition that a) did not already exist in the literature and b) obeyed appropriate oxidation/charge balance rules. Prototype structures were sourced from the ICSD and OQMD [2, 3] with further screening provided by the *Dscribe* package [4]. A pretrained MEGNet model [5] was used concurrently with DFT calculations as a surrogate model for formation energies and efforts were made to assess the efficacy of this model on unrelaxed configurations.

Results

In this space, there are 323 known compositions in the ICSD (excluding high pressure phases). Of the ~1000 relaxations, 71 lead to phases of novel compositions that are predicted to be stable or metastable (that is, on or close to the convex hull) at the PBE level. Initial results indicate that the MEGNet model performs well on relaxed structures across this wide materials space, indicating that it could decrease the number

of DFT calculations required, leading to a reduction in the required compute time by up to a factor of 2, and could at a very low cost, to accelerate the discovery of new materials. All results will be made publicly available in due course, both through conventional means, and through an OPTIMADE-compliant [4] REST API hosted at <https://optimade.odbx.science>.

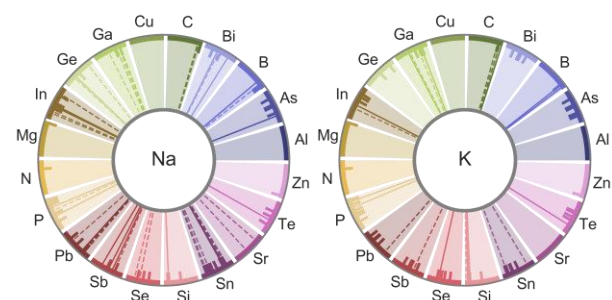


Figure 1 – Predicted stability of binary phases of Na and K. The shorter outer lines correspond to known stable compositions, the solid and dashed lines from the outer ring to the inner ring indicate novel DFT-predicted stable and metastable phases respectively.

Conclusions

By leveraging open crystal structure databases, the stability of binary alkali metal compounds has been assessed with DFT and surrogate ML models. The existence of several new low-lying phases arising from known prototypes is predicted in this battery-relevant space. This workflow is now being applied to ternary phases.

References

- [1] Evans, M <https://github.com/ml-evs/matador>.
- [2] Belsky, A et al. *Acta Cryst.* B58, 364-369 (2002).
- [3] Saal, J et al. *JOM* 65, 1501-1509 (2013).
- [4] Himanen, L et al. *Comp. Phys. Comm.* 247 (2020).
- [5] Chen, C et al. *Chem. Mater.* 31(9) 3564-3572 (2019).

Acknowledgements

The work has been performed under the Project HPC-EUROPA3 (INFRAIA-2016-1-730897), with the support of the EC Research Innovation Action under the H2020 Programme; in particular, the author gratefully acknowledges the support of Professor Adam Foster from the Department of Applied Physics at Aalto University and the computer resources and technical support provided by CSC.

The geometry of palladium doped gold clusters

P. Ferrari^{1,2}, *L. Delgado Callicó*¹, *J.M. Bakker*³, *E. Janssens*¹, *F. Baletto*²

¹Quantum Solid-State Physics, KU Leuven, Belgium; ²Department of Physics, King's College London, United Kingdom; ³Felix Laboratory, Radboud University, Nijmegen, The Netherlands

Introduction

Small Au_n^+ clusters have unique physical and chemical properties, directly influenced by the geometry these clusters adopt in their lowest-energy configuration, planar up to $n=7$ [1]. Pd doping has been shown to drastically modify the properties of Au_n^+ [2, 3], partly because the structures of the clusters are altered. This conclusion, however, has been addressed only by theoretical means. Here, the structures of $PdAu_{n-1}^+$ ($n \leq 9$) clusters are characterized by combining infrared spectroscopy with density functional theory (DFT) calculations.

Methods

Experiments were performed at the FELIX Laboratory in Nijmegen, The Netherlands. A beam of $PdAu_{n-1}^+$ ($n \leq 9$) clusters was produced by laser ablation using a carrier gas mixture of 2% Ar into He, forming $PdAu_{n-1}Ar_m^+$ complexes. The collimated beam was then exposed to the laser light of the free electron laser FELICE, before entering a time-of-flight mass spectrometer. IR spectra were obtained by comparing cluster–Ar complex intensities in mass spectra with (I) and without (I_0) IR light interaction. The IR signal was calculated as $Y_{IR} = -\ln(I/I_0)/E_{IR}$, with E_{IR} the normalized laser pulse energy.

IR spectra are also calculated by DFT calculations, using the NWChem software package [4]. The long-range corrected LC-wPBEh functional is employed in combination with the Def2-TZVPP basis set and Def2-ECP pseudopotentials. The vibrational modes of the $PdAu_{n-1}Ar_m^+$ ($n \leq 9$; $m \leq 6$) clusters are computed for several geometries, where not only the positions adopted by the metal framework are varied but also the adsorption sites of the Ar atoms. A benchmark analysis was performed to select the level of theory, in which IR spectra of the $PdAu_3Ar_6^+$ complex was calculated using different functionals. Comparison between the experimental data and the calculations showed that the LC-wPBEh functional had best performance.

Results

Figure 1 shows three examples of the geometry identification process, for the clusters $PdAu_3Ar_4^+$, $PdAu_6Ar_2^+$ and $PdAu_9Ar_1^+$. Each peak in the experimental data (in black) corresponds to a cluster vibrational mode at a specific energy. At the bottom, in blue, the DFT results are presented. These spectra are constructed by assuming a Gaussian shape around each calculated vibrational frequency, with a width of 5 cm^{-1} . In the three cases, experiment and theory agree very well, with all the features of the experimental curves well reproduced by the calculations. Other isomers miss the features of the experiment.

While Au_4^+ is known to adopt a planar tetragonal geometry [1], Pd doping induces a 2D to 3D transition, with $PdAu_3^+$ having a pyramidal 3D structure. The structure of Au_7^+ is a hexagon with an Au atom in the centre. This planar cluster is highly stable, with six delocalized valence electrons [3]. The

structure of $PdAu_6^+$, in contrast, is 3D, with the Au atoms adopting a planar pyramidal geometry having the Pd atom at the top. This cluster also possesses a high stability as revealed by photofragmentation experiments [3]. In $PdAu_6^+$, the Pd dopant delocalizes one of its d-electrons, giving six delocalized electrons. Finally, $PdAu_9^+$ adopts a highly symmetric tree-dimensional pyramidal structure. Previous experiments have shown that in this cluster, Pd does not delocalize any electron, so the cluster has eight delocalized electrons from the gold atoms; therefore, this cluster also possesses a high stability [3].

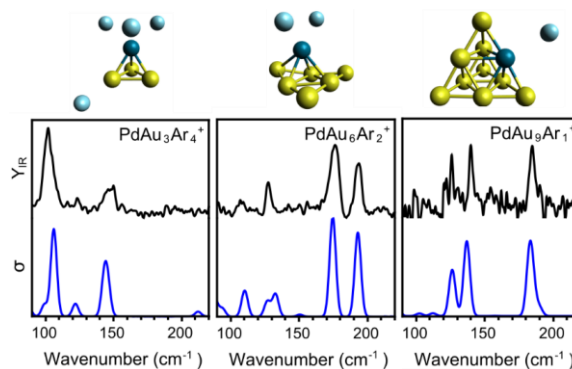


Figure 1 – Experimental (top, black) and simulated (bottom, blue) IR spectra of $PdAu_3Ar_4^+$, $PdAu_6Ar_2^+$ and $PdAu_9Ar_1^+$. The corresponding geometries are depicted at the top.

Conclusions

The geometries adopted by $PdAu_{n-1}^+$ ($n \leq 9$) clusters in their lowest-energy configuration have been identified by combining infrared spectroscopy experiments and DFT calculations. Pd doping is seen to drastically modify the structures of the pure Au clusters, inducing a transition from planar to three-dimensional geometries already from the tetramer, while Au_n^+ clusters remain planar up to $n=7$.

References

- [1] P. Ferrari, G.-L. Hou, O. L. Lushchikova, F. Calvo, J. M. Bakker, E. Janssens PCCP, 2020.
- [2] P. Ferrari, J. Vanbuel, P. Janssens, P. Lievens, Acc. Chem. Res. 51, 3174–3182, 2018.
- [3] P. Ferrari, H. A. Hussein, C. J. Heard, J. Vanbuel, P. Lievens, R. L. Johnston, E. Janssens, Phys. Rev. A 97, 052508, 2018.
- [4] M. Valiev et al., Comput. Phys. Commun. 1181, 1477, 2010.

Acknowledgements

The work has been performed under the Project HPC-EUROPA3 (INFRAIA-2016-1-730897), with the support of the EC Research Innovation Action under the H2020 Programme; in particular, the author gratefully acknowledges the support of F. Baletto at King's College London and the computer resources and technical support provided by Edinburgh Parallel Computing Centre (EPCC).

Modelling supernova-driven dynamo with cosmic rays

F. Gent¹, G. Sarson²

#1 Aalto University, Espoo, Finland, #2 Newcastle University Newcastle, UK

Introduction

The majority of galaxies, similarly to our own Milky Way, are rotating about a super-massive central black hole. Most of the visible mass in each galaxy is condensed into stars with the remaining 10% or more comprising the interstellar medium (ISM) of ionized plasma, gas and dust, which fills the voids between the stars. The ISM is highly turbulent and plays a critical role in galactic evolution and structure, star formation and stellar feedback, accretion of material between the galaxies and the intergalactic medium (IGM). Away from the galactic centre, most of the visible material is compressed into a thin disk about the axis of rotation, where most stars form. As some of the larger, fast-burning stars approach the end of their life cycle they become supernova (SN), exploding huge amounts of energy and recycling some of their mass into the ambient ISM. This energy heats and stirs the ISM to drive turbulence, which redistributes some of the ISM into cold dense clouds from which the next generation of new stars are subsequently born.

As part of this process the magnetic field, which is ubiquitous throughout astrophysical bodies, is stirred and twisted by the turbulence and the large-scale differential rotation and stratification within the disk to form a dynamo, which grows the magnetic field on the smallest scales, but also orders the field on the scale of the disk. As it grows and evolves large scale structure the magnetic field provides a back reaction to the flow, effecting its kinetic properties. It is increasingly understood by astronomers and astrophysicists that this magnetic field is pivotal in explaining some of the poorly understood processes at work in the life cycles of galaxies, and our understanding of cosmic processes. Another key feature of SN-driven turbulence is the acceleration in the blast waves of plasma particles [1] to relativistic (light) speeds, which are understood to contribute as much energy to the ISM as each of the thermal and kinetic energy. The trajectories of these charged cosmic rays (CR) is strongly coupled to the magnetic field lines [2].

Methods

We have previously successfully employed the Pencil Code [3] to solve the equations of magnetohydrodynamics (MHD) to model a galactic dynamo in a highly compressible, thermally unstable ISM without CR. We use a vertically stratified sliding periodic box to model a differentially rotating segment of ISM under conditions typical of spiral galaxies and the solar neighbourhood in particular. Now we apply fluid approximation equations for CR energy and CR flux [2], to be able to examine the dynamo and subsequent ISM dynamics under much more realistic physical conditions. From this we aim to make predictions about the processes that give rise to star formation, galactic outflows and fountain, and derive sub-grid scale models of turbulence relevant to many unresolved astrophysical problems.

Results

During this visit we implemented a suite of single SN simulations with uniform magnetic field and various diffusive

time-scales for the CR to identify the effect each has on the evolution of the remnant and most physically relevant diffusive behaviour of the model CR (Figure 1).

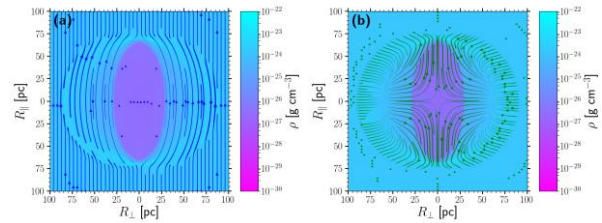


Figure 1 – Evolution of the magnetic field (a) and flow (b) in SN remnant

The analysis of the CR flux and interaction with the magnetic field has yet to be applied to the simulation data and shall continue remotely. Once evaluated hundreds (thousands) of such SN will then be applied in a stratified rotating segment of the galactic disk (Figure 2) as demonstrated in a prototype.

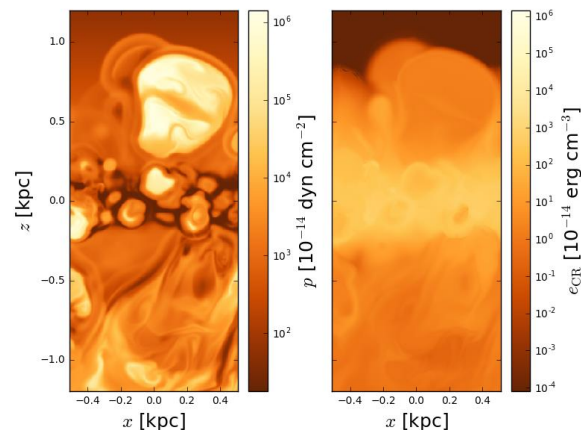


Figure 2 – 2D slices of thermal pressure and cosmic ray energy density from early kinematic dynamo stage.

Conclusions

We need to evolve the field over a Gyr to see the effect of a mean horizontal field on the CR distribution and its feedback on the global dynamics. Results from the local SN simulations shall be used to identify which CR parameters will be most appropriate.

References

- [1] Kulsrud R. M., 2004, Plasma Physics for Astrophysics. Princeton Univ. Press, Princeton, NJ. [2] Snodin A. P., et al., 2016, MNRAS, 457, 3975. [3] Gent F. A., et al., 2013, MNRASL, 430, L40.

Acknowledgements

The work has been performed under the Project HPC-EUROPA3 (INFRAIA-2016-1-730897), with the support of the EC Research Innovation Action under the H2020 Programme; in particular, the author gratefully acknowledges the support of Newcastle University and the computer resources and technical support provided by EPCC.

Role of complex glycans in epidermal growth factor receptor

M. Giryč¹, T. Rog¹, M. Grzybek², I. Vattulainen^{1,3}

¹University of Helsinki, Finland; ²Paul Langerhans Institute Dresden, Germany; ³Tampere University, Finland

Introduction

Human epidermal growth factor receptor (EGFR) is one of the most significant cancer-related membrane proteins. Recent findings in protein glycochemistry have shown that several cancers are linked to alterations in EGFR glycosylation [1]. Given that full sequences of EGFR glycans have been experimentally determined [1] and atomistic simulations have reached a level where protein dynamics can be examined over realistically long time scales, there is now an outstanding opportunity to unravel atomistic details of glycan-modulated conformational states of EGFR through atom-scale molecular dynamics (MD) simulations. In previous work [2], we unlocked the leading effects of glycosylation on EGFR conformation and dynamics using the known minimal-core glycan sequence. In this study, based on the previous results [2] and the full-sequence data on glycans observed in the EGFR [1], we investigated the glycan-mediated conformational dynamics of EGFR under conditions that reflect realistic circumstances.

Methods

We carried out all-atom MD simulations of an EGFR monomer embedded in a lipid membrane composed of DOPC (60 mol%), SM (20 mol%), and cholesterol (20 mol%). The ectodomain of EGFR was glycosylated. The systems were adapted from our previous work: details of system compositions, protein conformation, and simulation protocols are described in our recent paper [2]. The changes that were made for the present study dealt with EGFR glycan sequences. While in our previous work [2] EGFR was glycosylated with minimal-core glycans (approx. 30% of total glycans in EGFR), in the present work the glycans were chosen to describe glycosylation matching full-length glycan sequences [1]. The N-glycosylation sites were located at the residues N32, N151, N328, N337, N389, N420, N504, N544, N579, and N599 [1]. In the simulations, we used the OPLS3 (all-atom) force field for the protein and lipids and the GLYCAM (version 06h-3) force field for glycans. The simulations were performed using Gromacs 5.1.4.

Results

We performed simulations of EGFR with full-length glycans. The match between simulations and experiments [3,4] was found to be excellent. Particularly, to unveil the importance of glycans in the conformation of the EGFR ectodomain, we considered the average distance between the N-terminus of EGFR and the phosphates in the membrane plane. The larger this distance, the less tilted is the ectodomain, and the more visible is the ligand binding site. In non-glycosylated EGFR the distance observed in our previous work was about 3.3 nm [2]. For EGFR where glycosylation was based on minimal-core glycans, the distance increased to 4.5 nm [2]. However, when we here used glycan sequences matching realistic

circumstances [1], the ectodomain stood up, as demonstrated by an increase in the distance to a value of about 5.9 nm (see Figure 1). For comparison, the distance measured in FRET experiments between the N-terminal fluorescence tag in EGFR and a membrane was reported to lie in a range of 6.2-8.0 nm [3,4]. Considering that the contribution of the fluorescent tag to the protein-membrane distance is up to 2 nm, the simulation results observed here for EGFR with long glycans are in very good agreement with experiments.

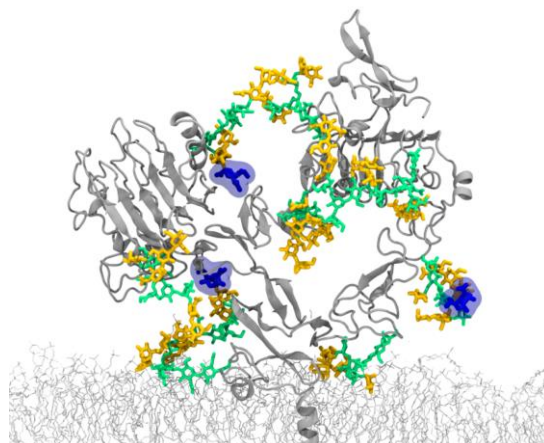


Figure 1 – Fully N-glycosylated EGFR monomer embedded in a lipid bilayer. Colour scheme: green (minimal core glycans); yellow (full glycans, see ref. [1]); blue (sialic acid residues).

Conclusions

These large-scale simulations demonstrate that glycosylation plays a decisive role in conformational behavior of complex membrane receptors, such as EGFR, and ligand-receptor binding is modulated by glycans. The results indicate that not only the length of glycan sequences but also their exact content modulate the conformational profile of membrane receptors' ectodomains. Based on these results, it would be highly justified to elucidate very closely how disease-specific glycan profiles control the orientation of membrane proteins, and hence their ligand binding and signaling. Extensive studies in this context are currently underway.

References

- [1] Liu YC et al., PNAS 108 (28):11332-11337, 2011.
- [2] Kaszuba K et al., PNAS 112 (14):4334-4339, 2015.
- [3] Ziolkiewicz I et al., Cytometry 83 (9):794-805, 2013.
- [4] Kozer N et al., Phys Biol 8 (6):5479-5492, 2011.

Acknowledgements

The work has been performed under the Project HPC-EUROPA3 (INFRAIA-2016-1-730897), with the support of the EC Research Innovation Action under the H2020 Programme. We gratefully acknowledge the computer resources and technical support provided by HLRS.

First-principles study of structure and magnetism in triazolium/guanidinium Cu hypophosphites and imidazolium Cu formate

J.N. Gonçalves, A. Stroppa

Departamento de Física and CICECO, Universidade de Aveiro, Aveiro, Portugal; CNR-SPIN, c/o Dip.to di Scienze Fisiche e Chimiche, Coppito (AQ), Italy

Introduction

Perovskite Metal-Organic Frameworks have shown fascinating properties [1]. Hypophosphites and formates allow for several different amine cations. A recent work used symmetry arguments to suggest that [Trz]Cu hypophosphite or [Him]Cu formate could be ferroelectric due to the combination of possible distortions [2]. Here we have explored these compounds using first-principles density functional theory calculations.

Methods

We have used the Vienna Ab initio Simulation Package, VASP (5.4.4) [3], which uses a plane wave basis set and the projector augmented-wave (PAW) method. We considered the GGA-PBE exchange-correlation functional and added an effective Coulomb repulsion U to Cu 3d orbitals, according to the simplified approach of Dudarev et al. The FINDSYM (7.0) program was used to find the symmetry of the optimized structure, the VESTA software for analysis and structural representation [25], and PHONOPY to post-process VASP results and calculate phonons.

Results

The structural optimization did not reveal significant ferroelectric distortions. Possible phonon instabilities revealed small energy lowering. We conclude the possibility for ferroelectricity with significant polarization or critical temperature is low. The results show, however, that Cu orders magnetically with unusual low-dimensional ordering (see Fig.1), with one- and two-dimensional ordering for the hypophosphite and for the formate, respectively.

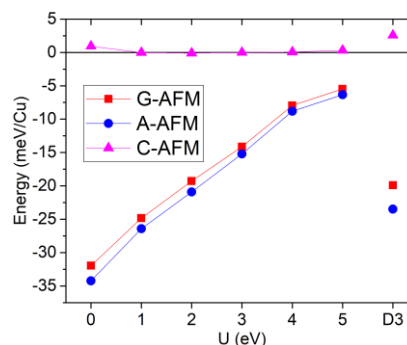


Figure 1 – Total energies, relative to the ferromagnetic state, for different AFM orders in [Trz]Cu(H₂POO)₃; GGA+U as a function of U, and GGA+D3(BJ).

Conclusions

Starting from the Mn analogues, we have explored the possible Cu hypophosphites and imidazolium Cu formate. We could not find significant energy lowering distortions with respect to the $P2_1c$ space group of the Mn analogues, which suggests these compounds are not ferroelectric. We have shown that [Trz]Cu hypophosphite and [Him]Cu formate exhibit strong, almost ideal 1D and 2D magnetism, respectively, highlighting the role of strong octahedral distortions in combination with different periodic orderings of the organic cations. These results motivate the future synthesis and characterization of these compounds.

References

- [1] W. Li, Z. Wang, F. Deschler, S. Gao, R. H. Friend, and A. K. Cheetham, Chemically diverse and multifunctional hybrid organic–inorganic perovskites, *Nature Reviews Materials* 2, 16099 (2017).
- [2] H. L. B. Boström, M. S. Senn, and A. L. Goodwin, Recipes for improper ferroelectricity in molecular perovskites, *Nature Communications* 9, 2380 (2018).
- [3] G. Kresse and J. Furthmüller, Efficient iterative schemes for ab initio total-energy calculations using a plane-wave basis set, *Physical Review B* 54, 11169 (1996).

Acknowledgements

The work has been performed under the Project HPC-EUROPA3 (INFRAIA-2016-1-730897), with the support of the EC Research Innovation Action under the H2020 Programme; in particular, J. N. Gonçalves gratefully acknowledges the support of Alessandro Stroppa and CNR-SPIN and the computer resources and technical support provided by CINECA.

Distribution and composition of functional groups on 2D MXene surfaces

R. Ibragimova, P. Rinke, H.-P. Komsa

Department of Applied Physics, Aalto University, Aalto, Finland

Introduction

MXenes are an abbreviation for the wide class of 2D materials with the general chemical formula of $M_{n+1}X_n$ denoting chemical composition, where M is a layer of a transition metal, X is a layer of carbon or nitrogen [1].

Synthesis of MXenes is usually done by selective etching of precursors using an acid solution, most commonly hydrofluoric acid (HF) [1]. Surface of MXenes is always covered by functional groups T_x which are adsorbed from the solution and usually are O, OH, and F. One of the commonly made assumptions for many computational studies is modelling the surface with a pure termination, either O, F, or OH [1-3]. This might be a reasonable assumption for some applications but not surface-sensitive applications (MXenes are mostly used for). To solve this simplification, we developed a multiscale computational scheme to find the composition and distribution of O, OH, and F functional groups on the MXenes' surfaces. Here we extend a number of MXenes simulated using our developed scheme to Ti_2N , Nb_2C , Ti_4N_3 , Nb_4C_3 .

Methods

Our multi-scale scheme developed earlier [4] is based on three steps. First, we adopt the cluster expansion (CE) method together with the density functional theory (DFT) to construct a Hamiltonian for the given system.

Second, the CE model together with Monte Carlo (MC) simulations enables us to access the configurational free energies and efficiently sample the configurational space. With the help of Monte Carlo simulations equilibrium distribution of the functional groups on the surface can be obtained for large supercells. To analyse the structures, the mixing energies of functional groups on the surface are evaluated. Then in order to access the thermodynamically averaged structure but on a smaller scale, the special quasi-random structures method is used. Thus, best representative structures with a suitable for DFT calculations size are obtained from larger supercells. Finally, we calculate the Gibbs free energy of formation in solution over the whole composition range, carefully accounting for the role of experimental factors, such as temperature, pH and the work function.

Results

In this study, we have combined multiple theoretical approaches to simulate functionalization of distinct MXene surfaces. Our results are consisting of description of mixing energies and the distribution of the functional groups from Monte Carlo simulations, Gibbs free energies of formation of best representative structures as function of composition, and how the surface functionalization changes the electronic properties. Surface distributions of functional groups over distinct concentrations have been obtained. We have shown that functional groups are equally distributed without any segregation regardless of the concentration. Continuously coloured surface distribution of functional groups on Ti_2N for

several distinct concentrations is shown in Figure 1. We find that mixing energies for all studied systems have a minimum at 50 % of O- and OH-terminations and without any F.

We demonstrate the similarity of surface composition and distribution of functional groups, despite the different chemical interior of MXenes. Distribution on the surface and their energetics looks similar for all studied systems. However, the electronic properties vary depending on the chemical nature of M layer, as well as on X layer variation.

Conclusions

In this study, we have shown that functional groups form mixed compositions on the surface of the most known MXenes. Our large-scale simulations show that mixed functional groups are equally distributed at the surfaces for certain concentrations. Furthermore, we have constructed Gibbs free energy diagrams for different concentrations of functional groups depending on pH and the work function. Our multiscale modelling approach for determining the distribution and composition of functional groups on a surface allows us to make a generalization for the class of 2D MXenes systems in order to more accurately predict their structures and properties.

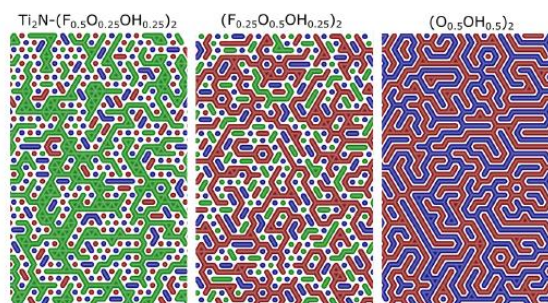


Figure 1 – Distribution of O, OH, and F on the surface of Ti_2N , where the nearest neighbour atoms of the same type are connected by bonds to highlight the ordering (F is represented by green, OH by blue and O by red colour).

References

- [1] Anasori B. et al., *Nat. Rev. Mater.*, 2(16098), 2017.
- [2] Khazaei M. et al., *Phys. Rev. B*, 92(075411), 2015.
- [3] Khazaei M. et al., *J. Mater. Chem. C*, 5:2488–2503, 2019.
- [4] Ibragimova R. et al., *ACS Nano*, 3:9171–9181, 2019.

Acknowledgements

The work has been performed under the Project HPC-EUROPA3 (INFRAIA-2016-1-730897), with the support of the EC Research Innovation Action under the H2020 Programme; in particular, the author gratefully acknowledges the support of Paul Erhart, Department of Physics, Chalmers University of Technology and the computer resources and technical support provided by KTH-PDC.

First principles simulations of pure and germanium-doped amorphous silica

G.M. Lo Piccolo

Università degli Studi di Palermo, Palermo, Italy

The network topology analysis of amorphous silica (α -SiO₂) was first addressed by King who proposed the shortest path criterion to identify closed paths of alternating Si–O bonds. According to this criterion, a ring is defined as the shortest closed path connecting two oxygen atoms bonded to the same Si atom. If the path is formed by n bonds (or, equivalently, by $2n$ atoms) the ring is called an n -membered ring. By applying King's algorithm to silica, the topological analysis results in a broad ring-size distribution and a quasi random orientation of the SiO₄ tetrahedra. These features arise from the flexibility of the Si–O–Si and Si–O–Si–O angles which determines a high degree of structural disorder beyond the short range.

By using molecular dynamics simulations and the "melt and quench" procedure within the SIESTA code, we generated different periodic cells by varying the cooling rate and cell pressure applied to the initial supercell. This allowed us to obtain a large number of silica models showing different ring-size distributions. Starting from a β -cristobalite supercell of 216 atoms, the system was subjected to the following simulation stages: (i) equilibration at 300K and 1 atm; (ii) melting by linearly increasing the temperature to 5000K using a Berendsen thermostat; (iii) equilibration at 5000K for 100 ps; (iv) quenching of the melt down to 0K at a rate of 8 to 80Kps⁻¹.

The ring distribution analysis of the final models revealed that higher quenching rates lead to less stable structures characterised by a higher number of three- and four-membered rings. The results obtained by applying a quenching rate of 10, 20, and 40Kps⁻¹ show that five- and six-membered rings are always the most frequent structures, followed by seven membered rings. This can be explained by considering that, when melted silica is cooled, it can undergo two different transformations. If the cooling is performed at a slow rate, the melt crystallises and cristobalite is formed. If the cooling is faster, the liquid cannot equilibrate with the forming solid and the result is the formation of amorphous silica. Despite having different properties, the two polymorphs ideally derive from the same silica melt and have similar local structures. In particular, the short- and medium-range topology of α -SiO₂ resembles that of cristobalite which exhibits only six-membered rings. By looking at the distribution of the so-called small-membered rings (size 3 and 4) in the ring statistics, we see that the populations depend on the simulation conditions and thermal history of the sample. In fact, when the temperature of the melt is lowered avoiding crystallisation, the liquid enters in the supercooled

phase and its structure rearranges in a continuous fashion to follow the system's temperature. This determines that the viscosity of the system increases with decreasing temperature up to the point at which it becomes too high and the structure of the supercooled liquid is frozen-in in the final glass.

Since small rings are typical of an out-of-equilibrium state of silica, their formation energy is higher than that of six-membered rings and part of the excess of energy is stored in strained Si–O–Si bond angles. The presence of distorted angles determines the formation of local high-energy structures like three- and four-membered rings. For regular planar three-membered rings, the Si–O–Si angle takes the value of 130:5° whereas for regular planar four-membered rings its value is 160:5°. In both cases the Si–O–Si angle is far from its energetically optimal value (144°–155°) and for this reason the rings tend to release the excess energy by breaking a strained bond and turn into a bigger ring. This behaviour can be observed when silica is exposed to UV light, X-rays, or γ -rays. In these cases, the strained bonds contained in three- and four-membered rings absorb the incoming photons and jump to the lowest electronic spin triplet state, causing the opening of the ring and the formation of a pair of point defects called E' centre and non-bridging oxygen hole centre (NBOHC). To study this phenomenon, we selected different small rings present in the silica models and simulated the E'–NBOHC pair formation by breaking a weakened Si–O bond and letting the network rearrange. This was done by gradually increase the Si–O distance and letting the system adapt to the perturbation. The same procedure was applied to simulate the rupture of non-strained bonds in six-membered rings. The analysis of the potential energy curves showed that the energy required to activate the reaction in strained silica is almost one order of magnitude lower than that found for unstrained silica (if expressed in eV). This result is consistent with the assumption that the higher the angular strain of a O–Si–O angle, the higher the reactivity of the sample to energetic radiation.

Nonetheless, in both cases, the reaction passes through different intermediate local minima which gradually move the NBOHC defect away from the E' centre. The product of the reaction is thus a set alternative structures in which the two defects are 5 to 8 Å far apart. These results will be refined by making new simulations and will be presented and discussed in an upcoming scientific paper.

Magnetic properties of nanodiamonds: theoretical investigation

Š. Masys¹, Z. Rinkevicius²

¹Institute of Theoretical Physics and Astronomy, Faculty of Physics, Vilnius University, Lithuania; ²Department of Theoretical Chemistry and Biology, School of Engineering Sciences in Chemistry, Biotechnology and Health, KTH Royal Institute of Technology, Stockholm, Sweden

Introduction

Nanodiamonds (NDs) belong to a family of carbon-based nanomaterials that recently gained a lot of attention in such biomedical areas as tissue engineering, labelling, quantum sensing, and drug delivery [1]. Concerning the latter, a combination with the bioimaging capabilities could make NDs a very promising platform for the clinical theranostic applications, thereby allowing a more effective exploitation of these nanoparticles.

In order to fully utilize the bioimaging potential of NDs, one has to be aware of their magnetic properties determined by a variety of the incorporated point defects. In this work, density functional theory (DFT) calculations were performed to find out the influence of the size of NDs on their electronic g -tensor values, with the emphasis put on the accuracy of the geometries of NDs obtained using very fast GFN2-xTB method developed by Stefan Grimme's group [2].

Methods

More than 20 point defects, including nitrogen-vacancy, silicon-vacancy, and germanium-vacancy centers that are especially attractive for biomedical applications, were introduced into fully hydrogenated and octahedrally shaped NDs of C_{84} and C_{165} size, visualized in Figure 1. In addition to GFN2-xTB method, PBEh-3c scheme [3] was also utilized for the geometry optimizations.

Concerning the electronic g -tensor calculations, they were performed within the hybrid DFT framework employing B3LYP functional [4, 5] and 6-311G(2d,2p) basis set [6] – a combination shown to give reliable results in our previous study [7].

Results

For $C_{84}H_{64}$, the largest deviation between the isotropic electronic g -tensor values of GFN2-xTB and PBEh-3c geometries was demonstrated by substitutional manganese, reaching 1165 parts per million (ppm). On the other hand, the smallest deviation of interstitial carbon did not exceed 1 ppm. For $C_{165}H_{100}$, the largest deviation was exhibited by copper in the semi-vacancy form with 205 ppm, while the smallest deviation of 1 ppm was given by hydrogen-vacancy, hydrogen-vacancy-nitrogen, and hydrogen-vacancy-oxygen complexes. On the whole, the average deviation for all 23 studied point defects was 153 ppm in case of $C_{84}H_{64}$ and 43

ppm in case of $C_{165}H_{100}$, pointing to the fact that as the size of NDs increases and the surface effects play less important role the geometries obtained with GFN2-xTB tend to more resemble those obtained with more sophisticated PBEh-3c method.

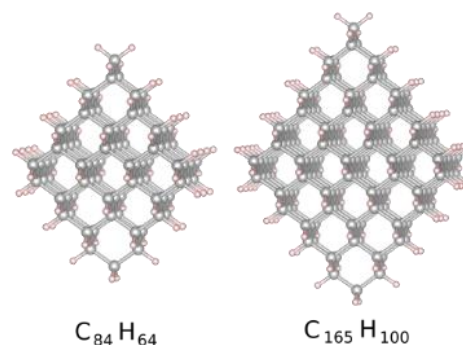


Figure 1 – Fully hydrogenated and octahedrally shaped NDs of C_{84} and C_{165} size. Carbon atoms are represented by gray, while hydrogen atoms by pink balls. Point defects were inserted as close to the center of NDs as possible.

Conclusions

The observed tendency indicates that magnetic properties of large enough NDs (~1.5 nm in diameter and larger) can be calculated with a good precision when their geometries are evaluated at the GFN2-xTB level, reducing the need for more sophisticated methods like PBEh-3c and thereby saving a huge amount of computational resources.

References

- [1] Chipaux M et al., *Small*, 14(24):1704263, 2018.
- [2] Bannwarth C et al., *J. Chem. Theory Comput.*, 15(3):1652-1671, 2019.
- [3] Grimme S et al., *J. Chem. Phys.*, 143(5):054107, 2015.
- [4] Becke A D, *J. Chem. Phys.*, 98(7):5648-5652, 1993.
- [5] Stephens P J et al., *J. Phys. Chem.*, 98(45):11623-11627, 1994.
- [6] Krishnan R et al., *J. Chem. Phys.*, 72(1):650-654, 1980.
- [7] Masys Š et al., *J. Chem. Phys.*, 151(4):044305, 2019.

Acknowledgements

The work has been performed under the Project HPC-EUROPA3 (INFRAIA-2016-1-730897), with the support of the EC Research Innovation Action under the H2020 Programme; in particular, the author gratefully acknowledges the support of Zilvinas Rinkevicius at the Department of Theoretical Chemistry and Biology (KTH Royal Institute of Technology) and the computer resources and technical support provided by KTH-PDC.

First-principles investigation of structural, electronic and magnetic properties of two-dimensional CrGeTe₃ magnet

A.A. Musari¹, D. Amoroso², S. Picozzi²

¹Physics with Electronics Unit, Department of Science Laboratory Technology, Moshood Abiola Polytechnic, Abeokuta, Nigeria; ²Consiglio Nazionale delle Ricerche, Istituto SPIN, UOS L'Aquila, Italy

Introduction

The recent growth of the family of two-dimensional (2D) materials in the last decades among scientists is quite impressive, and this can be fundamentally attributed to the effective and remarkable exfoliation of graphene from graphite [1]. This gave an insight on how basic structural elements can be strikingly different from their parent compounds, this in turn has been subsequently observed about large numbers of exfoliated 2D materials, to be rich in multi-billion dollar market applications. The layered transitional metal tri-chalcogenides with structural formula ABX₃ where A = Mn and Cr, B = Si and Ge while X = S; Se and Te have been studied widely as a promising candidate for 2D magnets. More so, the presence of transition metal atoms has however opened the interesting possibilities of emergence of magnetism, since some of the existing pristine 2D materials are experimentally found to be intrinsically non-magnetic.

Methods

The present work was carried out using the density functional theory as implemented in Vienna ab initio simulation package code (VASP) within the framework of generalized gradient approximation (GGA) with an effective Hubbard U parameter using projected augmented-wave (PAW) method. The exchange correlation functional as parameterised by Perdew, Burke and Ernzerhof was adopted [2]. These calculations also consider the van der Waals forces between the layers by adopting a correction based on DFT-D2 method of Grimme, this proves to improve the description of the system. The strong-correlated correction (GGA+U) method is considered to treat the localized 3d electrons of Cr. Dudarev method was adopted. For all the calculations a plane wave basis set expanded in energy with a cut-off 450 eV. The k-point sampling with a mesh of 9 x 9 x 3 and 9 x 9 x 1 Monkhorst-Pack scheme were used for the bulk and single-layer systems respectively. For the monolayer a large vacuum space of thickness 20 Å is incorporated in order to avoid any interaction between images.

The calculation of magnetic exchange interactions requires the four possible different magnetic configurations [3]. The exchange interaction parameters between spins were extracted by fitting the calculated total energies from various magnetic configurations to the Heisenberg spin Hamiltonian on a honeycomb lattice.

Results

The band structures for both bulk and single layer CrGeTe₃ are depicted in Figure 1 and it shows they are indirect semiconductors with estimated bandgaps for 0.416 eV and 0.168 eV for spin polarized and spin-orbit coupling respectively for the bulk system while for single layer the bandgaps are 0.386 eV and 0.149 eV for spin polarized and spin-orbit coupling respectively.

The magnetic interaction parameters were computed. The nearest neighbour (NN) exchange interaction J₁ and the third nearest neighbour (3NN) interaction J₃ are ferromagnetic of magnitude 6.69 meV and 0.437 meV respectively, but the second nearest neighbour (NNN) interaction J₂ is anti-ferromagnetic of magnitude 0.175 meV.

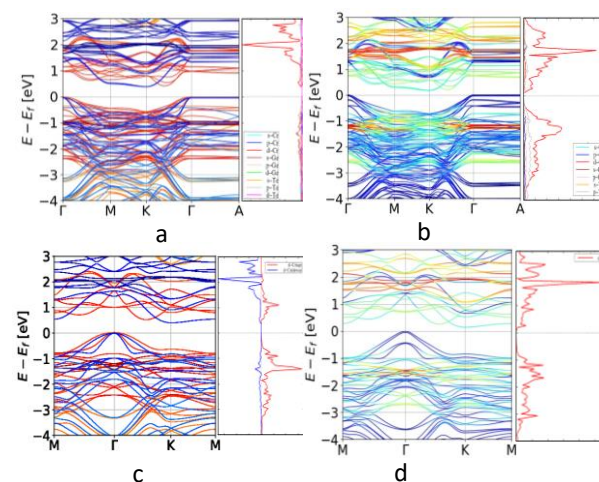


Figure 1 – The band structure and the partial density of state for (a) spin polarized (b) spin-orbit coupling for bulk CrGeTe₃ (c) spin polarized (d) spin-orbit coupling single layer CrGeTe₃.

Conclusions

Detailed investigations of structural, electronic of van der Waals transition-metal trichalcogenides (CrGeTe₃) and the exfoliated monolayer using density functional theory have been carried out. In order to understand the rich magnetic behaviour observed in the single layer CrGeTe₃, the local spin models using DFT energy of the magnetic ground state was used. The second and third nearest neighbour interactions J₂ and J₃ respectively, in addition to the first nearest neighbour J₁ were calculated and presented.

References

- [1] Novoselov, K. S. et al., Nature, 490: 192200, 2012.
- [2] Perdew, J. P. et al., Phys. Rev. Lett., 77: 38653868, 1996.
- [3] Sivasdas, N et al., Phys. Rev. B, 91:235425, 2015.

Acknowledgements

This work has been performed under the Project HPC-EUROPA3 (INFRAIA-2016-1-730897), with the support of the EC Research Innovation Action under the H2020 Programme; in particular, the author gratefully acknowledges the support of CNR-SPIN and University of Chieti, Italy, the computer resources and technical support provided by CINECA.

Topology and dynamics of confined three-dimensional active nematics

G. Negro

Dipartimento di fisica, Università degli studi di Bari and INFN, Sezione di Bari, Bari, Italy

Introduction

Active liquid crystals are soft materials characterized by self-driven units with an elongated shape. Physical realizations are suspensions of cytoskeletal filaments with molecular motors and bacterial cultures, which are known to develop structures with typical orientational order closely resembling nematic phases in liquid crystals. Confining a liquid crystal imposes topological constraints on the orientational order, allowing global control of equilibrium systems by manipulation of anchoring boundary conditions. A similar strategy can be used to control active liquid crystals, as previous studies have proven [1]. Using a coarse-grained description and numerical simulations we explore the different hydrodynamic regimes of active nematic shells, immersed in an isotropic fluid, in 3D.

Methods

In the past, continuum, active nematic theories have been proven successful in describing dense active materials that produce dipolar flow fields. In These continuum theories the relevant information for the description of the system state are encoded in a few coarse-grained fields. The hydrodynamic interaction between the suspended constituents and the underlying fluid is also considered, since advective phenomena occurring in active systems play a relevant role. Activity is usually introduced as a phenomenological (active) stress tensor, which accounts for the force density exerted on the surrounding fluid due to the autonomous movement of constituents. This approach has been widely used to study bidimensional systems numerically.

Due to the huge computational cost, much less attention has been given to fully three-dimensional geometries, despite a significant part of experimental research concerning the physics of shells and droplets of liquid crystals in fully three-dimensional environments. We have implemented a Lattice Boltzmann solver, coupled with finite difference methods, for the numerical solution of the hydrodynamic equations of active fluids. The use of MPI standard for parallelization allowed us to consider fully three-dimensional systems, with systems sizes big enough for the truthful description of shells.

Results

We focus on the case of extensile activity (positive values of the parameter controlling the strength of the active forcing) and tangential anchoring on shell surface. The dynamics of the active shell is controlled by a complex interplay between topological defects and their induced flows. For low values of activity, the shell (captured in Figure 1a as the contour plot of first parameter of the Westin metrics) is stationary and $4 + 1/2$ topological defects form (Figure 1a-b). These defects rotate regularly for high enough values of extensile activity. Enlarging activity the defects rotation is no more regular, the shell deforms (Figure 1c) and start to rotate in a chaotic way

as can be seen looking at the components of the angular velocity of the shell in panel (d) of Figure 1.

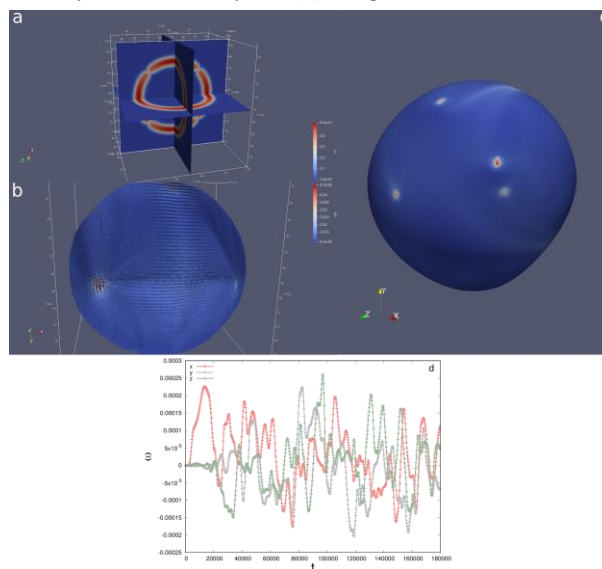


Figure 1 – (a) Contour plot, on two planes cutting the nematic shell, of the second parameter of the Westin metrics. High values correspond to nematic ordered regions. (b) Director field on the surface of the nematic shell. 4 half integer defects forms on shell surface, and rotate regularly for high enough values of extensile activity. (c) Enlarging activity the defects rotation is no more regular, the shell deforms and start to rotate in a chaotic way as can be seen looking at the angular velocity of the shell in panel (d).

Conclusions

Our simulations show that the dynamics of the active shell is controlled by a complex interplay between topological defects and their induced flows. Depending on the strength of activity, different dynamical behaviours are observed, ranging from the regular oscillations of topological defects on the shell surface to chaotic motion. Our model is also able to capture shell deformations in 3D. This allows for a more complete study of these systems and their characterization.

References

[1] Keber C. et al., *Science*, 345(6201):1135-1139, 2014

Acknowledgements

The work has been performed under the Project HPC-EUROPA3 (INFRAIA-2016-1-730897), with the support of the EC Research Innovation Action under the H2020 Programme; in particular, the author gratefully acknowledges the support of Davide Marenduzzo of the Department of physics of the University of Edinburgh and the computer resources and technical support provided by EPCC.

Quark production and chemical thermalization at the initial stages in ultra-relativistic heavy-ion collisions

J. Peuron

European Centre for Theoretical Studies in Nuclear Physics and Related Areas (ECT*) and Fondazione Bruno Kessler, Strada delle Tabarelle, Villazzano (TN), Italy

Introduction

In the extreme temperatures produced in ultra-relativistic heavy-ion collisions the atomic nucleus "melts" and a new state of matter resembling perfect fluid called Quark-Gluon Plasma (QGP) is formed [1,2]. The QGP consists of quarks and gluons, which in ordinary matter form composite particles such as protons and neutrons. Isotropization of QGP after the collision and equilibration between quarks and gluons, which is also called chemical thermalization, are still poorly understood. Due to computational limitations the evolution of the gluons has been studied in much more detail than that of the quarks. Thus, understanding the nonequilibrium evolution of the quarks is crucial in order to understand chemical thermalization.

The initial background gluon field after the collision is invariant under Lorentz boosts along the collision axis in the high energy limit. By deriving an initial condition for the quarks on top of this boost-invariant background field [3], the problem becomes effectively 2+1 dimensional and numerically tractable. The aim of the visit was to study the initial conditions [3] and adapt the existing code for this formulation. The ultimate aim of the project is to simulate the equilibration of quarks after an ultra-relativistic heavy-ion collision.

Methods

The initial gluon fields can be studied using real time lattice techniques in the classical approximation. Lattice treatment is also applicable for quarks, but unfortunately classical approximation is not because of the Pauli principle. Consequently, the computational cost of simulating quarks is considerably higher than that of gluons.

There are two main tasks. Firstly, one has to modify classical Yang-Mills simulation code with dynamical Wilson fermions successfully employed in previous HPC applications [4] to accommodate the formulation presented in [3]. Secondly one has to make sure that this is done correctly by cross-checking with analytically calculable test case, which is given by free spinors.

Results

The initial conditions for the boost-invariant spinors are currently mostly understood and adapted to our framework. We have also implemented the boost-invariant Dirac equation, which gives the time-evolution of the fermion fields. With this modification the code is adapted for the boost-invariant spinors presented in [3].

We have also carried out analytical calculations, which are needed for the cross-checks. We have derived free spinors in the continuum and on the lattice in the boost invariant

framework. Furthermore, we have cross-checked their correctness with free boost-invariant Dirac equation both in the continuum and on the lattice. At the moment we are still carrying out some of the remaining consistency checks for the free spinors before the implementation.

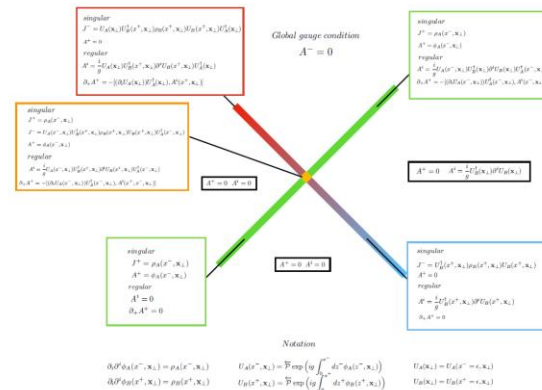


Figure 1 – The background gauge field configuration on top of which the spinors are evolved in order to obtain the initial condition. The two lines represent the nuclei. The spatial coordinate is represented by the x-axis and time-coordinate by y-axis.

Conclusions

Important progress was made during the visit, which provides the basis for an ongoing collaboration between the visitor and Prof. Schlichting’s research group in Bielefeld. Our future plans include measuring simple observables such as the particle number for free spinors and checking that it is conserved and well behaved under gauge transformations. When cross-checks are done, we implement the initial conditions and perform the simulations.

References

[1] BRAHMS Collaboration Nucl. Phys. A757 (2005) 1-27.
 [2] STAR Collaboration Nucl. Phys. A757 (2005) 102-183.
 [3] F. Gelis, N. Tanji, JHEP 02 (2016) 126, arXiv 1506.03327 [hep-ph].
 [4] M. Mace, N. Mueller, S. Schlichting, S. Sharma, Phys. Rev. Lett. 124 (2020) 19, 191604.

Acknowledgements

The work has been performed under the Project HPC-EUROPA3 (INFRAIA-2016-1-730897), with the support of the EC Research Innovation Action under the H2020 Programme; in particular, the author gratefully acknowledges the support of S. Schlichting and Faculty of Physics of the University of Bielefeld and the computer resources and technical support provided by HLRS.

Double quantum dots thermocouple

N.W. Talarico¹, M. Josefsson², M. Leijnse²

¹QTF Centre of Excellence, Turku Centre for Quantum Physics, Department of Physics and Astronomy, University of Turku, Finland; ²Solid State Physics and NanoLund, Lund University, Lund, Sweden

Introduction

The investigation of thermoelectric properties at the nanoscale has taken a leap forward in recent years due to the impressive experimental advances that were made in quantum transport in molecular and nano-scale devices. One promising candidate where to observe efficient ways of controlling heat flow and harvesting of thermal energy is represented by capacitively coupled quantum dots junctions.

Methods

The aim of the project is to discuss the problem of transport in double quantum dots systems by using the non-equilibrium Green's function method (NEGF) [1] for describing the effects of correlations in the charge and heat transport dynamics [2–4].

Moreover, we want to benchmark the results obtained with the former method with the master-equation based real time diagrammatic approach (RTD) that is also widely used to describe transport in nano-scale structures [5–7]. The two methods differ from the perturbative scheme built in their theoretical framework, explicitly the NEGF method is perturbative in the interaction strength, whereas the RTD technique is perturbative in the coupling with the external reservoirs or leads.

We have performed numerical simulations for the setup describing a quantum dot thermocouple as sketched in Figure 1 panel (a). The schematic shows the possible parameters that one can tune for the simulations.

The project was devoted to edit and set-up existing codes to simulate this new system and in finding the space of parameters where the two techniques give the same physical results. NEGF simulations were performed on energy grid spanning region from -400 GHz to +400 GHz with a grid spacing of 0.08 GHz.

Results

For a first comparison we have calculated the thermocurrent [3,6] in one of the cold contacts developed under the application of a thermal bias between left and right reservoirs $T_H = 2$ K, $T_C = 1$ K, as a function of the energy level position of one of the quantum dot $V_{g1} = -V_{g2}$ and for two different values of the tunnel coupling with the leads $\Gamma = 1$ GHz and $\Gamma = 10$ GHz. For simplicity we have considered a non-interacting system and electrically unbiased leads $U = 0$ and $V_b = 0$.

We have found that the two methods are in very good agreement for a whole decade change of the tunnel coupling, see Figure 1 panel (b) and (c).

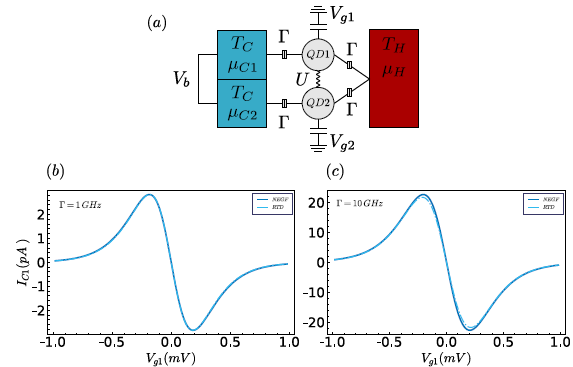


Figure 1 – (a) Schematic representation of the microscopic model considered in this work. Thermo-current in one of the cold contact calculated with NEGF method (solid blue) and the RTD approach (dash dot cyan) for tunnel coupling (b) $\Gamma = 1$ GHz and (c) $\Gamma = 10$ GHz.

Conclusions

This preliminary analysis has shown that the RTD technique, that is perturbative in the coupling with the external leads, is a reliable method in a wide range of the coupling strength that gives the same results of the NEGF approach that is an exact numerical method in the case of a non-interacting system.

We are currently exploring the values of the many-body interactions allowed by the two methods and the effects that they have on the thermo-electric properties of the system.

References

- [1] G. Stefanucci and R. van Leeuwen, Nonequilibrium Many-Body Theory of Quantum Systems: A Modern Introduction (Cambridge University Press, 2013).
- [2] N. W. Talarico, S. Maniscalco, and N. L. Gullo, physical status solidi (b) 256, 1800501 (2019).
- [3] N.W. Talarico, S. Maniscalco, and N. Lo Gullo, Phys. Rev. B 101, 045103 (2020).
- [4] B. Dutta, D. Majidi, N.W. Talarico, N. Lo Gullo, H. Courtois, and C. B. Winkelmann, Phys. Rev. Lett. 125, 237701 (2020).
- [5] M. Josefsson and M. Leijnse, Phys. Rev. B 101, 081408 (2020).
- [6] M. Josefsson, A. Svilans, H. Linke, and M. Leijnse, Phys. Rev. B 99, 235432 (2019).
- [7] A. Svilans, M. Josefsson, A. M. Burke, S. Fahlvik, C. Thelander, H. Linke, and M. Leijnse, Phys. Rev. Lett. 121, 206801 (2018).

Acknowledgements

The work has been performed under the Project HPC-EUROPA3 (HPC17U919Q), with the support of the EC Research Innovation Action under the H2020 Programme; in particular, the authors gratefully acknowledge the support of the Solid State Physics and NanoLund divisions at Lund University, and the computer resources and technical support provided by KTH.

Spatial distribution of oxygen abundance and nitrogen-to-oxygen ratio in galaxies

I.A. Zinchenko

Main Astronomical Observatory, National Academy of Sciences of Ukraine, Kyiv, Ukraine

Introduction

The chemical composition of galaxies plays an important role in their formation and evolution during the lifetime of the Universe.

In this work, we study the distributions of the oxygen abundance and the N/O abundance ratio for a large sample of 1431 nearby galaxies from the Mapping Nearby Galaxies at Apache Point Observatory (MaNGA) survey [1].

The robust estimation of the chemical abundance is crucial for studying such relations, therefore we take advantage of two precise strong line methods, which are based on different observational and theoretical sets of calibration data.

Methods

We analysed the MaNGA spectra following [2]. To fit the emission lines we used our code ELF3D for emission line fitting in the optical spectra. The code is based on the *iminuit* library, which in turn is based on the SEAL Minuit2 code. Since Minuit2 is sensitive to the choice of the initial parameters, we implemented an option of the Monte Carlo (MC) approach to choose the initial parameters of the fit. This approach significantly increases the robustness of line fluxes estimation. The computational time per one data cube in the robust MC mode has been reduced owing to the MPI parallelization of the code. Our sample of galaxies was processed on two clusters, MareNostrum4 at the Barcelona Supercomputing Center (BSC) and Golowood at the Main Astronomical Observatory of the NAS of Ukraine.

The oxygen abundance $12+\log(\text{O}/\text{H})$ and the nitrogen-to-oxygen ratio $\log(\text{N}/\text{O})$ were derived using the empirical R calibration [3] and the Bayesian model-based code HII-CHEMISTRY (HCm) [4]. We used HCm version 4.1, assuming photoionization models from Cloudy v.17.00 with spectral energy distributions (SEDs) from POPSTAR, with linear interpolations on the grid of O/H, N/O.

Results

In Figure 1 we show relations between the parameters of the derived linear radial fits for both O/H and N/O as a function of the stellar mass in the galaxies from our sample.

Both the R calibration and the HCm methods confirm negative O/H and N/O gradients for the majority of galaxies from our sample. On average, both the O/H and the N/O gradients correlate with the stellar mass of a galaxy.

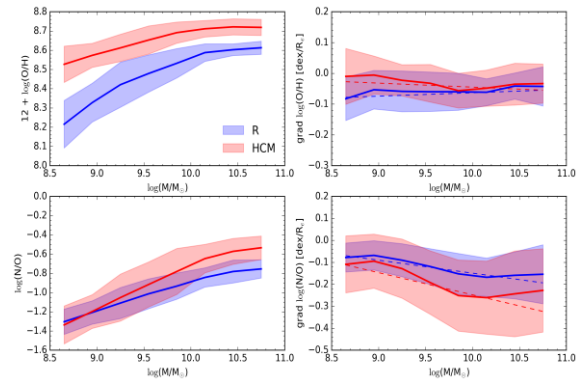


Figure 1 – The galaxy-center O/H, N/O, and their gradients as a function of galaxy mass.

Conclusions

Both methods of abundance determination confirm negative oxygen abundance gradients for the majority of galaxies. Median values of the oxygen abundance gradients are -0.06 dex/Re according to the R calibration and -0.03 dex/Re for the HCm method.

The median value of the N/O gradient is also negative, -0.12 dex/Re for the R calibration and -0.18 dex/Re for the HCm method.

Both methods of the abundance calculation show the correlation between the O/H gradient and the stellar mass of a galaxy.

References

- [1] Bundy K. et al., *ApJ*, 798:7, 2015.
- [2] Zinchenko I.A. et al., *MNRAS*, 462:2715, 2016.
- [3] Pilyugin L.S. et al., *MNRAS*, 457:3678, 2016.
- [4] Perez-Montero E., *MNRAS*, 441:2663, 2014.

Acknowledgements

The work has been performed under the Project HPC-EUROPA3 (INFRAIA-2016-1-730897), with the support of the EC Research Innovation Action under the H2020 Programme; in particular, the author gratefully acknowledges the support of the Instituto de Astrofísica de Andalucía and the computer resources and technical support provided by the Barcelona Supercomputing Center (BSC).